AD-A071 130   ADVISORY GROUP FOR AEROSPACE RESEARCH AND DEVELOPMENT--ETC F/G 20/14
                AEROSPACE PROPAGATION MEDIA MODELLING AND PREDICTION SCHEMES FO--ETC(U)
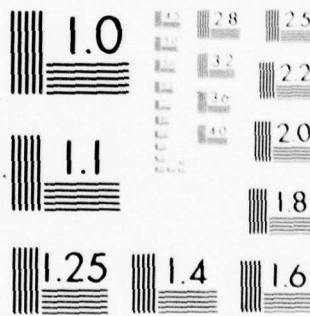   MAY 79

UNCLASSIFIED   AGARD-LS-99

                                                                        NL

1 OF 3

AD
A071130

1.0

1.1

1.25 1.4 1.6

2.8 2.5
3.2 2.2
3.6
4.0 2.0

1.8

MICROCOPY RESOLUTION TEST CHART
NATIONAL BUREAU OF STANDARDS-1963-A

AGARD-LS-99

AGARD

ADVISORY GROUP FOR AEROSPACE RESEARCH & DEVELOPMENT)

7 RUE ANCELLE 92200 NEUILLY SUR SEINE FRANCE

AGARD LECTURE SERIES No. 99

Aerospace Propagation Media Modelling and Prediction Schemes for Modern Communications, Navigation, and Surveillance Systems

NORTH ATLANTIC TREATY ORGANIZATION

79 07 13 054

NORTH ATLANTIC TREATY ORGANIZATION

ADVISORY GROUP FOR AEROSPACE RESEARCH AND DEVELOPMENT

(ORGANISATION DU TRAITE DE L'ATLANTIQUE NORD)

AGARD Lecture Series No.99

(6) AEROSPACE PROPAGATION MEDIA MODELLING AND PREDICTION SCHEMES FOR MODERN COMMUNICATIONS, NAVIGATION, AND SURVEILLANCE SYSTEMS.

(11) May 79   (12) 208 p.

400 043

79 07 12 051

THE MISSION OF AGARD

The mission of AGARD is to bring together the leading personalities of the NATO nations in the fields of science and technology relating to aerospace for the following purposes:

— Exchanging of scientific and technical information;

— Continuously stimulating advances in the aerospace sciences relevant to strengthening the common defence posture;

— Improving the co-operation among member nations in aerospace research and development;

— Providing scientific and technical advice and assistance to the North Atlantic Military Committee in the field of aerospace research and development;

— Rendering scientific and technical assistance, as requested, to other NATO bodies and to member nations in connection with research and development problems in the aerospace field;

— Providing assistance to member nations for the purpose of increasing their scientific and technical potential;

— Recommending effective ways for the member nations to use their research and development capabilities for the common benefit of the NATO community.

The highest authority within AGARD is the National Delegates Board consisting of officially appointed senior representatives from each member nation. The mission of AGARD is carried out through the Panels which are composed of experts appointed by the National Delegates, the Consultant and Exchange Programme and the Aerospace Applications Studies Programme. The results of AGARD work are reported to the member nations and the NATO Authorities through the AGARD series of publications of which this is one.

Participation in AGARD activities is by invitation only and is normally limited to citizens of the NATO nations.

PREFACE

This Lecture Series No.99 on the subject of Aerospace Propagation Media Modelling and Prediction Schemes for Modern Communications, Navigation, and Surveillance Systems is sponsored by the Electromagnetic Wave Propagation Panel.

The Lecture Series will review modelling and prediction topics which have been presented at a number of meetings of the AGARD Electromagnetic Wave Propagation Panel in the last few years. Modeling and Prediction Schemes of the aerospace radio and optical propagation environment based on media characterization have become essential to meet requirements of operational accuracies in communication, navigation, and surveillance in military and civilian systems.

The lectures include the following topics:
- General modelling and prediction schemes
- Aerospace (atmosphere, ionosphere, and the space environment) media-characterization
- Short- and long-term prediction techniques across the RF and optical spectrum and agreement with observational data
- Detection and communications through scattering channels
- Adaptability of prediction techniques to radio and optical communication, navigation and surveillance systems operating in the aerospace environment
- Effects of geophysical disturbances on the state of the media and their predictability

A Round Table Discussion will conclude the formal presentations, with participation of all speakers. Such interchange of ideas will serve as the basis for an up-to-date review of the state of the art.

H.SOICHER
Lecture Series Director

LIST OF SPEAKERS

Lecture Series Director: Dr. H.Soicher
                            Signal Processing Division
                            Center for Communications Systems
                            US Army Communication Research and
                            Development Command
                            Fort Monmouth
                            New Jersey
                            USA

Dr. P.A.Bradley   Professor E.Raschke
Science Research Council   Institute of Geophysics and Meteorology
Appleton Laboratory   University of Cologne
Ditton Park   Kerpener Strasse, 13
Slough SL3 9JX   5000 Cologne 41
UK   Germany

Professor R.S.Kennedy   Dr. C.M.Rush
Department of Electrical Engineering and United States Department of Commerce
Computer Science   Institute for Telecommunication Sciences
Massachusetts Institute of Technology   325 Broadway
Cambridge, Massachusetts 02139   Boulder, Colorado 80302
USA   USA

Dr. R.A.McClatchey   Dr. E.V.Thrane
Infrared Physics Branch   Norwegian Defence Research Establishment
Air Force Geophysics Laboratory   P.O. Box 25
AFGL/PHI   Kjeller
Hanscom Air Force Base   Norway
MA 01731
USA

CONTENTS

"AEROSPACE PROPAGATION MEDIA MODELING SCHEMES FOR MODERN COMMUNICATIONS,
NAVIGATION AND SURVEILLANCE SYSTEMS" - AN OVERVIEW
by
H. SOICHER
COMMUNICATIONS SYSTEMS CENTER
US ARMY COMMUNICATIONS R&D COMMAND
FORT MONMOUTH, NJ 07703

High-performance current and planned military and civilian systems operating in the aerospace environment across the electromagnetic spectrum require propagation media characterization to meet reliability and accuracy goals. The atmosphere, ionosphere, and the space environment constitute the media within which the EM (including optical) waves propagate. The operational users of communications, navigation, and surveillance systems must have continuous background information regarding the state of these media as well as their variability and their response to natural disturbances. Designers of future systems must have long range estimates of propagation parameters associated with these systems. Further, given the geographic (and geomagnetic) variability of the media and the global nature of today's and tomorrow's systems the state-of-the-media information has to be given on a regional as well as on a global basis.

The user requirements pertain to the specification of medium conditions on a variable time and space scale. The user would like to know the state of the medium through which his propagation circuit passes at the present and in the future. Further, should any change, either gradual or abrupt, occur, the user would like to know how his circuit is affected and how to compensate for a possible adverse effect. The system planner requires long-range (years in advance) predictions, while the systems operator needs short-term (days to weeks in advance) predictions which are sometimes referred to as forecasts.

A way of obtaining a prediction capability is through the creation of a model which encompasses the important physical parameters which describe the medium, and whose change cause a variability in the medium. There are two main types of models. The first is a morphological (empirical) model which attempts to provide a global description of the average behavior of the medium under given conditions. This type of model is based on a long-term data base taken at many locations under varying conditions. The extension and extrapolation of the localized measurements to entire regions, as well as from one set of conditions to another is implicit in the model. The second type is the physical model which aims at a description of the medium through the understanding of the interrelated physical processes which govern the state of the media and its variability. A world-wide long-term measurement program coupled with the availability of large scale computer systems able to "digest" the large quantities of data has greatly advanced the state-of-the-art in empirical modeling. In fact, the models may be reaching their limit in terms of accuracy of prediction, with further improvements possible through measurements previously unavailable at geophysically unique locations, and more sophisticated data evaluation techniques. The physical models which hold a greater promise of future improvement currently suffer from a lack of total understanding of the physics of the media.

What are the medium parameters that affect propagation and thus require characterization? They are best divided by the system frequency of operation and the medium of traversal. The earth's atmosphere (including ionosphere and the space environment) mainly hinders propagation. It provides a means to guiding propagation energy in only a few instances. The two regions of interest are the neutral lower atmosphere - the meteorological regions, and the ionized upper atmosphere which ranges from about 60 Km to several thousand Km from the earth's surface.

The gaseous lower atmosphere is of importance in refraction and time delay (due to its refractive index which is variable in space and time) and in attenuation (due to atmospheric gasses) at frequencies above 10 GHz at all angles of elevation. Hydrometeors (principally rain) are of importance in attenuation of frequencies above 5 GHz, and in the scattering of EM energy.

Large amplitude fluctuation, often referred to as multipath fadings, occurring on horizontal or low-elevation (below 5°) paths result from either reflection from the earth's surface under abnormal refractive conditions, or from the influence of large gradients of atmospheric layers. These fluctuations are the main factor in attenuation at frequencies below 10 GHz. Rapid fluctuations in signal amplitude (scintillations) may be produced by small scale turbulent fluctuations in the refractive index. These inhomogenities in the refractive index may also give rise to scattering of the waves.

In the infrared and visible frequency range the lower atmosphere's mixture of molecules, aerosols, (haze, fog, dust, clouds - anything which is a suspended particulate in the atmosphere) and hydrometeors which are variable in space and time, are the medium parameters. The relevant propagation effects caused are refraction, absorption, scattering, turbulence effects and path radiance. These hold for a wavelength range of $0.3\mu m$ up to $15\mu m$ which covers the area of optical and optronical systems.

The ionosphere guides EM energy at frequencies up to about 30 MHz through its reflective qualities. It may guide higher frequencies due to scattering ionization irregularities. However, the main effect, of the ionosphere at the higher frequencies is disruptive.

Low frequency (LF) and very low frequency (VLF) waves propagate in a waveguide mode with the upper boundary being the D layer (at about 100 Km) and the lower boundary being the earth's surface, and with electron density gradients along the waveguide boundaries. Changes in the time and space domain of these boundaries obviously affects the propagation characteristics. At the medium and high frequency (MF, HF) range to ~30 MHz) the denser ionospheric layers, the E layer and the F layer, reflect the waves and thus guides them.

At VHF and above a radio signal transmitted along an earth-space path normally penetrates the ionosphere and is modified by the presence of electrons and the earth's magnetic field. The signal is affected by large scale variation in the path integrated electron concentration as well as by small-scale density irregularities. The effects which are frequency dependent and generally decrease with increasing frequency include scintillation (VHF and above up to ~7 GHz), absorption, direction-of-arrival variations, propagation time-delay, frequency change and polarization variation.

At VHF and in the upper portions of the HF band sporadic E plays a significant role in the scattering radio waves. Ionization irregularities (patches of ionization with densities varying from ~2% and higher from the ambient density) also cause scattering of waves in these frequency ranges.

Superimposed on the normal variability of the near-earth environment (diurnal, seasonal, and solar cyclical variations) are the occasional abrupt emissions of electromagnetic and particulate radiation from the sun. These cause direct and indirect effects on the aerospace media that adversely affect the performance of EM Systems. Observation of the solar disc may be used for the prediction of an oncoming solar flare that will emit a burst of X-rays, radio waves, and energetic particles - although not accurately. Solar activity appears to intensify in 11-year intervals with the maximum level due to occur in 1979-1980. The solar flare generally gives rise to bursts of X-ray and extreme ultra violet (EUV) radiations, a burst of radio noise, emission of energetic particles, and emission of a plasma shock wave. X-rays affect the structure of the D layer of the ionosphere within minutes, and thus may serve as forecasters for future oncoming disturbances. Radio bursts, also almost instantaneous, cause an increase in radio noise. EUV bursts affect the density structure of the ionospheric layers. Solar particle (protons, heavier particles, and electrons) events may cause additional ionization at polar regions. The most energetic particles may reach the earth within 20-30 minutes, and the effects of solar particles may last for hours and up to several days. A blast of solar plasma into the interplanetary space, which reaches the earth after three or four days, results in a geomagnetic storm, aurorae, and the heating of the neutral atmosphere. These will cause alteration or propagation conditions, and in enhanced optical background (due to aurorae).

In the Lecture Series the interrelationship between the propagation parameters of the media and the design and performance of current and future EM systems operating in these media will be discussed. The physical structure of the media and its variability under normal and disturbed conditions will be presented. The modeling of the media and the prediction of their state in order to assure the reliability of system performance will emerge as the optimal solution.

PROPAGATION AT MEDIUM AND HIGH FREQUENCIES, 1 : PRACTICAL

RADIO SYSTEMS AND MODELLING NEEDS

by

P. A. Bradley

S.R.C., Appleton Laboratory, Ditton Park, Slough, Berks. SL3 9JX, U.K.

SUMMARY

The principal phenomena associated with ground wave and sky-wave propagation at MF and HF are discussed. Particular consideration is given to transmission loss and coverage range, the dependence on ground-reflection properties, the state of the ionosphere and the Earth's magnetic field. Regular temporal changes depending on time-of-day, season and solar activity, together with short-term fading are noted. The importance of antenna design in system operation is emphasised. Practical usage of the MF and HF bands is illustrated.

A review of propagation parameters susceptible to modelling is followed by an examination of requirements for long-term propagation models for system design, frequency allocation and assignment. Short-term models are shown to be of potential value for frequency management, but the logistic difficulties of producing and disseminating results from these models are emphasised.

1. INTRODUCTION

The medium and high frequency bands of the radio spectrum are used almost exclusively by terrestrial services; although under certain conditions transionospheric propagation is possible, space services employ higher frequencies for which propagation characteristics are more favourable. Ground-wave propagation is more effective the lower the frequency, but there are difficulties in providing efficient antennas. The MF band (300 kHz-3 MHz) is particularly suitable for sound broadcasting. HF (3-30 MHz) ground-wave signals are of value in certain mobile services requiring only a relatively short coverage range. Reflection from the ionosphere provides a means of long-distance propagation that has been exploited at HF since the earliest days of radio. MF sky-wave signals are usually only significant at night because of the large daytime ionospheric absorption; they tend to be a nuisance rather than supporting a primary service, but nonetheless their propagation characteristics need to be known.

The principal propagation phenomena encountered at MF and HF are reviewed : ground-wave propagation is considered in Section 2 and sky-wave propagation in Section 3. Section 4 gives particular consideration to current usage of these frequency bands and in Section 5 parameters susceptible to modelling are discussed. Some reference ground-wave models formulated by the International Radio Consultative Committee (CCIR) of the International Telecommunication Union (ITU) are presented. Sky-wave models are examined in depth in the companion account[1]. In Section 6 the requirements for propagation models are considered.

2. GROUND-WAVE PROPAGATION AT MF AND HF

In the case of propagation over a plane earth between elevated transmitting and receiving antennas the received signal is the resultant of a direct and a ground-reflected wave. The amplitude of the direct wave falls inversely with distance as in free space. The resultant of these two waves, depends on their difference in path lengths and on the ground-reflection properties. At reflection there is loss of amplitude and change of phase.

Fresnel theory leads to expressions for the ground-reflection coefficient ρ in terms of wave frequency f, elevation angle Δ and the electrical properties of the ground, characterised by its relative dielectric constant ϵ and conductivity σ. For horizontally polarised waves

$$\rho_H = \frac{\sin \Delta - (n^2 - \cos^2 \Delta)^{\frac{1}{2}}}{\sin \Delta + (n^2 - \cos^2 \Delta)^{\frac{1}{2}}} \tag{1}$$

and for vertically polarised waves

$$\rho_V = \frac{n^2 \sin \Delta - (n^2 - \cos^2 \Delta)^{\frac{1}{2}}}{n^2 \sin \Delta + (n^2 - \cos^2 \Delta)^{\frac{1}{2}}} \tag{2}$$

where n is the complex refractive index given as

$$n^2 = \epsilon - j \cdot \frac{18000}{f} \cdot \sigma \tag{3}$$

and when f is expressed in megahertz and σ in Siemens/metre. ϵ and σ depend on the nature of the soil, but are also a function of its moisture content and temperature, wave frequency, general geological structure of the ground, effective depth of penetration and lateral spread of the waves.

The moisture content of the ground is probably the major factor determining its electrical constants, but temperature changes are also important. As temperature is reduced conductivity decreases, but the effect on the dielectric constant is small down to freezing point; then there is a large reduction in both constants. Waves of different frequency penetrate the earth to different depths. At MF penetration depths of the order of 15 metres occur whereas at HF these are only one or two metres. Since annual temperature

variations decrease rapidly with depth, reflection properties at MF are relatively stable, whereas at HF and greater frequencies marked changes tend to arise. The CCIR has adopted reference values of ground constants for a range of conditions[2]. There is no variation of ϵ with frequency at MF and HF. It is taken as 80 for fresh and pure water at 20°C, 70 for sea water at 20°C, 30 for wet ground, 15 for medium-dry ground and 3 for very dry ground and ice. σ for these conditions is as shown in Figure 1.

The radio energy received does not travel solely via a single ground-reflection point, but rather by a large number of indirect paths distributed about the geometrical reflection position. It is necessary therefore to consider the constants of the ground over an area covered by the lateral spread of the wave paths. No definite limits can be ascribed to this area but it is taken as the first Fresnel half-wave zone. This consists of an elliptical area containing the geometrical reflection point and within which contributions from all other points lag in phase by 180° or less. Contributions from within the zone reinforce each other, but contributions from points outside the zone differ widely in phase and tend to cancel. Thus the contributions from within the zone are mainly responsible for the reflected wave, and the size of the zone therefore influences its field strength. Hence eq. (3) is frequency sensitive. Although surface objects and undulations have no direct influence on the constants of the ground itself, they can reduce the reflection coefficient; the effects of such energy losses may be taken into account by using appropriately modified values of the ground constants.

The first Fresnel half-wave zone ellipse has the transmitter and receiver positions as its foci and major and minor axes of length $(D + \lambda/2)$ and $\sqrt{D\lambda}$ respectively, where D is the length of the direct path and λ is the wavelength. Hence as D changes so the Fresnel zone size and the resulting signal strength vary. For finite transmitter-receiver separations the area of the ellipse is less than if the antennas have infinite separation, for which eqs. (1) and (2) apply. Reductions in area on typical paths at VHF and higher frequencies are usually less than 10% and the above models are adequate. However, at MF and sometimes also at HF a correction term must be applied. The derivation of this correction was first formulated by Sommerfeld[3] in 1909 and has been expressed in convenient form by Norton[4]. The direct and ground-reflected waves are together known as the space wave. The correction term can be identified with a further wave known as the surface wave produced by energy travelling close to the ground. The surface wave is so called because it is the only wave present when both antennas are a small fraction of a wavelength above the ground. Under these conditions the two components of the space wave have equal magnitude and opposite phase and so give zero resultant.

Extension of the above theory to a spherical Earth was first undertaken by van der Pol and Bremmer[5] and results have been presented in convenient form by Norton[6]. The surface wave is diffracted to follow the curvature of the Earth. The diffraction is dependent on the ratio of the wavelength to the Earth's radius, decreasing steadily as the wavelength is decreased. This means that surface waves are weaker at the higher frequencies. Diffraction is also influenced by the imperfect conductivity of the ground. Energy is absorbed by currents induced in the Earth so that energy flow takes place from the wave downwards. This produces wavefront tilting and the bending of the wave is assisted. The loss of energy dissipated in the Earth leads to attenuation dependent on conductivity and dielectric constant. At MF with wavelengths of around a kilometre elevated transmitting antennas are impracticable and vertical radiators are used. For horizontal polarisation with low antennas not only do the direct and ground-reflected waves cancel, but the theory shows that the surface wave suffers very rapid distance attenuation.

Now the space wave is also influenced by atmospheric refraction because the refractive index is a function of height above the ground. Assuming a spherical Earth surrounded by concentric refracting layers, this refraction can be taken into account in the calculations by giving the Earth an effective radius in excess of the true radius. At VHF and UHF this is 1.33 times the actual radius. At VLF, however, the thickness of atmosphere traversed is small compared with the wavelength and there is no significant refraction; hence the true Earth radius must be used. At LF, MF and HF the atmosphere has some effect on ground-wave propagation. This has been studied by Rotherham[7], who has shown that it can be allowed for by a frequency-dependent factor. At 1 MHz, for example, the effective radius is about 1.25 times the true radius. This topic is discussed in a text of the CCIR[8].

For practical purposes there is no need to apply the detailed theory repeatedly and families of reference propagation curves have been produced. In the past the CCIR has published sets of curves based on the true Earth radius. Figure 2 shows a sample of these for a selection of frequencies with propagation over dry ground ($\sigma = 10^{-3}$ S/m, $\epsilon = 4$) in comparison with an inverse distance attenuation. The curves relate to the vertical component of the electric field in the case of a transmitter dipole moment equivalent to 1 kW radiation from a short vertical grounded monopole antenna above a perfectly conducting ground (corresponding to a cymomotive force of 300 Volts). Other curves produced by the Federal Communications Commission in the U.S.A. for these frequencies assume an effective Earth radius factor of 1.33. The CCIR now recommends use of a frequency-dependent factor[9] and is in course of implementing a computer program based on this; it plans to publish curves in due course.

All curves relate to a given set of ground constants over the entire path, a condition rarely met in practice. For an all-land path with variable ground constants, sufficient accuracy can normally be obtained by using the propagation curve appropriate to weighted mean values of these constants. This approach is not sufficiently accurate, however, for mixed land-sea paths because of the marked differences in the constants. Instead an empirical method of evaluation developed by Millington[10] is recommended. In this, sections of curves corresponding to the lengths of path traversed with different sets of ground constants are combined to produce a continuous single curve and an estimate of the received signal strength thereby derived. The strength should be independent of direction of propagation, and so the process is repeated for propagation in the reverse direction and a mean of the two sets of results taken. This method may also be used for propagation over land where different conditions apply on separate sections of the path.

As already noted, for antennas close to the ground and vertically polarised radiation the direct and ground-reflected waves approximately cancel because of the phase reversal of the latter during reflection. As the antenna heights are increased there is a further phase change of the reflected ray due to the extra raypath length so that these two components no longer cancel. Hence the resultant signal must be computed

as the vector sum of the space and surface waves. The effect may be modelled through so called height-gain factors applied to the estimated surface-wave field strengths. Since the surface wave intensity is reduced at the higher frequencies, so the height-gain factor is increased. For antenna elevations which are a small fraction of a wavelength there is little change of field strength, but for typical heights of antennas, height-gain factors can be significant at frequencies above about 5 MHz. They can also be of importance at LF and MF when applied to links to aircraft.

Other phenomena influencing ground-wave propagation should be mentioned associated with obstacles along the path. Propagation in wooded terrain can lead to additional signal absorption and this has been shown to vary with season depending on the amount of foliage and with whether the leaves are wet or snow covered. The effect is most pronounced at VHF and UHF[11] but is also apparent at HF. Although practical data exist, empirical models to quantify this are limited. Buildings and hilly or mountainous terrain cause wave reflection, diffraction and absorption[12]. Again fortunately at MF and HF these are not so serious as at higher frequencies where more obstacles have a size comparable with a wavelength. The effects of isolated features such as mountain ridges may be modelled mathematically assuming knife-edge diffraction[13]. More commonly though resultant fields are subject to composite factors and it is difficult to model these, other than to fit empirical relationships to a wide range of measured data.

3. SKY-WAVE PROPAGATION AT MF AND HF

It is customary to say that the ionospheric layers reflect radio waves, but more accurately these waves experience successive refraction in regions of differing electron concentration and therefore of differing refractive index. The refractive index is always less than unity and usually decreases with increase of height so that the waves become bent away from the vertical. The net effect may lead to reflection. Magnetoionic theory provides equations for the refraction in a thin slab of ionosphere. This refraction depends not only on the electron concentration but also on the angle of incidence and the wave frequency, since the ionosphere is a dispersive medium. It is greater the lower the frequency and the more oblique the wave or ray.

Figure 3 shows the raypaths via the same single-layer model ionosphere for rays at three separate frequencies launched with a series of different elevation angles from a ground-based transmitter. A number of features are apparent -

   (i)   for the lowest frequency there is sufficient ionisation present to reflect the waves at all elevation angles, including the vertical; at the higher frequencies, rays launched with an elevation greater than some critical value escape from the ionosphere and travel into space

  (ii)   waves launched more obliquely in most cases travel to greater ranges

 (iii)   waves suffer more refraction at the greater heights

  (iv)   waves of higher frequency are reflected from a greater height

   (v)   waves launched more obliquely are reflected from a lower height.

In this example, the curvature of the Earth is taken into account and it is assumed that the same ionosphere exists at all ranges from the transmitter and is concentric with the Earth. If follows that the maximum range attainable after one ionospheric reflection arises for rays launched at grazing incidence and that this depends on the height and form of the model ionosphere and on the wave frequency. Changes with frequency and model form tend, however, to be of a secondary nature, and the principal dependence is on the layer height of maximum electron concentration. For typical E, F1 and F2-layers, the maximum range is 2000, 3400 and 4000 km respectively. Whilst undoubtedly greater ranges are sometimes possible, the above values represent practical upper limits when account is taken of poor antenna performance at low elevation angles and its influence on signal strength.

Because of the presence of the Earth's magnetic field, the ionosphere is a doubly refracting medium. Magnetoionic theory shows that there are two separate waves with differing but related polarisations that once excited can propagate within it. The polarisations change as these waves progress and are dependent on frequency and ray direction, the electron concentration and collision frequency, and the strength and direction of the field. In general the polarisations are elliptical with the so-called ordinary (O) wave having an anticlockwise sense of vector rotation viewed in the direction of propagation for an angle of less than $\pi/2$ between the ray and field directions. For these conditions the other wave, the extra-ordinary (X) wave, has a clockwise vector rotation. The O and X wave vector rotation senses reverse for greater angles between the ray and field directions. The O and X waves experience different amounts of refraction so that once excited at the base of the ionosphere they travel independently along somewhat displaced raypaths. Fortunately for prediction purposes the O-wave, which at HF suffers less absorption and so is usually the stronger and hence the more important, tends to follow a path which is nearly that which would arise if there were no field.

Returning to Figure 3, it is noted that for a given ionosphere there will be some limiting upper frequency which is reflected vertically. For this frequency the reflection occurs at the height of maximum electron concentration. The frequency is known as the critical frequency. At frequencies above the critical frequency there is a ground distance out from the transmitter at points along which illumination is not possible by waves reflected from the ionosphere. This distance is known as the skip distance. The skip distance increases as the wave frequency increases and in the limit for a very high frequency can extend to the maximum ground range possible for rays launched at grazing incidence; in that case all rays escape into space.

It follows for a fixed point of reception that there is some maximum frequency at which the waves can be reflected to it. This is the frequency making the distance from the transmitter to the point equal to the skip distance. The frequency is known as the maximum usable frequency (MUF). A distinction is made between the classical MUF which is the highest frequency providing illumination by the above means and the

standard MUF which is an approximation to it determined by some modelling technique such as the use of vertical-incidence ionospheric sounding data with an approximate distance-conversion factor, as discussed in Part 2[1]. The MUF increases with ground distance. Clearly it depends also on the amount of ionisation present - if the critical frequency is doubled, so will be the MUF for all distances. It depends too on the height of the ionosphere since the determining factor as to whether reflection or transmission occurs is the angle of incidence at the layer. The same incidence angle yields different ground ranges for different layer heights. The greater the layer height, the steeper the angle of incidence to achieve propagation to a fixed range, and therefore the lower the MUF. This means that although the critical frequency of the E-layer is less than that of the F1-layer which in turn is less than that of the F2-layer, sometimes the E-MUF can be the greatest of the three separate layer MUF's. This is most likely to be the case in the summer daytime at low solar epochs (when the ratio of E to F2 critical frequencies is greatest) over path ranges of 1000-2000 km. Again, the F1-MUF may exceed the F2-MUF beyond the maximum E range at distances of 2000-3000 km. Since the Earth's field leads to the production of O and X waves which follow different raypaths, these waves also have differing MUF's. The O wave is refracted less than the X wave, becomes reflected from a greater height and so has a lower critical frequency and MUF. For propagation between a pair of fixed terminals the path MUF is the greatest of the individual MUF's for reflection from the different layers. This frequency undergoes systematic variations with time-of-day, season and solar epoch as the electron concentration and layer heights vary; there are also large day-to-day changes which create problems for modelling. Figure 4 shows the maximum observed frequency (MOF) on a sample path recorded in a single month using an oblique sounder and, for comparison, the estimated monthly median standard MUF determined by conventional modelling techniques.

Now consider propagation to some point beyond the skip distance. Figure 3 shows that as the elevation angle is increased at a fixed frequency, rays travel to shorter ground ranges until the skip distance is reached. Rays of slightly larger elevation angle do not penetrate the ionosphere into space because, contrary to a popular misconception, ray apogee at the MUF is below the height of maximum electron concentration, except in the limiting case of vertical incidence i.e. propagation to zero ground range. These larger elevation rays are then reflected from a greater height, and they travel back to ground at increased range by virtue of having a significant length of near-horizontal path close to apogee. In principle such so-called high-angle or Pedersen rays can exist out to a limiting ground range where ionospheric reflection is from the layer maximum. This limiting range can exceed that of the low-angle ray and may well be in excess of 7500 km in temperate regions and 10,000 km in equatorial regions[14]. The band of elevation angles providing high-angle rays is usually only a few degrees. .There is then a range of ground distances at all points along which there are both low and high-angle rays. The path length through the ionosphere of the high-angle ray exceeds that of the low-angle ray by an amount which increases when moving out from the skip distance. So the strength of the high-angle ray tends to be less that of the low-angle ray both because of increased spatial attenuation and also, particularly in the case of reflection from the E-layer, because of increased ionospheric absorption. It is usual then in practice that signal-strength considerations determine the effective upper ground-range limit of the high-angle ray. Conversely for propagation to a fixed ground range, there is a band of frequencies below the MUF over which the high-angle ray has appreciable amplitude. As the frequency is reduced from the MUF so the excess path length and excess group-path length of the high-angle ray relative to the low-angle ray increase, whilst at the same time the differential absorption also rises. The presence of two rays with different group-path lengths is a disadvantage for it gives rise to signal distortions. Since the low and high-angle rays merge at the MUF, this frequency is sometimes alternatively known as the junction frequency JF. Both the O and X waves have their own separate families of high-angle rays and associated JF's. Figure 5 shows an oblique-incidence ionogram recorded over a 6700 km path in which propagation time is displayed as a function of wave frequency. The separate traces are associated with signals successively reflected twice, three and four times from the F2 region and being sustained by intermediate ground reflections. The corresponding junction frequencies, labelled 2F2JF, 3F2JF and 4F2JF respectively, together with the high-angle rays, can be seen. In this example there is some smearing of the record in the region of the JF's which is attributed to ionisation gradients along the path.

Aside from signal-strength considerations, for a particular propagation path to be possible, i.e. that mode to be present, the wave frequency must be below the MUF and, in the case of F-modes, also the lower ionosphere must not screen or blanket it. Screening of the 1F2-mode, but not of the 2F2-mode because of the lesser path obliquity, is a common summer daytime occurrence at certain frequencies. The strongest or dominant mode on a long path is usually the lowest-possible order F2-mode unless the antennas discriminate against this. Higher-order F2-modes traverse the ionosphere a greater number of times to become more absorbed and also experience more ground reflections, so that they tend to be weaker. A given range can be spanned by fewer F than E-hops. Modes involving more than two reflections from the E-layer are rarely of importance. Reflections from the F1-layer arise only under restricted conditions and the 1F1 mode is less common than the 1E and 1F2 modes. The 1F1 mode can be important at ranges of 2000-3400 km, particularly at high latitudes. Multiple-hop F1 modes are very rare in practice because the necessary ionospheric conditions to support an F1-layer reflection do not tend to occur simultaneously at separated positions.

So far, no discussion has been made of the effects of geographical changes in ionisation. These cause so-called mixed modes with successive reflection from different layers. Mixed modes are a common feature of transequatorial paths and east-west paths across a daylight-darkness boundary. Figures 6(a) and (b) show cases of a 1F2 + 1E mode for an eastwards path at dawn and of a 1E + 1F2 mode arising at dusk. (Modes are labelled in succession outwards from the transmitter). Other more complex examples of mixed modes are those involving upwards reflection from the E-layer between two F-reflections, known as M-modes (Figure 6 (c)).

Now geographical changes in ionisation of a smaller scale size influence raypaths on single hops. These changes are variously referred to as ionisation gradients, horizontal gradients, or ionospheric tilts. They cause the upwards and downwards legs of a hop to differ in length and they modify their directions so that the equivalent triangular path must be regarded as involving reflection from a tilted plane mirror. Longitudinal tilts (Figures 7(a) and (b)) produce differences in the elevation angles on the two legs; lateral tilts give rise to off-great-circle paths. Longitudinal tilts are usually the more important because they can give rise to changes in propagation modes. Lateral deviations are generally small in

comparison with antenna beamwidths. An exception, even for propagation via the regular modes, where iono-spheric tilts lead to marked departures from the great-circle-path, arises when the transmitter and re-ceiver are almost antipodal. Simultaneous propagation may then take place in several directions and the dominant mode direction may vary with time of day, season and frequency. An effective tilt may result from geographical changes in either electron concentration or layer height. For an upwards ray of elevation angle Δ a longitudinal plane-mirror tilt θ results in a downwards ray of elevation angle $\Delta \pm 2\theta$, i.e. there is a difference of 2θ for the two legs in the sense indicated in Figures 7 (a) and (b). It follows that longitudinal tilts modify the MUF over a fixed path length. On long paths with low elevation angles these longitudinal tilts can give rise to modes involving multiple reflection from the ionosphere without intermediate ground reflection (Figure 7 (c)). In such cases, if ray perigee at the middle of the path is within the ionosphere and above the D and lower E regions there is little resulting absorption so that received signals are relatively strong. Hence these so-called perigee modes can be important on long paths, particularly across the equator and at high latitudes where significant ionisation gradients commonly exist. Associated with perigee modes are ground dead zones, additional to the skip zone, for which raypath illumination is not possible.

In addition to propagation modes resulting from ionospheric reflections, there are others associated with scattering and ducting. Various mechanisms are believed involved and so it is not surprising that there are uncertainties in the interpretation of particular observational data and therefore in assessing the relative importance of the different phenomena. These create modelling difficulties. Signals are scattered by ionospheric irregularities in the D, E and F-regions - patches of varying electron con-centration such as those which give rise to the phenomena observed on vertical-incidence ionograms known as sporadic-E and spread-F. The scattering may result in onwards propagation (forward scatter), deviation out of the great circle (sidescatter) or return along the same path (backscatter). Ionospheric scatter modes are usually weaker than the corresponding reflected modes and they tend to fade more. However, they are important at the higher frequencies of the HF band since they enhance the practical (operational MUF) so that it exceeds the classical MUF. Their geographical and temporal occurrence is governed by the incidence of the irregularities. Sporadic-E is most prevalent at low latitudes in the daytime and at auroral latitudes by night. It tends to be opaque to the lower HF waves and partially reflecting at the higher frequencies. F-region irregularities can exist simultaneously over a wide range of heights. They are found at all latitudes, but are particularly common at low latitudes in the evenings where their occurrence is related to rapid changes in the height of the F-region. Hence forward-scatter modes associated with the vertical-incidence ionogram phenomenon of spread-F are important on long trans-equatorial paths. F-region irregularities are field aligned and sidescatter from these has been observed on paths at high and low latitudes; in some instances the received signals were incident simultaneously from a range of directions.

Normal ground terrain is sufficiently rough that it too scatters significant signal power out of the great-circle direction. Ground sidescatter and backscatter result. Since sidescatter paths are longer than the more direct routes, they tend to have correspondingly greater MUF's. There is some practical evidence supporting a dependence of signal intensity on scattering angle and whether sea or land is in-volved. The backscatter mechanism is of value in providing a means of remote probing (e.g. studying the state of the sea) or for monitoring ionospheric conditions. Special backscatter sounders can be used to determine the skip distance and deployed in support of systems operation. It is believed that another mechanism for wave propagation in the ionosphere concerns chanelling as in a waveguide. This waveguide may be formed within the F-layer and have an upper but no lower boundary, being sustained by the concave ionosphere, or it may be a double-walled duct in the electron-concentration minimum between the E and F-regions. The waveguide is sometimes known as a whispering gallery. Signal coupling into the waveguide is assumed to involve ionospheric tilts like those which develop in the twilight periods or to be caused by the existence of ionisation irregularities such as Es or those responsible for spread-F. A further ducted type of signal propagation occurs along columns of field-aligned ionisation. Figure 8 illustrates a number of the separate propagation features discussed in the above paragraphs arising on paths at high latitudes.

Mention has been made of ionospheric absorption. This arises from inelastic collisions between the free electrons, oscillating under the influence of the incident radio wave and the neutral and ionised constituents of the atmosphere. Expressions for the absorption are given from magnetoionic theory[15,16]. For propagation along the direction of the Earth's magnetic field the absorption in decibels $L(f_v)$ at vertical incidence in traversing a height region h at a wave frequency f_v is given as

$$L(f_v) = K \int \frac{N\nu}{\mu} \cdot \frac{dh}{(f_v \pm f_L)^2 + \frac{\nu^2}{4\pi^2}} \tag{4}$$

where K is a constant of proportionality, N is the electron concentration, ν is the collision frequency, μ is the refractive index and f_L is the electron gyrofrequency. This equation applies approximately over a considerable range of wave directions with f_L taken as the electron gyrofrequency about the component of the Earth's magnetic field along the direction of propagation. The positive sign is taken for the O-wave and the negative sign for the X-wave. For ground-based reflection the limits of integration are from the base of the ionosphere to the height of wave reflection. For propagation at oblique incidence the absorption is proportionately increased because of the greater lengths of path traversed. Inspection of eq. (4) shows :

(i)   the absorption in a given slab of ionosphere is proportional to the product of electron con-centration and collision frequency. Electron concentration increases with increase of height whereas the collision frequency for electrons, which is proportional to the atmospheric pressure, decreases. Hence the absorption reaches a maximum in the lower E-region with most of the con-tribution to the total absorption occurring in the D-region.

(ii)   large amounts of additional absorption arise near the height of reflection where μ is small.

This is known as deviative absorption in contrast to the non-deviative absorption in regions where there is little refraction.

(iii)   absorption decreases with increase of frequency.

(iv)   the O-wave absorption is less than that of the X-wave and differences are accentuated the lower the frequency, provided the first term of the denominator of eq. (4) remains dominant.

Some of the above features can be seen in the data of Figure 9 showing estimated values of oblique-path ionospheric absorption at two high frequencies in different seasons. The absorption is low at night-time because of the reduced D and E-region ionisation. The non-deviative absorption reaches a maximum around local noon in the summer, but the influence of deviative absorption can modify the resultant seasonal variation. Ionospheric absorption is one of the most important factors influencing received sky-wave signal strengths at MF and HF so that accurate methods of modelling it are needed. There are particular difficulties at MF because raypath reflection heights of around 85-90 km are common and much of the absorption is deviative absorption occurring within 2-3 km of ray apogee. Such electron-concentration data as exist at these heights display considerable irregular variations.

Both sky-wave and ground-wave signal strengths are dependent on transmitting and receiving antenna gains and in system design the aims are to choose antennas with beamwidths and directions of maximum gain most appropriate to the principal propagation paths encountered. Unfortunately at MF there is little scope for optimisation. Transmitting antennas tend to be large vertical monopoles less than a wavelength high and for reception short whip or loop antennas are used. Particularly for broadcasting with intended reception via the ground wave there are advantages in using so-called anti-fading antennas[17] aimed at suppressing high-angle radiation which can propagate via the sky wave, thereby leading to self interference. At HF there is more flexibility in available antennas. Rhombic or log-periodic antennas are favoured for point-to-point transmissions and curtain arrays of dipoles for broadcasting. Antennas for reception depend on whether these are for fixed or mobile terminals. There is renewed interest in the design of arrays of receiving antennas capable of steering for optimum signal reception or for interference rejection. Reference data for a range of antennas are contained in the CCIR handbook of antenna diagrams[18]; other computer formulations to determine antenna gain are available[19]. Practical tests show that typical antennas often display a performance which differs from that predicted[20] and for design purposes the CCIR has recommended standards for minimum values of radiation in directions where theory indicates the existence of nulls[21]. Further work is needed in the modelling of antenna performance at MF and HF, particularly the inclusion of allowances for imperfect ground on radiation resistance and the separate determination of the polarisation of the waves to which the antennas respond.

When signals are propagated between terminals via multiple paths, whether these involve different modes, low and high-angle rays or O and X-waves, there exists a difference in the group paths of the separate components. Hence there is a spread in time of the received signals. Multipath time dispersions can limit system performance just as can an inadequate signal/noise power ratio. Large time spreads are often associated with scatter propagation and under these conditions classical-type oblique-incidence iono-grams are replaced by others with diffuse traces; in some cases the traces associated with the different modes coalesce (Figure 10). There are also large variations in the angles of elevation of the incident signals (Figure 11). It seems unlikely that such features can ever be modelled satisfactorily.

If the ionosphere were unchanging the signal amplitude over a fixed path would be constant. In practice, however, fading arises as a consequence of variations in propagation path, brought about by movements or fluctuations in ionisation[22]. The principal causes of fading are (i) variations in absorption (ii) movements of irregularities producing focusing and defocusing (iii) changes of path length among component signals propagated via multiple paths, and (iv) changes of polarisation, such as for example due to Faraday rotation. These various causes lead to different depths of fading and a range of fading rates. The slowest fades are usually those due to absorption changes which have a period of about 10 minutes. The deepest and most rapid fading occurs from the beating between two signal components of comparable amplitude propagated along different paths. A regularly reflected signal together with a signal scattered from spread-F irregularities can give rise to so-called 'flutter' fading, with fading rates of about 10 Hz.

Amplitude fading is accompanied by associated fluctuations in group path and phase path, giving rise to time and frequency-dispersed signals. When either the transmitter or receiver is moving, or there are systematic ionospheric movements, the received signal is also Doppler-frequency shifted. Signals propagated simultaneously via different ionospheric paths are usually received with differing frequency shifts. Frequency shifts for reflections from the regular layers are usually less than 1 Hz, but shifts of up to 20-20 Hz have been reported for scatter-mode signals at low latitudes. Frequency spreads associated with individual modes are usually a few tenths of a Hertz (Figure 12).

The effect of ionospheric propagation on a radio signal may therefore be expressed in terms of a corresponding channel-scattering function (Figure 13) in which each mode has its own attenuation due to transmission loss and its own time and frequency offsets and dispersions. As a caution, it must however be noted that even this representation is an over simplification. Particularly for transequatorial and auroral paths the modes coalesce because the spread associated with each is so great. Time spreads of several milliseconds and frequency spreads in excess of 10 Hz have been reported under such conditions (Figure 12).

4.   PRACTICAL USAGE OF THE MF AND HF BANDS

Use of the radio spectrum is controlled by the ITU. Emissions are authorised which fulfil the technical requirements specified in the Radio Regulations[23] - a set of standards laid down and amended from time to time by special international Administrative Radio Conferences. The Radio Regulations define various types of radio service (e.g. broadcasting, maritime mobile, amateur) and allocate sub-bands of frequencies for use by these separate services. This allocation is a compromise based on a consideration of potential service usage, bandwidth requirements and propagation characteristics.

Allocations are considered separately for three specifically defined longitude regions and within a tropical zone given approximately as follows :

        Region 1   : Europe, Africa and northern Asia
        Region 2   : North and South America
        Region 3   : southern Asia and Australia
        Tropical Zone : latitudes less than about $\pm$ 30°.

Some frequency sub-bands are shared between two or more services, either on an equal basis or with certain services designated as secondary. Individual transmissions are assigned to specific frequencies within the allocated sub-bands for their particular service on the basis that no new transmitter shall create unacceptable interference or be judged likely to interfere with any existing co-channel or adjacent channel system. In the case of a secondary service there is no such security of tenure if an established system is found to cause interference to some new system and no protection is afforded against interference created by any new primary service station. The ITU maintains a body known as the International Frequency Registration Board (IFRB) to carry out technical examinations of proposed new emissions including assessments of the likelihood of causing or being influenced by interference; also to keep a master register of all assigned transmitters and their schedules.

The MF band is defined as the frequency range 300-3000 kHz and the HF band as 3-30 MHz. Below 1605 kHz there are four principal sub-bands, representing 95% of the available MF spectrum, with common allocations in the three regions :

        325-405 kHz   Aeronautical radio navigation
        415-490 kHz   Maritime mobile
        490-510 kHz   Mobile distress
        535-1605 kHz   Sound broadcasting

Other sub-bands below 1605 kHz, varying for the different regions, are allocated to maritime radio-navigation and aeronautical mobile services.

Aeronautical and maritime services at MF, like those also operating at LF, rely principally on the ground-wave mode. However, since there is also some propagation by the sky wave, fading occurs particularly at night due to interference with the sky wave. Ground-based aeronautical non-directional radio beacons at frequencies of 200-1750 kHz are used in conjunction with direction-finding equipment in aircraft for navigation purposes over a few hundred nautical miles and as locators to final approach out to ranges of 10-25 nautical miles. Long-distance aeronautical navigation aids include Loran A with frequencies around 2 MHz based on reception of pulses from a chain of transmitter sites and Consol (200-415 kHz) consisting of morse transmissions in which a count is made in the aircraft of the dot-dash characters heard during the keying transmission period. By reference to appropriate charts the observer determines a position line. Maritime coast stations at MF provide radiotelegraphy and radio direction-finding facilities.

Sound broadcasting has traditionally relied on the medium frequency ground-wave signal[24]. Despite the advantages of improved signal quality afforded by alternative VHF services, particularly in geographically densely populated regions such as Central Europe where MF co-channel interference by night is a problem, a recent ITU Administrative Broadcasting Conference[25] showed no lack of interest in retaining this allocation. With transmitter powers typically of 100 kW or more and tall vertical antenna masts giving omnidirectional azimuthal radiation, coverage ranges of 50-100 km are usually adequate for domestic reception of the same programme material. The spread of television in recent years has detracted from peak evening sound broadcast reception requirements, but the need to maintain coverage remains.

The remainder of the MF band is occupied with fixed and mobile services, radionavigation and meteorological aids. Maritime elements include coast stations, ship station radiotelephone working to coast stations and intership working. Aeronautical systems include single-sideband HF radiotelephone links between aircraft and the ground in the aeronautical mobile channels of the 2-22 MHz band and radioteletype links between ground terminals in the aeronautical fixed channels in the 2.5-30 MHz band. These employ FSK modulation with frequency shifts of 200-500 Hz. Variations in frequency allocations between the regions arise principally from changes in operational requirements, rather than from propagation effects. However, the tropical region has been defined to allow specifically for the differing propagation phenomena and increased background noise from thunderstorms at low latitudes. Sound broadcasting in the tropical zone is permitted between 2300-2495 kHz, as well as in three other special sub-bands in the lower part of the HF band.

At HF there are a multitude of frequency sub-bands for the different services with many of these being shared among services. Some sub-bands are common to the land mobile and maritime mobile services; others are separate. Of the 27 MHz of available spectrum this is estimated as being occupied at the present (prior to the 1979 World Administrative Radio Conference) approximately as follows :

        Fixed service   60%
        Land and maritime mobile services   15%
        Sound broadcasting service   10%
        Aeronautical mobile service   10%

The remaining 5% of spectrum is used by the amateur service, the standard frequency and space-research services.

To obtain information on the path lengths of typical circuits operating in the principal separate services and for which propagation data are needed, a statistical study has been carried out at HF using samples of information contained within the International Frequency List of the IFRB (Samuel and Hurst, private communication). Their analysis considers changes with frequency within the band. Here results for all frequencies grouped together are shown in Figure 14. There are seen to be proportionately greater numbers of circuits of range 500 km or less operating in the fixed and aeronautical mobile services than in

the broadcasting and maritime mobile services. The maritime mobile service aims to provide longer-distance communication than the aeronautical mobile service. Use of broadcasting at the longer distances is no doubt associated with the apparent needs of many countries to provide overseas news and propaganda information. There is currently an upsurge in the use of the HF band, both for civilian and military applications. Whereas the majority of long-distance fixed radio circuits now rely on satellites and cables, increases in the numbers involved mean that there are actually more HF circuits than say 20 years ago. Particularly for military purposes, HF systems are regarded as providing a necessary back-up service to fixed links primarily established by other means. High frequencies create a useful way of establishing communications with small isolated communities in such places as the Arctic and Middle Eastern desert areas. Commercial use of HF systems continues in the provision of feeder links to satellite terminals. The requirements are for high-grade circuits that can be integrated into a general network. Figure 14 shows that the median range for the fixed circuits is around 1500 km.

5. PARAMETERS SUSCEPTIBLE TO MODELLING

A radio wave is specified in terms of five parameters : its amplitude, phase, direction of propagation, polarisation and frequency. In general, propagation leads to changes of each of these so that there are modelling requirements to be able to estimate the extent of the resulting modifications. The most important parameter to model is amplitude, since without adequate signal strength at the receiver use cannot be made of the information contained within the wave. Estimates of direction of propagation are of value to antenna selection and are needed in many cases to assess the transmission loss on which the received signal strength depends. Particularly for applications in which waves are used for navigation and remote probing purposes, a knowledge is needed of phase-path length, which is given approximately as the integral of the refractive index with respect to the raypath length, and of the group delay, together with statistical changes in these parameters. Background noise intensities also are required to be known.

For communication system modelling, signal and noise intensities may be compared with reference to standard required values of signal/noise power ratio for a satisfactory grade of service. Account can also be taken in the modelling of acceptable values of multipath depending on the modulation type and data rate. Interference effects of specific co-channel signals can also be modelled for application to possible frequency-sharing situations.

For sound broadcasting the minimum usable field strength[26], defined as that necessary to permit a desired reception quality in the presence of natural and man-made noise but in the absence of interference from other transmitters, may be modelled. For planning purposes, however, use must be made of the usable field strength[26], which is the minimum field strength necessary to permit a desired reception quality in the presence of noise and interference, either in an existing situation or as determined by agreement or frequency plan. The service area is then given as the area within which the field strength equals or exceeds the usable field strength. Required values of r.f. signal to interference ratio for satisfactory reception are internationally agreed[27]. These vary depending on the frequency separation of the unwanted and wanted signals and are different for ground wave and sky-wave signals. Use of these data is important to considerations of broadcast coverage. Area coverage factors may be evaluated for sychronised trans-mitter groups[28] based on reference propagation and protection ratio data, either in the absence of, or with account for specific interfering signals.

6. PROPAGATION MODEL REQUIREMENTS

Since the earliest days of radio transmissions, the requirements for signal propagation and noise pre-dictions were recognised. Many groups in different countries have, over the years, been pursuing the perfection of prediction techniques. Their efforts stand as testimony to the difficulties of the tasks and the disparity of views as to how these should be accomplished. A distinction can be made between long-term prediction models that may be produced at any time from existing reference data and short-term models relying on parameters measured in near real-time. Short-term models are of value in cases where the quantities to be estimated change in an irregular way. Long-term models have applications at both MF and HF for ground wave and sky-wave propagation, but it is for HF sky waves that procedures need to be most complex. Ground-wave signals tend to be relatively stable and MF broadcast service characteristics cannot be changed at short notice. Hence short-term prediction models have greatest potential application to HF sky-wave systems.

6.1 Long-term prediction models

Long-term predictions are needed for system planning. They can yield estimates of the frequency coverage required and of the necessary transmitter power to provide a specified grade of service; also they enable the types and size of the most suitable antennas to be determined. In the case of sky-wave systems, predictions commonly are made for every two or four hours throughout the 24 hours for sample summer, equinox and winter months at reference epochs of low and high solar activity, depending on the intended usage. Calculations assuming the use of omnidirectional antennas serve to indicate the mean wave launch and arrival directions of the strongest signals and their variations. Recourse to standard antenna design data[18] then indicates the optimum choice of antenna type and the preferred dimensions. The inclusion of allowances for the gains of the selected antennas, together with estimates of transmission loss, required signal/noise power ratio and mean noise powers leads to the determination of the necessary transmitter power. If continuous coverage is required the transmitter power needs to be selected on the basis of data for summer noon at sunspot maximum when signals are weakest because of ionospheric absorption.

Related to system design is the selection of the required frequency assignments and, if a decision is made to have simultaneous multifrequency transmissions, the choice of the number of separate transmitters wanted. The more assigned frequencies, the greater should be the achievable performance. A typical re-quirement is likely to involve the use of two frequencies, one selected principally for night-time and the other for day working. Long-term predictions can aid in these respects. By comparing results for the different occasions an optimum frequency selection may be made.

For commercial systems it is nowadays a common requirement that organisations who tender to supply

these must demonstrate to their prospective customers that the proposed installation is the minimum necessary to fulfil the intended function. In some cases, particularly those concerned with the refurbishing of established links, past experience may well prove preferable to the use of predictions. Infrequently though the need is for the best prediction models possible. Greatest accuracy is probably needed in signal-intensity prediction. A prediction accuracy of 6 dB appears a reasonable objective to seek to attain; any sky-wave model achieving this for 90% of occasions would almost certainly represent a significant improvement over existing procedures. For system design, where calculations may be regarded as 'once off', the cost of these is small by comparison with the total system costs. Hence model accuracy is of paramount importance and its complexity is of less concern.

A second requirement for long-term predictions is associated with transmitter licensing and the assessment of the possible interference caused by any new system. The IFRB is charged with this task. Use is made of Technical Standards to give estimates of the intensities of proposed new transmissions at the receiving sites of all existing co-channel and adjacent channel systems which may possibly be affected. Since there are several thousand frequency notifications made to the IFRB each week it follows that some loss in accuracy of the models used by that Organisation may have to be tolerated in order to bring the amount of calculation, even with modern computing aids, to manageable proportions. Hence, the IFRB needs a model, within the constraints of available computers, relying more on data storage and less on calculation. The system designer is not restricted in this way.

In addition to the above needs, a further separate requirement has been identified for predictions where more limited aids than a full-sized computer are available and where reduced accuracy is acceptable. This requirement arises, for example, in technical meetings where approximate results are needed and there is no wish to suspend discussions for a day or more whilst awaiting computations. In such cases look-up tables, charts, or simple algorithms for use with a pocket calculator or desk-top computer may prove adequate. It is evident that in each application the requirements are for the simplest prediction model giving acceptable accuracy, but not so obvious what this accuracy should be. A case can be made for a family of different prediction models ranging from the most sophisticated needing high-speed computers with considerable storage to simple manual methods requiring only modest aids.

Both for the IFRB studies and also when submitting tender documentation in support of international contracts, the requirements are for internationally accepted prediction methods. Hence, the CCIR has Study Programmes in being to develop such agreed procedures. The policy which is being followed in order to finish ultimately with a heirarchy of prediction methods meeting the above needs is to concentrate at present on the development of the most accurate methods possible, without overdue regard for their complexity. It is argued that controlled simplifications can then be introduced when their effects have been examined and quantified. That is not to say the task of agreeing internationally what simplifications are acceptable will be easy, but rather that this exercise must be accomplished later. There is now a growing awareness of the complexity of existing prediction models and ample evidence that the production of efficient and faithful computer programs to match the technical bases which have been formulated is a lengthy task. Difficulties arise in implementing those programs produced on the range of computers in worldwide use. In some cases computational differences arise which it is not easy to ascribe either to programming errors or changes in computer characteristics. It is to the credit of the international community that in recent years there has been, through the medium of the CCIR, acceptance of models which many participants would really prefer to see changed in some (but differing) respects.

6.2 Short-term prediction models

There is no doubt that predictions are also of potential value for frequency management of HF sky-wave systems, to determine what frequency from the assigned complement is likely to be most suitable on a given occasion. Unfortunately, though, in this role they are not too successful because the requirement is for a so-called short-term prediction based on a knowledge of the ionosphere for the particular day. The ionosphere is subject to considerable spatial and temporal variability, and methods of modelling its state must rely either on a few sample direct measurements or incomplete correlations with other geophysical parameters that can be measured. Furthermore, there are major logistic difficulties in devising operational procedures to make use of such models. Both the above approaches involve measurements followed by calculations. Schemes based on the general broadcasting of small numbers of parameters for incorporation in simple calculations by transmitter personnel could perhaps be envisaged. Whilst information on storm or abnormal conditions could be processed in this way, there is real doubt whether more usually such calculations would be adequate. The detailed evaluations probably needed are likely to be beyond available manpower and computational resources at transmitter sites. This suggests deploying a few centralised measurement and computer installations to serve large numbers of radio circuits, but then there is a need for extra communication links to convey the predicted data, leading to extra costs. Moreover, delays in providing predictions mean that these have to be produced further in advance, leading to reduced accuracy. It is evident that there are other difficulties with any real-time frequency-management system in ensuring that both transmitter and receiver operators know what frequency to use. Information on changes in frequency can be supplied to the receiver once a link is established, but initial setting-up seems likely to involve a search process.

It should also be realised that optimum selection of operational frequency depends on having a clear channel. Whilst models exist for some of the types of background noise[1], it is not possible to predict co-channel interference from other transmissions. This points to the need for duplex working with measurements of noise at the receiver being transmitted back to the other terminal. Clearly this too adds to the complexity of the system, adds to spectrum congestion and raises the question of whether a two-way real-time sounding system using only assigned frequencies would not be preferable. A particular application of such a procedure would be for communication from mobile terminals where there are often difficulties of restricted transmitter power, inefficient antennas and varying circuit length leading to operator unfamiliarity with the likely range of propagation conditions to be experienced.

7. CONCLUSIONS

A review of the principal propagation phenomena encountered at MF and HF, together with a consideration

of the operational use of these frequency bands leads to an assessment of the parameters useful to model. It is concluded that a case can be made for a family of different prediction models ranging from simple manual procedures to others requiring advanced computing aids.

8. REFERENCES

1. BRADLEY, P. A. (1979) Propagation at medium and high frequencies, 2 : Long and short-term models, Aerospace propagation media modelling and prediction schemes for modern communications, navigation and surveillance systems, AGARD Lecture Series 99 (this volume).

2. CCIR (1978) Electrical characteristics of the surface of the earth. Recommendation 527, Documents of XIVth Plenary Assembly, International Telecommunication Union, Geneva.

3. SOMMERFELD, A. (1909) The propagation of waves in wireless telegraphy. Ann. Physik, 28, 665.

4. NORTON, K. A. (1936) The propagation of radio waves over the surface of the Earth and in the upper atmosphere. Proc. IRE, 24, 1367-1387 and (1937), 25, 1203-1236.

5. VAN DER POL, B. and BREMMER, H. (1937) Phil. Mag. 24, 141-176 and 825-864.

6. NORTON, K. A. (1941) The calculation of ground-wave field intensity over a finitely conducting spherical earth. Proc. IRE, 29, 623-639.

7. ROTHERHAM, S. (1970) Ground-wave propagation at medium and low frequencies. Electronics Letters, 6, 794-795.

8. CCIR (1978) Ground-wave propagation in an exponential atmosphere. Report 714, Documents of XIVth Plenary Assembly, International Telecommunication Union, Geneva.

9. CCIR (1978) Ground-wave propagation curves for frequencies between 10 kHz and 30 MHz. Recommendation 368-3, Documents of XIVth Plenary Assembly, International Telecommunication Union, Geneva.

10. MILLINGTON, G. (1949) Ground-wave propagation over an inhomogenous smooth earth. Proc. IEE, 96, Pt. III, 53-64.

11. CCIR (1978) Electrical characteristics of the surface of the earth. Report 229-3, Documents of XIVth Plenary Assembly, International Telecommunication Union, Geneva.

12. CCIR (1978) Influence of terrain irregularities and vegetation on tropospheric propagation. Report 236-4, Documents of XIVth Plenary Assembly, International Telecommunication Union, Geneva.

13. CCIR (1978) Propagation by diffraction. Report 715, Documents of XIVth Plenary Assembly, International Telecommunication Union, Geneva.

14. CCIR (1978) Long-distance ionospheric propagation without intermediate ground reflection. Report 250-4, Documents of XIVth Plenary Assembly, International Telecommunication Union, Geneva.

15. RATCLIFFE, J. A. (1959) The magneto-ionic theory and its applications to the ionosphere. Cambridge University Press, Cambridge.

16. BUDDEN, K. (1961) Radio waves in the ionosphere. Cambridge University Press, Cambridge.

17. CCIR (1978) Transmitting antennae in LF and MF broadcasting. Report 401-3, Documents of XIVth Plenary Assembly, International Telecommunication Union, Geneva.

18. CCIR (1978) Antenna diagrams. International Telecommunication Union, Geneva.

19. BARGHAUSEN, A. F., FINNEY, J. W., PROCTOR, L. L. and SCHULTZ, L. D. (1969) Predicting long-term operational parameters of high-frequency sky-wave telecommunication systems, ESSA Tech. Report ERL 110-ITS 78, U.S. Government Printing Office, Washington.

20. CCIR (1978) Transmitting antennae in HF broadcasting. Report 32-3, Documents of XIVth Plenary Assembly, International Telecommunication Union, Geneva.

21. CCIR (1978) Directional antennae in HF broadcasting. Recommendation 80-1, Documents of XIVth Plenary Assembly, International Telecommunication Union, Geneva.

22. CCIR (1978) Ionospheric propagation characteristics pertinent to terrestrial radiocommunication systems design (fading). Report 266-4, Documents of XIVth Plenary Assembly, International Telecommunication Union, Geneva.

23. ITU (1976) Radio Regulations. International Telecommunication Union, Geneva.

24. CCIR (1978) Operational aspects of MF broadcasting coverage. Report 616-1, Documents of XIVth Plenary Assembly, International Telecommunication Union, Geneva.

25. ITU (1975) Final acts of the regional administrative LF/MF broadcasting conference (Regions 1 and 3). International Telecommunication Union, Geneva.

26. CCIR (1978) Definitions of specific field strengths and service area in LF, MF, HF and VHF sound broadcasting. Recommendation 499-1, Documents of XIVth Plenary Assembly, International Telecommunication Union, Geneva.

27. CCIR (1978) Protection ratios in LF, MF and HF broadcasting. Report 794, Documents of XIVth Plenary Assembly, International Telecommunication Union, Geneva.

28. CCIR (1978) Coverage in MF broadcasting. Report 400-3, Documents of XIVth Plenary Assembly, International Telecommunication Union, Geneva.

29. CROFT, T. A. (1969) A review of oblique ray tracing and its application to the calculation of signal strength. Oblique ionospheric radiowave propagation at frequencies near the lowest usable high frequency, ed. T. B. Jones, AGARD Conf. Proc. 13, Technivision, Slough, 137-169.

30. BRADLEY, P. A. and HOWARD, D. R. (1973) Transmission loss at high frequencies on 3260 km temperate-latitude path. Proc. IEE, 120 (2), 173-180.

31. KIFT, F., BRADLEY, P. A., MARTIN, L. T. J. and BRAMLEY, E. N. (1969) HF oblique sounding measurements over a 6700 km temperate-latitude path. Proc. IEE, 116 (12), 1985-1991.

32. BUCHAU, J. (1972) Instantaneous versus averaged ionosphere. Air Force Surveys in Geophysics No. 241, Air Force Systems Command, U.S. Air Force, 1.

33. VINCENT, W. R., DALY, R. F. and SIFFORD, B. M. (1968) Modeling communication systems. Ionospheric radio communications in the arctic, ed. K. Folkestad. Proc. NATO institute, Plenum Press, New York, 321-340.
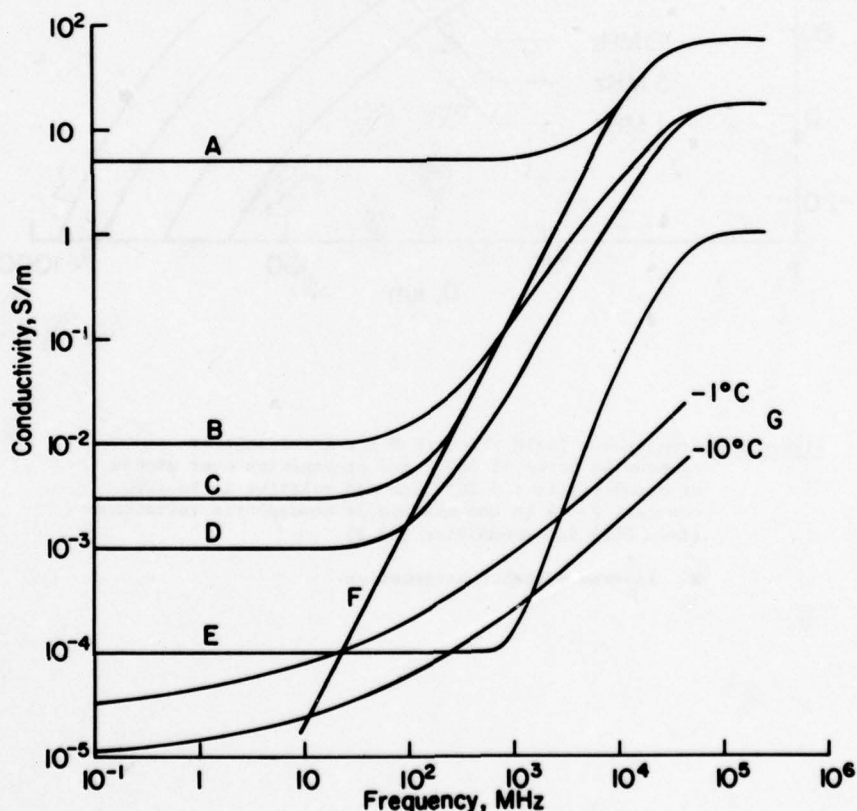
9. ACKNOWLEDGEMENTS

Figure 1   Ground conductivity as a function of frequency
(from CCIR Recommendation 527)

A   sea water (average salinity), 20°C
B   wet ground
C   fresh water, 20°C
D   medium dry ground
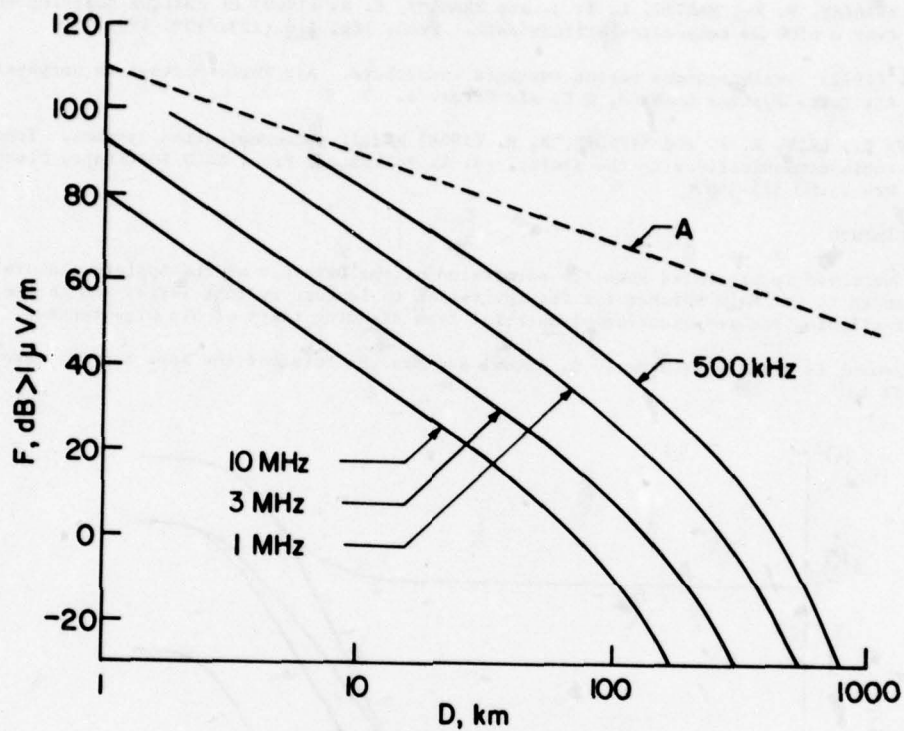E   very dry ground
F   pure water, 20°C
G   ice (fresh water)

Figure 2   Ground-wave field strength F for a transmitter
cymomotive force of 300 V and propagation over ground
of conductivity $\sigma = 10^{-3}$ S/m and relative dielectric
constant $\epsilon = 4$ in the absence of atmospheric refraction
(from CCIR Recommendation 368-2).
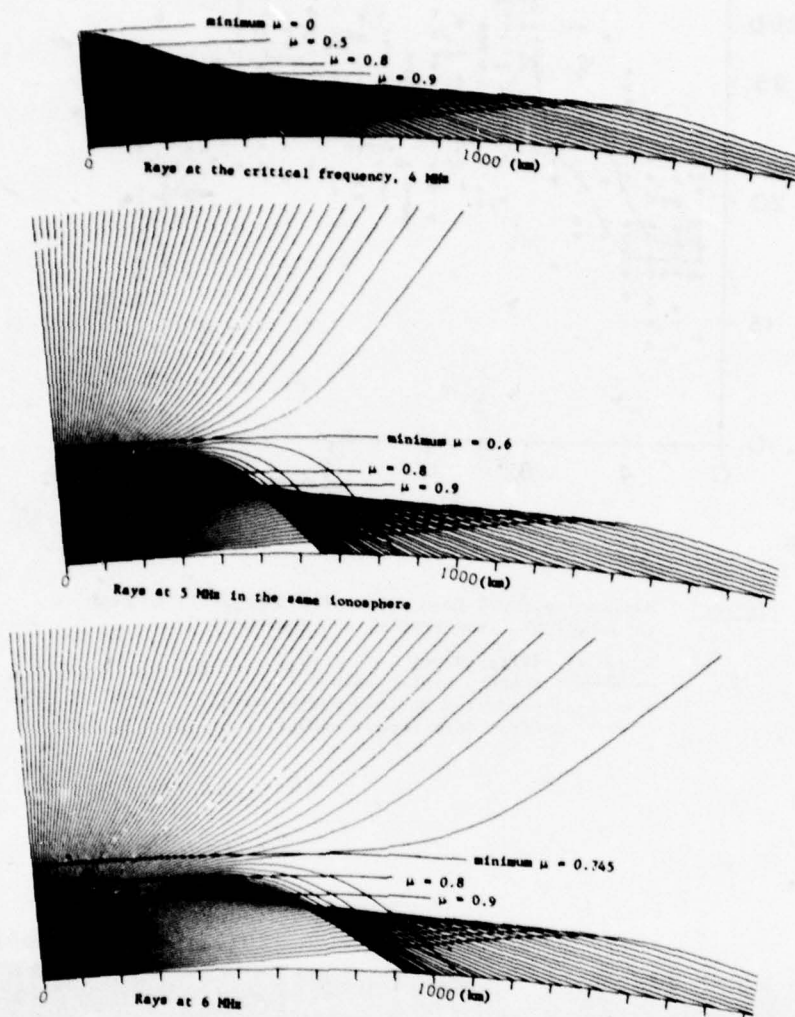
A   inverse distance attenuation

Figure 3 Raypaths for propagation at three frequencies via a single Chapman model ionosphere of critical frequency 4 MHz, height of maximum electron concentration 300 km and scale height 100 km (from Croft[29]). Curves indicate heights with selected values of refractive index μ.
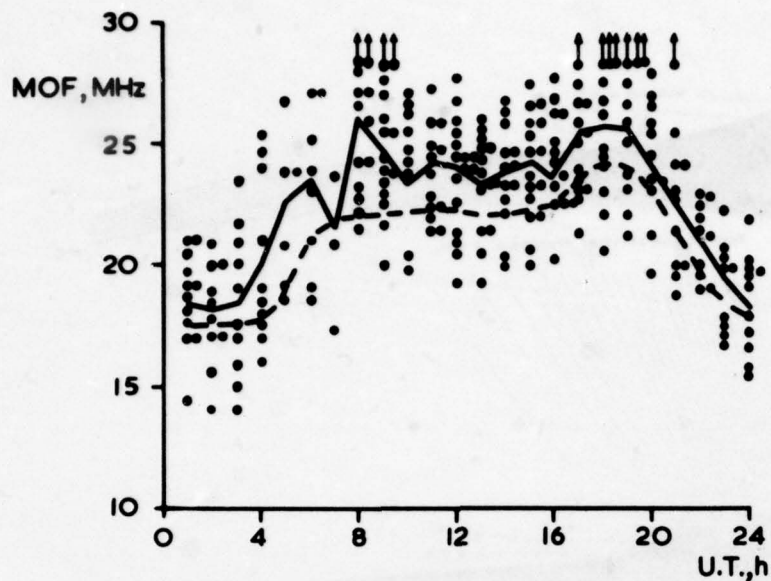
Figure 4   Maximum observed frequencies for Cyprus-Slough path
in July 1969 (from Bradley and Howard[30])

        .   daily values
    ―――――   monthly median values
    - - - -   predicted monthly median values
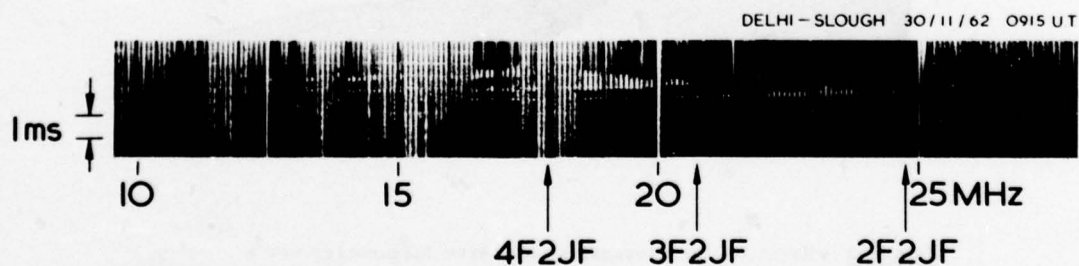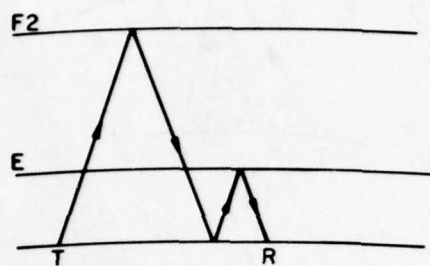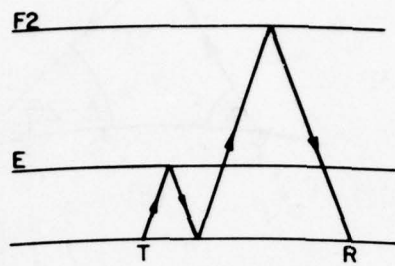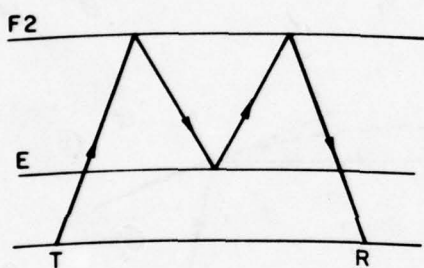   (from CCIR Report 340)

DELHI – SLOUGH   30/11/62   0915 UT

Figure 5   Sample oblique-incidence ionogram with classical 'noses'
(from Kift et al.[31])

(a) 1F2+1E mode

(b) 1E + 1F2 mode

(c) M-Mode

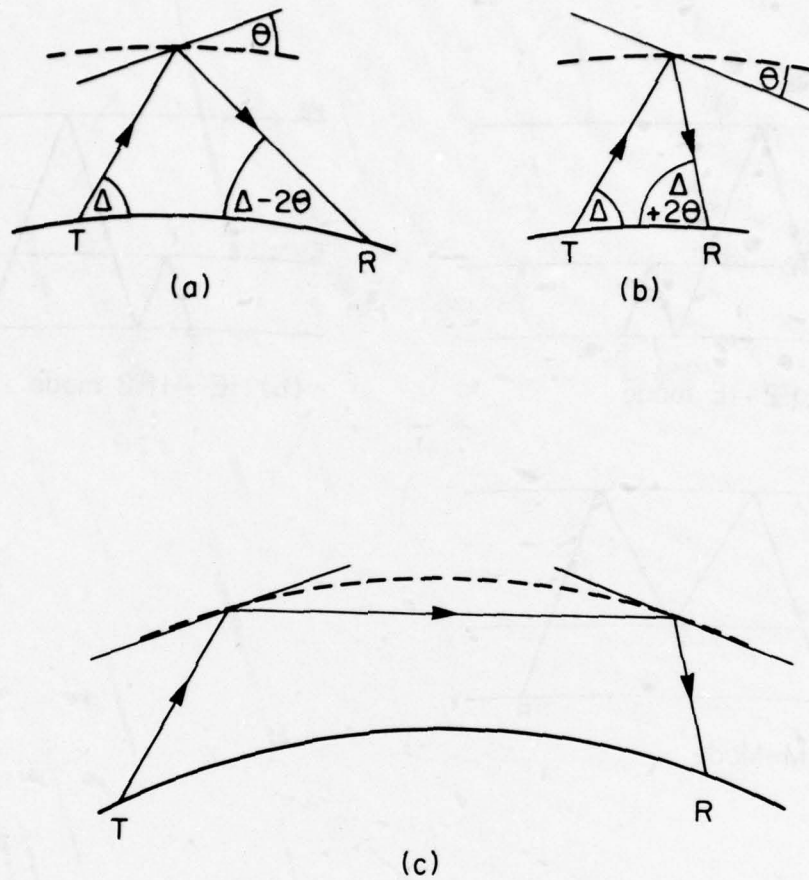**Figure 6**   Propagation modes for a geographically varying ionosphere

Figure 7   Propagation modes for a tilted ionosphere

(a)   equivalent mirror height increasing with range from transmitter

(b)   equivalent mirror height decreasing with range from transmitter

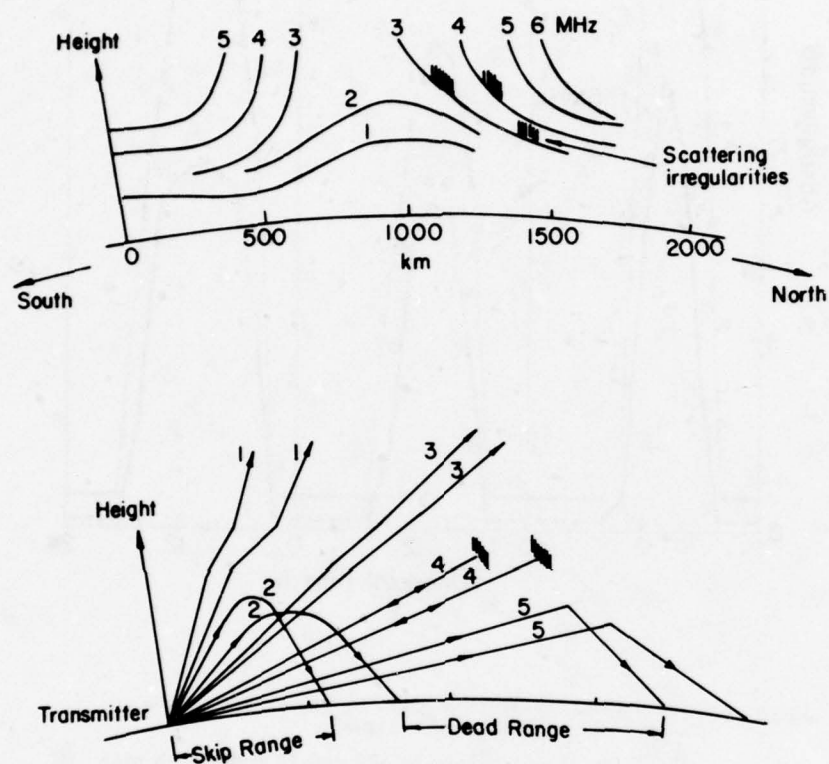(c)   perigee mode involving multiple ionospheric reflections without intermediate ground reflection

Figure 8   HF propagation paths via the ionosphere at high latitudes
            (from Buchau[32])

            top section   : sample distribution of electron concentration
                            (arbitrary units) in northern hemisphere high-
                            latitude ionosphere

            lower section : raypaths for signals of constant frequency
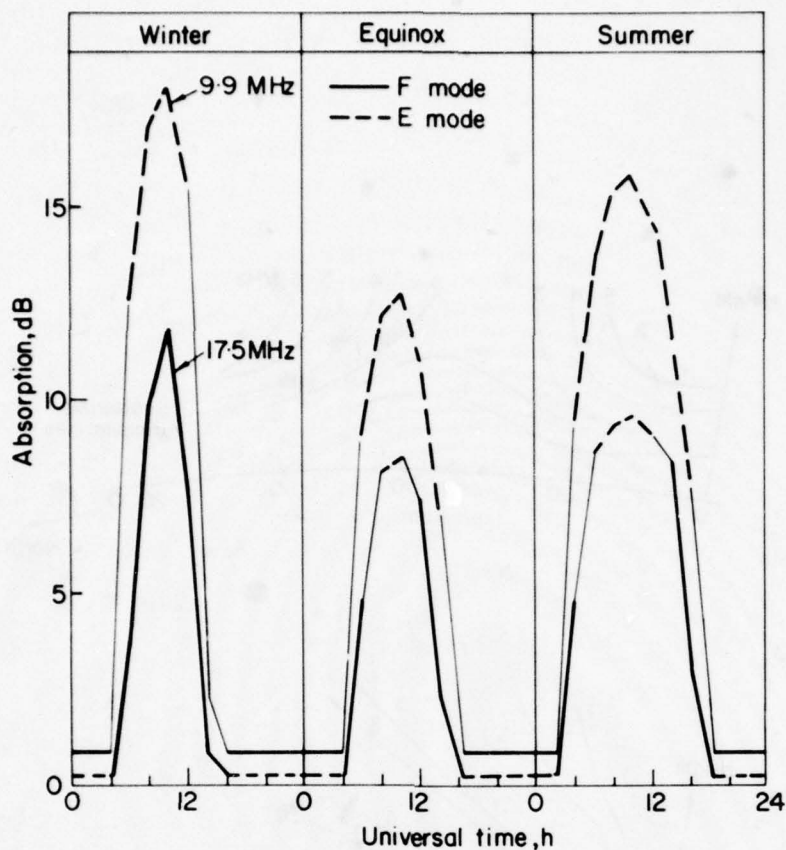   launched with different elevation angles

Figure 9   Ionospheric absorption given by the method of the
Supplement to CCIR Report 252-2

The calculations relate to 1F2 and 1E modes each with
an elevation angle of 4° over paths centred on 45°N,
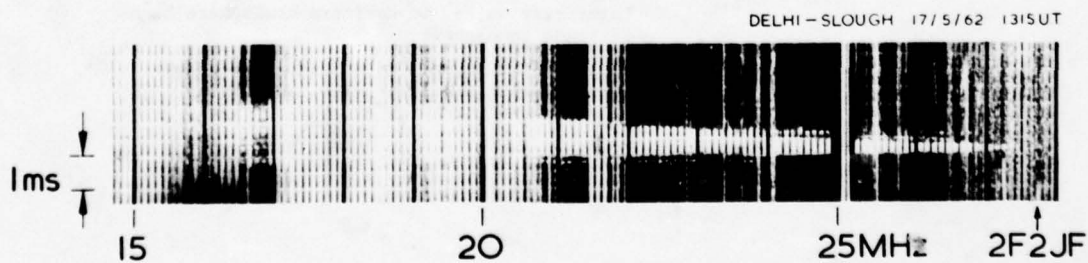20°E at high solar activity ($R_{12} = 100$)

Figure 10   Sample oblique-incidence ionogram with single
diffuse trace (from Kift et al.[31])

concentration and collision frequency. Electron concentration increases with increase of height whereas the collision frequency for electrons, which is proportional to the atmospheric pressure, decreases. Hence the absorption reaches a maximum in the lower E-region with most of the contribution to the total absorption occurring in the D-region.

(ii)   large amounts of additional absorption arise near the height of reflection where μ is small.
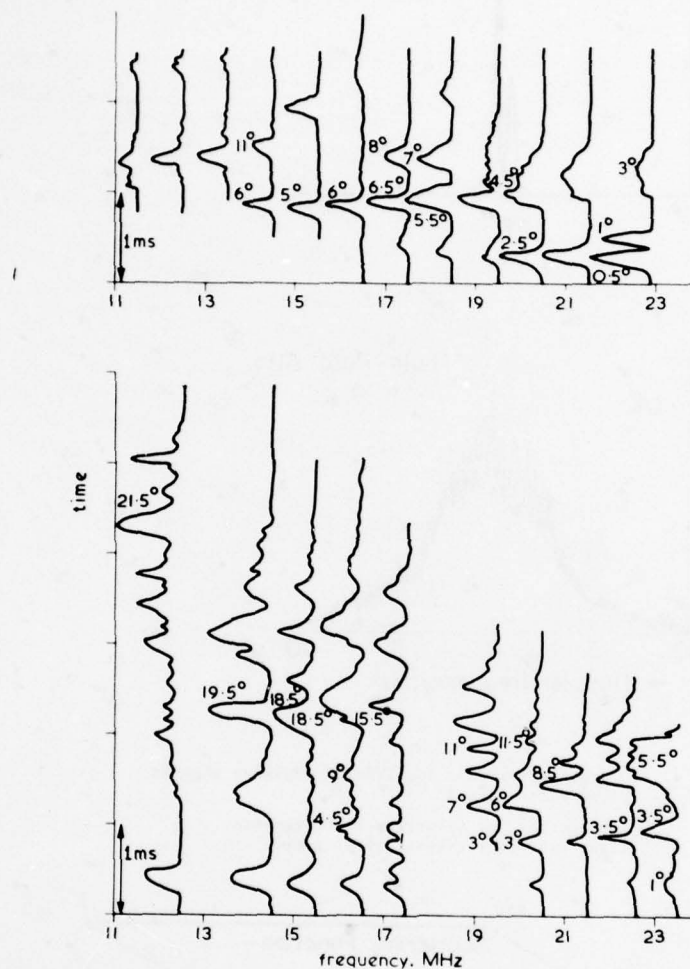
Figure 11   Received instantaneous pulse patterns and associated measured angles of elevation for Delhi-Slough path (from Kift et al.[31])

top section   : 0804-0847 h UT on 30 November 1962
lower section : 1340-1427 h UT on 17 May 1962

Figure 12   Doppler spectra of received HF sky-wave signals (from Vincent et al.[33])

top section   : temperate-latitude path
lower section : trans-auroral path

Figure 13   Channel-scattering function for three-moded ionospheric signal propagation

Figure 14   Distribution of path lengths of sample circuits for different radio services (from Samuel and Hurst)

Transionospheric Radio Propagation

by
Dr. Charles M. Rush
Chief, Performance Predictions and Model Development Group
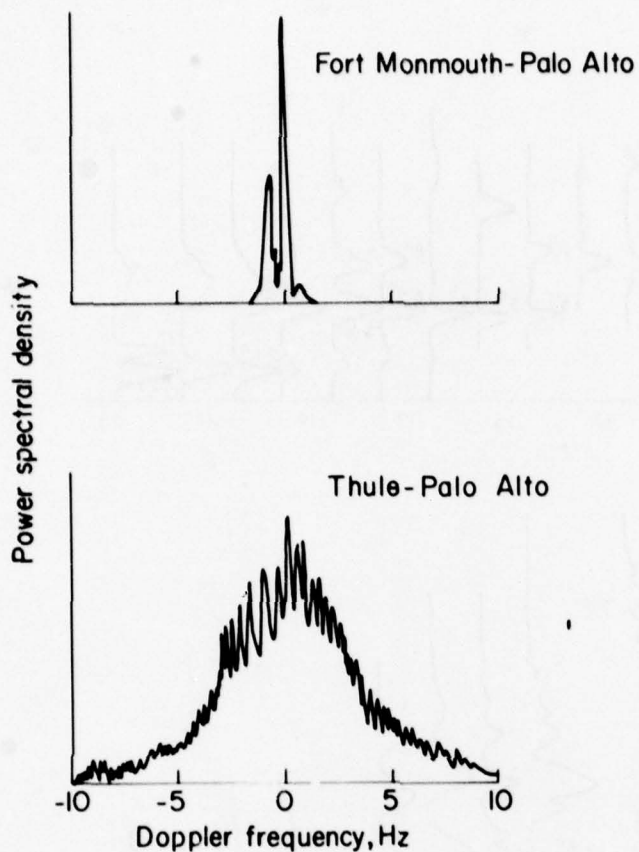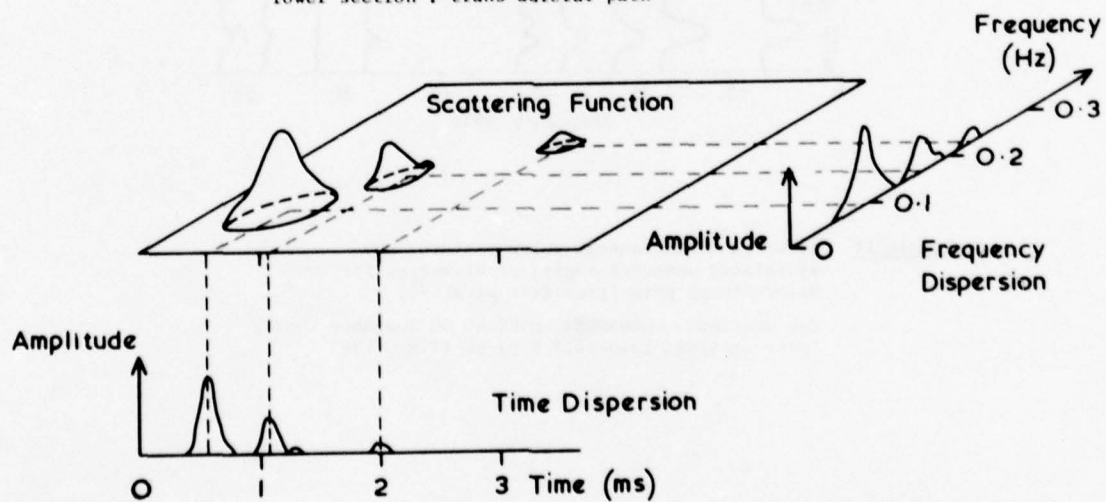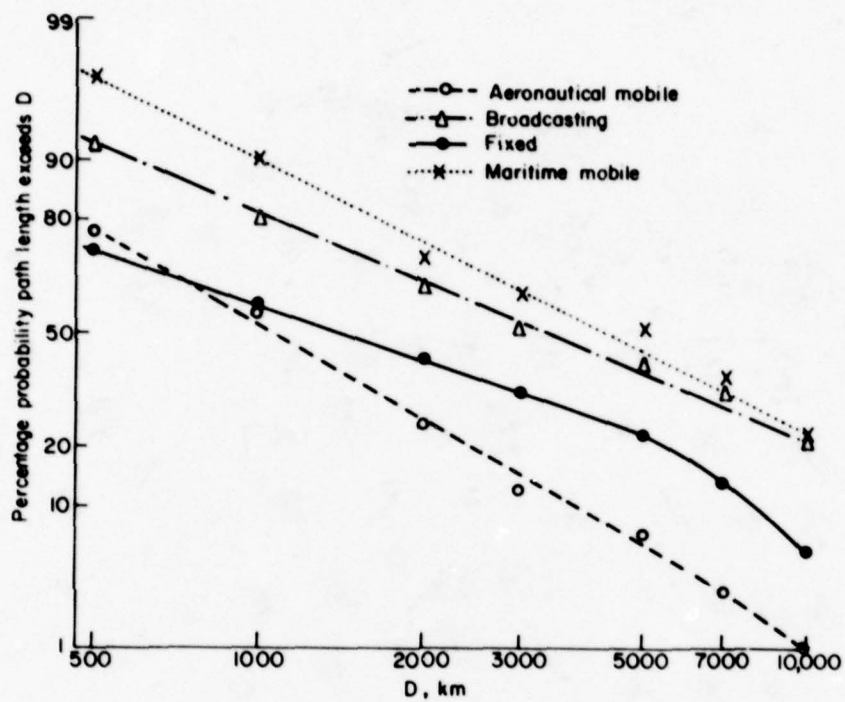Institute for Telecommunication Sciences
National Telecommunications and Information Administration
U. S. Department of Commerce
Boulder, Colorado 80303
United States of America

SUMMARY

The effects of the earth's ionized atmosphere on radio waves that propagate through the ionosphere are reviewed. Emphasis is placed on transionospheric radio propagation systems and how their operational performance is impacted by the structure of, and changes in the structure of, the ionosphere. The normal ionosphere leads to refraction and slowing down of radio waves that propagate through it. This refraction and slowing down varies as the ionosphere itself varies. Irregularities in the ionospheric electron density can impart fluctuations or scintillations onto radio waves that pass through the irregularities. The morphological behavior of the ionospheric characteristics pertinent to transionospheric systems, as well as actual observations of these characteristics are discussed in terms of impact on system performance. Also discussed are models that have been developed to represent these characteristics under conditions of varying geophysical activity.

1.0 INTRODUCTION

A radio signal which penetrates the ionosphere is modified by the medium due to the presence of electrons and the earth's magnetic field. Any frequency can penetrate the ionosphere when the critical frequency of the ionosphere is lower than the frequency of the radio wave. Thus, it is possible for frequencies as low as 2-3 MHz to pass through the ionosphere in regions of the ionosphere that are characterized by low critical frequencies. For most applications, however, propagation of radio waves through the ionosphere is considered only for frequencies greater than 20 to 30 MHz.

A radio wave passing through the ionosphere will be slowed down by an amount that is directly proportional to the total (integrated) number of electrons along the radio propagation path. This slowing down of the radio wave is referred to as ionospheric time delay in order to distinguish it from the normal delay or transit time associated with the propagation of radio waves in free space. In addition, radio waves that are linearly polarized will be subjected to a rotation in their plane of polarization upon passage through the ionosphere. A radio wave passing through the ionosphere will be bent from its straight line trajectory by the electrons along the radio propagation path. This bending or refraction results in the radio wave appearing to be at a higher location than it actually is for waves propagating in directions other than truly vertical. These effects as well as others to be discussed later are all dependent upon the large scale ionospheric structure and the total electron content (TEC) along the radio path.

In addition to effects associated with the large-scale ionosphere, radio waves passing through the ionosphere are also impacted by small-scale structures in the ionosphere. These small-scale structures are irregularities in the electron density and are referred to simply as "irregularities." These irregularities have wavelengths from a few meters to several kilometers and can give rise to fluctuations in the amplitude, phase, polarization and angle of arrival of a received signal. The fluctuation or variation in signal characteristic is known as scintillation. Ionospheric scintillation is the variation imparted to radio waves by ionospheric irregularities as the radio wave passes through the ionosphere.

In this paper we will describe in some detail the impact of the ionosphere on the performance of electromagnetic systems that rely on the propagation of radio waves through the ionosphere. The discussion will be concerned almost exclusively with radio waves whose frequencies are greater than 100 MHz in keeping with operational and proposed transionospheric propagation systems.

2.0 IONOSPHERIC EFFECTS ON TRANSIONOSPHERIC PROPAGATION

2.1 Ionospheric Group Delay

The time delay above the free space transit time between a signal transmitted through the ionosphere is given by $\Delta T = 40.3 / cf^2$ TEC (seconds) where TEC is the Total Electron Content; c is the velocity of light in meters/second, and f is the operating frequency in Hertz. The TEC is generally expressed as the number of electrons in a unit cross-section column of one square meter area along this path. Extreme values of this TEC parameter vary from 10^{16} el/m^2 to 10^{19} el/m^2. For a system operating at 1.0 GHz, a typical TEC value

of 10^{18} el/m^2 would yield an ionospheric time delay of 133 nanoseconds or about 40 meters.

2.2 Polarization Rotation

When a linearly polarized radio wave traverses the ionosphere the wave undergoes rotation of the plane of polarization. At 100 MHz and higher frequencies the amount of this polarization rotation can be described (Klobuchar[1]) by:

$$\Omega = \frac{2.36 \times 10^{-5}}{f^2} \int B \cos\theta \, N \, dl \text{ (radians)} \tag{1}$$

where the quantity inside the integral is the product of electron density N times the longitudinal component of the earth's magnetic field (B cosθ) integrated along the radio wave path. Ionospheric workers have used this effect, called the Faraday effect, to make measurements of the TEC of the ionosphere. Since the longitudinal magnetic field intensity changes much slower with height than the electron density of the ionosphere, the equation can be rewritten as

$$\Omega = \frac{K}{f^2} B_L * TEC \tag{2}$$

where $B_L = \overline{B \cos\theta}$ taken at a mean ionospheric height, usually near 400 kilometers, K = 2.36 * 10^{-5} and TEC is $\int N \, dl$. Typical values of polarization rotation for northern mid-latitude stations viewing a geostationary satellite near their station meridian are 1 to 500 radians. The largest portion of TEC data available today from stations throughout the world have come from Faraday rotation measurements.

2.3 Refraction

The refractive index of the earth's ionosphere is responsible for bending of radio waves from a straight line geometric path between satellite and ground. This angular refraction or bending produces an apparent higher elevation angle than the geometric elevation. Klobuchar[1], using a relationship derived by Millman and Reinsmith[2] relates angular refraction to range error by:

$$\Delta E = \frac{(R + r_o \sin E_o)(r_o \cos E_o)}{h_i(2r_o + h_i) + r_o^2 \sin^2 E_o} \frac{\Delta R}{R} \tag{3}$$

where E_o is the apparent elevation angle, R is the apparent range, ΔR is computed from $\Delta R = (40.3/f^2) * TEC$, r_o is the earth's radius and h_i is the height of the centroid of the TEC distribution, generally between 300 and 450 km.

For high elevation angles and satellites well above most of the ionization, the angular refraction can be expressed as:

$$\Delta E \approx \frac{\cos E_o}{2h_i} \Delta R \tag{3a}$$

For low elevation angles:

$$\Delta E \approx \cos E_o \frac{\Delta R}{R} \tag{3b}$$

Typical values of elevation refraction error at 1.6 GHz for an assumed worst case elevation angle of 5 degrees and a 10^{19} el/m^2 ionosphere will be 0.3 milliradians. For the same viewing angle and TEC and an operation frequency of 400 MHz the angular refraction error will be approximately 4 milliradians.

2.4 Phase Path Effects

A radio wave propagated into the ionosphere will have its phase advanced with respect to what it would be in the absence of an ionosphere. For a radio wave passing through the ionosphere, this phase increase (which is related to group delay discussed in 2.1) is given by:

$$\phi = \frac{1.34 * 10^{-7}}{f} TEC \text{ (cycles)} \tag{4}$$

where f is the system operating frequency in Hertz, and TEC is in el/m^2. In practice, the amount of this phase advance cannot readily be measured on a single frequency.

The change in phase between two coherent signals transmitted through the ionosphere can be used to determine ionospheric electron content unambiguously along the entire radio wave propagation path. This method provides one of the best methods of deducing TEC.

2.5 Doppler Shift

Since frequency is simply the derivative of phase, a Doppler shift results due to changing TEC. This additional frequency shift is generally small compared to the Doppler shift due to satellite motion but can be computed by:

$$\Delta f = \frac{d\psi}{dt} = \frac{1.34 \times 10^{-7}}{f} \frac{d(TEC)}{dt} \quad (Hertz) \tag{5}$$

For high orbit satellites where the diurnal changes in TEC are greater than orbital changes, an upper limit to the rate of change of TEC is approximately 0.1×10^{16} el/m^2 per second. This value yields an additional frequency shift of less than one tenth of a Hertz at 1.6 GHz which would not be significant compared with a typical required receiver loop bandwidth of at least a few Hertz.

2.6 Scintillations

Scintillations are fluctuations in the amplitude and phase of a received signal that result from the passage of the wave through electron density irregularities. Scintillations in amplitude can be characterized by a depth of fading index and a fading period. A useful index to compare scintillation data is the scintillation index, S_4, which is defined as the square root of the variance of received power divided by the mean values of the received power (Briggs and Parkin[3]). An alternative, less rigorous quantitative measure of scintillation index which has been adopted by the Joint Satellite Studies Group (JSSG) to ensure a standard method of data scaling in long-term statistical analysis is: $SI_{JSSG} = P_{max} - P_{min}/P_{max} + P_{min}$ where P_{max} is the power amplitude of the third peak down from the maximum excursion of the scintilations and P_{min} is the power amplitude of the third peak up from the minumum excursion, measured in dB.

Scintillation in the phase of the received signal is defined as those variations that are as fast or faster than the slowest amplitude scintillation. The magnitude of phase scintillation is usually characterized by the deviation of the phase denoted as σ_ϕ.

3.0 SPECIFIC TRANSIONOSPHERIC PROPAGATION SYSTEMS

A number of radio propagation systems are currently in operation or are in the planning stages that depend upon the propagation of radio waves through the ionosphere. These systems can involve the propagation of radio waves between satellites and earth terminals, the propagation of radio waves between pairs of satellites or the propagation of radio waves from the surface of the earth to a space object. For the purposes of this discussion, any radio propagation system having a satellite at one of its terminals will be referred to as a satellite system while systems relying on radio waves propagated from the ground without a specific airborne or space-borne receiver as part of the overall design will be referred to as a radar.

Transionospheric satellite systems usually operate at frequencies greater than 200 MHz although substantial data concerning transionospheric propagation have been obtained from experiments using frequencies as low as 136 MHz. The exact frequencies used for ground-to-satellite and satellite-to-ground links and for the different types of systems are in accord with the internationally agreed frequency allocation rules and regulations. Navigation, communication and surveillance functions are performed by transionospheric satellite systems.

Radar systems employing transionospheric propagation tend to be surveillance-oriented systems. For the most part, they are operated as part of the national defense system in a given country. These radars have functions that include detecting and tracking aircraft, ballistic missiles, and space objects. The systems also operate on frequencies that are in accord with internationally agreed rules and regulations.

In the following sections, examples of transionospheric satellite and radar systems are discussed in terms of the effects of the ionosphere on overall performance. As a means of providing an indication of the magnitude of the possible ionospheric effects, Table 1 gives the estimated maximum values for ionospheric effects at a frequency of 100 MHz. It is assumed that the total zenith electron content of the ionosphere is 10^{18} electrons/m^2. An elevation angle of about 30° is also assumed. The values given are for the one-way traversal of the waves through the ionosphere.

Table 1. Estimated maximum ionospheric effects at 100 MHz for elevation angles of about 30° one-way traversal

EFFECT	MAGNITUDE	FREQUENCY DEPENDENCE
Faraday rotation	30 rotations	$1/f^2$
Propagation delay	25 μs	$1/f^2$
Refraction	$<1^\circ$	$1/f^2$
Variation in the direction of arrival	20 min of arc	$1/f^2$
Dispersion	0.4 ps/Hz	$1/f^3$
Scintillation	See Sec. 5 of this paper	See Sec. 5 of this paper

3.1 Satellite Navigation Systems

The United States is currently developing an advanced satellite navigation system called NAVSTAR-Global Positioning System (GPS). The GPS will basically consist of three constellations of eight satellites each, in twelve-hour synchronous orbits, at 63 degrees inclination. The transmissions from each satellite give the satellite ephemeris, clock error and capability of determining the ionospheric time delay correction along the direction to the satellite. The latter capability is achieved by the use of two carrier frequencies spaced sufficiently far apart to enable a direct measurement of the ionospheric time delay to be made. The ephemeris and satellite clock frequency standard error are sent at low data rates on carriers that are modulated with pseudo-random noise codes. Each user must have knowledge of the unique PRN codes which will enable him to synchronize his receiver to each of the satellites. The satellite orbits are chosen such that for all time at least four satellites are in view of any point on the earth. Satellites at optumum viewing angles are chosen to obtain the maximum geometric precision in the measurements. Elevation angles from five degrees to the zenith are used. Due to tropospheric time delay errors elevation angles lower than five degrees are avoided.

The operational frequency of this system is 1.6 GHz. To allow users with high accuracy position requirements to automatically correct for the ionospheric time delay, a second frequency at 1.2 GHz is available. The actual ionospheric time delay is obtained by measuring the difference in arrival time of 10 MHz modulation envelopes on both the carriers. This is an actual measurement of the group delay.

The ionospheric time delay for each of the two frequencies can be written:

$$\Delta T_1 = \frac{K}{cf_1^2} \text{ TEC}, \qquad \Delta T_2 = \frac{K}{cf_2^2} \text{ TEC} \tag{6}$$

where ΔT_1 is the value needed to correct for the ionospheric error on the frequency f_1, and ΔT_2 is the ionospheric error encountered on the frequency f_2. If the normal system operational frequency is f_1 and we choose f_2 at a lower frequency for ionospheric correction purposes, we obtain

$$\Delta(\Delta T) = \frac{K*TEC}{c} \left(\frac{1}{f_2^2} - \frac{1}{f_1^2} \right) = \Delta T \left(\frac{f_1^2 - f_2^2}{f_2^2} \right) \tag{7}$$

or

$$\Delta T_1 = \frac{f_2^2}{(f_1^2 - f_2^2)} \Delta(\Delta T) \tag{8}$$

The value $\Delta(\Delta T)$ is obtained from the difference of the simultaneous measurements of the total range, including ionospheric time delay, at the two frequencies f_1 and f_2, since the geometric distance is, of course, the same at all frequencies. The quantity $f_2^2/(f_1^2 - f_2^2)$ is called the ionospheric scaling factor. For small ratios of f_1/f_2 this factor is much larger than unity and the required precision of the differential measurement may be unreasonably large. A plot of this quantity, normalized by f_1, is given in Figure 1.

If the user does not correct for the ionospheric time delay using a two-frequency receiver system, then a model of the time delay must be employed. Models of ionospheric time delay will be described later; however, it is worthwhile for illustrative purposes to obtain some idea of the magnitude of the time delay that could occur for the GPS operating frequency of 1.6 GHz. Figure 2 shows the world-wide delay at a universal time of 20 hours for equinoctial conditions (March 1968). This figure was presented by Klobuchar[1] and was derived from the time delay model developed by Bent et al.[5].

In addition to time delay effects, scintillation effects could also impact on the performance of satellite navigation systems. Fading of the signal could result in low signal margin for some users and prevent acquisition of the signal. Also the phase coherence across the band could be degraded by phase scintillations.

3.2 Satellite Communication Systems

The advent of the satellite era significantly changed the methods by which man can communicate with his fellow man. Satellite communication systems provide enhanced bandwidth, permitting more data to be transmitted at more rapid data rates. Although they operate at frequencies greater than conventional high frequency (HF) communication systems, satellite communication systems are impacted by the ionospheric structure and irregularities in the structure of the ionospheric electron density. These irregularities give rise to scintillation of the signal.

Many of the satellite communications systems employ satellites in geostationary orbit (INTELSAT, COMSAT, DSCS, NATO, MARISAT) but lower orbit communications satellites (AFSATCOM) are also operating. Satellite communication systems have recorded fading effects at frequencies to 6 GHz (with peak-to-peak values of a few dB); fading of over 20 dB was noted recently at 1200 MHz, in the band used by MARISAT (Fremouw et al.[6]). A high occurrence

of fading greater than 20 dB peak-to-peak has been noted at 250 MHz, in the band of frequencies used by FLEETSATCOM and AFSATCOM[7]. In system operations, attention must also be paid to this phenomenon at equatorial latitudes by MARISAT and AEROSAT (the L Band Maritime and Aeronautical Satellite Systems). At both equatorial and high latitudes, scintillation effects will be seen on UHF communications systems (100 - 600 MHz) as well as L band systems.

Figure 3 is a figure given by Aarons[7] and gives a tracing of observations made of equatorial scintillations at Huancayo, Peru, while observing the synchronous satellite LES-6. The top portion of the figure shows the amplitude and fade duration while the lower portion shows the statistics of fade duration and signal probability. This illustrates how ionospheric scintillation can impact the performance of satellite communication systems.

3.3 Satellite Surveillance Systems

In addition to communication and navigation systems, satellites are used for surveillance purposes. Examples of this type of system are the SEASAT system that was designed to monitor activity in the ocean areas of the world and the LANDSAT system which provides information about the earth's natural resources. Both these systems utilize frequencies between 2.0 and 3.0 GHz. Signals are sent from the satellite to the earth's surface and the satellite observes the return signal. It is assumed that as the satellite moves between the time that the signal is sent and it is returned that the propagation medium remains frozen in space. The moving satellite gives the appearance of a wide aperture antenna and such systems have been denoted as synthetic-aperture radar systems.

During passage of the signal from the satellite to the earth and return, the medium does not remain constant. Irregularities in the medium can introduce fading and changes in the phase of the signal. The synthetic-aperture radar surveillance systems rely on the principle of coherently integrating the return signals over a (simulated) large antenna aperture. Phase scintillations could result in loss of coherence across the aperture. In addition, fading due to ionospheric irregularities could limit the amount of time the systems integrate on a single target.

3.4 Space-Object Identification Radars

There exist in actual operation and in the planning stages, ground-based radars whose function is to detect and track space objects. These objects can be either ballistic missiles or orbiting satellites. The radars designed to perform these functions operate at frequencies as low as 250 MHz and as high as 1600 MHz. The effects of the ionosphere on the performance of space-object identification radars are to slow down the transmitted radar wave and to refract the wave. This results in the detected object appearing to be at a further range and a lower height from the radar than it actually is.

Detection radars could conceivably employ dual frequencies in order to reduce the uncertainty in range and elevation angle resulting from the ionosphere. Suppose that such a radar is operating at 400 MHz and that a correction for an electron content of 10^{18} el/m^2 is required. At 400 MHz, this value of TEC corresponds to an ionospheric time delay of 840 nanoseconds, or 250 meters of range error. To determine the 840 nanosecond delay at 400 MHz, further suppose that a second system frequency at 350 MHz is utilized. The differential delay will then be 4.27 times smaller, or 197 nanoseconds. To measure this differential time delay to a one percent precision requires a 2 nanosecond accuracy. Rather than use two frequencies, most space-object radars relay on single frequency operation. Thus, some compensation for ionospheric effects must be employed.

At VHF and higher frequencies, the electron density along the radio propagation path is the only variable that needs to be considered. The radar wave can be considered to travel a straight line from the radar to the space object with a first order correction for the change in the apparent range (ΔR). The apparent range is related to the group path delay given in Eq.(6) by:

$$\Delta R = c \, \Delta T \tag{9}$$

where c is the velocity of light or

$$\Delta R = \frac{K}{f^2} \, TEC \tag{10}$$

In the case of Eq.(10), TEC must be evaluated from the base of the ionosphere up to the height at which the space object is located. The change in elevation angle is simply related to the change in range by Eqs.(3a) and (3b).

The correction for ΔR may be modeled using ionospheric models. These models tend to be monthly median in nature and help account for the average range error introduced by the ionosphere. Because the range correction depends on ionospheric electron density, it shows the same diurnal, seasonal and solar cycle dependencies as do the electron density and the TEC. Figure 4 given by Allen et al.[8] provides an indication of the monthly mean range correction that must be applied to a 425 MHz radar operating at 50°N geographic latitude. In developing this figure, Allen et al.[8] assumed that the radar was looking at a target at 1000 km altitude with an elevation angle of five degrees. The values of range correction were computed from the model of Bent et al.[5] and are applicable for the midday period when the electron content (and hence the range correction) is maximum.

The range correction is given for various levels of solar activity (denoted by $\bar{R}_z$, the twelve-month running mean sunspot number). It is readily apparent that the range correction is greatest in winter and equinoctial months and minimum in summer months.

Because of radar accuracy requirements coupled with the fact that the ionosphere displays significant variations on time scales considerably shorter than a monthly median, there have been developed methods to adapt and update the median corrections using real-time or quasi-realtime time delay, range correction or ionospheric data [8-11]. These methods attempt to account for the observed ionospheric variability in reducing overall system uncertainty.

3.5 Satellite Power System

It is worthwhile pointing out a possible ionospheric impact on the performance of the proposed Satellite Power System (SPS). The SPS is not a typical telecommunication system but it does represent a new and unique application of satellite transmission of electro-magnetic energy.

The SPS, according to current systems concepts, will involve a number of satellites in geostationary orbit collecting solar energy using solar cells. The radiant solar energy will be converted to microwave energy and transmitted to a station on the earth's surface. The effects of the passage of the high-power microwave beam through the iono-sphere will not be discussed here. The interested reader is referred to the work of Perkins and Roble[12]. It is worthwhile to mention, however, that the control and beam steering sub-systems that will be part of the SPS rely on a pilot beam operating near the SPS frequency of 2.45 GHz. The pilot beam will transmit energy to the satellite to steer the microwave power beam to the receiving station on the earth. If there are irregularities in the ionosphere along the path traversed by the pilot beam, it is possible that the control sub-system could be impacted. Studies to investigate these and other SPS-related phenomena are being undertaken within the United States.

4.0 TOTAL ELECTRON CONTENT

Because the range errors, group path delay and elevation angle deviations that a transionospheric radio propagation system experiences all depend on the integrated electron density between the two terminals of the system, the total electron content (TEC) represents a convenient parameter for characterizing ionospheric effects. Knowing the TEC as a function of time and space and the TEC as a function of various heights above the earth, enables one to assess the potential impact of the earth's ionized medium on the performance of a transionospheric propagation system simply by employing the appropriate geometry and frequency dependencies. Generally the range error is the main ionospheric problem for advanced navigation systems, and elevation angle errors are insignificant. Satellite detection radar systems, on the other hand, have require-ments to know accurate pointing elevation angles for their large aperture arrays, though generally the accurate tracking is done by using range rate information, and elevation angle is of secondary importance as long as the radar can see the target.

Because of the importance of TEC on systems that have military missions, Department of Defense laboratories such as the Air Force Geophysics Laboratory and the Ionospheric Laboratory at Fort Monmouth, New Jersey, have been instrumental in the collection of, distribution of, coordination of, and description of total electron content data. It is for that reason that the discussion which follows borrows heavily from the work of Klobuchar[1].

Much of the data on TEC have been obtained from Faraday rotation measurements. These measurements are such that the TEC up to about 2000 km altitude is obtained. Fortunately, most of the ionization in the ionosphere is contained at the altitudes below this height and the Faraday data and models derived from them are extremely effective in assessing system performance. These data and the resultant models can be adjusted to include the effects of ionization observed well above 1000 km. The models can also be used to determine the integrated electron content at heights below 1000 km by again adjusting the models according to specific system data. The changes in TEC that result from diurnal, seasonal and solar cycle variations all tend to display comparable periodicities that are not too dependent upon the height to which the electron content is integrated. Obviously, the magnitude of the TEC is dependent upon the height to which the content is integrated.

In the following sections, we shall discuss the morphology, the models and the obser-vations of total electron content. Since TEC is directly related to group delay (Eq.(6)) and range correction (Eq.(10)), these terms will be used interchangeably. Figure 5, taken from CCIR Report 263-4[13], provides a convenient display of the time delay in seconds as a function of frequency for various levels of TEC.

4.1 Morphological Behavior of Total Electron Content

Sufficient TEC data are now available from various locations throughout the world to be able to describe the diurnal, seasonal, geographic, solar cycle, and magnetic activity dependence of this parameter so that systems design engineers are able to determine the potential effects on any new transionospheric system. To a first approximation, the global

behavior of TEC is comparable to that of the critical frequency of the F2 region foF2, accounting for the fact that the electron density is proportional to the critical frequency squared. The daytime values are larger than the nighttime values and the summertime values are less than those in winter or equinoxes. The TEC of the ionosphere depends strongly on latitude, local time, and geomagnetic activity. At low magnetic latitudes, TEC exhibits the same latitudinal behavior and equatorial anomaly as does foF2[14]. In the mid-latitudes, the TEC has been observed for many years at a number of stations and the behavior of TEC is well documented[15,16]. A continuing effort is underway to enlarge the TEC observing network and data base.

As mentioned above, most of the TEC measurements have been obtained using the Faraday method. This TEC is usually referred to as ionospheric TEC as distinct from the total content measured up to the geostationary satellite height which will be denoted as TEC_T. TEC_T can be measured by a VHF group delay method which is practically independent of the geomagnetic field[17].

Continuous TEC data have been recorded at various stations. An example of a year's TEC data taken at Hamilton, Massachusetts, with the daily values for each month over-plotted, is given in Figure 6. Note the large day-to-day variability within each month and the seasonal changes, with the lowest TEC values occurring during the summer months and the largest values during the equinoxes. Some, but by no means all, of the daily variability of TEC about the monthly mean curve is due to magnetic storms which have been extensively studied for the behavior of the TEC parameter[18].

The distribution of the differences of TEC from monthly mean values is approximately normal or Gaussian. The standard deviation of daily TEC values from the average behavior for Hamilton, Massachusetts, for 1969 is given in Figure 7 separately for the winter, summer, and equinox seasons as a function of local time of the day. The percentage standard deviation is perhaps most important during the midday period when the absolute values of TEC are highest. During this midday period, the standard deviation is approximately twenty percent. Figure 8 shows similar data for the solar minimum period of 1974-75 when the midday standard deviation of TEC at Hamilton is between 20 and 25 percent. The nighttime values of standard deviation are considerably higher, but the absolute TEC values are much lower at night during solar minimum conditions than at other times. These are the deviations of TEC that must be taken into account in many transionospheric systems in addition to the average level of TEC.

While the standard deviation does give a good estimate of the variability of ionospheric time delay, there are rare times when the distribution of TEC values departs greatly from a normal curve, such as during a large magnetic storm when worst case departures from monthly average conditions are likely to occur. Any system design engineer must be careful to consider worst case TEC values, even though they occur infrequently.

Under certain conditions involving transmissions between the surface of the earth and high altitude satellites or other space objects, the TEC_T is needed. Recent studies by Soicher[19] have shown that the portion of TEC_T not due to the ionosphere but due to the ionization in the plasmasphere varies anywhere from 45 percent (during the night) to 10 percent (during the day) of the ionospheric content, TEC. The plasmaspheric portion of TEC_T shows a much smaller diurnal, seasonal, and day-to-day ionospheric contribution. The relatively small magnitude of these variations suggest that the models of TEC can be adjusted to give TEC_T simply by adding a constant correction[19].

4.2 Models of Total Electron Content

Because measurements of TEC are made at discrete points on the globe and because system requirements are such that the system engineer requires the flexibility to evaluate TEC and its effects at any point on the globe, models of the world-wide distribution of TEC have been developed. These models generally represent the average behavior of the ionospheric density or total electron content. Models of the ionization density in the form of profiles can be used to evaluate total electron content simply by numerically integrating the electron density profile for the base of the ionosphere up to the desired height. Models of TEC can be classified as either physical or empirical in nature.

A physical model is one in which attempts are made to mathematically describe the physical processes which result in the free electrons in the earth's ionosphere. Given initial conditions of the earth's atmosphere, the solar ionizing radiation which impinges upon it, and a knowledge of the many reaction rates involved, electron density profiles as a function of geographic position and height can be calculated. Such electron density values can then easily be integrated along any radio wave path used to compute ionospheric time delay at a system operating frequency. The Penn State Model[20] developed by Nisbet is perhaps the most well known physical model.

While physical models certainly have the greatest long term potential of solving and describing the world-wide TEC, at present, their use and accuracy are severely limited by a knowledge of the input conditions. Also, considerable computer resources are required to run such models. Their use by system design engineers is not recommended at this time[1] for other than initial planning purposes.

Empirical models are usually mathematical descriptions of available experimental data that have been grouped in some coherent manner. Many of these models combine specific representations of the behavior of selected ionospheric parameters with formulae describing

the vertical distribution of the ionized atmosphere. Perhaps the most complete empirical model is that given by the CCIR in Report 340[21]. This model gives values of the global behavior of various ionospheric parameters in the form of equations and coefficients that are related to solar activity. Empirical models developed to represent the vertical distribution of the ionospheric electron density have been given by Flattery et al.[22]; Chiu[23]; Bradley and Dudeney[24]; Rawer et al.[25]; and Rush and Miller[26].

An ionospheric profile model from which TEC can be easily obtained has been developed by Bent[5] in which he used the analytic representations as a base and developed topside ionospheric thickness parameter values from the Alouette satellite topside sounder. His model, while world-wide in application, contains topside information mainly from the 70°W longitude meridian region, and is expected to work best in that region. The Bent model is perhaps the best presently available state-of-the-art empirical TEC model.

Klobuchar[27] constructed an algorithm of ionospheric time delay for users who do not have large computer resources. It was designed to obtain an approximate 50 percent correction for ionospheric time delay including day-to-day variability. His model representation attempts to fit the monthly average TEC at those times of the day when time delay values are greatest. He makes no attempt to update for day-to-day variability, though the model representation can easily be adapted for this purpose. Only eight coefficients are used to represent the world-wide behavior of ionospheric time delay.

An example of how these models can be utilized in systems design applications is given in Figures 9 and 10. These figures, deduced using the model of Bent[5], show contours of the percentage of yearly daytime hours that the time delay at 1.6 GHz (determined for TEC by Eq.(6)) exceeds the indicated number of nanoseconds. Figure 9 shows the results for low sunspot number (SSN=10) and Figure 10 shows the results for high sunspot number (SSN=110). The highest percentage contours occur over the equator and the lower latitudes. Unless a system is designed that can operate with time delays of this magnitude, correction factors in the form of models must be developed.

The models of TEC fairly well represent the monthly average values at many locations. In the near-equatorial locations, there are little available data against which the models may be tested, except for a few locations such as Hawaii and Hong Kong. The near-equatorial regions are very important for world-wide navigation systems which require TEC corrections because the highest TEC values are found in this part of the world.

To make any significant improvement upon the monthly average climatology of TEC near-realtime measurements must be made. DuLong[28] has shown that, for data taken from the same location in the same direction, useful improvements to climatology can be made with data up to three hours old. Figure 11, derived from DuLong, shows the percent TEC remaining after correction for near-realtime TEC data. The improvement over monthly climatology is high during solar maximum daytime periods when the absolute values of TEC are highest, which is when a good correction is most required. During solar minimum periods, a three-hour forward prediction based upon actual measurements, in the same direction as the one for which an updated TEC value is required, is not any better than the use of a monthly or seven-day running value. During the sunrise and sunset periods, the useful time interval over which a measurement can improve upon climatology is shorter, due to the large geographic gradients which exist during these periods.

Because the TEC that is used to update the models may be measured at locations that are not exactly those where the models are to be applied operationally, it may be necessary to extend and extrapolate the observations. The usefulness of the observations in providing accurate information decreases quite rapidly with increasing distance between the observation location and the location where the updated information is to be applied[29-31].

4.3 Behavior of TEC During Magnetic Storms

Because of the variations in TEC that occur during some geomagnetic disturbances, a great deal of attention has been devoted to describing and predicting the effects. The changes in TEC during magnetic storms can be larger, faster, and more extensive than those associated with normal day-to-day variations. The changes in the ionosphere resulting from magnetic activity have long been the subject of detailed studies. Figure 12 provides an indication of the percentage change in TEC as a function of local time. This figure was taken from the work of Mendillo et al.[32] and represents the disturbed daily variation of TEC averaged over 75 mid-latitude magnetic storms.

The electron content in the plasmosphere usually shows a marked depletion as magnetic activity increases but enhancements in electron content have been observed (Davies[33] and references contained therein). The plasmospheric content appears to return to values comparable to the monthly average anywhere from seven to fourteen days after the onset of the magnetic storm[33].

5.0 TRANSIONOSPHERIC SCINTILLATIONS

5.1 Basic Theory of Ionospheric Scintillation

When a radio wave passes through irregular structures in electron density of the ionosphere, it is diffracted and fluctuates in amplitude and phase. Early studies revealed that the irregularities giving rise to ionospheric scintillation occurred mainly in the F-region and were aligned along the geomagnetic field lines. It is now known that irregularities associated with precipitation of charged particles at high latitudes give rise to irregularities at heights in the E-region of the ionosphere which also induce scintillation phenomena on signals traversing the irregularity structure.

The status of scintillation theory and the agreement between theoretical predictions and observations have recently been reviewed in detail by Crane[34]. The interested reader is referred to the work of Crane for the details of the mathematical treatment necessary to derive the pertinent equations. We will concern ourselves here only with selected pertinent aspects of scintillation theory.

The electron-density irregularities responsible for ionospheric scintillation form a volume of random refractive index irregularities along the propagation path. A complete theory for wave propagation through a medium with random dielectric constant fluctuations is not available. Approximate solutions or models have been proposed that apply under restrictive conditions. Contributions to the development of these models have come from the areas of optical propagation through the lower atmosphere, acoustical propagation through the ocean and the atmosphere, and radiowave propagation through the lower atmosphere, ionosphere, and interstellar space.

Using the assumptions that the wave may be represented by $E = Ee^{i\omega t}$, where $\omega = 2\pi F$, F is the carrier frequency, t is the time, and E is the electric field vector; that a component of E is represented by u; that the dielectric properties of the medium change slowly in time in comparison with $1/F$ and slowly in space in comparison with the wavelength λ; and that polarization effects are not important, the propagation of the wave through the the irregularity region is governed by the scalar wave equation.

$$\nabla^2 u + k^2 \varepsilon u = 0 \tag{11}$$

where $k = 2\pi/\lambda$, ε is the dielectric constant ($\varepsilon = 2n$, n is the index of refraction), and both u and ε are random variables. If further, the dominant variations in dielectric constant occur on scale sizes of the order of the size of the first Fresnel zone ($r_o = \sqrt{\lambda Z}$ where Z is the reduced distance equal to $\rho(L - \rho)/L$, L is the path length and ρ is the distance from one end of the path to the irregularity) or larger, the energy is scattered into the forward direction and (11) may be replaced by the diffusion approximation:

$$-i2k \frac{\partial U}{\partial x} + \nabla_{\perp}^2 U + k^2 \varepsilon U = 0 \tag{12}$$

where $u = Ue^{-ikx}$, x is the direction of propagation, and $\nabla_{\perp}^2 = \partial^2/\partial y^2 + \partial^2/\partial z^2$, the transverse Laplacian.

In order to solve either Eq.(11) or Eq.(12), certain approximations must be made concerning the refractive index (the spectrum of the irregularities) and the manner in which the radio wave interacts with the irregularities.

The generally accepted model for ionospheric scintillation has been the thin phase diffraction screen model[35]. In this approximation, the irregularity region or the effect of the irregularities is assumed to occur in a thin layer. The thin phase screen approximation, however, does not provide a recipe for establishing a connection between the electron-density fluctuations in the generally thick irregularity region above the reference plane which is used for the thin phase changing screen. The phase fluctuations at the screen are calculated using geometrical optics. The geometrical optics approximation may be obtained by assuming that the scale sizes of the electron-density fluctuations are much larger than the size of the first Fresnel zone for propagation from the source to the screen. In this approximation, the effect of diffraction by irregularities above the screen is ignored by calculating the field at the screen. This approximation is justified if the layer is thin enough for $\sqrt{\lambda Z} \ll l_o$ where l_o is the size of the smallest irregularity, a situation rarely encountered in transionospheric propagation.

Recent work in the analysis of strong scintillation has attempted to use the concept of multiple thin screens to remove the requirement for the use of the geometrical optics approximation in the thin-screen model[34].

The intensity at which scintillations are observed depends upon the position of the observer relative to the irregularities in the ionosphere that cause the scintillation. Keeping both the thickness of the irregularity region and ΔN, the electron density deviation of the irregularity, constant, geometrical factors have to be considered to evaluate data. Among these factors are:

(1) the zenith distance of the irregularity at the ionospheric layer;

(2) the propagation angle relative to the earth's magnetic field;

(3) the distance from the irregularity region to the source and to the observer.

Concerning the frequency dependence of scintillation, observations[36] employing ten frequencies between 138 MHz and 2.9 GHz transmitted from the same satellite, show a consistent $\lambda^{1.5}$ behavior of S_4 for S_4 less than about 0.6. The frequency dependence is less steep for stronger scintillation, with S_4 attaining a maximum value near unity with a few rare exceptions. The same observations show that the phase scintillation index, σ_ϕ (defined as the standard deviation of phase in the fluctuation-spectral range containing intensity scintillations), varies as λ under most conditions.

The fading period of scintillation varies over quite a large range. The fading period depends both upon the apparent motion of the irregularities relative to the ray path and in the case of strong scintillation on its severity. For strong scintillation with $S_4 > 0.4$ or where peak to peak fading is greater than 8 dB, the fading period is shorter than for weak scintillation with the same relative velocity. The fading period of gigahertz scintillation at the equator ranges from 2-15 seconds. The gigahertz measurements were in the weak scintillation limit and were made when both the transmitter and receiver were stationary; therefore, the observed fading periods reflect the motion of the ionospheric irregularities.

The fading rate is a function of ground pattern size and motion of the ionospheric winds, the observer and the source. Essentially at all latitudes the ground pattern size is frozen when observing low altitude satellite signals. When observing synchronous satellites from ground stations, the wind pattern determines the fading rate.

5.2   Ionospheric Scintillation in Equatorial Regions

The morphological behavior of scintillations in the equatorial regions of the globe and a discussion of the causes of the scintillation producing ionospheric irregularities has been recently given by Aarons[37]; the discussion presented here will closely follow that work. Further information is available in Aarons et al.[38].

In the equatorial region, the typical development of scintillation from an ionosphere devoid of intense irregularities to that where deep fading is observed is often abrupt and dramatic as shown in Figure 13. The start of scintillations can often be noted to take place within a few seconds. An example of the fast onset, the deep rapid continuous fluctuation and finally the slowing and more sporadic fading is shown in the top panel of the figure. The observations illustrated are of the 254 MHz transmissions of LES-6. The use of a large antenna (in this case, 28 ft in diameter) has allowed deep fading to be observed, frequently of the order of 20 dB below mean level. Rapid deep fading characterizes the beginning of the scintillation activity. As the night progresses, the scintillation frequently becomes more sporadic. The small scale irregularities are contained in the large scale patches that move across the path. Finally, at the end of the scintillation activity, the scintillations change character, and long fades may remain below fade margins of 6 dB for 5 to 30 seconds.

The patterns of scintillation activity show great variety. One pattern that has been observed frequently is of a patchy nature. Scintillations on one satellite path start and stop during the night several times, with the patch moving through the propagation path in times of the order of 20 minutes to several hours. Similar lifetimes of the patches of irregularities, as well as their velocities, have been reported in transequatorial studies of irregularities by HF transmissions.

In the equatorial region, experiments were performed to study the development and maintenance of the large scale irregularity patches (several hundred kilometers EW and many times that NS) which often contain the small scale irregularities of approximately 3 m to 1 km which produce VHF to microwave scintillation.

Figure 14 shows typical patch three-dimensional structure at local times depending on the stage of formation or dissolution. With the formation of a thin layer of irregularities (approximately 1930 local time) UHF scintillations start with 5 dB peak-to-peak values typical. Fading rates (on the ground) are typically 10/min. During the formation of the plume, scintillations show greater depth (approximately 20 dB peak-to-peak); irregularity thickness increases as well as strength of returns; rates exceed 10/min. It is during this time that microwave scintillations are probably observed.

After formation, an irregularity structure moves east at speeds between 50 and 150 m sec^{-1}. Scintillations observed during this phase are still high. At a later stage, irregularities within a specific patch begin to decrease in intensity, resulting in lower scintillation levels. Limited observations suggest that the eastward motion of these patches slows down in the later stage, around midnight.

There are seasonal maxima of the occurrence of equatorial scintillations. The precise pattern varies as a function of longitude and solar flux. The seasonal pattern and the solar cycle dependence can best be illustrated with the aid of Figures 15a and 15b, utilizing observations at Huancayo, Peru, of ATS-3 transmitting at 137 MHz.

Figure 15a utilizes data taken at the peak of the solar cycle (August 1969 to July 1970) with another period (Figure 15b) centered around a minimum in the solar cycle (August 1973 to July 1974). There is a higher occurrence of deep scintillations (a scintillation index (SI) greater than 60 (6 dB peak-to-peak)) with an S_4 of 0.3 during a year of high solar flux (August 1969 to July 1970) than during a year with low solar flux (August 1973 to July 1974). The magnetic index K_p range is in both cases from 0-3 to avoid possible confusion with magnetic storm effects.

Mullen and Hawkins[39] found that the peak of the equinoctial activity took place in November and March at Accra, Ghana, whereas Huancayo data show a diffuse maximum from October through March, with only a slight decrease in scintillation activity in December.

The seasonal pattern for the eastern region of Asia is not clearly ascertained. Nichols[40] found the seasonal pattern of 250 MHz fades to maxmize between April and October. Taur[41], using 4 and 6 GHz data, found maximum occurrence in February to April and September to November. He worked with global statistics. Basu et al.[42] presented the estimated worldwide equatorial morphology of percentage scintillation greater than or equal to 4.5 dB at 140 MHz for November-December 1969 and 1970 during 1900-2300 LT on magnetically quiet days based on 250 Ogo-6 orbits (Figure 16). A great variability in occurrence as a function of longitude is seen.

5.3 Ionospheric Scintillation at High Latitudes

In the high latitude ionosphere, scintillation tends to maximize above the aurora[43]. At polar latitudes, the observed scintillation level is high but somewhat lower than at auroral latitudes[38].

During magnetic storms, scintillation levels increase dramatically with local excursions of the magnetic field. Statistically, scintillation levels increase with K_p and with AE index[44]. Recent analysis of data of several high latitude stations show a general trend of an increase of scintillation excursions with both increasing solar flux and increasing K_p[45]. This trend is affected by the seasonal character of the scintillation excursions. These are shown in Figures 17a and 17b for a station at approximately $63^{\circ}\Lambda$ under both quiet and disturbed magnetic conditions. The mean scintillation index as a function of invariant latitude varied with magnetic activity. At latitudes above 53°, a higher K_p was associated with increased scintillation, while below 53° there was a small decrease in scintillation with increasing K_p.

Perhaps the largest contribution to understanding the causes of ionospheric irregularities is due to in situ measurements of various ionospheric parameters. These include electric fields, thermal electrons, superthermal electrons, and ion density measurements.

Correlating in situ measurements with scintillations can only be done under conditions involving several assumptions. In situ measurements give no indication of thickness, an effect of importance on scintillation excursions. In situ measurements are frequently higher in altitude than the 350 km level found to be the predominant height of the (often) thin layer irregularities. In situ measurements, unless configured carefully, do not show the effects of irregularity elongation, field alignment or zenith angle. More basically, however, in situ measurements may measure the causal element for the production of the irregularities (superthermal electrons), for example; therefore, the ambient atmosphere must be taken into consideration.

One series of significant measurements was obtained with an electrostatic probe on ISIS-1; thermal positive ion observations were made[46]. A spatial resolution of 150 meters was possible. The equatorial boundary of the irregularity region was defined as the latitude of onset of persistent small scale ionization irregularities extending over at least a few degrees in latitude with amplitudes amounting to 20 percent or more of the mean background levels.

The boundary of the irregularity zone was found to be 3° to 9° closer to the pole in the southern hemisphere than in the northern hemisphere. The seasonal variation of the mean location was small. The boundary is closest to the pole in June and farthest in December. No poleward boundaries for the irregularity zone were found; the inhomogeneities extend across the pole. Comparison of the irregularity boundary of this technique and that of the scintillation boundary were excellent at night and between 2100 and 0600 local time but differed at 1700 LT (Figure 18).

The severe topside irregularity zone was observed using the ionosonde on ISIS-2[47]. On the dayside of the earth, the equatorward boundaries of this zone and of the < 300 eV electron precipitation coincide. However, the boundary does not coincide with electron precipitation above 300 eV. The zone extends beyond the poleward boundary of the particle precipitation, probably due to magnetospheric convection transporting irregularities poleward of the region of production.

5.4 Scintillation Effects on Transionospheric Systems

In order that the observations of ionospheric scintillation can be readily utilized to assess the performance of telecommunication systems that rely on the propagation of electromagnetic energy through the ionosphere, various indices have been developed. The intensity of the scintillation may be characterized by the variance in received power or by the variance in the logarithm of received power. The measure S_4 is defined as the square root of the variance of received power divided by the mean value of the received power. The measure σ_χ is the square root of the variance of the logarithm of the received power. For periods of scintillation having a constant value of either one of these measures, the signal level fluctuations may be described by an empirical probability density function (pdf). Sample empirical pdfs are given in Figure 19 for several S_4 values. The strength of phase scintillation may be characterized by the standard deviation of phase, σ_ϕ. Empirical pdfs for phase fluctuations are given in Figure 20 for the same cases shown in Figure 19. The data depicted in Figures 19 and 20 were obtained at a mid-latitude station at 150 and 400 MHz[34].

Attempts have been made to model the observed amplitude pdf. Whitney et al.[48] and Crane[34] have constructed model distribution functions based upon the use of the Nakagami-m distribution ($m = (S_4)^{-2}$) and have shown that the models provide a reasonable approximation to their observed empirical distribution functions. In addition, the Rayleigh pdf provided a good fit to the data under conditions of very strong scintillation ($S_4 \gg 0.9$). The Nakagami-m distribution is a Rayleigh distribution for $m = 1$ (strong scintillation), and is a log-normal distribution for $m > 1$ (weak scintillation).

The log-normal and Nakagami-m distributions are both characterized by a single parameter which can be related to either S_4 or σ_χ. More complex models exist with more parameters that can be adjusted to fit the data.[x]

Signal fluctuations may also be described by their power spectrum. The power spectrum for phase fluctuations shown in Figure 21 continues to increase with decreasing frequency, showing the domination of phase fluctuations by the large-scale refractive-index changes as predicted by geometrical optics. These data show that for a sufficiently long observing time, the variance of log-amplitude (proportional to σ_χ^2) reaches a fixed level, but the variance of signal phase continues to increase with increasing observing time. Since the power spectrum for phase fluctuations behaves approximately as f^{-3}, and doppler or angle-of-arrival fluctuations may be related to the temporal or spatial derivative of the phase fluctuations, the power spectra for doppler fluctuations will vary as f^{-2}. The angle-of-arrival or doppler variances will also continue to increase with increasing observing time.

The data depicted in Figure 21 were obtained using a rapidly moving low orbiting satellite. During the portion of the satellite pass used to generate the spectra, the ionosphere could be considered frozen. The temporal fluctuations, therefore, may be interpreted as spatial fluctuations. The scale sizes at a height of 300 km are indicated on the second scale. For a geostationary satellite, the spatial fluctuations will not change, but the temporal fluctuations will. The spatial fluctuations may be expressed either as fluctuations at a point in the ionosphere or fluctuations on the ground (and normal to the line-of-sight). At the ground, the peak of the log-amplitude power spectrum occurs at scale sizes near $\ell = 2.5\, r_o z_2/(z_2-z_1)$. The data shown in Figure 21 are for motion of the satellite nearly perpendicular to the magnetic field. The resultant scale sizes, therefore, are for a direction perpendicular to the field. For a direction along the field, the scale size increases by the axial ratio of the irregularities.

The effects of ionospheric scintillation on satellite communication systems have been described by numerous workers. Whitney and Basu[49], for example, demonstrated how scintillation observations made using the ATS-6 satellite could be interpreted in terms of message reliability. Figure 22 shows an indication of the message reliability deduced using ATS-6 signals at 137 and 360 MHz measured during a period of intense scintillation. The curves show that as the message length increases, the reliability decreases as would be expected. For a message length of four seconds, 40 percent of the messages would be perfectly received at the -8 dB fade margin level at 137 MHz. As the fade margin decreases, the message reliability decreases for a message of constant length. More recently, Davies[33] has described in detail other studies that have been undertaken to demonstrate how ionospheric scintillation impacts the performance of satellite communication systems, particularly as revealed by the observations of the ATS-6 satellite.

Because of the potential for degradation of circuit performance due to scintillation, efforts have been undertaken to overcome possible degrading effects. Most of these efforts are directed toward developing optimum diversity schemes.

Diversity schemes attempt to reduce the effects of fading during a scintillation event by combining two signals that are fading independently. For a Rayleigh process, signal fades are greater than 18.4 dB for one percent of the time. For two independent Rayleigh processes, the larger of the two signals at any sample point fades to 9.5 dB for one percent of the time yielding a gain in protection against fading of 9 dB. In general, the diversity gain depends upon the correlation between the two samples of the fading process. If the correlation coefficient is less than 0.6, the diversity gain is 8 dB or better. A correlation coefficient of 0.6 may be used as a threshold for diversity action for a fading process although it strictly applies only to a Rayleigh fading (strong scintillation). In the limit of weak scintillation, a correlation coefficient less than 0.6 occurs between observations at two frequencies for signals propagating along the same path only if the carrier frequencies are separated by more than a factor of three suggesting that frequency diversity is not generally effective in combating scintillation[34].

Two diversity schemes are viable for both weak and strong scintillation conditions: time and space. For a two-way station configuration, time diversity requires that the same message be sent at two different times separated far enough for the correlation coefficient to be less than 0.6. Space diversity requires that the same message be detected at two receiving points separated far enough for the coefficient to be less than 0.6. The correlation function may be calculated from the power spectrum for the received signal fluctuations. The time separation corresponding to a correlation coefficient of 0.6 is given by $\tau = 0.3\, r_o/v$. For space diversity, the distance for a correlation coefficient of 0.6 is $\ell = 0.3\, r_o z_2/(z_2-z_1)$ for a direction normal to the line-of-sight and normal to the field, and $\ell = 0.3\, r_o \alpha(z_2/z_2-z_1)$ for a direction normal to the line-of-sight in the direction of the field, where α = axial ratio of the irregularities. For oblique incidence, the projection of these distances onto the ground is required for the estimation of diversity distance.

Diversity schemes are normally only required to overcome the effects of intense scintillations; weak scintillations are offset by a reasonable fade margin. In the equatorial zone, measurements of the spatial cross-correlation function for strong scattering conditions have given typical values for the correlation coefficient of 0.6 for 300 m antenna separation and 0.3 for 1000 m separation[13]. Space diversity seems only practical for fixed ground stations.

5.5 Scintillation as an Indicator of Ionospheric Processes

Because ionosphere scintillation results from the passage of radio waves through regions of irregularities in the ionospheric structure, observations of scintillations can assist in depicting the dominant physical processes at work in the ionosphere under certain conditions. For example, the large scintillations observed at the equatorial regions have spurred work directed toward obtaining an understanding of the causes of irregularities in the equatorial region. In recent years, an understanding of the formation, generation, and maintenance of equatorial irregularities has emerged.

After sunset, for reasons still under study, a localized depletion of electron density may form in the lower F layer which then rises and moves into the middle and upper F layer. This upwelling results in "plumes" on VHF radar maps of irregularity intensity versus height and time.

Another phenomenon, observed on many backscatter records and not necessarily related to the plumes, is the formation of a thin layer of irregularities of moderate intensity near the bottomside of the F-region. Scintillation activity associated with this backscatter is of the order of 5 dB on UHF records at 249 MHz whereas VHF records at 136 MHz show a sharp onset of scintillation with rapid and deep fading when the bottomside irregularities appear. The apparent difference between the behavior of the two bands is probably due to the frequency dependence of scintillation[50].

From in-situ measurements[51] it appears that in the equatorial F region ambient electron density depletions over 50 km may be of one to two orders of magnitude. Small scale perturbations within these depleted bubbles produce scintillation effects. From a study of in-situ irregularity data, irregularity amplitudes ranging from 10 percent to 100 percent are found to occur in the equatorial region[42]. The electron density deviation ΔN (10 percent of the ambient in one case cited) responsible for moderate level UHF scintillations appears typically of the order of 6×10^{10} m^{-3} with a thickness of 200 km. Stronger electron density deviations result in S-band scintillation activity[52].

With the formation of a thin layer of irregularities (approximately 1930 local time), UHF scintillation starts with approximately 5 dB peak-to-peak values. Fading rates (on the ground) are of the order of 10/min. During the formation of the plume, scintillations show greater depth (approximately 20 dB peak-to-peak). Irregularity thickness and radar returns become stronger; fading rates exceed 10/min. The occurrence of microwave scintillations most probably takes place during this time.

After formation, irregularity structures move east at speeds between 50 and 150 m sec^{-1}. Scintillations observed during this phase are still strong. At a later stage, irregularities within a specific patch begin to decrease in intensity, resulting in lower scintillation levels. Limited observations suggest that the eastward motion of these patches slows down in the later stage, around midnight[50].

High latitude scintillation observations have also been a spur to better understanding the physical processes at work in the high latitude ionosphere. Recent studies by Rino et al.[53], for example, demonstrate that irregularities in electron density in the polar region give the appearance of being sheet-like (due to alignment along the geomagnetic field lines). These sheet-like irregularities exist in the region of the instantaneous nighttime auroral oval. The cause of these irregularities is proposed to be due to acceleration mechanisms in the magnetosphere that are manifested in the auroral region of the ionosphere[53].

6.0 CONCLUSION

In this paper, we have attempted to point out how the ionosphere impacts on the performance of telecommunication systems whose energy is propagated through the ionosphere. The discussion has concerned itself almost entirely with the propagation of radio waves in the VHF and UHF portions of the electromagnetic spectrum. Telecommunication systems that employ these frequencies (30 MHz to 3.0 GHz) as a means of propagating energy can suffer a degradation in performance because of the ionosphere and its structure. The ionosphere can be considered as a nuisance for these systems since the system performance can be degraded compared to propagation of energy in free space (or in the absence of the ionosphere). This is in complete contrast to telecommunications systems operating in the HF portion of the spectrum where the very existence of the ionosphere permits long distance propagation. For HF systems, the ionosphere is an integral part of the system; for VHF/UHF systems, the ionosphere is a potential source of error.

Telecommunications systems--satellite communication, satellite navigation, radars, etc.--can be impacted by the ionosphere. Regardless of their ultimate application, radio waves propagated into and through the ionosphere will be slowed down and refracted by the ionospheric electron content and the same waves can fluctuate in amplitude and phase as a

result of encountering irregularities in the electron content along the propagation path. Thus, system designers and planners, telecommunication policy makers, and engineering personnel must have at their disposal methods to assess the effects of the ionosphere on the performance of their systems and must develop, if warranted, techniques to mitigate these effects. Through systematic observation and understanding of the phenomena giving rise to potential adverse impacts, this information can be supplied.

The future course for telecommunication utilization appears to be one of expanded capabilities resulting from greater demands. It is rather safe to speculate that requirements for increased system reliability and performance will ensue. It is also safe to speculate that in this age of silicon devices and computer "chips" that the errors in overall system performance will primarily result from causes other than equipmental. The medium through which the systems propagate their energy can in the end provide the final limitations to overall performance. It is for these reasons that a great deal of activity is devoted toward assessing the impact of the natural atmosphere on the performance of radio propagation systems and why such activity should reasonably continue in the foreseeable future.

7.0 ACKNOWLEDGEMENTS

8.0 REFERENCES

1. Klobuchar, J. A., AGARD Lecture Series No. 93, Recent Advances in Radio and Optical Propagation for Modern Communications, Navigation and Detection Systems; Ionospheric Effects on Satellite and Air Traffic Control Systems, 1978, AGARD-LS-93, 7-1 to 7-17.

2. Millman, G. H., and G. M. Reinsmith, An Analysis of the Incoherent Scatter-Faraday Rotation Technique for Ionospheric Propagation Error Correction, General Electric Technical Information Series, R74EMH2, February 1974. Available from HMES Technical Publications, Box 1122 (CSP4-24), Syracuse, N.Y. 13201.

3. Briggs, B. H. and I. A. Parkin, On the variation of radio star and satellite scintillation with zenith angle, J. Atmos. Terr. Phys., 25, 1963, 339.

4. Cretcher, C. K., Ionospheric effects in NAVSTAR-GPS, in Effects of the Ionosphere on Space Systems and Communications, Edited by J. M. Goodman, Naval Research Laboratory, Washington, D. C., 20375, 1975, U. S. Government Printing Office Stock No. 008-051-00064-0, 403-410.

5. Bent, R. B., S. K. Llewellyn, G. Nesterczuk, and P. E. Schmid, The development of a highly-successful worldwide empirical ionospheric model and its use in certain aspects of space communications and worldwide total electron content investigations, in Effects of the Ionosphere on Space Systems and Communications, Edited by J. M. Goodman, Naval Research Laboratory, Washington, D. C., 20375, 1975, U. S. Government Printing Office Stock No. 008-051-00064-0, 13-28.

6. Fremouw, E. J., M. D. Cousins, and G. K. Durfey, Wideband satellite observations, Bimonthly Progress Report 5, Contract DNA 001-75-C-0111, Stanford Research Institute, March 9, 1977.

7. Aarons, J., AGARD Lecture Series No. 93, Recent Advances in Radio and Optical Propagation for Modern Communications, Navigation and Detection Systems; Ionospheric Scintillations: An Introduction, 1978, AGARD-LS-93, 8-1 to 8-22.

8. Allen, R. S., D. E. Donatelli, G. K. Hartmann, and R. Leitinger, Adaptive mapping of mid-latitude ionosphere, Air Force Surveys in Geophysics No. 372, August 3, 1977, AFGL-TR-77-0176.

9. Allen, R. S., D. E. Donatelli, and M. C. Picardi, Correction for onospheric refraction for COBRA DANE, Air Force Surveys in Geophysics No. 376, November 18, 1977, AFGL-TR-77-0257.

10. Katz, A. H., M. Grossi, R. A. Allen, and D. Donatelli, Adaptive correction of the effects of the ionosphere on range determination by terrestrial radars, Preprints of Proceedings, 1978 Symposium on the Effect of the Ionosphere on Space and Terrestrial Systems, Naval Research Laboratory and the Office of Naval Research, January 24-26, 1978, Washington, D. C., 20375, Paper 6-8.

11. Tomljanovich, N. M. and R. J. Lang, Satellite-referenced ionospheric propagation correction for USAF spacetrack radars, AGARD Conference Proceedings No. 238, Operational Modelling of the Aerospace Propagation Environment, Edited by H. Soicher, 1978, AGARD-CP-238, Vol. I, 8-1 to 8-12.

12. Perkins, F. W. and R. G. Roble, Ionospheric heating by radio waves: predictions for Arecibo and the satellite power station, J. Geophys. Res., 83, 1978, 1611-1624.

13. CCIR Report 263-4, Ionospheric Effects Upon Earth-Space Communication, Kyoto, 1978.

14. CCIR Report (6/356), Ionospheric Properties, Documents of the 14th Plenary Assembly, Kyoto, 1978.

15. Amayenc, P., F. Bertin, and J. Papet-Lepine, Sur l'evolution du contenu electronique de l'ionosphere, An. de Geophys., 27, 1971, 345-357.

16. Mendillo, M. and J. A. Klobuchar, Investigations of the ionospheric F-region using multi-station total electron content observations, J. Geophys. Res., 80, 1975, 643-650.

17. Soicher, H., Comparative ionospheric and plasmospheric electron contents for three world regions, Nature, 264, 1976, 46-48.

18. Mendillo, M. and J. A. Klobuchar, An atlas of the midlatitude F-region response to geomagnetic storms, February 1974, AFCRL-TR-74-0065.

19. Soicher, H., Ionospheric and plasmaspheric effects in satellite navigation systems, IEEE Trans. Antennas and Prop., AP-25, 1977, 705-708.

20. Nisbet, J. S., On the construction and use of a simple ionospheric model, Radio Science, 6, 1971, 437-464.

21. CCIR Report 340-3, CCIR Atlas of Ionospheric Characteristics, Kyoto, 1978.

22. Flattery, T. W. and A. C. Ramsay, Derivation of total electron content for real time global applications, in Effects of the Ionosphere on Space Systems and Communications, Edited by J. M. Goodman, Naval Research Laboratory, Washington, D. C., 20375, 1975, U. S. Government Printing Office Stock No. 008-051-00064-0, 336-344.

23. Chiu, Y. T., An improved phenomenological model of ionospheric density, J. Atmos. and Terr. Phys., 37, 1975, 1563-1570.

24. Bradley, P. A. and J. R. Dudeney, A simple model of the vertical distribution of electron concentration in the ionosphere, J. Atmos. and Terr. Phys., 35, 1973, 2131-2146.

25. Rawer, K., S. Ramakrishnan, and D. Bilitza, Preliminary Reference Profiles for Electron and Ion Densities and Temperatures Proposed for the International Reference Ionosphere, Institut für physikalische Weltraumforschung, Heidenhofstrasse, 8, Freiburg, Federal Republic of Germany, July 1975.

26. Rush, C. M. and D. Miller, A three-dimensional ionospheric model using observed ionospheric parameters, September 10, 1973, AFCRL-TR-73-0567.

27. Klobuchar, J. A., A first-order, worldwide, ionospheric time-delay algorithm, September 25, 1975, AFCRL-TR-75-0502.

28. DuLong, D. D., Reduction of the uncertainty of radar range correction, June 1977, AFGL-TR-77-0125.

29. Rush, C. M., Limitations of mapping techniques to predicting total electron content at a distant point, Effects of the Ionosphere on Space Systems and Communication, Edited by J. M. Goodman, Naval Research Laboratory, Washington, D. C., 20375, 1975, U. S. Government Printing Office Stock No. 008-051-00064-0, 392-401.

30. Klobuchar, J. A. and J. M. Johanson, Correlation distance of mean daytime electron content, August 22, 1977, AFGL-TR-77-0185.

31. Soicher, H., Correlation and prediction of transionospheric signal time delays at widely separated locations, AGARD Conference Proceedings No. 238, Operational Modelling of the Aerospace Propagation Environment, Volume I, edited by H. Soicher, 1978, AGARD-CP-238-Vol. 1, 26-1 to 26-4.

32. Mendillo, M., M. J. Buonsanto, and J. A. Klobuchar, The construction and use of storm-time corrections for ionospheric F-region parameters, Effects of the Ionosphere on Space Systems and Communication, Edited by J. M. Goodman, Naval Research Laboratory, Washington, D. C., 20375, 1975, U. S. Government Printing Office Stock No. 008-051-00064-0, 361-371.

33. Davies, K., Recent progression in satellite radio beacon studies with particular emphasis on the ATS-6 radio beacon experiment, submitted to Space Science Rev. 1979.

34. Crane, R. K., Ionospheric scintillation, Proc. IEEE, 65, 1977, 180-199.

35. Rufenach, C. L., Ionospheric scintillation by a random phase screen: spectral approach, Radio Science, 10, 1975, 155-165.

36. Fremouw, E. J., R. G. Livingston, C. L. Rino, M. Cousins, B. C. Fair, and R. L. Lead-abrand, Complex-signal scintillation--Early results from the DNA-002 coherent beacon, Radio Science, 13, 1978, 167-187.

37. Aarons, J., Equatorial scintillations: A review, IEEE Trans. Ant. Prop., AP25, 1977, 729-736.

38. Aarons, J., E. M. MacKenzie, and K. Bhavnani, Equatorial and high latitude empirical models of scintillation levels, AGARD Conference Proceedings No. 238, Operational Modelling of the Aerospace Propagation Environment, Volume I, edited by H. Soicher, 1978, AGARD-CP-238-Vol. 1, 20-1 to 20-20.

39. Mullen, J. and G. Hawkins, Equatorial scintillation at 136 MHz observed over half a sunspot cycle, Effect of the Ionosphere on Space Systems and Communications, Edited by J. M. Goodman, Naval Research Laboratory, Washington, D. C., 20375, 1975, NTIS CSCL 04/1 N75-30714#, 95-100.

40. Nichols, B. E., UHF Fading from a Synchronous Satellite Observed at Kwajalein, October 1968 through June 1970, 1974, Tech. Note, Lincoln Laboratory, 1974-19, Air Force Contract F19628-73-C-0002.

41. Taur, R. R., Simultaneous 1.5 and 4 GHz ionospheric scintillation measurements, Radio Science, 11, 1976, 1029-1036.

42. Basu, Sunanda, S. Basu, and B. K. Khan, Model of equatorial scintillations from in situ measurements, Radio Science, 11, 1976, 821-832.

43. Martin, E. and J. Aarons, F-layer scintillations and the aurora, J. Geophys. Res., 82, 1977, 2717-2722.

44. Basu, Sunanda, Universal time seasonal variations of auroral zone magnetic activity and VHF scintillations, J. Geophys. Res., 80, 1975, 4725-4728.

45. Aarons, J., J. Mullen, H. Whitney, E. Martin, K. Bhavnani, and G. Whelan, A high-latitude empirical model of scintillation excursions: Phase 1, September 17, 1976, AFGL-TR-76-0210.

46. Sagalyn, R. C., M. Smiddy, and M. Ahmed, High latitude irregularities in the top side ionosphere based on ISIS-I thermal ion probe data, J. Geophys. Res., 79, 1974, 4252-4261.

47. Dyson, P. L. and J. D. Winningham, Topside Ionospheric Spread F and Particle Precipitation in the Dayside Magnetospheric Clefts, 1973, AFCRL F19628-72-C-0230.

48. Whitney, H. E., J. Aarons, R. S. Allen, and D. R. Seeman, Estimation of the cumulative amplitude probability distribution function of ionospheric scintillations, Radio Science, 7, 1972, 1095-1104.

49. Whitney, H. E. and S. Basu, The effect of ionospheric scintillation on VHF/UHF satellite communication, Radio Science, 12, 1977, 123-133.

50. Whitney, H. E., J. Aarons, J. Buchau, E. Weber, and J. P. McClure, The evolution of scattering equatorial F-region irregularities and resultant effects on trans-ionospheric radio waves, AGARD Conference Proceedings No. 244, Aspects of Electromagnetic Scattering in Radio Communications, Edited by A. N. Ince, 1978, AGARD-CP-244, 8-1 to 8-11.

51. McClure, J. P., W. B. Hanson, and J. H. Hoffman, Plasma bubbles and irregularities in the equatorial ionosphere, J. Geophys. Res., 82, 1977, 2650-2656.

52. Basu, Sunanda and S. Basu, Correlated measurements of scintillations and in situ F-region irregularities from OGO-6, Geophys. Res. Lett., 3, 1976, 681-684.

53. Rino, C. L., R. C. Livingston, and S. J. Matthews, Evidence for sheet-like auroral ionospheric irregularities, Geophys. Res. Lett., 5, 1978, 1039-1042.
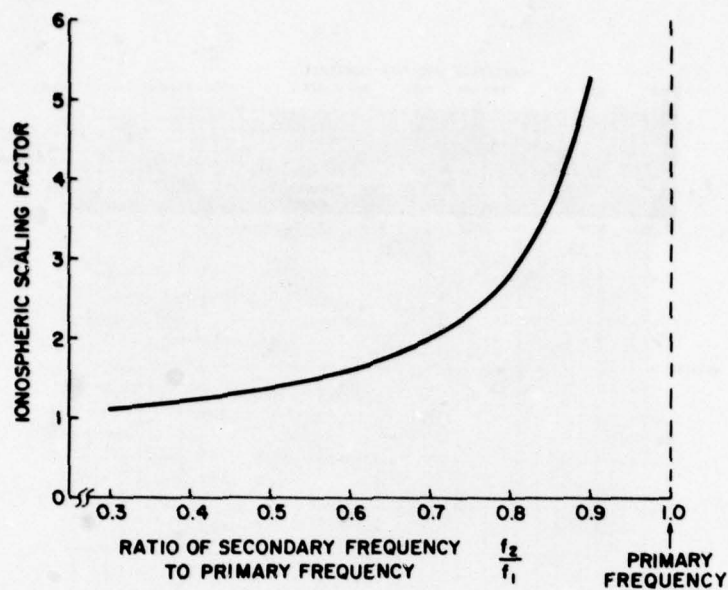
Figure 1.   Ionospheric scaling factor for two frequency differential time delay measurements versus the ratio of the secondary to the primary frequency (Klobuchar[1]).
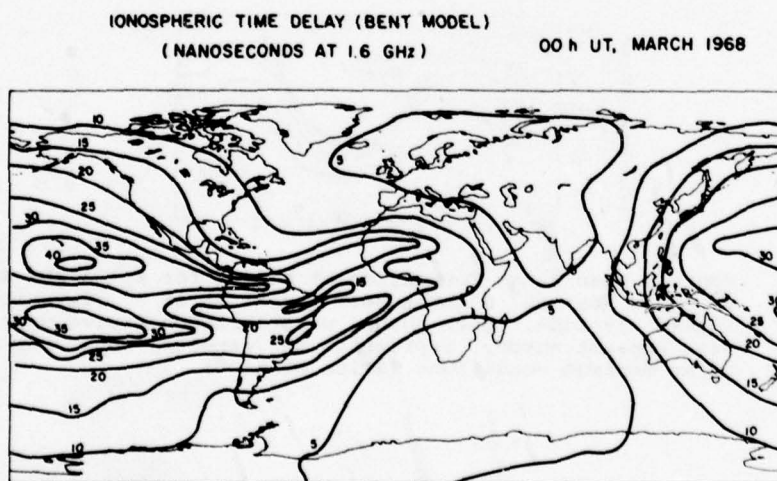

Figure 2.   Worldwide average vertical ionospheric time delay at 1.6 GHz for 00 hours universal time March, 1968, an average solar maximum year (Klobuchar[1]).
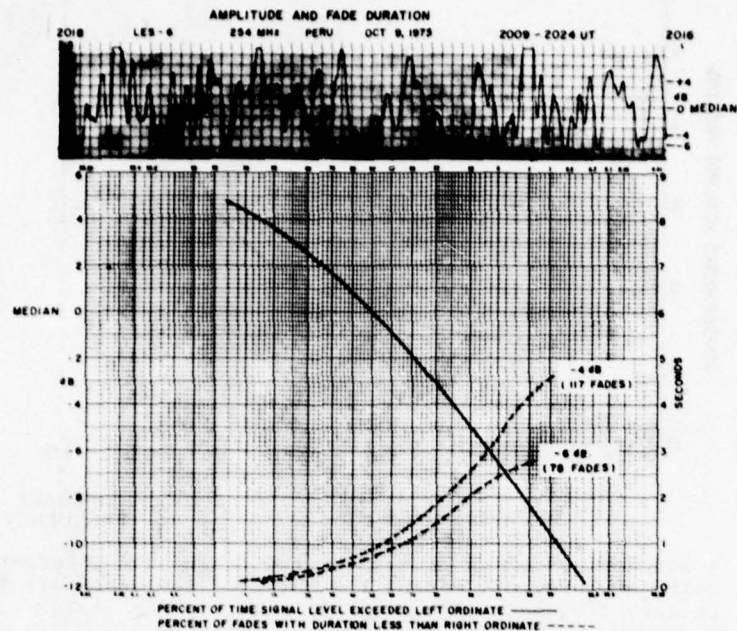
Figure 3.   Retracing of Huancayo, Peru, LES-6 observations with statistics on fade duration and probability of time signal is below certain levels (Aarons[7]).
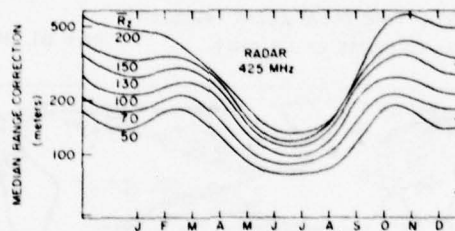

Figure 4.   Monthly Mean Range Correction at Midday for a 425 MHz Radar Situated Near 50° N Latitude.   Target is at 5° elevation angle, 1000 km altitude.   Each curve, parametric on twelve month running mean sunspot number, represents the expected range correction for solar maximum conditions (Allen et al.[8]).
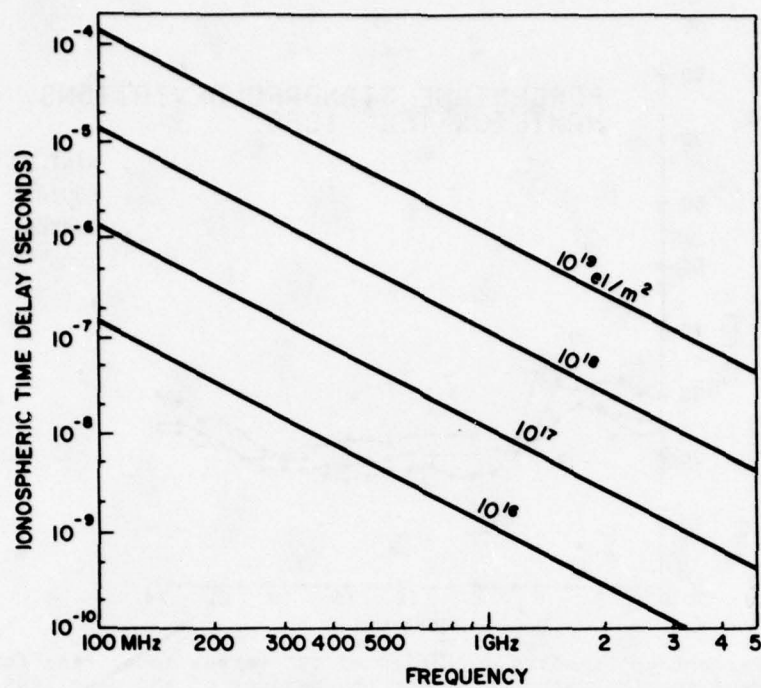
Figure 5.   Ionospheric time delay versus frequency for several values of TEC (Klobuchar[1]).
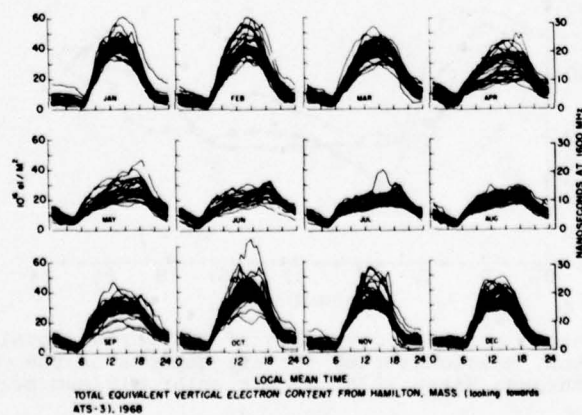

Figure 6.   Monthly overplots of equivalent vertical TEC from Hamilton, Massachusetts for the year 1968, a solar maximum year (Klobuchar[1]).
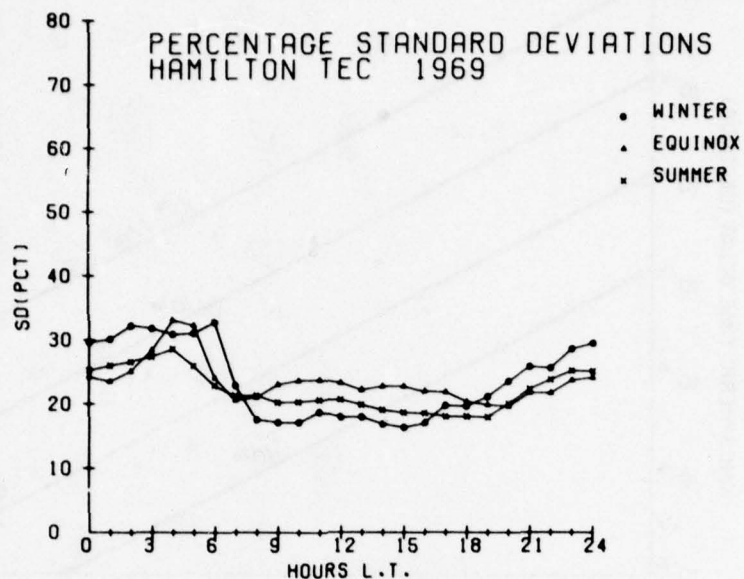
Figure 7.   Percentage standard deviation of TEC versus local time for
              Hamilton, Massachusetts, for the seasons of the year 1969, a
              solar maximum year (Klobuchar[1]).

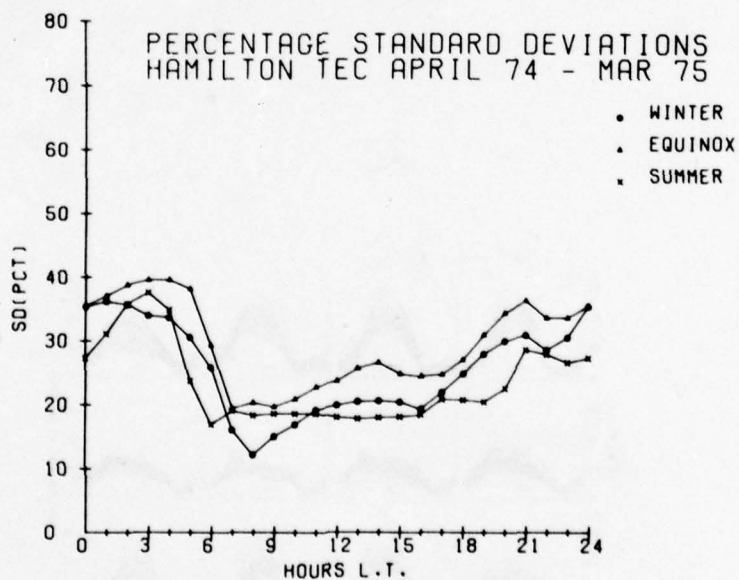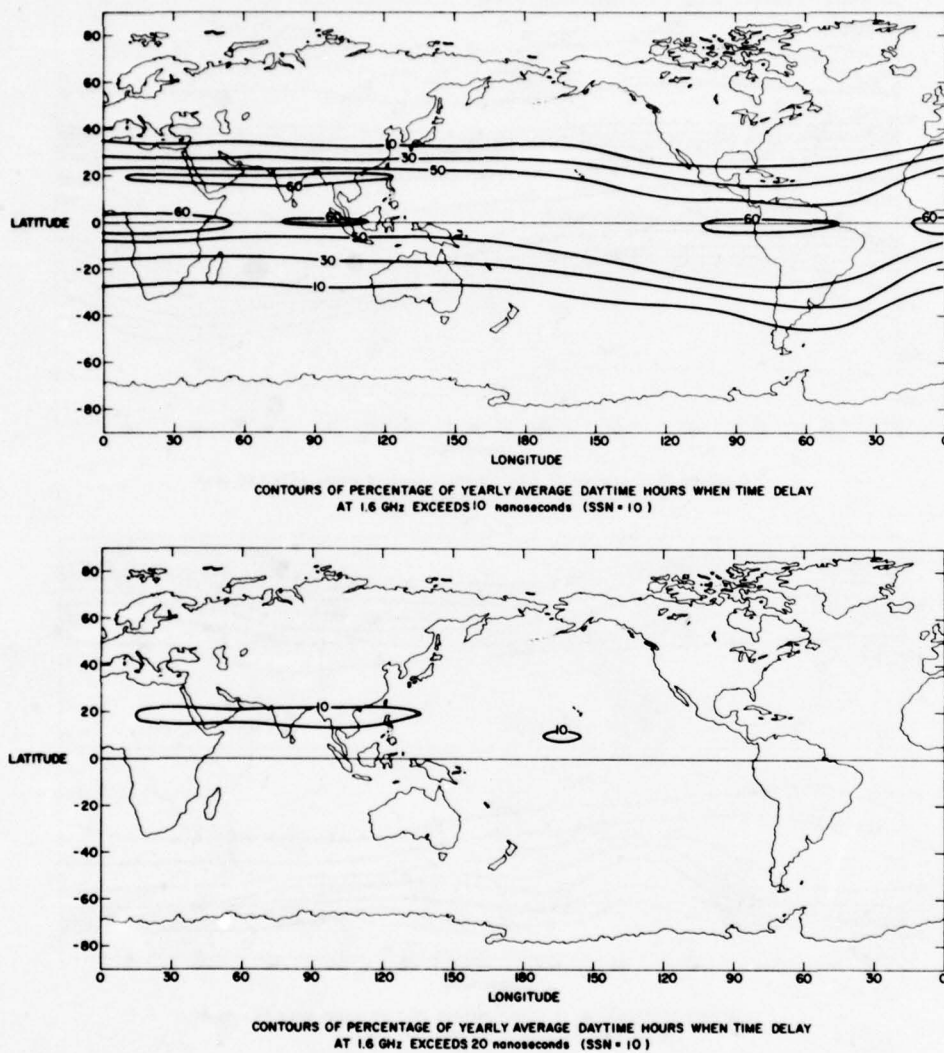Figure 8.   Percentage standard deviation of TEC versus local time for
              Hamilton, Massachusetts, for the seasons of the period April
              1974 through March 1975, a near solar minimum period (Klobuchar[1]).

CONTOURS OF PERCENTAGE OF YEARLY AVERAGE DAYTIME HOURS WHEN TIME DELAY
AT 1.6 GHz EXCEEDS 10 nanoseconds (SSN = 10)

CONTOURS OF PERCENTAGE OF YEARLY AVERAGE DAYTIME HOURS WHEN TIME DELAY
AT 1.6 GHz EXCEEDS 20 nanoseconds (SSN = 10)

Figure 9.   Percentage of yearly daytime hours during solar minimum
that the time delay at 1.6 gigahertz exceeds 10 and 20
nanoseconds.

CONTOURS OF PERCENTAGE OF YEARLY AVERAGE DAYTIME HOURS WHEN TIME DELAY
AT 1.6 GHz EXCEEDS 20 nanoseconds (SSN = 110)

CONTOURS OF PERCENTAGE OF YEARLY AVERAGE DAYTIME HOURS WHEN TIME DELAY
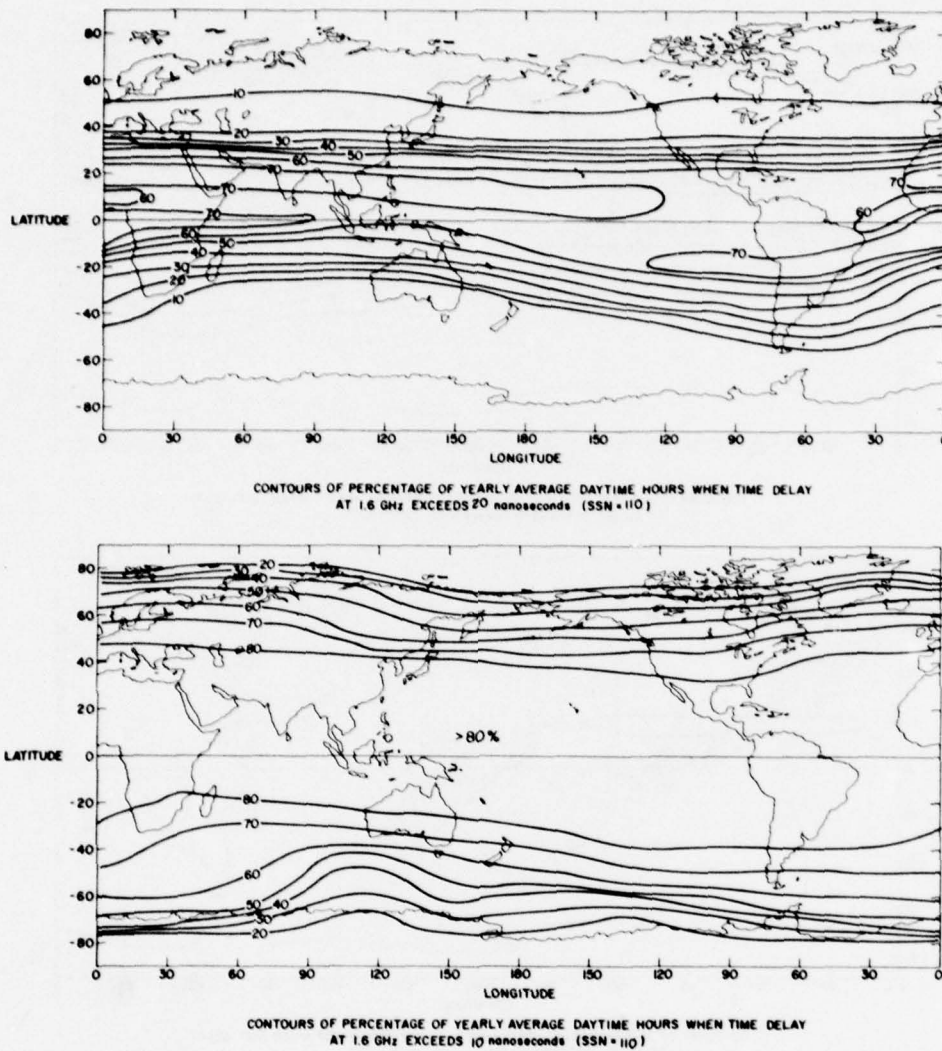AT 1.6 GHz EXCEEDS 10 nanoseconds (SSN = 110)

Figure 10.   Percentage of yearly daytime hours during solar maximum
that the time delay at 1.6 gigahertz exceeds 10 and 20
nanoseconds.

	WINTER	VERNAL EQUINOX	SUMMER	AUTUMNAL EQUINOX
		SOLAR MAXIMUM (Rz = 110)		
TOTAL R (MR. AT 400 MHz)	258	327	189	310
% REMAINING AFTER MONTHLY MEAN CORR.	18	17	16	18
% REMAINING AFTER 3 HOUR OLD MEAS.	12	11	11	10
% REMAINING AFTER 1 HOUR OLD MEAS.	7	6	7	4
		SOLAR MINIMUM (Rz = 10)		
TOTAL R (MR. AT 400 MHz)	77	77	69	86
% REMAINING AFTER MONTHLY MEAN CORR.	18	24	17	14
% REMAINING AFTER 3 HOUR OLD MEAS.	18	20	17	18
% REMAINING AFTER 1 HOUR OLD MEAS.	11	11	8	10

Figure 11.   Total range error and percent error remaining after correction for monthly mean value, and after correction including actual data, taken at different times before required value. All data are for the daily maximum TEC value. (Derived from DuLong[28].)
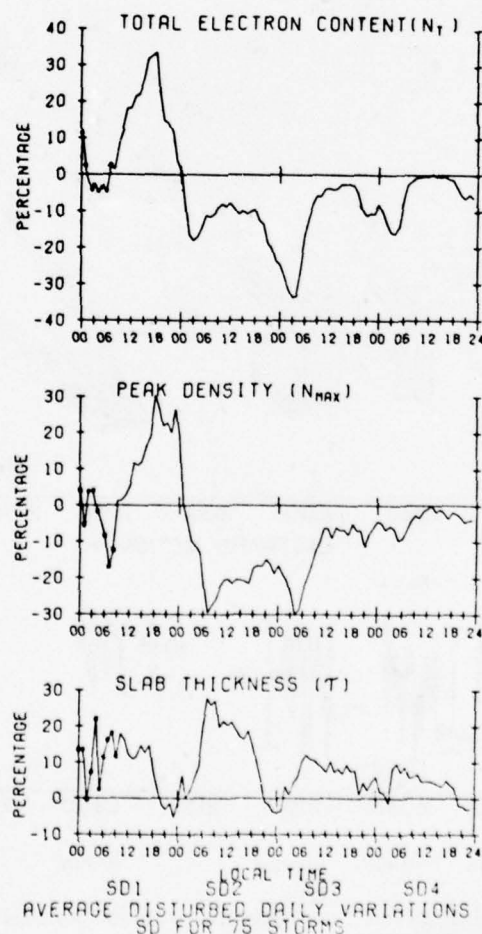

Figure 12.   Average local time disturbance variations (SD, in percent) for the three ionospheric parameters total electron content, peak density and equivalent slab thickness (Mendillo et al.[32]).
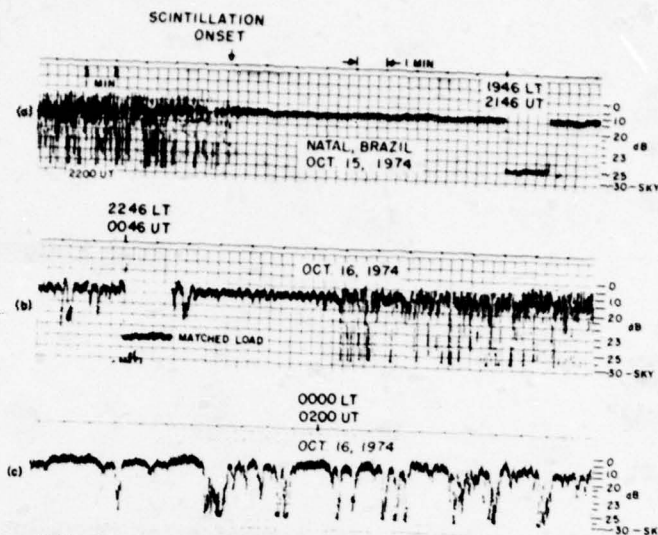
Figure 13(a,b,c).   LES-6 observations recorded at Natal, Brazil, on October 15-16, 1974, showing scintillation onset and cessation (Aarons[7]).
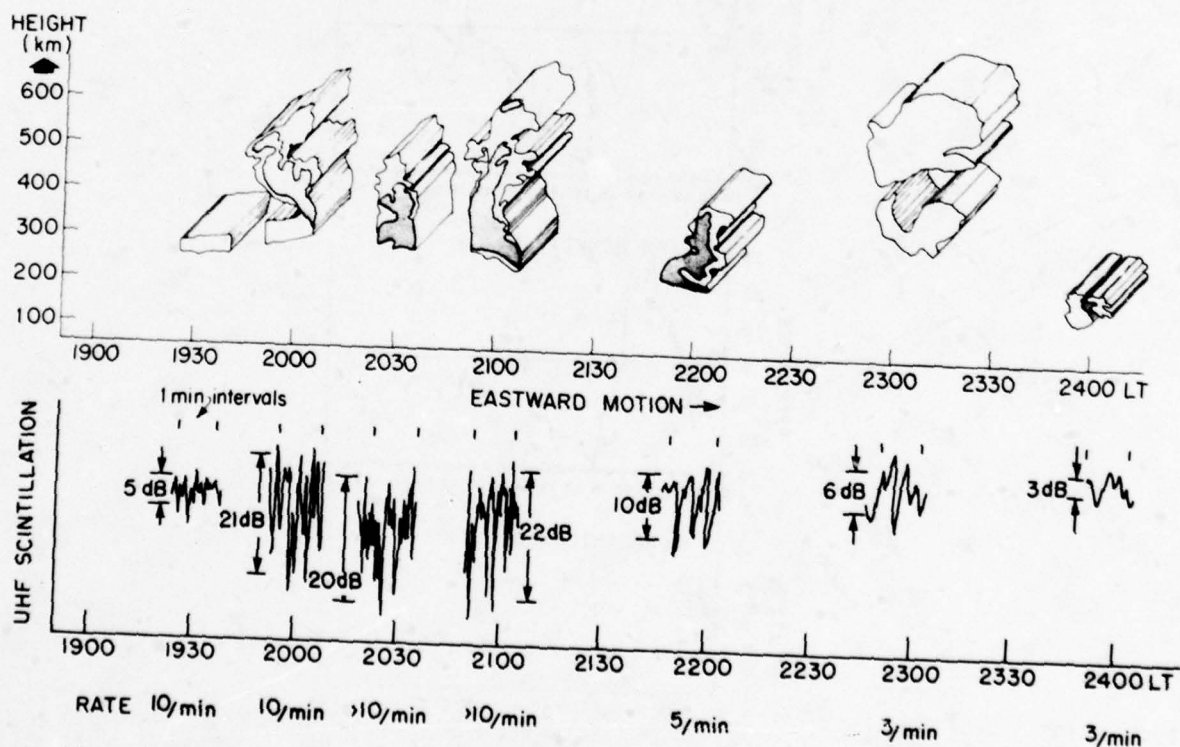

Figure 14.   Typical patch development with associated scintillation amplitude and rates (Aarons[7]).
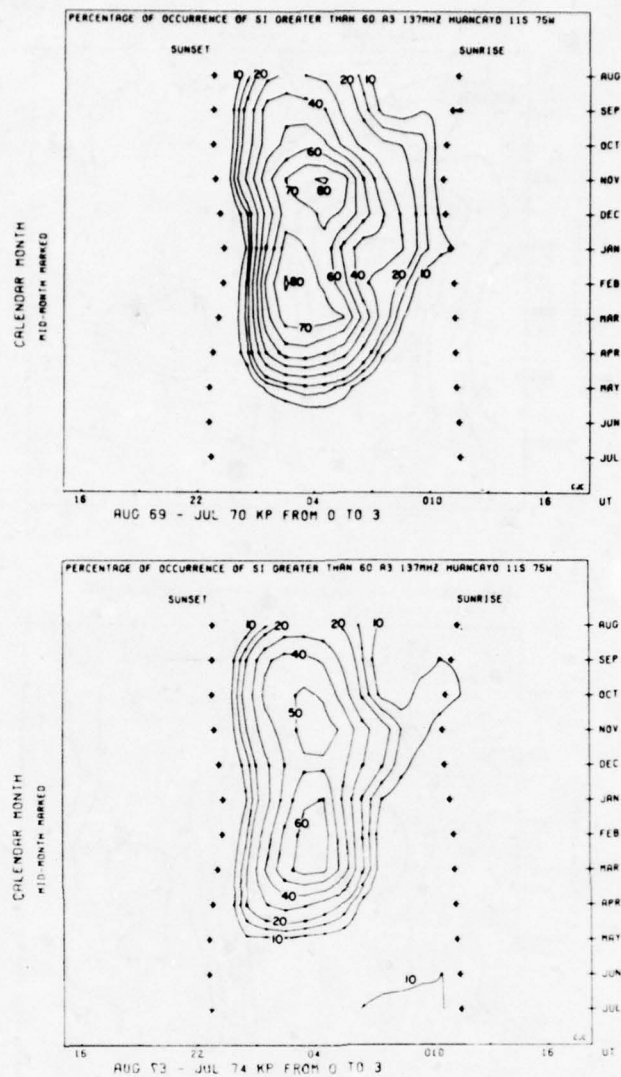
Figure 15. Seasonal character of scintillation observations from Huancayo, Peru, during solar maximum and solar minimum periods (Aarons[7]).
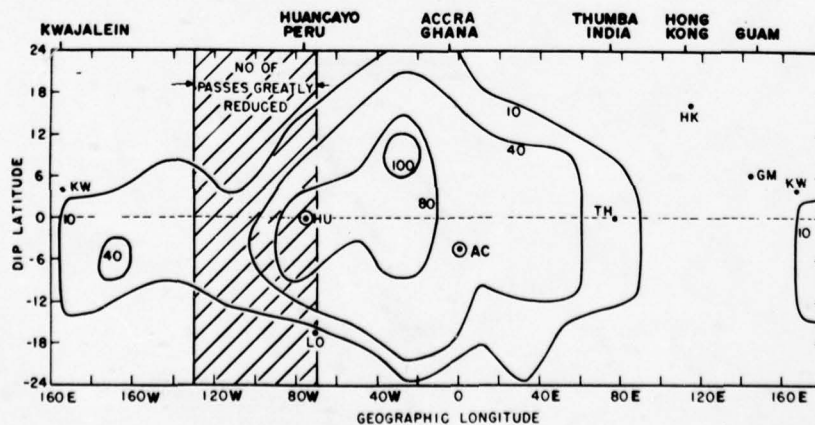

Figure 16. Percentage occurrence of scintillations $\geq$ 4.5 dB at 140 MHz (1900-2300 LMT, Nov.-Dec., 1969, 1970) $A_p < 12$ over a wide longitudinal swath using scintillation data and Ogo-6 observations (Aarons[7]).

MEAN SCINTILLATION INDEX ATS-3 137MHz NARSSARSSUAQ
1968-1974   Kp = 0-3

MEAN SCINTILLATION INDEX ATS-3 137MHz NARSSARSSUAQ
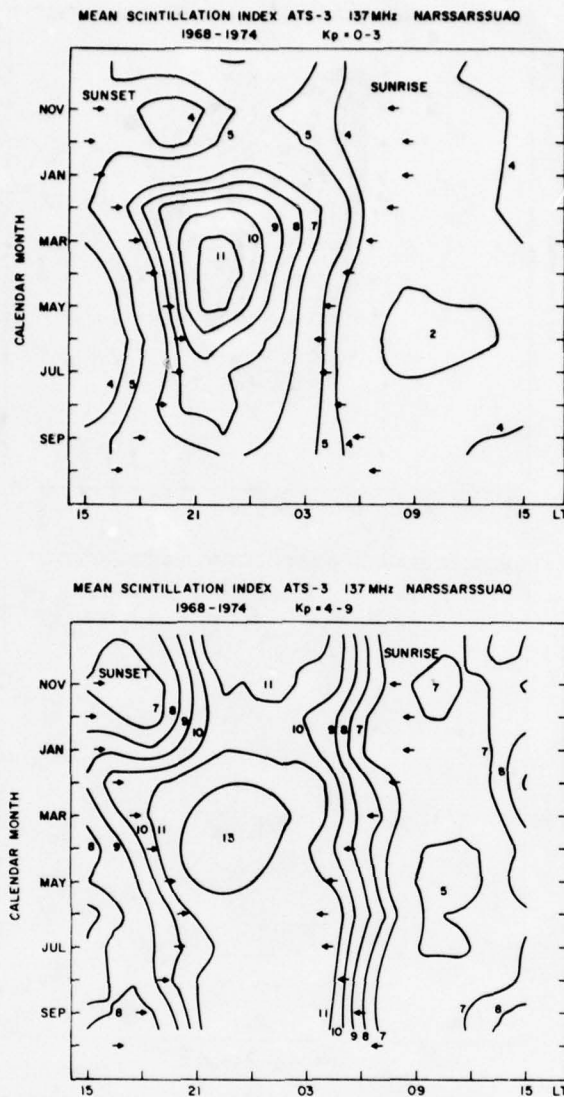1968-1974   Kp = 4-9

Figure 17.   Seasonal character of scintillation excursions (dB) of
Narssarssuaq, Greenland, observations under quiet and
disturbed magnetic conditions (Aarons[7]).

NORTHERN HEMISPHERE
INVARIANT LATITUDE VS LOCAL TIME

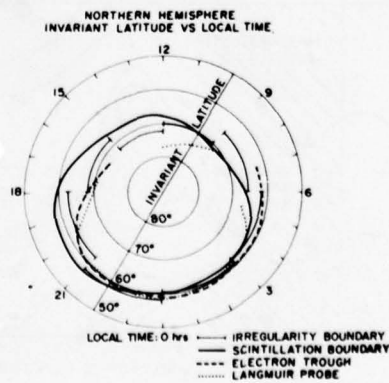Figure 18.   Comparison of equatorward boundary from ISIS-1 data with other
boundaries: Scintillation boundary, Electron Trough, and
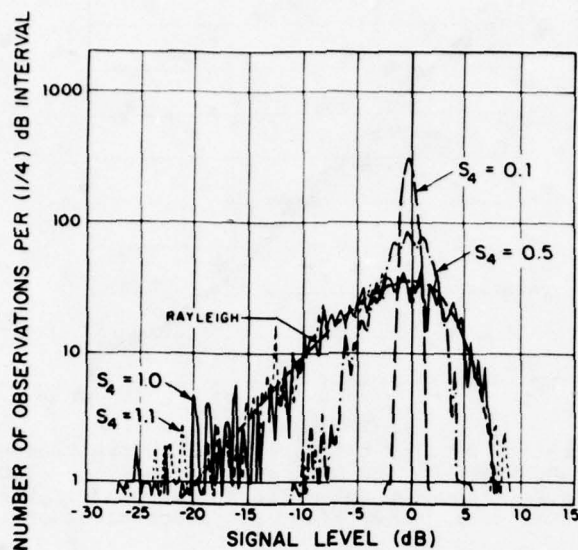Langmuir Probe (Aarons[7]).

Figure 19.   Empirical amplitude probability density functions.   Data obtained from Millstone Hill Radar Facility (Crane[34]).
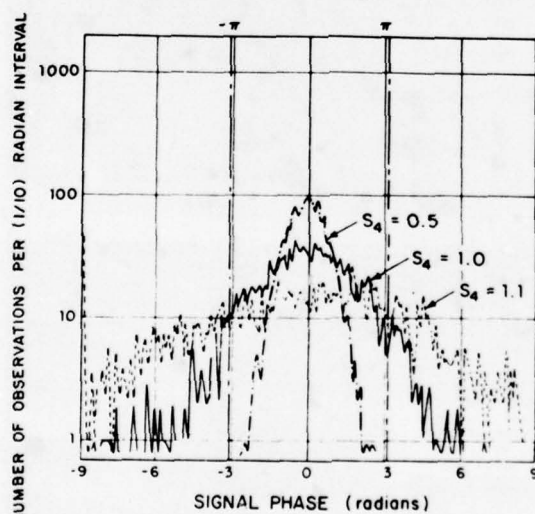
Figure 20.   Empirical phase probability density functions.   Data obtained from Millstone Hill Radar Facility (Crane[34]).
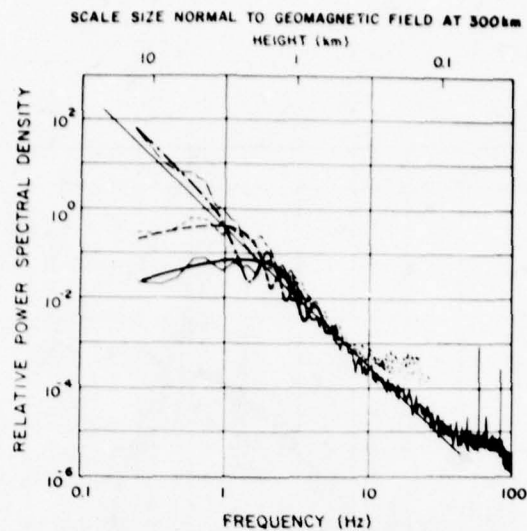
Figure 21.   Power spectral density estimates for low orbiting satellite at
              150 and 400 MHz: —— 400 MHz log amplitude, --- 150 MHz log
              amplitude, -·- 150-400 MHz differential phase. Light lines for
              experimental data, heavy lines for theoretical estimates (Aarons[7]).
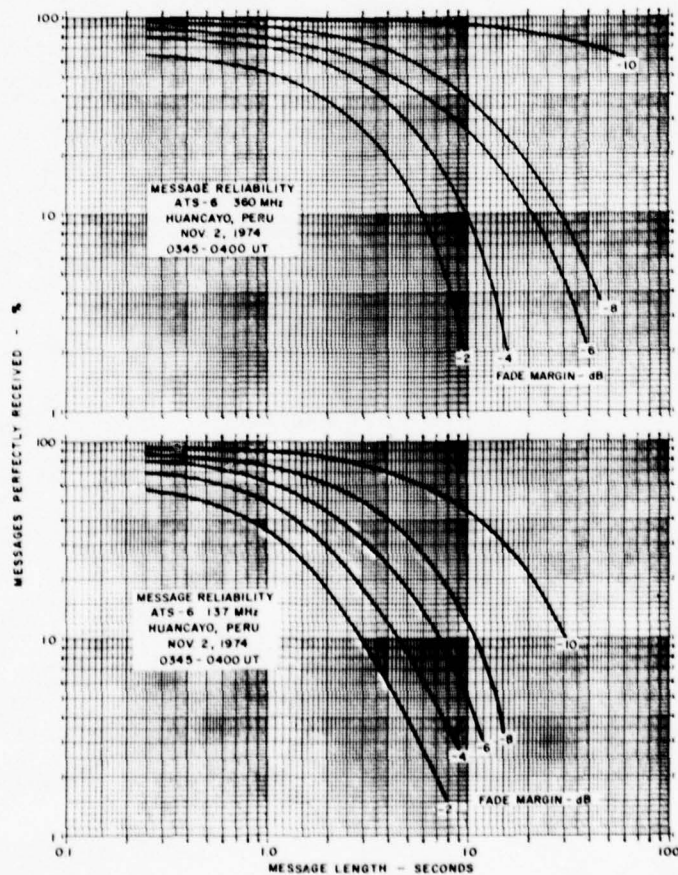
Figure 22.   Effect of the scintillations on the reception of perfect messages
              for various message lengths; S_4 = .96 at 137 MHz, S_4 = .77 at
              360 MHz (Whitney and Basu[49]).

MODELLING OF THE VISIBLE/INFRARED PROPAGATION ENVIRONMENT

by

Robert A. McClatchey
Air Force Geophysics Laboratory
Hanscom Air Force Base
Bedford, Massachusetts   01731
U.S.A.

SUMMARY

The optical modelling of the atmosphere requires both a knowledge of the physical properties of the atmosphere and the spectroscopic properties of the gases and particulates of which it is composed. The pertinent atmospheric properties of temperature, pressure and constituent distribution will first be discussed. The AFGL Atmospheric Absorption Line Parameters Compilation will then be described with emphasis on the accuracy of the data base and its application to high resolution propagation modelling. The necessity to deal with molecular continuum absorption and its relationship to absorption line formation will be discussed. A discussion of the knowledge and application of aerosol optical properties to the development of aerosol models is presented. Finally, the LOWTRAN atmospheric transmission model will be described with emphasis on its accuracy, its applicability and its limitations.

CONTENT

1. INTRODUCTION

2. ATMOSPHERIC MODELS AND MEASUREMENTS

    2.1 Standard Meteorological Parameters
    2.2 Composition

3. OPTICAL DATA (MOLECULAR) AND COMPUTATION TECHNIQUES

    3.1 The HITRAN Data Base and Computation Techniques
    3.2 Continuum Absorption
    3.3 Model Validation

4. OPTICAL DATA (AEROSOLS)

    4.1 Aerosol Model Development
    4.2 Model Validation

5. OPERATIONAL TRANSMISSION MODELS

    5.1 Low Resolution Propagation (LOWTRAN)
    5.2 Application of HITRAN to Laser Transmission
    5.3 Modelling the Background Radiation Environment

REFERENCES

1. INTRODUCTION

There are many military systems which depend on the ability either to transmit radiation through the atmosphere or to detect an object against a complex radiation background. In general such systems fall into two broad classes: 1) High spectral resolution systems typified by laser sources; and 2) Broad-band detection systems typified by a Forward Looking Infrared (FLIR) imaging system operating over the 8-13 micrometer region. These different types of systems dictate substantially different requirements on atmospheric propagation modelling. Both kinds of modelling techniques and the relationship between the two will be described here.

The ultimate objective of atmospheric transmission modelling is to be able to predict the opacity of the atmosphere along any geometric path under any atmospheric condition at any wavelength given a set of measured or predicted meteorological parameters. We would like to carry out such predictions at extremely high spectral resolution pertinent to the transmission of laser radiation or at low spectral resolution consistent with broad-band systems. For the purpose of this presentation, the spectral range will be limited to the region from 0.25 µm to the submillimeter region (about 22 GHz).

In order to understand the propagation characteristics of the atmosphere for radiation in this broad spectral region, it is necessary to understand the details of molecular extinction processes (both absorption and scattering) as well as the details of aerosol absorption and scattering processes.

Beer's law for linear propagation of monochromatic radiation at frequency ν in a homogeneous medium can be expressed as follows:

$$\frac{dI(X,\nu)}{dX} = - \gamma(\nu) \, I(X,\nu) \qquad (1)$$

where $I(X,\nu)$ is the intensity of the radiation at distance X and $\gamma(\nu)$ is the attenuation coefficient.

Transmittance of radiation in the atmosphere is complex owing to the dependence of scattering and absorption coefficients on a number of different physical properties of the atmosphere. Solving Equation 1, we have for the monochromatic radiation observed at distance, X, from the source:

$$I(X,\nu) = I(O,\nu) \, \tau(\nu) \qquad (2)$$

where $I(O,\nu)$ is the intensity of radiation at the source, and $\tau(\nu)$ is the monochromatic transmittance which is given by

$$\tau(\nu) = \exp{-\gamma(\nu)} \qquad (3)$$

where $\gamma(\nu)$ is an attenuation coefficient and X is the length of the path traversed by the radiation. The attenuation coefficient $\gamma(\nu)$ is given by

$$\gamma(\nu) = \sigma(\nu) + k(\nu) \qquad (4)$$

where $\sigma(\nu)$ is the scattering coefficient and $k(\nu)$ is the absorption coefficient. Equation 3 is only strictly valid when applied to monochromatic radiation.

The scattering and absorption coefficients defined in Equation 4 depend on both the constituent molecules and aerosols in the atmospheric path. If electro-magnetic radiation is incident on a molecule or an aerosol, a portion of the radiation is absorbed and the rest is scattered in all directions. Thus, we must make the following definitions:

$$\sigma(\nu) = \sigma_m(\nu) + \sigma_a(\nu) \qquad (4a)$$

$$k(\nu) = k_m(\nu) + k_a(\nu) \qquad (4b)$$

where the subscripts, m and a, indicate molecule and aerosol respectively. In order to compute the attenuation quantatively, it is necessary to consider all four of the quantities defined in Equations (4a) and (4b).

The molecular scattering coefficient depends only on the number density of molecules in the radiation path, whereas the molecular absorption coefficient is a function of not only the amount of absorbing gas, but also the local temperature and pressure of the gas. The wavelength dependence of molecular (Rayleigh) scattering is very nearly $\sigma_m \sim \lambda^{-4}$. The variation of the molecular absorption coefficient with wavelength is much more complicated, being a highly oscillatory function of wavelength due to the presence of numerous molecular absorption band complexes as is indicated in Figure 1. These band complexes result for the most part from minor atmospheric constituents. The responsible molecules are (in order of importance): H_2O, CO_2, O_3, N_2O, CO, O_2, CH_4, N_2. All of these molecules except for H_2O and O_3 are assumed to be uniformly mixed by volume in the models presented.
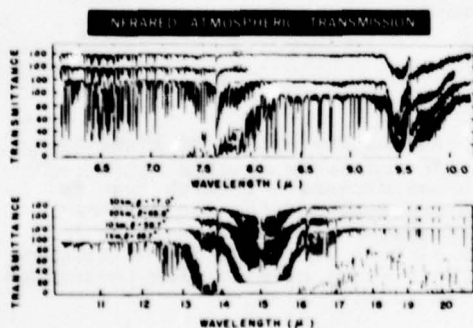

FIGURE 1. High Resolution Measurements of Solar Spectra made from Indicated Altitudes and Observing the Sun at the Indicated Zenith Angles.

The quantities k_a and σ_a depend on the number density and size distribution of aerosols as well as on their complex index of refraction. In addition, the sizes of atmospheric aerosols are known to depend on the relative humidity of the atmosphere. The problem of accurately modelling aerosol effects is currently the most difficult and least resolved problem area (especially for broad-band applications). The reason for this is related to the difficulty of measuring aerosol effects and their great variability in the atmosphere, both in time and space. In the case of molecular absorption and scattering, the distributions of molecules are either rather well known or can be readily obtained from standard meteorological measurements (such as relative humidity in the case of water vapor). The only commonly measured (or observed) variable of direct use in aerosol modelling is the visibility (or visual range). Despite the unreliability of many visual range measurements, its use as an important input parameter in the aerosol models will be discussed.

In order to model the optical properties of the atmosphere, it is necessary to study and understand the spectral properties of the apporpriate molecules and aerosols and in addition, it is necessary to define the atmosphere in terms of constituent distributions, temperature and pressure. Concerning the problem of molecular absorption, it is required that we know the frequencies, intensities, widths and shapes of all spectral lines in the region of interest. In addition we must be able to model or measure the distributions

of water vapor, ozone, and the other absorbing atmospheric gases as well as temperature and pressure along the intended atmospheric path. An uncertainty in the definition of the physical properties of the atmosphere can affect the computed atmospheric trans- mittance in much the same way as an uncertainty in the parameters defining the absorp- tive properties of a particular molecule.

In order to provide a base for transmittance modelling, we will discuss the varia- bility and uncertainties in physical models of the atmosphere. We will then describe the AFGL Atmospheric Absorption Line Parameters Compilation, indicating the requirements for such a data compilation and some of the remaining omissions and uncertainties. The Line-By-Line (LBL) transmittance calculation technique will be briefly described and some results pertinent to laser propagation will be presented. A discussion of the LOWTRAN model will be presented with an emphasis on the accuracy and efficiency of the model for system applications.

2. ATMOSPHERIC MODELS AND MEASUREMENTS

2.1. Standard Meteorological Parameters

A series of six standard atmospheres are described by McClatchey, et al[1] in terms of height, pressure, temperature, density, water vapor density and ozone density. With the exception of the water vapor and ozone distributions, these models are taken directly from the U.S. Standard Atmosphere Supplements, 1966 and the Handbook of Geophysics and Space Environment, (Valley[2]). The water densities above 11 km were taken from Sissenwine et al[3]. Three of these model atmospheres are summarized in Figures 2 and 3. More details can be found in the references cited above.
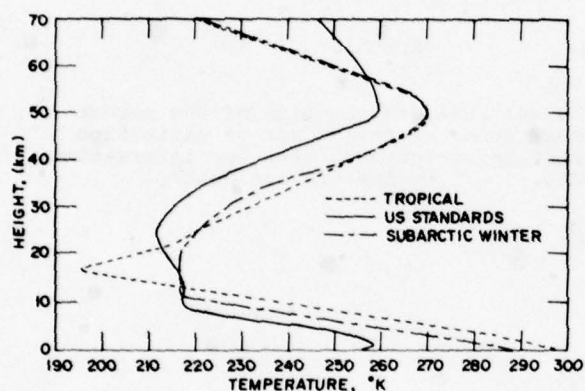

FIGURE 2. Temperature Distributions for Three of the Standard Model Atmospheres.
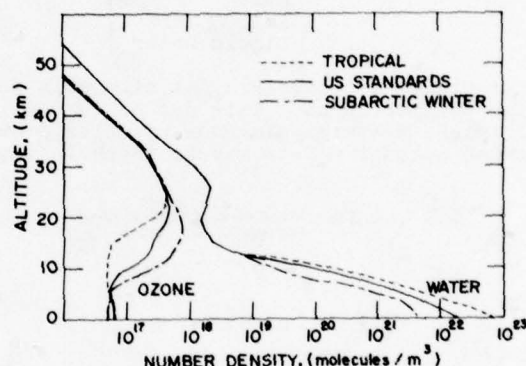
FIGURE 3. Water Vapor and Ozone Distribu- tions for Three of the Standard Model Atmos- pheres.

2.2 Composition

The atmospheric path, over which the atmospheric transmission is to be computed, must be completely described in terms of the parameters responsible for both molecular and aerosol extinction. As will become more clear later, the description of the atmos- phere in terms of its temperature, pressure and the concentrations of molecular species along the path will completely describe the meteorological properties of the atmosphere for purposes of molecular scattering and absorption.

Table 1 is a list of atmospheric constituents, together with a representative atmospheric abundance. It is important to realize that although nitrogen and oxygen are the most abundant molecules in the atmosphere, their effect on atmospheric propaga- tion is small due to their lack of a permanent dipole moment. Atmospheric gases of main interest here are carbon dioxide, water vapor, ozone, methane, carbon monoxide and nitrous oxide. Although with the exception of water vapor and ozone, a single mixing ratio has been listed for each molecular constituent, there is substantial evidence for variability for all species except nitrogen and oxygen. However, reasonable results can be expected in the troposphere based on the constant mixing ratios indicated in Table 1. Fortunately, the required quantities for the computation of atmospheric mole- cular absorption are regularly measured at most meteorological stations around the world. In the case of aerosols, however, this is not so. The only quantity measured routinely at some stations is visibility and there is great non-uniformly in the methods of measurement. Furthermore, the relationship between a measured visibility at visible wavelengths and the required aerosol quantities (concentration, size distri- bution and refractive index) is not straightforward and is certainly not unique. There- fore we must depend on our general understanding of aerosol distributions and properties to develop models for general use. We must then develop the relationships between these models and standard meteorological information so that the models can be optimally applied to real atmospheric situations or to atmospheric statistics.

TABLE 1

ATMOSPHERIC CONSTITUENTS

Constituent	Fraction by Volume
Nitrogen (N_2)	0.78
Oxygen (O_2)	0.21
Argon (A)	0.0093
Carbon Dioxide (CO_2)	0.00033
Methane (CH_4)	1.6×10^{-6}
Nitrous Oxide (N_2O)	3.5×10^{-7}
Carbon Monoxide (CO)	7.5×10^{-8}
Ozone (O_3)	variable (10^{-8})
He, Ne, Kr	$< 10^{-4}$
Water Vapor	variable ($<.03$)
Aerosols Dust Salt Liquid Water	variable

Figure 4 provides a set of models for the vertical distribution of the number of aerosol particles. This set of curves is based on an extensive set of extinction coefficient measurements made by a large number of investigators. Further information on these aerosol models may be found in the AGARD report by Shettle and Fenn[9].
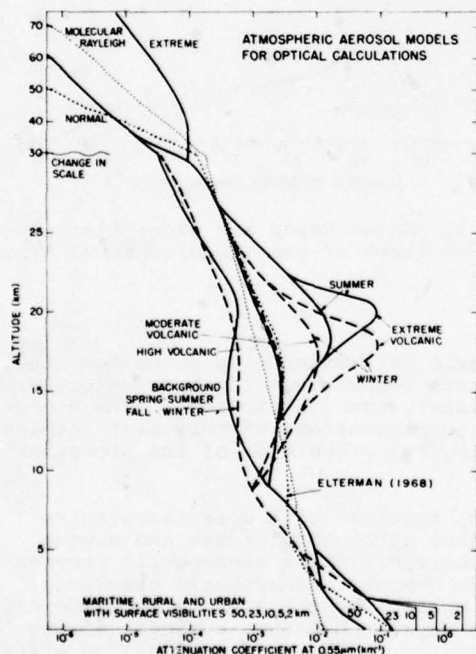
FIGURE 4. Vertical Structure of Aerosol Models.
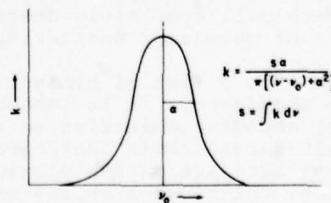
FIGURE 5. Lorentz Line Shape Used in Atmospheric Calculations from the Surface to 30km.

3. OPTICAL DATA (MOLECULAR) AND COMPUTATION TECHNIQUES

3.1. The HITRAN Data Base and Computation Techniques

The AFGL Atmospheric Absorption Line Parameters Compilation (McClatchey, et al[5]) is the data base available for computing the contributions to the atmospheric extinction from discrete molecular absorption lines. It forms the basis of the various HITRAN transmission codes. The HITRAN transmission codes are designed to replicate measured spectra of the kind shown in Figure 1. The spectral resolution of these measurements is about 0.5 cm^{-1} and they were taken from a balloon platform viewing the sun from the indicated altitudes and at the indicated zenith angles. Absorption features of water vapor, carbon dioxide, ozone and methane are clearly visible in the figure.

The seven molecules for which parameters are contained in this data compilation include water vapor, carbon dioxide, ozone, nitrous oxide, carbon monoxide, methane and oxygen. Calculations proceed from the description of an atmospheric model, the input spectral data from the compilation and the application of Beer's law to compute a network of monochromatic transmittances. The parameters which make up this data compilation include (for each absorption line) the line position (frequency), intensity, half-width, energy of the lower state, quantum numbers,[6,7,8] isotopic identification and molecular identification. Efforts have continued to update this compilation as new experimental results become available.

The utilization of the Line Parameters Compilation requires a knowledge of molecular absorption line shapes. Our HITRAN model currently assumes a Lorentz line shape in the lower atmosphere for all pressures less than 10 mb, a Voigt shape in the region from 10 mb to 0.1 mb and a pure Doppler line shape at lower atmospheric pressures. Although the applicability of the Lorentz line shape remains in some doubt for distant line wings, it has generally been found to represent experimental data adequately within a few wavenumbers of the centers of absorption lines. The Lorentz line shape is indicated in Figure 5 and the mathematical form is given in Equation 5. Equation 6 represents the temperature dependence of the line intensity.

$$k = \frac{S\alpha}{\pi\left[(\nu - \nu_o)^2 + \alpha^2\right]} \qquad S = \int k d\nu \tag{5}$$

$$\text{where } \alpha_L = \alpha_o \frac{p}{p_o} \sqrt{\frac{T_o}{T}}$$

$$S(T) = S(T_o)\left(\frac{T_o}{T}\right)^n \exp - \frac{hc}{k} E''\left(\frac{T_o - T}{T_o T}\right) \tag{6}$$

Apart from constants, an examination of Equations 5 and 6 show that the absorption coefficient as a function of frequency is determined if the line position (frequency), intensity, half-width at standard conditions of temperature and pressure, and the energy of the lower state (E'') are defined for each line. These are the four fundamental parameters used in the HITRAN calculations for each absorption line.

The application of the molecular data compilation to the generation of a monochromatic transmission or to a high resolution spectrum then follows the straightforward application of Equations 7-10. Equation 7 computes the monochromatic transmittance due to a single line of a single molecular species. Equation 8 then sums the contributions to the absorption coefficient at the frequency, ν, from all lines associated with a given molecular species as well as all lines associated with different molecular species. Equation 9 indicates the necessity to integrate this result through an atmospheric path containing temperature, pressure, and concentration gradients. Finally, Equation 10 indicates that, in general, it is necessary to convolve the resulting monochromatic transmittance results with some kind of finite instrument spectral response function if one is to generate a spectrum for comparison with measurements. Examples of such calculations are shown in Section 3.3.

$$\tau(\nu) = \exp - \left[k(\nu)m\right] \tag{7}$$

$$\tau(\nu) = \exp - \left[\sum_j \sum_i k_{ji}(\nu) \, m_j\right] \tag{8}$$

$$\tau(\nu) = \exp - \sum_j \left[\int \left(\sum_i k_{ji}(\nu) \, dm_j\right)\right] \tag{9}$$

$$\overline{\tau}(\nu) = \frac{\int \tau(\nu) \, g(\nu - \nu_o) \, d\nu}{\int g(\nu - \nu_o) \, d\nu} \tag{10}$$

Applications of this calculation scheme repeatedly at small frequency increments will generate a high resolution absorption spectrum. The AFGL data Compilation continues to be updated and modified. Recently, a Trace Gas Tape has been made available to users (see Reference 9). This tape contains data on four additional trace gases (NH_3, NO, NO_2 and SO_2) not contained on the original AFGL Compilation. On the original data tape recent modifications have been made to the methane data and previously omitted data on water vapor in the visible and near infrared have now been added. A complete review of all CO_2 bands has led to some significant modifications in addition. All water vapor half-widths have been revised and additional oxygen bands at visible wavelengths have been added. The AFGL Compilation now contains parameters on more than 139,000 absorption lines in the spectral region from 0.3 to 17,880 cm^{-1}.

3.2   Continuum Absorption

As noted above, in addition to molecular absorption by discrete absorption lines, there exists a slowly varying component of the absorption coefficient which is observed experimentally in the laboratory under certain conditions when absorption by some atmospheric gases is studied. This same kind of absorption has also been observed in the atmosphere, particularly in "window" regions where absorption by discrete lines is small.

It is difficult to separate this "continuum" absorption from absorption in the distant wings of strong discrete absorption lines. Indeed, for our purposes, it really doesn't matter as long as we understand the dependence of this continuum absorption on the physical parameters describing the atmospheric path. In regions of more substantial line absorption, the problem reduces to that of deciding how far into the wings of each line to assume individual line contributions and how much of the experimentally observed absorption to model as a "continuum", even when we are quite certain that most of this contribution results from line wings. Two significant absorption features, treated as continuum absorption and of particular significance in atmospheric window regions will now be described.

Water Vapor Continuum

The absorption coefficient per precipitable centimeter of water vapor is given in Equation 11 where $C_S(\nu,T)$ is a self-broadening coefficient due to collisions of water molecules with other water molecules, $C_N(\nu,T)$ is a nitrogen broadening coefficient due to collisions of water molecules with air (primarily nitrogen) molecules, P_S is the partial pressure (in atmospheres) of water vapor and P_N is the partial pressure of the remainder of the atmosphere (primarily nitrogen). It is necessary to establish the C_S and the C_N quantities and their frequency and temperature dependence in both the 8-14 and 3-5 micrometer regions. As of this writing, existing laboratory measurements have been analyzed thoroughly and the resulting coefficients and temperature dependences are described here. The laboratory evidence for the 8-14 μm continuum absorption is given in Figure 6 (Taken from Burch[10]).

$$k(\nu,T) = C_S(\nu,T)\ P_S + C_N(\nu,T)P_N \tag{11}$$

i)   The 8-14 micrometer continuum[11,12,13]

$$C_S(\nu,T) = C_S(\nu,296)\ \exp - 1800 \left(\frac{1}{T} - \frac{1}{296}\right) \tag{12}$$

where $C_S(\nu,296) = 4.18 + 5578 \exp (-7.87 \times 10^{-3}\ \nu)$ (pr. cm)$^{-1}$ atm^{-1}

and $C_N(\nu,T) = 0.002 \times C_S(\nu,296)$ (pr. cm)$^{-1}$ atm^{-1}

ii)   The 3.5-4.2 micrometer continuum[11]

$$C_S(\nu,T) = C_S(\nu,296)\ \exp - 1350 \left(\frac{1}{T} - \frac{1}{296}\right)\ \text{(pr.cm)}^{-1}\ \text{atm}^{-1} \tag{13}$$

$$C_N(\nu,T) = 0.12 \times C_S(\nu,T)$$

where the $C_S(\nu,296)$ values are given in Table 2.

Using these continuum functions and a series of atmospheric models,[1] Figure 7 has been constructed to show the relative effects of the water vapor continuum at 4 and 10 μm.
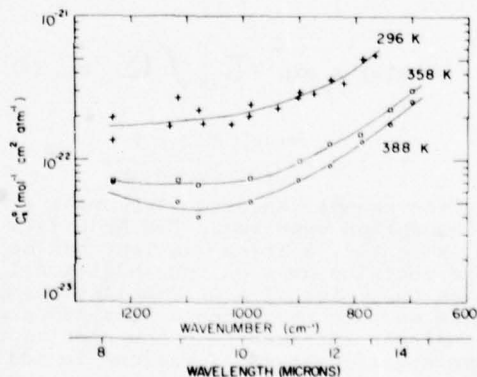

FIGURE 6.   Measurements of the 10 μm Water Vapor Continuum Self-Broadened Absorption Coefficient (see Burch, 1970).

ABSORPTION COEFFICIENT DUE TO
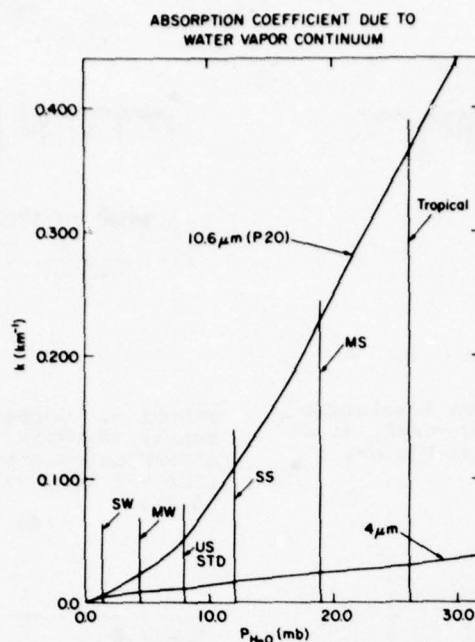WATER VAPOR CONTINUUM

FIGURE 7. Absorption Coefficients Due To
The Water Vapor Continuum.

TABLE 2

SELF-BROADENING ABSORPTION COEFFICIENTS FOR
WATER VAPOR CONTINUUM (3.3-4.2 μm)

ν (cm^{-1})	(pr.cm^{-1}) (atm.$^{-1}$) $C_S(\nu,296)$	ν	(pr.cm^{-1}) (atm.$^{-1}$) $C_S(\nu,296)$
2350	0.230	2700	0.120
2400	0.187	2750	0.147
2450	0.147	2800	0.174
2500	0.117	2850	0.200
2550	0.097	2900	0.240
2600	0.087	2950	0.280
2650	0.100	3000	0.330

Nitrogen Continuum

In addition to the more or less continuous absorption due to water vapor described above, there is another quasi-continuous absorption feature due to molecular absorption by the nitrogen molecule centered near 4.3 μm (2350 cm^{-1}). In the spectral region from 2400 cm^{-1} to about 2800 cm^{-1} this absorption feature is of particular importance to laser transmission as it tends to provide a background transmission level for paths in the lower atmosphere regardless of the presence or absence of absorption lines and regardless of how dry the atmosphere may be. It is of little importance at frequencies smaller than 2400 cm^{-1} due to the overwhelming absorption by atmospheric carbon dioxide.

3.3   MODEL VALIDATION

The validation of the HITRAN models against careful measurements both in the laboratory and in the field constitutes an important continuing element of our research. Figure 8 is an example of such a comparison made with the laboratory measurements of Gryvnak, et al[14] at a spectral resolution of 0.5 cm^{-1} in the 15 μm CO$_2$ band. Figure 9 compares a calculation with a portion of the 1-km spectrum shown in Figure 1. Most lines can be seen to agree favorably, although there are some discrepancies, particularly in line intensities. Figure 10 compares a calculation with measurements made by Dowling, et al[15] in the 4 micrometer region. The results, aside from a small continuum shift are in excellent agreement. Many other workers are now making measurements and checking their results against the AFGL data compilation after performing HITRAN transmission calculations. Another example is shown in Figure 11 which is an example of a solar spectrum compared with a HITRAN calculation (see Nordstrom, et al[16]). Aside from a continuum discrepancy, we note a line near 1208 cm^{-1} which is absent in the upper computed spectrum.
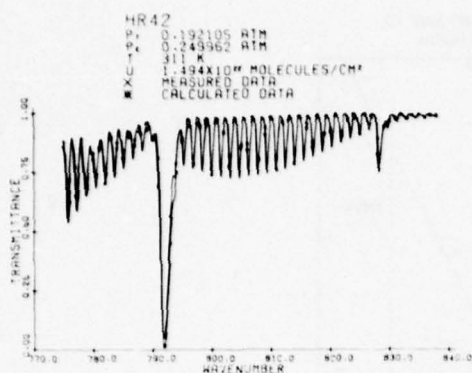
FIGURE 8. Comparison of High Resolution Laboratory Measurements of Gryvnak, et al[14] and Calculations in the 15 μm Region. ($\Delta\nu = 0.5$ cm^{-1}).
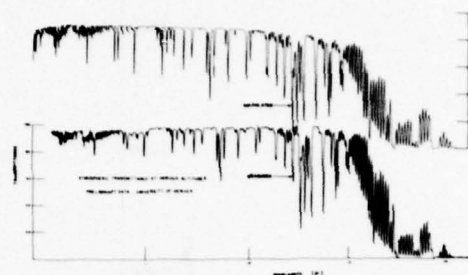
FIGURE 9. Comparison of University of Denver (Murcray) Measurements and HITRAN Calculation. Height of Observation = 1 km. Solar Zenith Angle = 55.7°.
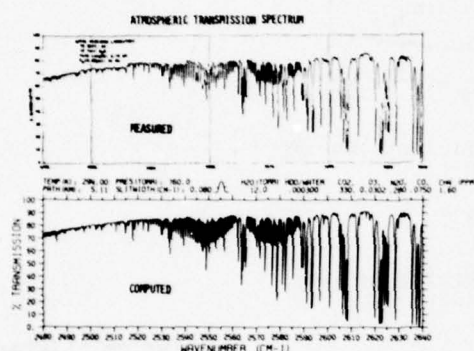
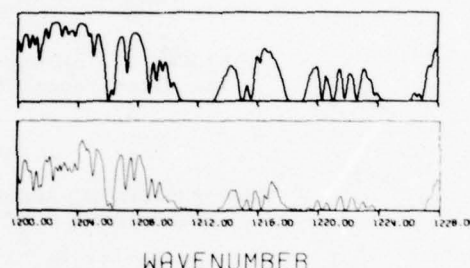FIGURE 10. Comparison of NRL Measurements[15] and HITRAN Calculations.

FIGURE 11. Comparison of High Spectral Resolution (0.125 cm^{-1}) Measured (lower curve) Solar Spectrum with Calculated (upper curve) Spectrum (from Nordstrom, et al)[15].

The applications of HITRAN are numerous. The ability to confidently generate a high resolution synthetic spectrum is of great value in establishing the best frequencies for the operation of any kind of high resolution system. It is of particular value in generating laser transmission results for selected frequencies. Recently, a computer code has been described and made available called, LASER, (see McClatchey and D'Agati[17]) which places this capability into the hands of the user. There has been much recent interest in the application of HITRAN techniques to the computation of exhaust plume signatures as seen through the atmosphere. This application requires a careful analysis of the HITRAN data base at elevated temperatures. We are constantly applying the HITRAN codes to the problem of remote sensing of atmospheric gases and meteorological variables. All these applications are plagued by the requirement for large amounts of computer time. Therefore, substantial efforts are underway to find mathematical procedures to reduce this burden without substantial compromise in the resulting calculations. An example of such an effort is contained in the new HITRAN development known as FASCODE (see Smith, et al[18]). A final application of the HITRAN calculation technique is the development and validation of LOWTRAN, a transmission model of great computer efficiency and reasonable accuracy for many systems applications, but which is limited to a spectral resolution of 20 cm^{-1} or lower. LOWTRAN will be more fully discussed later in this paper.

4. OPTICAL DATA (AEROSOLS)

4.1. Aerosol Model Development

In addition to the continuum absorption by atmospheric molecules described above, extinction by aerosols (absorption and scattering) is treated in much the same way in our transmission models. That is, it can be thought of as a slowly varying continuum function which is added to the more complex rapidly varying molecular absorption coefficients. The primary difficulty in the case of aerosol extinction is our lack of a complete description of the physical models for any given atmospheric path.

The fundamental quantities required in the determination of extinction coefficients due to aerosols are the concentration and size distribution of the particles and the complex index of refraction of the aerosol material[4]. Assuming spherical particles, Mie theory can then be applied and extinction coefficients for both scattering and

absorption determined. A great deal of work has been carried out to determine the complex index of refraction of atmospheric aerosols[19]. Figure 12 presents the complex refractive index data used in the construction of the Rural and Maritime models.

In addition to the complex refractive index, the size distribution of aerosols plays an important role in determining the extinction as a function of wavelength, particles having a dimension similar to the wavelength having a greater effect on scattering coefficients than other particle sizes. Particle size distribution measurements made by a large number of investigators[4,20,21] indicate that they can best be represented by some form of bimodal distribution. Examples of the size distributions used in constructing the Rural and Maritime aerosol models are provided in Figure 13.
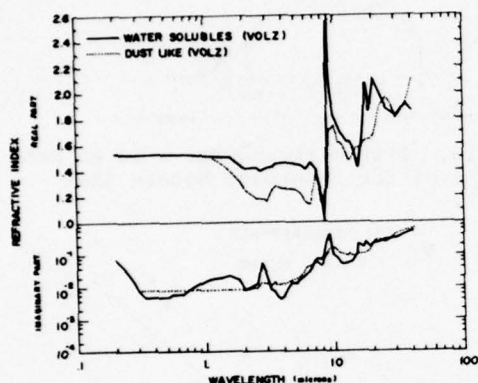
FIGURE 12. Refractive Index of Aerosol Material Used in Construction of Rural Aerosol Model. (After Volz[19]).
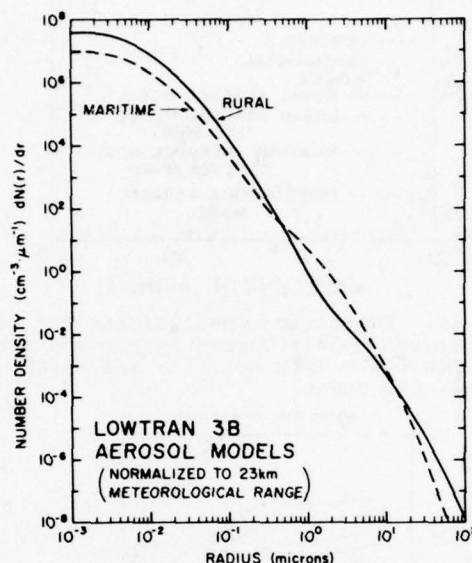
FIGURE 13. Aerosol Size Distributions Used in Construction of Rural and Maritime Aerosol Models (See Reference 4).

Aerosols can be continental in origin (dust and organic matter) or maritime in origin (sea-salt component). In urban industrial regions the aerosols can include soot-like particles. At stratospheric altitudes the background aerosols are predominantly about 75% sulfuric acid solution, although significant amounts of volcanic particles may also be present. At higher altitudes (above 30 km), a significant portion of the larger aerosols may be meteoric dust. They can be dry or they can contain substantial quantities of liquid water, especially as relative humidities increase above 70%. A series of models representing a Rural, Urban, Maritime and Tropospheric environment have been constructed based on a variety of experimental data and these models have been incorporated into our LOWTRAN transmission model.

The application of Mie theory to the complex index of refraction data and particle size distributions produces the normalized extinction coefficient (scattering plus absorption) curves shown in Figure 14. These aerosol models have been included in the current (LOWTRAN 4)[13] transmission model. Applying these models to a 10-km horizontal path at sea level for a visual range of 23 km and including all molecular absorption effects generates the transmittance spectra given in Figure 15.

Low values of the visibility (less than 2 km) are usually associated with the transition from haze to fog and the concurrent growth of particles by accretion of liquid water. This occurs more rapidly the higher the relative humidity. These effects are not accounted for by the present aerosol models. Therefore, we are currently extending our aerosol modelling efforts to describe this particle growth with increasing relative humidity. Figure 16 shows the results of applying our knowledge of this particle growth process to the Maritime aerosol model. It is apparent that the wavelength dependence becomes much less as the relative humidity is increased. Such humidity effects are being included in our LOWTRAN transmission model.

4.2 Model Validation

The validation of aerosol models is particularly difficult because we seldom have measurements of all the required parameters. However, it is important that the range of validity of the different aerosol models be determined even when we do not have all the required supplementary data. In general, we may have to make estimates of some quantities based on a broader knowledge of the air mass and meteorology in which the measurements take place. Two examples of model validation are given here. The first involves some measurements made by EMI Ltd. in the U.K.[22] Figures 17 and 18
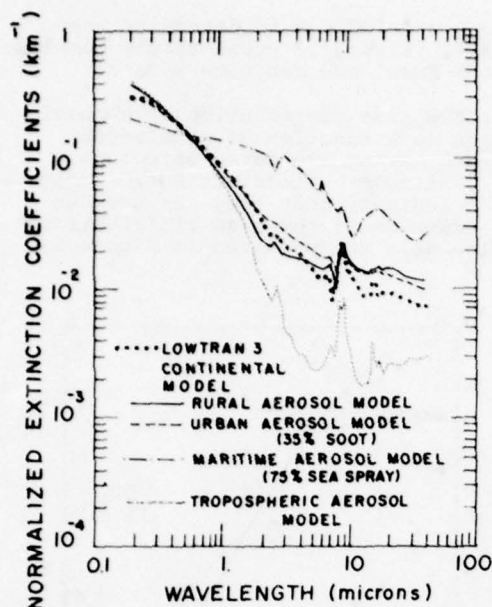
FIGURE 14. Extinction Coefficients for Sea Level Aerosol Models Currently Incorporated in the LOWTRAN 4 (See Ref. 13) and LASER (See Ref. 16) Codes.
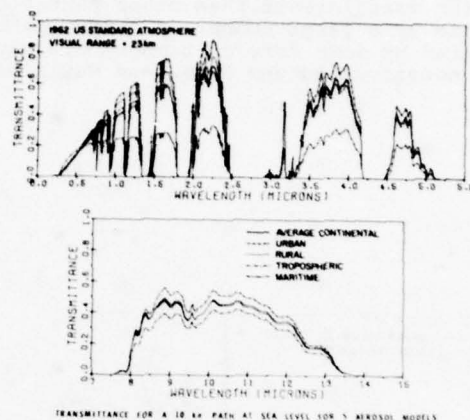
FIGURE 15. Transmittance for a 10 km Path at Sea Level for 5 Aerosol Models (See Ref. 13).
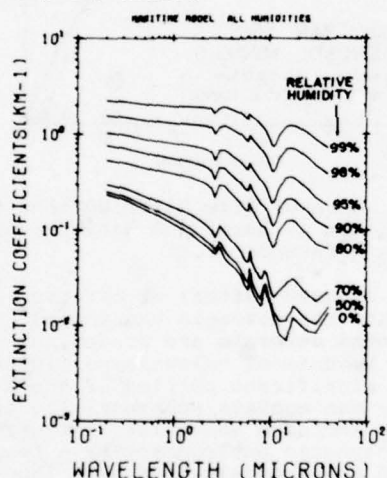
FIGURE 16. Relative Humidity Dependence of Extinction Coefficient for the Maritime Aerosol Model.
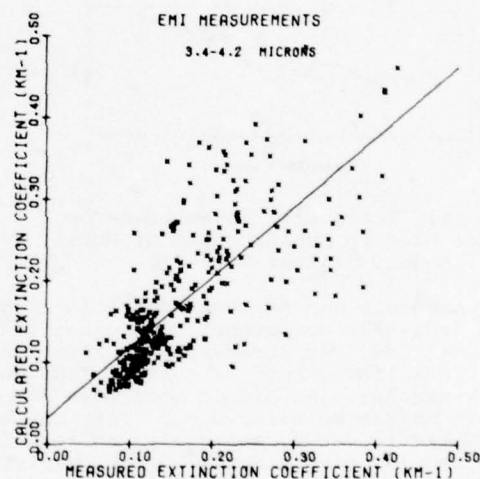
FIGURE 17. Comparison of LOWTRAN Calculations and EMI Measurements (See Ref. 22).
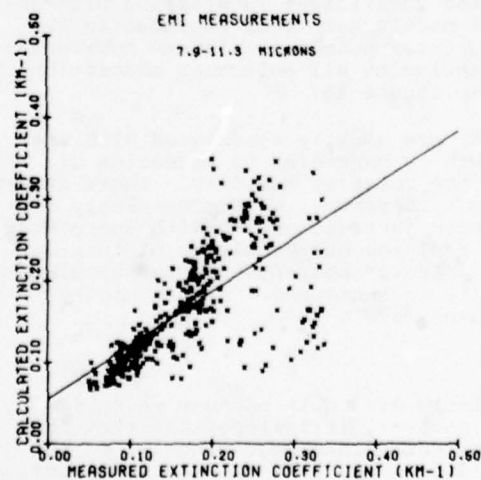
FIGURE 18. Comparison of LOWTRAN Calculations and EMI Measurements (See Ref. 22).
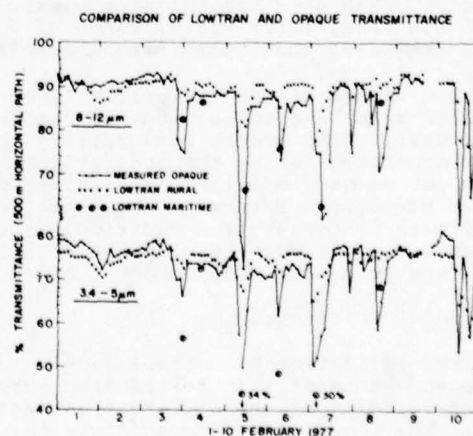
FIGURE 19. A Comparison of LOWTRAN Calculations and OPAQUE Transmittance Measurements at Meppen, Germany.

compare the results of the Maritime aerosol model with the measurements in the near infrared (3-5 micrometer region) and the 7-11 micrometer region. Due to the very subjective nature of the available visibility values, visible transmission measurements were used to determine the visibility.

The second example of aerosol model validation is shown in Figure 19. This figure represents a time history during the winter of 1977 of the broad-band transmission over a 500 meter path in Meppen, Germany and was collected as part of the OPAQUE (Optical Propagation Quantities in Europe) Program. The LOWTRAN result for both a Rural and a Maritime aerosol model are included and compared with the measurements. Visibility was an input to the LOWTRAN calculations. An indication of an apparent air-mass change can be seen in the curve corresponding to the rural model. It is clear that the Maritime model represents the measurements much better during low visibility conditions. We will depend strongly on the measurements made as part of the OPAQUE Program and elsewhere for data to continue and extend these aerosol model validation studies.

5. OPERATIONAL TRANSMISSION MODELS

5.1. Low Resolution Propagation (LOWTRAN)

As indicated previously, the LOWTRAN transmission code is applicable to a spectral resolution of 20 cm^{-1} or degradable to any lower spectral resolution. The primary motivation for the construction of the LOWTRAN code is computer efficiency, flexibility, and applicability to broad-band systems problems. We feel that all of these goals are met with this code. It covers the spectral region from 0.25 to 28.5 micrometers and handles extinction by both molecular and aerosol atmospheric constituents. A recent modification to the code has generated the LOWTRAN 4 model, (See Selby, et al[13]) capable of computing atmospheric thermal emission as well as transmission. The construction of such an efficient and flexible model of necessity involves some approximations. Our aim is to make the program accurate in transmission to ±15% of the transmission value. Although we are close to this accuracy overall, some atmospheric conditions remain where this accuracy is difficult to achieve. Problems involving molecular continuum effects and aerosol extinction continue to receive the majority of our attention. Figure 15 shows the effect of the different sea level aerosol models on the total LOWTRAN computed transmission over a 10 km sea level path. The major difficulty is to decide which of the several aerosol models to use for a given atmospheric path. Some meteorological judgement, not currently included in the LOWTRAN model is required in order to achieve the best results.

Efforts are continuing to validate the LOWTRAN model, particularly against field measurements. An example of a recent comparison is shown in Figure 20. These measurements made at General Dynamics by Ashley, et al[23] were made over a 1.3 km path at sea level containing 0.72 pr. cm/km of water vapor. Figure 21 compares a LOWTRAN 4 emission result with measurements of atmospheric emission made from a balloon platform by Murcray et al[24].
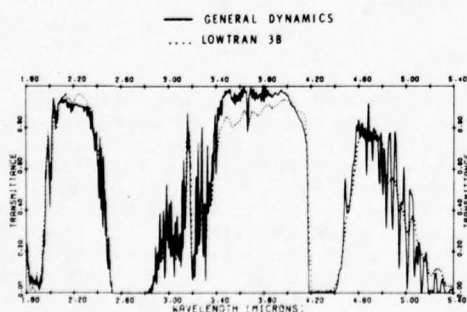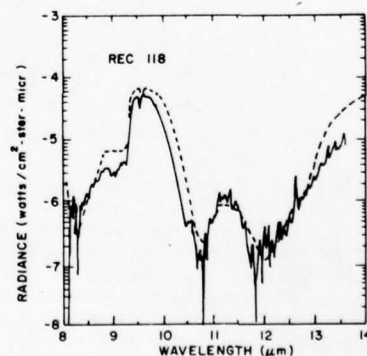

FIGURE 20. Comparison of LOWTRAN Calculations with Field Measurements of Ashley, et al[23].

FIGURE 21. Comparison of the LOWTRAN 4 Code with Atmospheric Emission Measurements of Murcray, et al[24].

Excellent agreement has been achieved here across this atmospheric "window" region and includes the nitric acid feature near 11 micrometers inserted for the first time into LOWTRAN 4. Other LOWTRAN validation efforts are aimed primarily at aerosol model comparisons and have already been discussed in Section 4.2.

5.2 Application of HITRAN to Laser Transmission

A version of the general HITRAN transmission code known as LASER[15] has been developed and is available to the community. This model uses the HITRAN data base described in Section 3.1 and also includes the same continuum absorption models and several of the same aerosol models contained in the LOWTRAN transmission model. Output from this model provides extinction coefficients for absorption and scattering by both the molecular and aerosol species in the atmosphere as a function of altitude. An example of an output extinction coefficient chart is shown in Table 3. The report describing this code also provides computed high resolution spectra which can be used to judge the high resolution propagation characteristics of the atmosphere at any wavelength between 3.3 and 13.5 micrometers.

TABLE 3.

EXTINCTION COEFFICIENT FOR LASER PROPAGATION

WAVELENGTH = 10.591033 MICROMETERS
FREQUENCY = 944.155 WAVENUMBER

ht(km)	U.S. STANDARD ℓ_m(km⁻¹)	σ_m(km⁻¹)	TROPICAL ℓ_m(km⁻¹)	MIDLAT SUMMER ℓ_m(km⁻¹)	MIDLAT WINTER ℓ_m(km⁻¹)	SUBARCTIC SUMMER ℓ_m(km⁻¹)	SUBARCTIC WINTER ℓ_m(km⁻¹)	AEROSOL CLEAR ℓ_a(km⁻¹)	σ_a(km⁻¹)	AEROSOL HAZY ℓ_a(km⁻¹)	σ_a(km⁻¹)
0	1.25E-01	0.	4.80E-01	3.19E-01	7.58E-02	1.85E-01	3.46E-02	2.99E-03	4.00E-03	1.26E-02	4.35E-02
0 - 1	1.04E-01	0.	3.71E-01	2.46E-01	6.73E-02	1.50E-01	3.92E-02	1.98E-03	2.64E-03	3.26E-02	4.15E-02
1 - 2	9.07E-02	0.	2.32E-01	1.50E-01	5.47E-02	1.02E-01	3.77E-02	2.52E-04	4.80E-05	4.02E-03	7.64E-04
2 - 3	6.10E-02	0.	1.14E-01	9.55E-02	4.57E-02	7.17E-02	3.12E-02	1.29E-04	2.45E-05	6.79E-04	1.29E-04
3 - 4	4.71E-02	0.	7.97E-02	6.69E-02	3.75E-02	5.60E-02	2.85E-02	1.05E-04	2.00E-05	3.72E-04	7.07E-05
4 - 5	3.74E-02	0.	5.23E-02	5.14E-02	3.34E-02	4.39E-02	2.32E-02	8.10E-05	1.54E-05	1.93E-04	3.69E-05
5 - 6	3.01E-02	0.	4.68E-02	4.29E-02	2.49E-02	3.49E-02	1.84E-02	6.01E-05	1.14E-05	1.23E-04	2.11E-05
6 - 7	2.45E-02	0.	3.76E-02	3.54E-02	2.03E-02	2.71E-02	1.44E-02	4.16E-05	7.91E-06	1.00E-04	1.31E-05
7 - 8	1.96E-02	0.	3.03E-02	2.86E-02	1.65E-02	2.16E-02	1.12E-02	2.63E-05	5.00E-06	6.71E-05	1.23E-05
8 - 9	1.56E-02	0.	2.50E-02	2.31E-02	1.34E-02	1.70E-02	9.23E-03	4.76E-05	0.	7.16E-05	6.07E-06
9 - 10	1.23E-02	0.	1.99E-02	1.88E-02	1.06E-02	1.32E-02	8.58E-03	3.56E-05	0.	5.23E-05	5.49E-06
10 - 11	9.54E-03	0.	1.59E-02	1.49E-02	9.37E-03	1.17E-02	8.56E-03	3.03E-05	0.	5.65E-05	6.37E-06
11 - 12	9.34E-03	0.	1.24E-02	1.18E-02	9.19E-03	1.16E-02	5.59E-03	2.76E-05	0.	6.51E-05	7.51E-06
12 - 13	9.34E-03	0.	9.54E-03	9.17E-03	9.01E-03	1.16E-02	8.54E-03	2.60E-05	0.	7.45E-05	6.44E-06
13 - 14	9.33E-03	0.	7.09E-03	8.11E-03	9.77E-03	1.17E-02	8.54E-03	2.56E-05	0.	8.13E-05	9.15E-06
14 - 15	9.33E-03	0.	5.61E-03	8.41E-03	8.64E-03	1.19E-02	8.57E-03	2.60E-05	0.	8.31E-05	9.35E-06
15 - 16	9.32E-03	0.	4.16E-03	9.15E-03	8.44E-03	1.12E-02	8.41E-03	2.59E-05	0.	6.09E-05	9.11E-06
16 - 17	9.29E-03	0.	3.19E-03	8.02E-03	8.24E-03	1.16E-02	8.22E-03	2.51E-05	0.	7.43E-05	9.35E-06
17 - 18	9.30E-03	0.	3.41E-03	8.05E-03	8.13E-03	1.15E-02	8.01E-03	2.35E-05	0.	6.50E-05	7.33E-06
18 - 19	9.29E-03	0.	4.17E-03	8.19E-03	7.99E-03	1.15E-02	7.81E-03	2.13E-05	0.	5.43E-05	6.11E-06
19 - 20	9.29E-03	0.	4.38E-03	8.55E-03	7.76E-03	1.16E-02	7.59E-03	1.85E-05	0.	4.35E-05	4.90E-06
20 - 21	9.44E-03	0.	6.02E-03	8.27E-03	7.88E-03	1.14E-02	7.40E-03	1.56E-05	0.	3.47E-05	3.31E-06
21 - 22	8.79E-03	0.	7.16E-03	5.29E-03	7.43E-03	1.15E-02	7.22E-03	1.31E-05	0.	2.77E-05	3.12E-06
22 - 23	9.13E-03	0.	8.10E-03	9.65E-03	7.60E-03	1.15E-02	7.03E-03	1.08E-05	0.	2.16E-05	2.43E-06
23 - 24	9.50E-03	0.	9.66E-03	1.06E-02	7.68E-03	1.17E-02	6.95E-03	9.69E-06	0.	1.67E-05	1.89E-06
24 - 25	9.84E-03	0.	9.49E-03	1.07E-02	8.23E-03	1.23E-02	6.68E-03	6.84E-06	0.	1.32E-05	1.44E-06
25 - 30	1.06E-02	0.	1.15E-02	1.27E-02	7.77E-03	1.33E-02	6.34E-03	1.56E-05	3.40E-06	3.98E-05	2.61E-06
30 - 35	9.47E-03	0.	1.16E-02	1.24E-02	6.66E-03	1.33E-02	5.60E-03	4.60E-06	1.05E-06	9.14E-06	1.93E-06
35 - 40	9.51E-03	0.	1.08E-02	1.24E-02	6.61E-03	1.15E-02	4.89E-03	2.36E-06	0.	2.96E-06	0.
40 - 45	8.18E-03	0.	8.73E-03	1.04E-02	5.96E-03	1.17E-02	4.04E-03	1.16E-06	0.	1.16E-06	0.
45 - 50	5.63E-03	0.	5.95E-03	7.45E-03	4.14E-03	9.03E-03	3.04E-03	0.	0.	0.	0.
50 - 70	9.50E-04	0.	9.43E-04	1.08E-03	8.03E-04	1.03E-03	7.66E-04	0.	0.	0.	0.
70 - 100	1.47E-05	0.	1.52E-05	1.73E-05	1.56E-05	1.74E-05	1.77E-05	0.	0.	0.	0.

ALTERNATE BOUNDARY LAYER AEROSOL MODELS

	CLEAR ℓ_a(km⁻¹)	σ_a(km⁻¹)	HAZY ℓ_a(km⁻¹)	σ_a(km⁻¹)
URBAN	········	········	4.16E-02	3.29E-02
MARITIME	4.79E-03	6.57E-03	5.22E-02	7.15E-02
TROPOSPHERIC	1.00E-03	1.91E-04	········	········

5.3 Modelling the Background Radiation Environment

Figure 22 shows the relative importance of sunlight and thermal emission as they both contribute to background radiation levels. We can see that during daylight hours, the background radiation environment results primarily from thermal emission beyond about 5 micrometers. Similarly, at wavelengths shorter than about 3 micrometers, the background radiation arises primarily from scattered sunlight. Between 3 and 5 micrometers, both sunlight and thermal emission contribute to the background radiation environment. In any event, we can be sure (day or night) that the emission of thermal radiation by the atmosphere and surfaces will dominate the backgrounds at wavelengths longer than 5 micrometers. Furthermore, once our transmission model has been shown to generate valid transmission results, it is relatively straightforward to use the same model to compute the thermal emission of the atmosphere. The LOWTRAN 4 model provides this capability and a comparison with measurements has already been shown in Figure 21. For shorter wavelengths, the development of a simple model to generate the scattered radiation field is more complex. It will depend on solar angle and in the general case depend in a complex way on the particle size distribution. Therefore, to date no simple models exist for carrying out this calculation. However, if single scattering is assumed and if an average phase function for scattering is assumed, a simple model could be

developed. The validity of such a model would have to be carefully tested and limitations noted before such a model can be generally distributed. In the meantime, we must fall back on more complex and time-consuming procedures of calculation or resort directly to measurements in order to estimate the scattered radiation field.
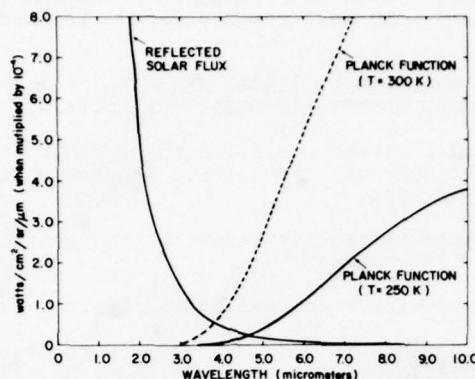

FIGURE 22. Comparison of the Level of Reflected Sunlight and the Thermal Emission from the Earth-Atmosphere System.

REFERENCES

1. McClatchey, R.A., Fenn, R.W., Selby, J.E.A., Volz, F.E. and Garing, J.S. (1972), Optical Properties of the Atmosphere (Third Edition), AFCRL-72-0497, ERP No. 411, 1972.

2. Valley, S.L., Ed., (1965) Handbook of Geophysics and Space Environment, AFCRL.

3. Sissenwine, N., Grantham, D.D., Salmela, H.A., (1968) Humidity Up to the Mesopause, AFCRL-68-0550.

4. Shettle, E.P. and Fenn, R.W. (1975) Models of the Atmospheric Aerosols and Their Optical Properties, AGARD Conference Proceedings No. 183, Optical Propagation in the Atmosphere, pp. 2.1-2.16, presented at the Electromagnetic Wave Propagation Panel Symposium, Lingby, Denmark, 27-31 Oct. 1975. (Available from NTIS, Acc. No. N76-29817.) (Note: A more complete version of this report will soon be published as an AFGL Technical Report.)

5. McClatchey, R.A., Benedict, W.S., Clough, S.A., Burch, D.E., Calfee, R.F., Fox, K., Rothman, L.S. and Garing, J.S. (1973) AFCRL Atmospheric Absorption Line Parameters Compilation, AFCRL-TR-73-0096.

6. Rothman, L.S. and McClatchey, R.A. (1976) Updating of the AFCRL Atmospheric Absorption Line Parameters Compilation, Applied Optics, 15, p. 26216.

7. Rothman, L.S. (1977) Atmospheric Optics, OSA Technical Group Meeting, Tucson, 19 October 1976, Applied Optics, 16, No. 2, p. 277, February 1977.

8. Rothman, L.S. (1978) Update of the AFGL Atmospheric Absorption Line Parameters Compilation, Applied Optics, November 1978.

9. Rothman, L.S., Clough, S.A., McClatchey, R.A., Young, L.G., Snider, D.E. and Goldman, A., (1978) AFGL Trace Gas Compilation, Applied Optics, 17, February 15, 1978.

10. Burch, D.E. (1970) Semiannual Technical Report, Investigation of the Absorption of Infrared Radiation by Atmospheric Gases, U-4784, January 1970.

11. Selby, J.E.A., Shettle, E.P. and McClatchey, R.A. (1976) Atmospheric Transmittance from 0.25 to 28.5 μm: Supplement LOWTRAN 3B (1976), AFGL-TR-76-0258, ERP 587, November 1976.

12. Roberts, R.E., Selby, J.E.A. and Biberman, L.M. (1976) Infrared Continuum Absorption by Atmospheric Water Vapor in the 8-12 μm Window, Applied Optics 14:2085.

13. Selby, J.E.A., Kneizys, F.X., Chetwynd, J.H. and McClatchey, R.A. (1978), Atmospheric Transmittance/Radiance: Computer Code LOWTRAN 4, AFGL-TR-78-0053.

14. Gryvnak, D.A., Burch, D.E., Alt, R.L. and Zgonc, D.K. (1976), Infrared Absorption by CH_4, H_2O and CO_2, AFGL-TR-76-0246.

15. Dowling, J.A., Haught, K.M., Horton, R.F., Hanley, S.T., Curcio, J.A., Garcia, D.H., Gott, C.O. and Agambar, W.L. (1977), Atmospheric Transmission Measurements Using IR Lasers, Fourier Transform Spectroscopy, and Gas Filter Correlation Techniques, Report of NRL Progress, March 1977.

16. Nordstrom, R.J., Shaw, J.H., Skinner, W.R., Calvert, J.G., Chan, W.H. and Uselman, W.M. (1976) A Comparison of High Resolution Observed and Computed Air Spectra Between 700 and 2300 cm^{-1}, OSU Research Foundation Technical Report RF 4221, August 1976.

17. McClatchey, R.A. and D'Agati, A.P. (1978) Atmospheric Transmission of Laser Radiation: Computer Code LASER, AFGL-TR-78-0029, ERP No. 622, January 1978.

18. Smith, H.J.P., Dube, D.J., Gardner, M.E., Clough, S.A., Kneizys, F.X., and Rothman, L.S. (1978) FASCODE-Fast Atmospheric Signature Code (Spectral Transmittance and Radiance), AFGL-TR-78-0081.

19. Volz, F.E. (1972) Infrared Refractive Index of Atmospheric Aerosol Substances, Applied Optics, 11, pp. 755-759.

20. Junge, C.E. (1963) Air Chemistry and Radioactivity, pp. 382, Academic Press, N.Y.

21. Whitby, K.T., Husar, R.B. and Liu, B.Y.H., (1972) The Aerosol Size Distribution of Los Angeles Smog, J. Colloid and Interface Science, 39, 177-204.

22. Arnold, D.H., Lake, D.B. and Sanders, R., 1970, Comparative Measurements of Infrared Transmission Over a Long Sea Path, EMI Electronic Report, DMP 3736 and DMP 3858.

23. Ashley, G.W., Gastineau, L. and Blay, D. (1973), Private Communication.

24. Murcray, D.G., Brooks, J.N., Goldman, A., Kosters, J.J. and Williams, W.J. (1977) Water Vapor Nitric Acid and Ozone Mixing Ratio Height Profiles Derived from Spectral Radiometric Measurements, U. of Denver, Denver, CO 80203, Contract Report No. 332.

Acknowledgement

The Transfer of Electromagnetic Radiation in the Turbulent Atmosphere
By E. Raschke, University Köln, Federal Republic of Germany

Summary and Introduction
Electromagnetic radiation on its way through the terrestrial atmosphere interacts with the environment by absorption, thermal reemission, scattering, reflection and refraction. In the mathematical description of these interactions, as required for the interpretation of fields measurements, not only the properties of the quiet atmosphere, but also turbulent phenomena need to be considered.

In this paper are briefly reviewed the principle properties of the terrestrial atmosphere up to an altitude of about 50 km, with inclusion of general principles of theoretical models for the calculation of its motion fields. This is followed by a description of the transfer of electromagnetic radiation in the turbulent atmosphere and a brief outline of the general radiative transfer theory.

Since McClatchey's paper in this Lecture Series 99 describes in great detail the modelling of radiative transfer in the atmosphere, we give only a short basic outline of it.

1. The Atmosphere of the Earth
The composition of the atmosphere in its present state, the stratification of its mass field in the vertical and horizontal direction and the circulation phenomena occuring in it are result of a long time history and of complicated interactions between the atmosphere and its boundaries: Through exchange of radiative energy with space, and through physical and chemical processes occuring at the lower boundary, the land-ocean-ice system.

1.1 Composition and Thermal Stratification
Our lower atmosphere consists mainly of gases with constant mixing ratios. These are nitrogen, oxygen, argon. For its motions and stratification, however, are of great importance the carbon dioxide (and perhaps also for the glass house effect the nitrogen oxides), and water vapor and ozone.

The latter two gases occur with mixing ratios variing considerably with space and time, due to atmospheric circulation phenomena and phase changes (H_2O) or photochemical reactions (O_3).

In Table 1 are summarized the mixing ratios of the most important gases. Figs. 1-3 provide an overview on horizontal and vertical distributions of water vapor and ozone and their changes with time. The liquid and ice phases of water vapor in the air, i.e. clouds, influence dominantly the transfer of electromagnetic radiation of all wavelengths up to the centimeter regions. Their occurence is a result of up- and downward motions in the atmosphere and turbulence and water vapor supply. Due to their importance on the heat budget and also precipitation, their climatology belongs to an old desire of research. But no quantitive correct statistics has been obtained so far.

Fig. 4 shows a world map of total cloudiness, i.e. fractional cloud cover, as obtained from satellits and ground-based observations.

The average vertical and meridional thermal structure of the well mixed lower atmosphere is illustrated in Fig. 5. We describe the lowest layer of 5000 m to 2000 m thickness as the <u>planetary boundary layer</u>, where the dynamics are considerably effected by groud effects (dray, differential heating). It belongs to the <u>troposphere</u>, where the temperature drops with about 6.5 K/1000 m up to 10-17 km altitude, the <u>tropopause</u>. In the <u>stratosphere</u> above the temperature rises with height. Above the <u>stratopause</u> at about 50 km altitude, the <u>mesophere</u> is located; and about that spere follows the <u>mesopause</u> at about 85 km altitude.

This average temperature structure, although it is a result of complicated circulation phenomena, can be explained to a large portion by the pure assumption of radiative equilibrium, i.e. absorption of incident solar radiation by O_3, O_2, H_2O and CO_2 and the ground and thermal emission by the ground and the same gases back to space.

Sinking motions in the troposphere, but also radiative cooling of the ground and adjacent

air layers cause the formation of inversion layers, i.e. layers where the temperature increases with height. At the top and bottom of such layers strong fluctuations of the temperature, due to vertical motions may occur.

1.2   Scales of Motion Phenomena, the Mean Circulation

Our ceaseless atmosphere shows motions whose scales range from wavelenghts of several thousand kilometers down to the molekular scale turbulence. A descriptive overview including "typical" life times of phenomena is given in Fig. 6.

A height-latitude diagram shows the mean zonal (east-, westward) wind field in Fig. 7. There are, however, in the average and caused by many disturbances also meridional winds. In general, one may explain the mean circulation in the troposphere, being driven by the steady heating of equatorial regions and cooling at the poles, where the Coriolis forces cause a pronounced meridional circulation. Statistical investigations show a three-cell structure (Fig. 8).

1.3   Modelling of the Circulation

The modelling of the circulation of any scale, either in global models or for a vertical profile, requires a simultaneous consideration of the motion field, the heat budget, the continuum and the state. These basic principles are usually formulated by

- the Navier-Stokes-Equations, which are another formulation of Newton's second axiom;
- the first and second heat law (thermodynamic equation), which explicitely includes also diabatic heating due to radiation
- the euqation of continuity, and
- the equation of state

In any atmospherical model this set - formulated in more or less trunkated or modified versions - need to be solved at each grid-point, with careful considerations of energy transfer processor - in particular at the boundary layer.

This might be a very simplified explanation of the basis of numerical models currently used for weather forecast or the modelling of the global circulation. Such models are now widely in use, where a large variety of the mathematical treatment is used.

The current most advanced circulation models are global. However, they are in many cases still bounded below by ocean and land surfaces with prescribed properties. Moreover, the lack in a complete hydrological cycle, in particular the formation of cloud fields. The parametrisation of such processes, whose full-detail description is in many cases hardly possible only by a large number of field experiments.

During the last years, many of such experiments have been conducted under the coordination within the GARP-program.

As an example of present-days model capabilities an example of computed precipitation fields is shown in Fig. 9.

2.   Radiative Transfer in a Turbulent Atmosphere

Atmospheric turbulence "elements" whose "size" is smaller or comparable to or slightly larger than the wave lenght may interact with an electromagnetic wave passing through it, if its index of refraction deviates from that of its environment. Einstein (1910) and also von Smoluchowski (1908) considered, perhaps at first time, these scattering processes and obtained equations which were similar to Rayleighs formula, when the disturbances are much smaller than wavelenght of radiation.

In this paper we will consider only the interaction of turbulence with plane electromagnetic waves. Recent developments with very narrow beams such as of alser and radars, require a more sophisticated treatment. They will not be covered here, although they might be of fundamental interest to the audience.

2.1   The Atmospheric Index of Refraction

For optical wave lenghts the index of refraction for air n may be given approximately by

$$N = (n-1) \times 10^6 = 77.6 \times (1 + 7.52 \times 10^{-3} \cdot \lambda^{-2}) \cdot \frac{p}{T} \quad (1)$$

where (n-1) is the derivation of n from its free space value, λ is the wave lenght in µm, p is the pressure of ambient air in millibars and T is the temperature in Kelvin. Further terms of partly less significance describe the effect of atmospheric water vapor on N, which is of particular importance over water paths (Wesely and Alcaraz, 1973). For radio waves, usually the following equation is used:

$$N = 77.6 \cdot \frac{p}{T} + 3.73 \cdot 10^5 \cdot \frac{e}{T^2} \quad (2)$$

where e is the water vapor pressure.

2.2 A Short Description of Atmospheric Turbulence

Laminar flows become turbulent, when the Reynold's number reaches large values. Obstacles or buoyant forces force the formation of turbulence. Turbulence in principle acts on the account of the kinetic energy of the mean flow, which through it is weakened and trans-formed into heat in the final stage, the dissipation. We should consider here only such turbulent motions, whose amplitude is much weaker than the mean displacement flow. In principle turbulence is treated as a random process. Kolmogorov (1961) defined a structure tensor by

$$D_{ij} = \left\langle \left[v_i(\vec{r_1} + \vec{r}) - v_i(\vec{r_1}) \right] \cdot \left[v_j(\vec{r_1} + \vec{r}) - v_j(\vec{r_1}) \right] \right\rangle \quad (3)$$

which is the mean square difference of velocities at two points, separated by the distance r. v_i and v_j are the two velocity components.
Usually several assumptions are now made:

- local homogeneity: difference depends only on r
- local isotropy: only the magnitude of r is important
- imcompressible turbulence: v = 0

Then the structure function for the displacement parallel to r, D_{rr}, can be expressed by

$$D_{rr} = \left\langle \left[v_r(\vec{r_1} + \vec{r}) - v_r(\vec{r_1}) \right]^2 \right\rangle \quad (4)$$

In the socalled inertial subrange of turbulence, where turbulence cascade develops itself from larger to smaller sized turbulence elements (eddies), D_{rr} has a universal form:

$$D_{rr} = C_v^2 \times r^{2/3} \quad (5)$$

where C_v^2 is the velocity structure constant.
It can be shown now, that also a conservative property of air, the potential temperature, can be described by a structure function

$$D_\theta = C_\theta^2 \times r^{2/3} \quad (6)$$

2.3 Turbulent Variations of the Index of Refraction

With the above described very simple turbulence models we can relate the turbulence of air to variations of the refractive index.
From (1) we obtain

$$\sigma_n = 77.6 \times (1 + 7.52 \times 10^{-3} \lambda^{-2}) \cdot \frac{p}{T} \cdot \left(\frac{\sigma_p}{T} - \frac{\sigma_T}{T} \right) \cdot 10^{-6} \quad (7)$$

Since pressure fluctuations σ_p are usually much smaller than temperature fluctuations, and with the introduction of the definition of the potential temperature θ, we may write in analogy the structure constant of the refractive index   by

$$C_n^2 = \left[77.6 \times (1 + 7.52 \times 10^{-3} \lambda^{-2}) \times \frac{p}{T^2} \cdot 10^{-6} \right]^2 \times C_\theta^2 \quad (8)$$

Thus, we have found an expression relating the variations of n to those of θ.

The behaviour of C_n and C_T is illustrated in Fig. 10. Variations of C_T can easily be observed with acoustic sounding techniques.

2.4 The "Classical" Theory of Radiative Transfer in a Turbulent Medium

As in the classical theory for optical propagation in quiet media, as used by G. Mie (1908)

this theory starts with the wave equation, derived from Maxwell's euqations, which is then solved for small perturbations.

wave equation: $$\nabla^2 E + k^2 n^2 E = 0 \qquad (9)$$

E = magnitude of the electric field

k = ω/c = wave number, ω= radian frequency

with $E = E_0 + E_1 + E_2 + \ldots$, where E_i = small perturbations, and

$$E_0 = exp[ikz] \qquad (10)$$

one obtains after some manipulation and dropping all terms E_m (m > 1):

$$\nabla^2 E_1 + k^2 E_1 = -2 k^2 n_1 e^{ikz} \qquad (11)$$

where n_1 = local refractive index fluctuation.
The solution is known by

$$E_1(\vec{r}) = \frac{1}{4\pi} \int [2 k^2 n_1(r') e^{ikz}] \cdot \frac{e^{ik|\vec{r}-\vec{r}'|}}{|\vec{r}-\vec{r}'|} d^3r' \qquad (12)$$

which is the electric field strength at r originating from a spherical wave emitted at r'. The further analysis requires now the calculation of the Poynting vector, which determines the flux of scattered power. By integrating over a volume element and over time, to obtain the average power, the covariance function of turbulence is introduced. In the case of a Kolmogorov-spectrum, this function is related to the structure function D_n. By the definition of the scattering cross-section dσ as the fraction of the incident energy flux per unit area per unit time, that is scattered into the solid angle dΩ, one finally may obtain

$$d\sigma(\theta) \sim const. \cdot C_n^2 \cdot k^{1/3} \cdot \frac{\sin \chi}{\sin \theta/2} \lambda^{1/2} d\Omega \qquad (13)$$

where χ = an angle between the incident wave and the vector r, and θ scattering angle. This equation holds for the range

$$L_0 > \frac{1}{2k \cdot \sin \theta/2} > l_0 \qquad (14)$$

where L_0 and l_0 are the outer and inner scale of turbulence. Near the groud L_0 is of the order of several meters, the size of eddies, while l_0 is of the order of millimeters. There are more modern approaches, where larger perturbations are considered, since this "classical" approach does not explain many observed features, i.e. strong scintillations over long paths or lines-of-sight. Since this paper may be considered as an introduction to the hole subject of the lecture series, we should not go into deeper details of this subject.

2.5 The Radiative Transfer Theory - a General Outline
Depart from scintillations, easily observed in star light or near groud paths, the atmospheric constituents by themselves absorb, scatter and reemit radiation. In such a medium the transfer of monochromatic radiation is described by the well-known differential equation below.

$$\frac{dL}{d\tau} = -L + (1-\tilde{\omega}) \cdot B + \frac{\tilde{\omega}}{4\pi} \int p(\Omega,\Omega') L(\Omega') d\Omega' \qquad (15)$$

where   L = monochromatic radiance

B = Planck-Function of thermal emission

$\tilde{\omega}$ = single scattering albedo; $(1-\tilde{\omega})$ = absorption number

τ = optical "distance" between two points

p = angular scattering characteristics of a volume element (phase function)

In this equation the change of radiance along an "optical path" dτ is related to the incident radiance L and source terms, due to thermal emission and scattering of radiation incident from all directions. This is illustrated in Fig. 11.
Formal solutions are easy available, in particular, if the medium is modelled as a plane-parallel layer with horizontal uniformity. But, there are also solutions for spheric shell-atmospheres available, which ar in particular required for the interpretation of

limb radiance measurements.

Computation methods, easier now due to the availability of large and fast-enough computers, than during the beginning of this century when simple approximations we used, range up to line-by-line integrations. The major difficulties arise in the formulation of radiative transfer input data.

The optical depth between two points P_1 and P_2 separated by the distance ds can be calculated from

$$\tau(P_1, P_2) = \int (\sigma_a + \sigma_s) \, ds \qquad (16)$$

where σ_a and σ_s are the volume absorption and scattering coefficients.

The single scattering albedo $\tilde{\omega}$ is defined by

$$\tilde{\omega} = \frac{\sigma_s}{\sigma_a + \sigma_s} \qquad (17)$$

and expresses the fraction of scattering as compared to the total extinction. The phase function is simply a directional function. A typical example of such phase functions computed for a mixture of gas and aerosols is shown in Fig. 12.

Values of the absorption coefficients σ_a can be obtained from atomic theory and for laboratory measurements for all gases involved. The requirements of modern remote sensing techniques led to a very large number of such fundamental investigations, that for almost all gases such values σ_a are available. There are also numerous approaches to integrate over finite spectral intervals.

The determination of scattering coefficients and phase functions, however, may be even more difficult, since it requires at present still the assumptions, that such scattering is due to turbulence (see chapter above) and to spherical particles. There are very few investigations, where now also non-spherical particles are considered. Such are related for instance with investigations of the scattering cirrus ice needles or the interplanetary matter. The basic treatments are due to Rayleigh (1881) and later G. Mie (1908), where the first considered the case, when the wavelength is much larger than the size of the scattering element, while the latter considered the more general case.

Recently there have been many laboratory experiments where the scattering properties of more irregular particles are measured directly by illuminating them with laser or microwave radiation. An example of such measurements is shown in Fig. 13.

3.   References in this Paper

(1)   J.J.Barnett,1974, Q.J.R. Met. Soc., 600, 5o5-53o

(2)   A.Einstein, Ann. d. Physik, 33,1275-1298 (1910)

(3)   A.Ghazi, 1971, Cospar Space Research, Vol. XVII, 1o3-11o

(4)   A.Ghazi, A. Ebel, 1976, J. Geoph. Res., 81, 5365-5373

(5)   J.London, 1976, NCAR, Techn. Note 113+STR, Boulder, Colorado

(6)   E.Lorenz, 1967, The Nature and Theory of the General Circulation of the Atmosphere World Meteorological Organization, Geneva

(7)   G.Mie, Ann. d. Physik, 25, 577-445 (19o8)

(8)   F.Möller, 1973, Einführung in die Meteorologie,Bibl. Institut, Mannheim

(9)   NAS, 1975, Understanding Climatic Change, A Program for Action National Academy of Sciences

(10)   E.Palmén, 1954, Über die atmosphärischen Strahlströme. Meteorol. Abhandl. (Berlin), 2, 35-5o

(11)   E.Raschke, U.Stucke, Theoretische Studien des Transportes solarer Strahlung in einem realistischen Modell des Systems Ozean-Atmosphäre, BMFT-FBW 73-13, Research Report

(12)   Lord Rayleigh, Phil. Mag. (5) 12, 81-1o1 (1881)

(13)   M. von Smoluchowski, Ann. d. Physik, 25, 2o5-226 (19o8)

(14)   M.L.Wesely, E.C.Alcaraz, J. Geophys. Res., 78 (1973)

(15)   R.Zerull, 1973, Mikrowellenanalogieexperimente zur Lichtdtreuung von Staubpartikeln BMFT-FBW 73-18, Research Report

4. Other Books of Interest for this Lecture

4.1 Atmospheric Physics and Turbulence

(1) G.T. Csanady, 1973, "Turbulence Diffusion in the Environment", D. Reidel Publ. Comp. Doordrecht-Holland

(2) A.Defant, F.Defant, 1958, "Physikalische Dynamik der Atmosphäre", Akad. Verlagsgesellschaft, Frankfurt

(3) J.A,Dutton, 1976, "The Ceaseless Wind", McGraw-Hill Book Comp.; New York

(4) G.J.Haltiner, 1971, "Numerical Weather Prediction", J.Wiley, New York

(5) J.T.Houghton, 1977, "The Physics of the Atmosphere", Cambridge Univ. Press

(6) P.Morel, ed., 1973, "Dynamic Meteorology", D.Reidel Publ. Comp., Doordrecht-Holland

(7) F.Pasquill, 1962, "Atmospheric Diffusion", Van Nostrand Comp. Ltd, London

(8) V.I.Tatarskii (origi lly 1967); "The Effects of the Turbulent Atmosphere on Wave Propagation", US Dept. of Commerce, NTIS, Springfield (1971)

(9) H.Tennekes and J.L.Lumley, 1972, "A First Course in Turbulence", MIT-Press, Cambridge

4.2 Radiative Transfer and Remote Sensing

(1) B.R. Bean, E.J.Dutton, 1966, "Radio Meteorology", NBS Monograph 92, Superintendent of Documents, Wash. D.C.

(2) D.Clarke, J.F.Grainger, 1971, "Polarized Light and Optical Measurement", Pergamon Press Oxford

(3) B.Crosignani, P. di Porto, M.Bertolotti, 1975, "Statistical Properties of Scattered Light", Academic Press, New York

(4) V.E.Derr, ed., 1972, "Remote Sensing of the Troposphere", NOAA-ERL, Bouldex, Colo.

(5) R.M.Goody, 1964, "Atmospheric Radiation", Oxford, Clerendon Press

(6) H.V.Harrimond, H.L.Mason ed., 1971, "Precision Measurement and Calitration", NBS Special Public. 3oo, Vol.7, Superintendent of Documents

(7) E.D.Hinkley, ed., 1976, "Laser Monitoring of the Atmosphere", Springer-Verlag, Berlin, Heidelberg

(8) K.Ya. Kondratiev, 1969, "Radiation in the Atmosphere", Academic Press, New York

(9) E.J. McCartney, 1976, "Optics of the Atmosphere", J.Wiley, New York

(10) W.I.Thompson III, ed., 1971, "Atmospheric Transmission Handbook" Nat. Aeronautics and Space Administration, Wash. D.C.

(11) W.L.Wolfe, ed., 1965, "Handbook of Military Infrared Technology", Superintendent of Documents, Wash. D.C.

Verteilung der relativen Feuchte(%) im Januar   Verteilung der relativen Feuchte(%) im Juli
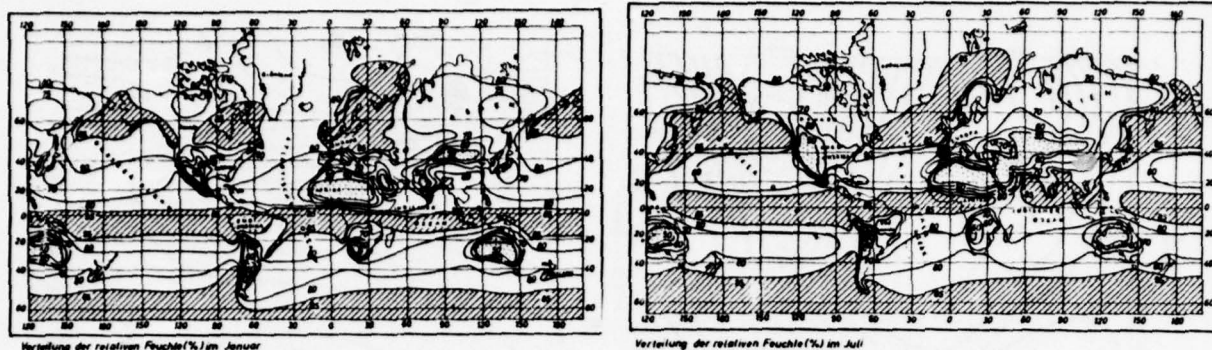
Fig. 1: Map of the mean tropospheric relative humidity. In the average the mixing ratio decreases exponentially with increasing altitude, in the stratosphere it amounts to about $2-5 \cdot 10^{-6}$ g/g (after Möller, 1973)
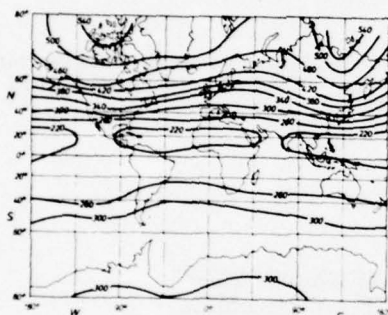
Fig. 2: Map of the total ozone content in the stratosphere, where about 9o percent of it are concentrated in a layer between about 2o-35 km. The ozone concentration in the troposphere is very low (after Ghazi, 1977)
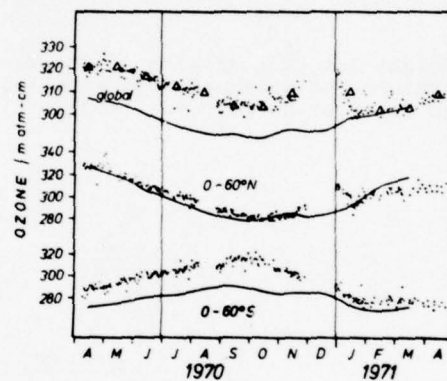
Fig. 3: The annual change of the total ozone content, as observed from groud (-) and with satellits (dots) (afetr Ghazi, Ebel, 1976).
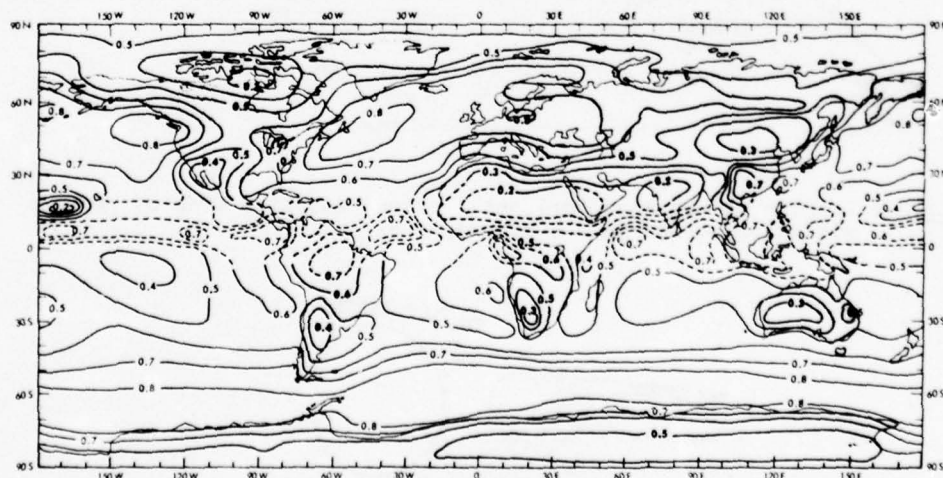
Fig. 4: Mean fractional cloud-cover, obtained from ground-based and satellite observations (from NAS, 1975)
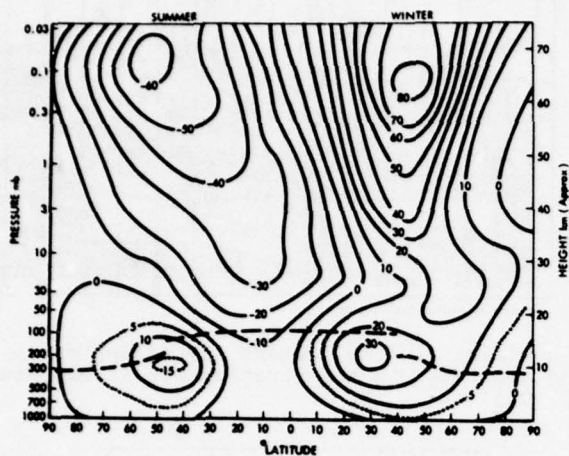
Fig. 5: Height-latitude diagram of the mean air temperature, as obtained from satellite measurements (after Murgatroyd, 1969)
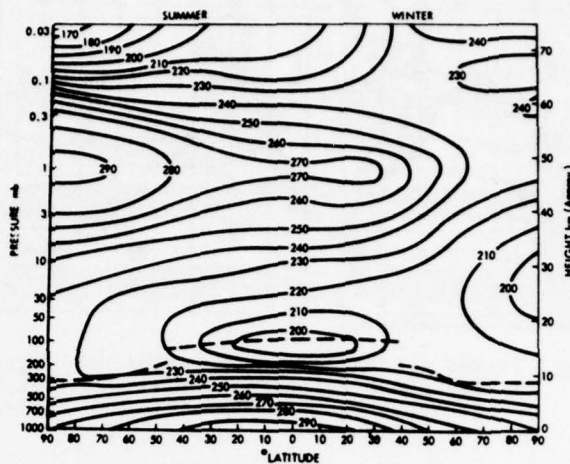
Fig. 7: Height-latitude diagram of the mean zonal wind field (after Murgatroyd, 1969)
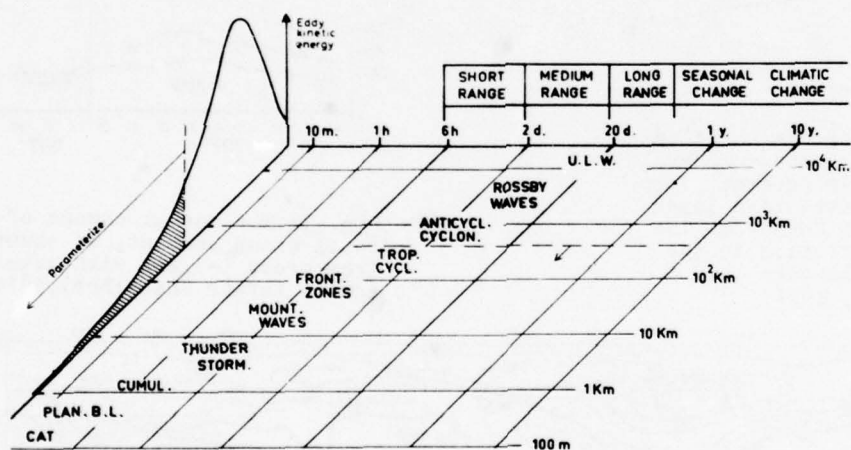
Fig. 6: Diagram of the mean horizontal extent and life time of various motion phenomena in the troposphere.
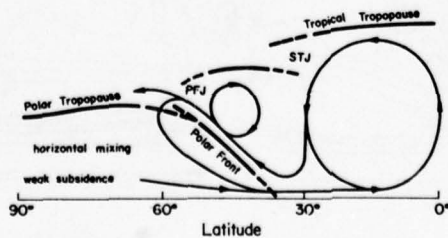
Fig. 8: Illustration of the mean atmospheric circulation cells. The equatorial and polar cells are driven directly by radiative heating and cooling, respectively (after Palmén, 1954)
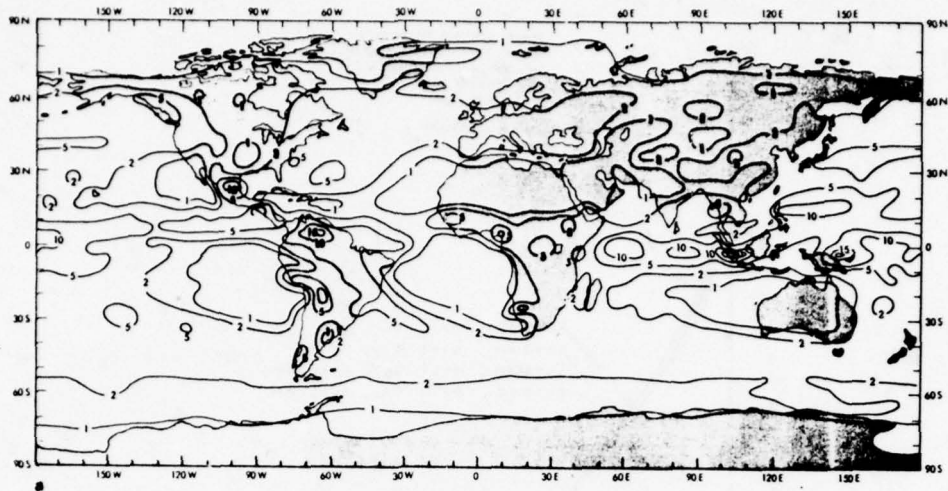
Fig. 9: Global distribution of precipitation patterns; climatology and computed data (from NAS, 1975)
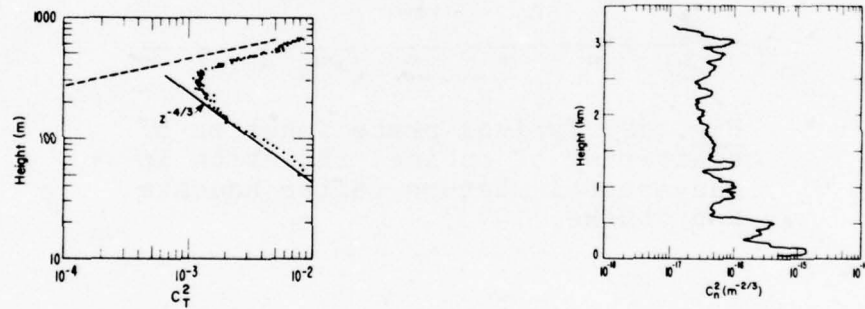
Fig. 10: Height-profiles of C_T and C_n derived from acoustic sounders and airborne temperature measurements, respectively (after Strohbehn, 1978)
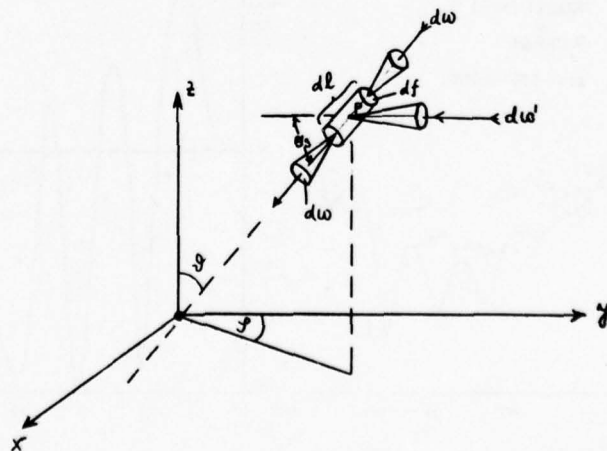
Fig. 11: Illustration of the radiative tranfer equation (afetr Strohbehn, 1978)
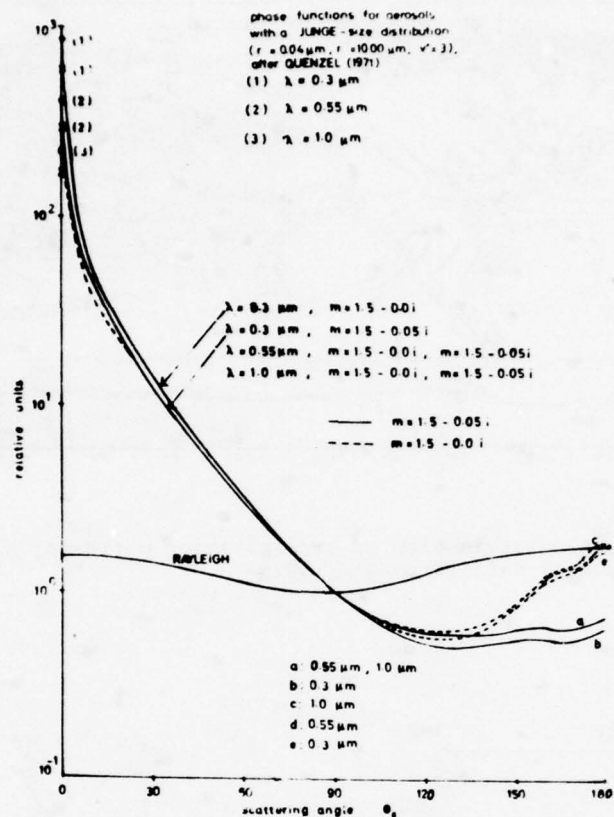
Fig. 12: Typical phase function of scattering of optical radiation in gas-aerosol mixture (after Raschke and Stucke, 1973)
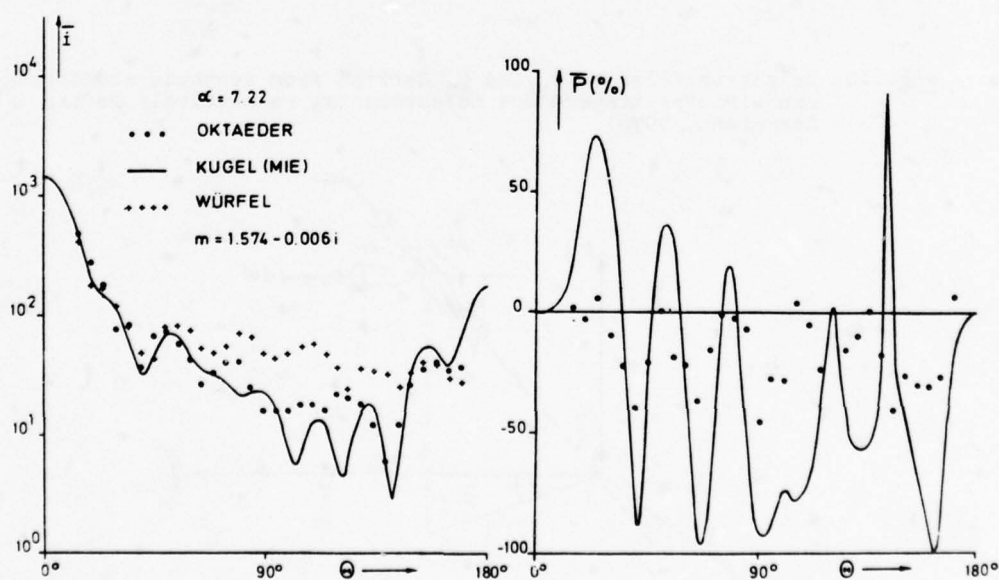
Fig. 13: Phase function of non-spherical particles measured with a microwave analogon-experiment. (after Zerull. 1973)

OPTICAL COMMUNICATION AND DETECTION
THROUGH OPTICAL SCATTERING CHANNELS
by
Robert S. Kennedy
Professor of Electrical Engineering
Department of Electrical Engineering
and Computer Science
and Research Laboratory of Electronics
Massachusetts Institute of Technology
Cambridge, Massachusetts 02139

It is abundantly clear that severe scattering in the atmosphere interferes with the operation of many optical systems. It is equally clear that a thorough understanding of propagation in such atmospheres is lacking, particularly when multiple scattering is prevalent. On the other hand, from a system designer's perspective, understanding the propagation itself is only a means to the end of obtaining a model for the optical field in the system aperture. Therefore it is instructive to shift the emphasis from understanding the propagation itself and consider instead:

1) The effects of multiple scattering upon received signals.

2) The impact of these effects upon the performance of systems that were designed to operate in the absence of scattering.

3) The essential features of systems that are best able to operate through channels in which the propagation is dominated by multiply-scattered radiation.

That is the purpose of the lectures that are briefly summarized in these notes.

In Section 1 a plausible, but incomplete, statistical model for the aperture field is introduced and the change in the qualitative feature of the field with increasing scatter is reviewed. In Section 2 the performance degradation that systems designed for clear weather operation suffer in the face of increased scatter is noted as a prelude to a deeper discussion of the essential features and performance of systems that are designed to operate in multiple-scattering atmospheres.

1. The Aperture Field

Were it not for the atmosphere, the signal component of the optical field at the aperture of the receiver would be related to the transmitted field through the Fresnel or Fraunhofer integral. In the presence of the clear, but turbulent, atmosphere the received optical field will be distorted in space and, to some extent, in time and frequency. The effects of atmospheric turbulence have been studied extensively; they are not our concern here.

As the particle content of the atmosphere increases, through the presence of haze, smoke, fog, rain, or snow, the received optical field will become increasingly corrupted in time, space, and frequency. For example, what might have been a plane wave in the clear atmosphere (with little turbulence) will now be received as a random field which contains a deterministic unscattered component and a random (zero mean) scattered component.

To the extent that the receiver is responsive only to the unscattered component of the field, as most existing receivers are, the major effect of atmospheric scattering is to increase the path loss for this component by a factor of $\exp(-\alpha\ell)$, where ℓ is the path length and α is the spatially-averaged extinction coefficient of the medium. Although the relationship between α and visibility is tenuous, at best, some appreciation for the magnitude of the attenuation is provided by the commonly accepted approximation that, at visible wavelengths, $\exp(-\alpha\ell)$ will be on the order of 10^{-2} when the operating range ℓ equals the visibility. That is, when ℓ is approximately equal to the visibility, the power that reaches the receiver without being scattered is only 1% of that which would have reached it in the absence of scattering. Clearly, if reliable operation is to be maintained over distances comparable to or greater than the visibility, there is merit in attempting to utilize the information contained in the component of the received field that has been scattered.

Whether or not such utilization is possible depends in detail upon the statistical properties of the scattered field in the aperture. These properties are very complicated functions of the transmitted field, the composition of the scattering media and the geometry of the problem. In general, such a description is essentially impossible to obtain and, even if it were available, it would be far too complicated to use for system analyses. This is so even though, for the channel geometries of interest here, the scattered field is almost certainly a zero mean Gaussian random process for which it is

only necessary to specify a space-time correlation function [1-4]*

Fortunately, the situation is not as bleak as it might seem. In particular, past experience with random scattering channels, at both optical and non-optical wavelengths, leads to the conclusion that they can almost invariably be adequately characterized, for purposes of system analysis, by a few parameters, or functions [1-4]. These quantities measure the behavior of the received field in the dimensions that most influence the systems performance. Among the most important of them are:

i)   The total average received energy incident upon the receiving aperture in response to a transmitted impulse, or equivalently the average power in response to a constant transmitted power.

ii) The distribution in angle of the average received energy (or power). This is essentially the angular spectrum of the received energy. A simpler but more limited characterization is the width of the angular spectrum or the coherence length in the aperture.

iii) The distribution in time of the average received energy in response to a transmitted impulse. A simpler but less informative quantity is simply the multipath spread or the coherence bandwidth.

iv) The distribution in frequency of the average received power in response to a constant transmitter power. This "Doppler" spectrum contains information about the fading rate of the signal. In particular, the reciprocal of its width is a measure of the coherence time of the channel.

Clearly, these parameters do not completely specify the space-time correlation function of the aperture field and in some situation other parameters may be important. For example, if the multipath spread of the photons arriving from a given angle depends strongly upon that angle, the single multipath spread mentioned above must be replaced by the spread as a function of angle. However in many situations the listed parameters are all that the system designer requires.

Of course, the listed parameters are all functions of the channel geometry, the constituents of the scattering media, the receiver aperture size and the transmitter wavelength, beamwidth and modulation. Thus, even they are not trivial to determine. However their values play a fundamental role in determining both the performance that can be realized with scattering systems and the structure that such systems should have. In principle they can be evaluated in a variety of ways. For example, in the extreme of little scattering, the approach is a straightforward single-scatter calculation that has been widely used [5-10]. As the scattering becomes more pronounced, as it will when the aerosol concentration or the operating range increases, the problem becomes more difficult and has yet to be satisfactorily solved.

As stated in the introduction, that difficulty will not be addressed here. Instead, the design problem will be formulated in terms of the aperture parameters. However before addressing that design problem, it is instructive to describe the way in which the parameter values differ for scattering and non scattering atmospheres and the physical cause of these differences.

The change in the total average energy incident upon the aperture results from two opposing effects: the extinction of photons that would reach the aperture in the absence of scattering (the decrease of the unscattered field) and the scattering into the aperture of photons that would not have reached it without scatter (the increase of the scattered field). Usually the total energy will decrease with increasing scatter, but much less rapidly than does the unscattered field alone.

In the absence of scattering the angular spectrum of the aperture field will be an impulse broadened slightly by atmospheric turbulence. That is the photons incident upon the aperture will all arrive from essentially the same direction, or equivalently, the field incident upon the aperture is a plane wave. Closely related to the angular spectrum is the spatial correlation function whose width measures the area over which the aperture field behaves as a plane wave. In the absence of scattering and turbulence this correlation function will be a constant.

As scattering becomes significant the contribution of photons that arrive from other angles will become noticeable and the angular spectrum will broaden as shown in Fig. 1. Equivalently, as shown in the figure, the spatial correlation function will narrow as the plane waves arriving from different scatterers interfere with each other and with the unscattered field.

Some appreciation for the magnitude of the spectrum broadening that can occur can be gained by an examination of Fig. 2. The figures show representative angular spectra

---

* That it is Gaussian follows from the very large number of essentially independent events (scatterings) that contribute to the received scattered field in an additive way -- so many that the sum converges to a Gaussian random process. Moreover, each of the scatterings introduces an essentially random phase that causes the mean value of its contribution to the field to be zero. Hence the statistical characterization of the process reduces to the specification of its space-time correlation function.

obtained through a coastal fog at a wavelength of 0.25 μm over a 1,000 foot path with an omnidirectional source [11]. Note that the broadening is significant at optical thicknesses, τ, of 2 to 9 and is severe when τ exceeds 10.

Increased scattering also results in multipath spreading of a short transmitted pulse. As illustrated in Fig. 1, in the absence of scatter the transmission of an impulse in time will result in the reception of an impulse. However as scatter becomes prevalent photons can reach the receiver by scattering paths of different lengths and the received impulse will be spread into a wider pulse. The magnitude of the spreading depends upon the characteristics of the channel but values in excess of microseconds have been observed in some situations [12]. The amount of multipath spreading is important in that its reciprocal is usually the coherence bandwidth of the channel, i.e., the maximum bandwidth that may be used without suffering selective fading.

The final listed effect is caused by the motion of the scattering particles. This motion imparts a Doppler frequency shift to the field scattered from each particle. Since different particles may have different velocities and since even for the same velocity they may introduce different Doppler shifts if their angles to the receiver differ, the bandwidth of the received field will spread in frequency. The reciprocal of this spread is a measure of the correlation time of the channel and is particularly important in that it is a measure of the time over which the channel characteristics do not change [4]. In a channel measuring system it is this time over which measurements would be made.

2. System Considerations

In this section we first briefly review the effect of scatter upon a system that is designed to utilize only the unscattered component of the field. Then the essential features of systems designed to operate through scattering channels are introduced. Finally the performance of such systems is discussed for a representative situation.

The discussion of performance is not intended to be the most general one possible. Rather, in the interests of simplicity, only simple on-off binary detection or communication will be considered. The results presented are, however, representative of more general ones.

To see why it is important for systems that operate through scattering channels to utilize the scattered component of the field, let us briefly examine the performance of systems that utilize only the unscattered field. Assuming that 1) the energy incident upon the aperture is not random, 2) state-of-the-art optical filters are employed, and 3) the system is not thermal noise limited, the error probability of such a system is given approximately by [13, 1]

$$P_e \simeq \exp - N_s E(\mu) \tag{1}$$

where N_s is the average number of photons detected when the on-signal is detected,

$$\mu = \frac{N_s}{N_n} \tag{2a}$$

where N_n is the average number of noise photons detected and

$$E(\mu) = \frac{(1 + \mu)\ln(1 + \mu) - \ln[(1 + \mu)\ln(1 + \mu)] - 1}{\ln(1 + \mu)} \tag{2b}$$

The function $E(\mu)$ measures the degrees to which the system performance is quantum limited or thermal limited. For μ much larger than one, $E(\mu)$ equals one and the system is quantum limited. For μ much less than one, $E(\mu)$ can be shown to approximately equal $\mu/8$ and the system is background limited. For our purposes $E(\mu)$ can be approximated by

$$E(\mu) \simeq \begin{cases} 1 & \mu >> 1 \\ \mu/8 & \mu << 1 \end{cases} \tag{3}$$

Now suppose that such a system is used with a scattering atmosphere. Since it responds only to the unscattered field N_s will drop markedly as the scattering increases. This alone will quickly cause the performance to become unacceptable; a process that is accelerated by the attendant decrease in μ. Moreover, although the details differ, the same conclusion applies when thermal noise dominates background noise. Thus as stated in Section 1, there is merit in attempting to utilize the information contained in the scattered component of the received field.

The extent to which such utilization is possible depends upon the energy contained in the scattered component of the received field and upon the way in which this energy is divided between the statistical degrees of freedom of the field. Most important, however, is the fact that the energy contained in the scattered component is sometimes substantially larger than that contained in the unscattered component. For it has been found repeatedly that the performance of a communication system is determined more by the total signal energy available to the receiver than by the degree of coherence of the

signal--provided that the signal is properly processed by the receiver.

The conceptual nature of the required signal processing depends upon the statistical structure of the received signal field and is relatively well understood [1-4]. For our present purposes it suffices to say that the receiver should separately detect each of the statistically independent components, or modes, of the received field and then combine the results in a manner akin to diversity combining.

The needed structure is illustrated in a somewhat abstract form in Fig. 3 for the situation in which the receiver has essentially no knowledge of the modal amplitudes and phases. Then, as shown, the energy in each of the modes should be separately detected; or in the language of diversity systems, incoherent combining should be employed.

Although instructive, and useful in determining system performance, the structure of Fig. 3 is not usually suited to direct implementation in a system. The difficulty is that it calls for the separate detection of each of the many statistically independent parts of the received signal prior to combining the results. Fortunately the operations of detection and diversity combining sometimes can be implemented approximately in a single distributed operation that is much simpler to implement.

One important example of such an implementation is provided by a direct detection receiver whose predetection spatial and temporal bandwidth and postdetection integration time are chosen to match the regions of time, space, frequency, and angle within which signal energy is expected to be found [1]. Such a receiver which is illustrated in Fig. 4b for on-off signaling, provides a useful approximation to the receiver that would be optimum in the absence of modal phase information.

At information rates less than the channel coherence bandwidth, the receiver of Fig. 4b will be affected by scattering only through the changes in the total collected signal and noise energies. Indeed, in the limit of severe multiple scattering (low photon coherences), the bound to the error probability, P_e, of the on-off system shown in Fig. 4b is identical in form to Eq(1) and (2). That is

$$P_e \simeq \exp - N_s E(\mu) \qquad (4a)$$

$$\mu = \frac{N_s}{N_n} \qquad (4b)$$

Here, however, N_s and N_n are the total average numbers of signal and noise photon collected by the receiver.

It is interesting to note that the loss of coherence through scatter does not cause the performance to suffer so long as the signal energy (N_s) and classical signal-to-noise ratio (μ) remain constant. Of course, in most situations, even if N_s can be kept relatively constant with increasing scatter by opening up the receiver's field of view, μ will decrease. That is the noise power collected by the receiver will increase as the signal energy becomes spread over a larger space-time-frequency-angle domain with decreasing visibility and increasing scatter. Hence, as scattering increases, the system will ultimately fall below the quantum threshold and its performance will become limited by other noise sources even if the average received signal energy remains fixed. When that occurs the performance will drop markedly below that of a comparable system operating in the absence of scattering.

This limitation can be overcome when knowledge of the complex modal amplitudes are available to the receiver [1, 13]. Then, coherent combining of the modal complex amplitudes, i.e., coherent diversity combining allows the receiver to limit the domain of the signal, and hence of the detected noise, to a single mode. In such situations that system is almost sure to be quantum limited, i.e. except for the possible consequences of N_s being random, the performance will be given by Eq. 4 with μ equal to infinity [1].

Realistically, of course, the complex modal amplitudes are not known a priori to the receiver. However, if they are varying slowly enough relative to the basic detection or estimation interval it may be practical to measure them i.e. it may be possible to track the channel. In more physical terms, the amplitude and phase of the field must be tracked within each coherence area contained within the receiving aperture.

Since the number of such areas may well exceed 10^6 in a strongly scattering channel, the implementation of a tracking receiver might seem to be an impossible task. However, it may well be possible if the needed measurements and mode combining are implemented by a distributed operation that does not require the separate detection of each complex modal amplitude. When the amplitude fluctuations over the aperture are much less severe than the phase fluctuations one can conceive of correcting for them with the system shown in Fig. 5.

The key element of the system is a "phase plate" whose local spatial phase delay can be adjusted so as to cancel the spatial phase variation in the received signal field. To the extent that amplitude variations in the received signal field can be neglected, the output of the plate is a spatially coherent field, e.g., a plane wave. The resulting

field can then be processed by a receiver which responds to a single spatial mode, that is, which has a diffraction limited field of view.

References

1. R. S. Kennedy, "Communications through Optical Scattering Channels: An Introduction," Proc. IEEE, Vol. 58, No. 10, October 1970, pp. 1651-1665.

2. R. Price, "Optimum Detection of Random Signals in Noise, with Application to Scatter-Multiplath Communication, I," IRE Trans. Inform. Theory, Vol. IT-2, December 1956, pp. 125-135.

3. R. Price and P. E. Green; Lincoln Laboratory, M.I.T., "Signal Processing in Radio Astronomy – Communication via Fluctuating Multipath Media," 1960, Tech. Report 234, DDC 246782

4. R. S. Kennedy, Fading Dispersive Communication Channels, New York: Wiley, 1969.

5. M. King and S. Kainer, "Some Parameters of a Laser-type Beyond-the-Horizon Communication Link," Proc. IEEE, Vol. 53, February 1965, pp. 137-141.

6. J. A. Curcio, "Propagation of Visible and Infrared Signals over the Horizon by Forward Scattering from Aerosols in the Lower Atmosphere," Electro-Optical Systems Design Conference, New York, September 16-18, 1969.

7. J. C. Eachus, et al., "An Experimental Optical Scatter Communication Link," CLEA, 1971.

8. E. S. Fishburne, M. E. Neer, and G. Sandri; A.R.A.P., "Voice Communication via Scattered Ultraviolet Radiation," February 1976, A.R.A.P Report No. 274, Vol. 1, U.S. Army Electronics Command, Ft. Monmouth, N.J.

9. G. C. Mooradian, V. J. Adrian, P. H. Levine, and W. R. Stone; Naval Electron. Lab. Ctr., "Extended Line-of-Sight Optical Communications Study," June 30, 1976, NELC Tech. Report 1988 (TR1988).

10. D. M. Reilly, "Atmospheric Optical Communications in the Middle Ultraviolet," M.S. Thesis, Dept. of Elec. Engr. & Comp. Sci, M.I.T., May 1976.

11. W. R. Ross; Research Laboratory of Electronics, M.I.T., "An Investigation of Atmospheric Optical Scattered Non-Line-of-Sight Communication Links," September 26, 1978, Final Report US ARO Contract DAAG29-77-C-0048.

12. E. A. Bucher and R. M. Lerner, "Experiments on Light Pulse Communication and Propagation through Atmospheric Clouds," Applied Optics, Vol. 12, October 1973, pp. 2401-2414.

13. E. A. Bucher, "Error Performance Bounds for Two Receivers for Optical Communication and Detection," Applied Optics, Vol. 11, April 1972, pp. 884-889.

Acknowledgement

EFFECTS of SCATTERING

Total Energy

Decreases   (but not exponentially)

Angular Spectrum
Broadens
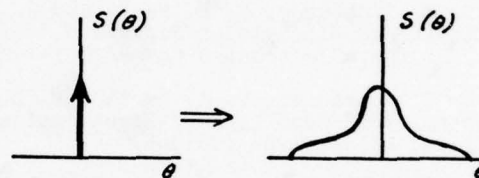
Spatial Correlation
Narrows
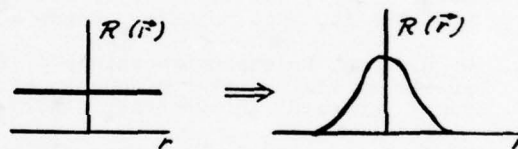
Impulse Response
Broadens
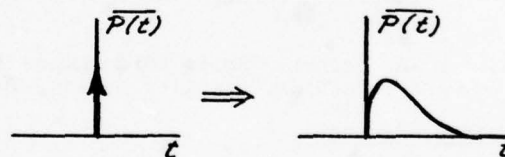
Temporal Spectrum
Broadens
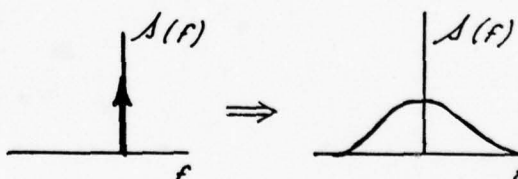
FIG 1:   MANIFESTATIONS OF SCATTERING IN THE APERTURE FIELD
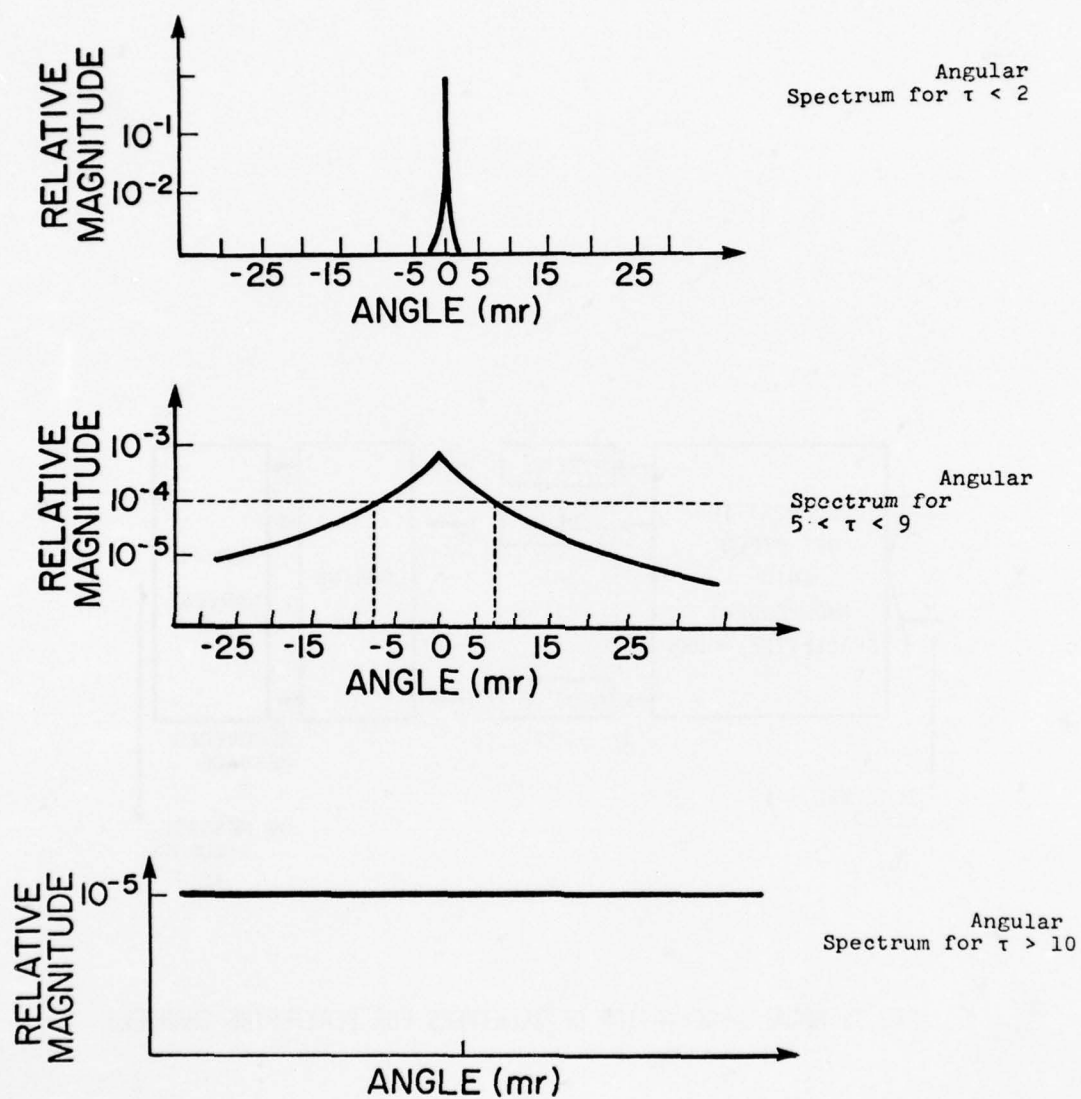
FIG 2: REPRESENTATIVE ANGULAR SPECTRA
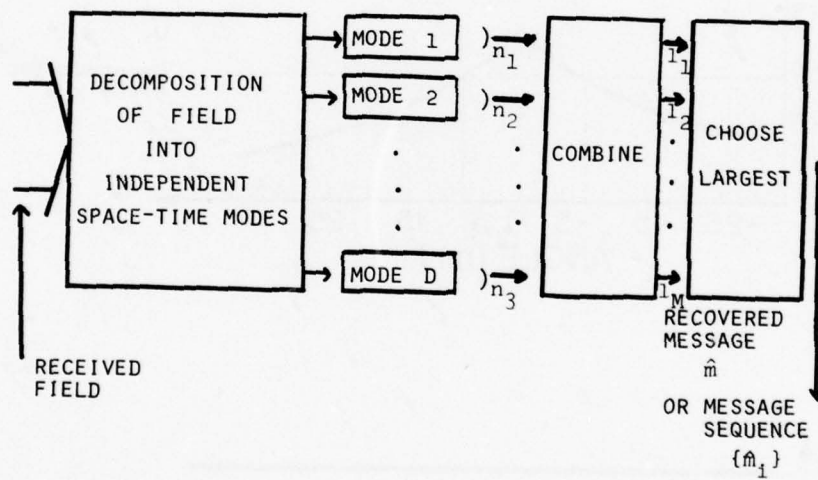
FIG 3: MODAL DESCRIPTION OF RECEIVERS FOR SCATTERING CHANNELS
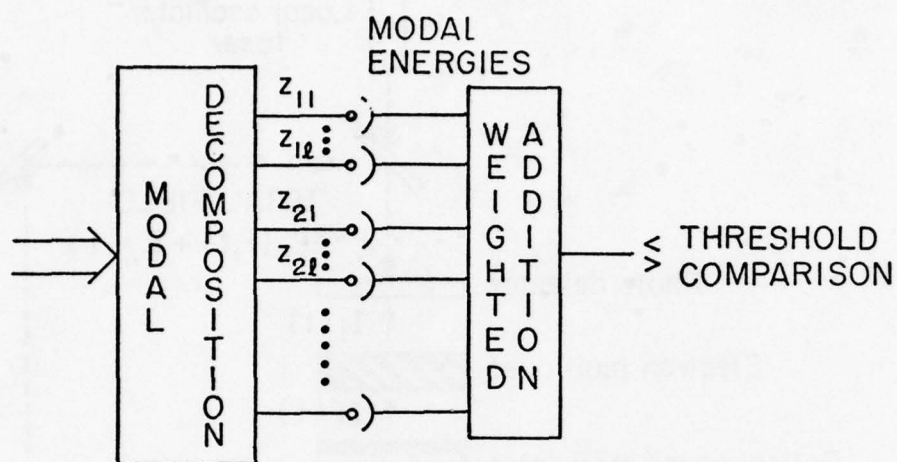
(a) GENERAL FUNCTIONAL FORM
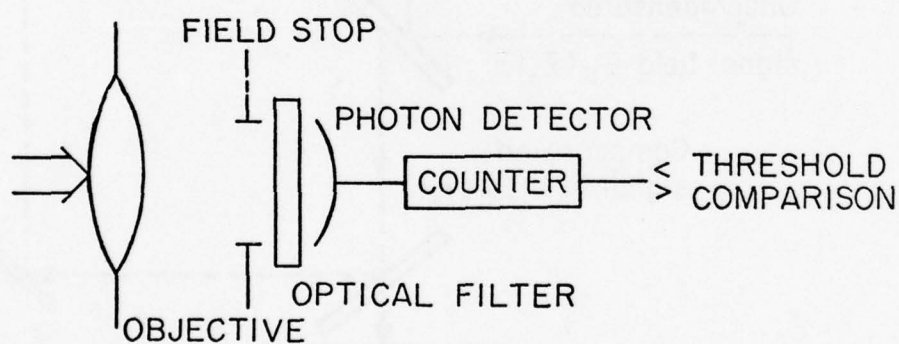
(b) IMPLEMENTATION OF OPTIMUM RECEIVER
FOR EQUAL MODAL AMPLITUDES:
PHOTON COUNTING RECEIVER

FIG 4: NEAR OPTIMUM RECEIVERS
FOR ON-OFF SIGNALING
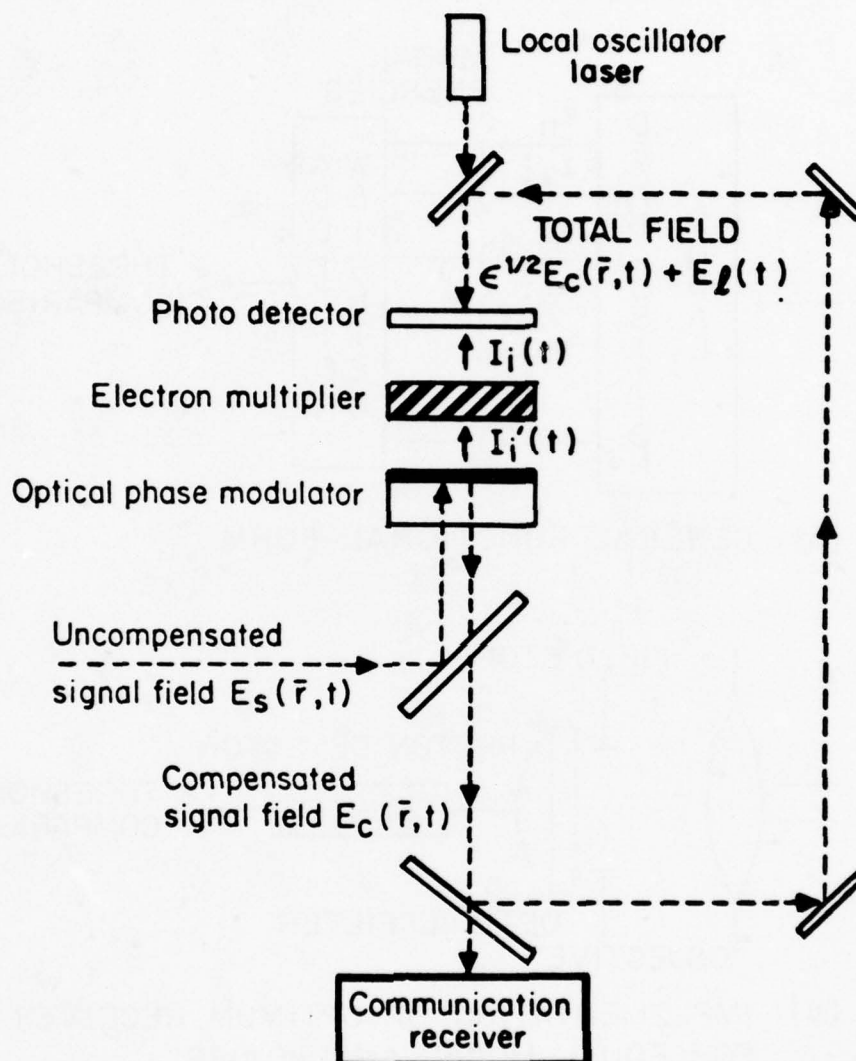
FIG 5: A PHASE SPATIAL COMPENSATING
RECEIVER (AFTER SHAPIRO AND WARDE)

GEOPHYSICAL DISTURBANCE EFFECTS ON THE STATE OF THE PROPAGATION MEDIUM AND THEIR PREDICTABILITY

E V Thrane
Norwegian Defence Research Establishment
P O Box 25 - N-2007 Kjeller, Norway

ABSTRACT

Different types of disturbances in the upper atmosphere can change its properties as a propagation medium for electromagnetic waves. The paper reviews the most important of these disturbances, and discusses the possibility of predicting, not their actual occurrence, but rather their effect on the atmosphere once they have occurred. The review is based upon current knowledge of ionospheric and upper atmosphere physics, and concentrates on effects of importance to radio wave propagation. Both natural phenomena, such as magnetic storms, and man-made disturbances are discussed.

1. INTRODUCTION AND OUTLINE

Different types of geophysical disturbances influence the state of the upper atmosphere and change its properties as a propagation medium for electromagnetic waves. This paper discusses the problem of predicting these changes. The prediction of the actual occurrence of a certain disturbance will not be dealt with here. I shall start by assuming that the occurrence of a disturbance with certain characteristics has been (correctly) predicted, and then discuss the possibilities we have at present for estimating the atmospheric changes, relevant to wave propagation, that will result. An exhaustive review of the effects of D-region ionization on radio wave propagation has recently been given by Larsen (1979).

A definition of a geophysical disturbance in the context of this paper is not straightforward, and will of necessity be somewhat arbitrary. The upper atmosphere has certain regular variations that repeat from day to day and from year to year. Superimposed on this regular pattern are changes that do not repeat themselves in a systematic manner. These irregular changes are, to the extent that they influence radio wave propagation, the disturbances that are of interest in this discussion. When the irregular changes are frequent and pronounced it may not be easy to establish a regular background pattern. Such is the case at high latitudes, particularly in the auroral zones, where strongly irregular behaviour of the medium is the rule, rather than an exception. Although it is difficult to give an exact definition of what we mean by a disturbance, certain types of major disturbances may usually be identified, and these are discussed in the following sections. Section 2 briefly describes the important types of disturbances and their effect on radio wave propagation. The remaining sections deal with these types of disturbance one by one, discussing their causes and the possibility of predicting their effects on propagation.

2. THE MOST IMPORTANT TYPES OF DISTURBANCE

There are many ways of classifying upper atmospheric, or ionospheric disturbances, none of them very satisfactory. Most, but not all disturbances of importance for radio wave propagation are part of the sequence of very complicated phenomena called a magnetic storm. Time does not permit a discussion of all aspects of magnetic storms, and I choose to list and discuss a few selected important types of disturbance, without any attempt at systematic classification according to cause. Table 1 gives this list.

TABLE 1   IONOSPHERIC DISTURBANCES (Rishbeth and Garriott, 1969)

Disturbance	Propagation effects	Time and duration	Possible cause
Sudden Ionospheric Disturbance (SID)	In sunlit hemisphere, strong absorption, anomalous VLF-reflection, F-region effects	All effects start approx simultaneously Duration $\sim\frac{1}{2}$ hour	Enhanced solar x-ray and EUV flux from from solar flare
Polar Cap Absorption (PCA)	Intense radiowave absorption in magnetic polar regions. Anomalous VLF-reflection	Starts a few hours after flare. Duration one to several days	Solar protons 1-100 MeV
Magnetic Storm	F-region effects; increase of foF2 during first day, then depressed foF2, with corresponding changes in MUF E-region effects, storm E_s D-region effects, enhanced absorption, VLF-anomalies	May last for days with strong daily variations	Interaction of solar low energy plasma with earth's magnetic field, causing energetic electron precipitation
Auroral Absorption (AA)	Enhanced absorption along auroral oval in areas hundred to thousand kilometers in extent. Sporadic E may give enhanced MUF	Complicated phenomena lasting from hours to days	Precipitation of electrons with energies a few tens of keV
Relativistic Electron Precipitation (REP)	Enhanced absorption VLF-anomalies at sub-auroral latitudes	Duration 1-2 hours	Precipitation of electrons with energies of a few hundred keV
Travelling Ionospheric Disturbances (TID)	Changes of foF2 with corresponding changes of MUF sometimes periodic	Typically a few hours	Atmospheric waves
Winter Anomaly (WA)	Enhanced absorption at midlatitudes	One to several days	Probably many causes, such as changes in concentration of minor species, temperature changes, particle precipitation
Stratospheric Warming	Changes in absorption, VLF-anomalies	Days or weeks, in late winter	Changes in global circulation pattern

We are interested in the propagation effects of the disturbances. Propagation is determined mainly by the spatial and temporal variations of the electron density in the ionosphere. For extremely low frequencies ions may also be important. Our primary concern is therefore to predict the changes in plasma density resulting from a disturbance. Once these changes are known, the propagation effects can normally be estimated with reasonable certainty.

3. SUDDEN IONOSPHERIC DISTURBANCES (SID's)

It is well established that SID's are associated with solar fluxes and are caused by enhanced X-ray and EUV emissions. Whereas the X-ray intensity may increase by orders of magnitude during such a flare, the EUV flux normally only increases by a few tens of per cents. The main propagation effects are produced in the lower ionosphere by radiation with wavelengths in the range 0.05 - 102.7 nm, and extend over the sunlit hemisphere. They are: HF-absorption, sudden frequency deviations (SFD) of HF-signals, sudden phase anomalies (SPA) of VLF-signals (See Figure 1). The capability of a flare to produce an SID depends upon the flux level as well as on spectral composition. Bain and Hammon (1975) find that SPA's are the most sensitive indicators of an SID, and report on the observed percentage of optical (Hα) flares of various classes associated with SPA's. The percentage increases from 12% for subflares to 100% for class 3 flares. Fluxes greater than $6\cdot10^{-7}$ $Jm^{-2}s^{-1}$ in the 0.05 - 0.3 nm band will always give an SPA. Detailed studies of SID effects by for example Rowe et. (1970), Montbriand and Belrose (1972) and Mitra and Deshpande (1972) have shown that the X-rays not only cause enhanced ion production, but that they also influence the ion chemistry and produce changes in the ionization loss rate. Figure 2 shows electron density profiles $N_e(h)$ measured during a flare of moderate strength (Montbriand and Belrose 1972). From satellite measurements of X-ray and EUV flux, the ion production profiles $q(h)$ may be determined, provided that the height variations of the density of the major neutral atmospheric constituents are known. Using a simple form of the continuity equation

$$\frac{dN_e}{dt} = q(h) - \psi(h)N_e^2(h) \tag{1}$$

the effective recombination rate $\psi(h)$ may be determined.

There are several problems involved in estimating the ionospheric effects of a flare. First, very accurate knowledge of the spectral composition is required to compute an accurate ion production profile. The usual satellite instrumentation, such as the Vela satellites, did not provide sufficient spectral resolution, particularly at the shortest wavelengths, and model spectra have had to be fitted to the observed X-ray intensities. New satellites have brought the evaluation of SID's to a turning point, however. The EUV and X-ray fluxes over the full wavelength region are now available with high time resolution and in near real time (Donnelly 1976).

Secondly, the ion production profile will be quite sensitive to the state of the neutral atmosphere, and accurate information on atmospheric density and composition is necessary.

Thirdly, accurate knowledge of the ion chemistry in the lower ionosphere is required to predict the changes in effective ionization loss rate during an SID. Figure 3 shows experimental evidence that the loss rate decreases during a flare, and that the decrease depends upon the strength of the flare. Thus the changes in loss rate will enhance the effects of an increase in ion production. Studies of the lower ionosphere by means of mass spectrometers have given us very detailed knowledge of the positive ion chemistry. In terms of this chemistry a decrease in loss rate between 70 and 85 km may be explained by a decrease in the concentration of hydrated cluster ions with large recombination rates, relative to the concentration of the molecular ions O_2^+ and NO^+ which recombine rapidly. The reaction chains leading to cluster ion formation are not completely mapped, however, and modelling is still bound to be uncertain. This is even more true for modelling of the negative ion formation, that is important below about 75 km. The effective loss rate derived during a moderately strong flare by Montbriand and Belrose (1972) shows a very large decrease relative to normal conditions near 70 km and below. This indicates that the negative ion population may have been depleted during the flarre, but no models of the negative ion chemistry have as yet been developed to explain such observations. We must conclude that the effects of an X-ray flare can only be described in gross terms at the lowest heights in the ionosphere.

In the absence of adequate D-region models, predictions may be based upon empirical relationships between X-ray spectral characteristics and SID parameters, such as phase height and field strength changes of reflected VLF- and LF waves, and increased absorption of HF waves. Desphande et al. (1972) have shown that the flare X-ray spectrum may be reasonably well described in terms of two parameters, available from satellite observations. These are the peak gray body flux in the wavelength band 0.1 - 0.8 nm, indicating the size of the event, and the ratio R_{12} of the peak gray body fluxes in the bands 0.05 - 0.3 nm and 0.1 - 0.8 nm, indicating the hardness of the spectrum. The two parameters and the solar zenith angle then specifies the peak ion production rate in the D-region. Figure 4 (Desphande 1978 private communication) shows an example of the empirical relationship between measured electron densities at selected heights and the peak gray body flux at 0.1 - 0.8 nm. The zenith angle is in the range 40° - 65° and R_{12} in a narrow range 0.03 - 0.04. In this case a clear simple relation emerges. The relation between the loss rate and the flare intensity is shown in Figure 3.

Such results indicate the possibility of predicting the SID effects of moderate and strong flares, given the X-ray spectrum and its temporal variation. However, there are still uncertain factors. For example the D-region effects of a flare depends to some extent upon preflare aeronomic conditions, and here our models are still inadequate to explain the observations. Furthermore, whereas the empirical approach has shown promise for VLF and HF effects, no clear patterns emerge for LF signals. This is presumably because LF waves are reflected in the upper D-region and the reflection coefficient depends critically upon the detailed structure of the ionization density profile at the reflection point. In any case, considering the complexity of the photochemistry of the lower ionosphere, further work to establish statistical empirical relations of SID parameters may be the most practical approach to SID predictions for some years to come.

4. POLAR CAP ABSORPTION EVENTS (PCA)

The energetic particle bombardement of the polar cap ionospheres during a PCA cause long-lasting and large changes of plasma density, particularly in the lower ionosphere. Severe disruptions of HF-communication as well as large errors in positioning by means of VLF-navigation systems result. The frequency of occurrence of PCA events varies from a few events per year during sunspot minimum conditions to one or more per month in sunspot maximum years (see Figure 5). A PCA covers the entire polar caps down to about 60° magnetic latitude and lasts for a few to several days per event. The intense ionization in the lower ionosphere is caused mainly by solar protons. Figure 6 (Reagan, 1977) shows the ion production profile for the August 1972 event, one of the strongest ever recorded. In the region below 80 km the ion production is enhanced by a factor of 10^3-10^4 relative to quiet daytime conditions. From a knowledge of the proton energy spectrum the ion production profile may be computed, but such events are also believed to have profound influence on the chemistry of the region, and therefore on the electron loss rate. Figure 7 (Reagan 1977) shows results of a neutral and ion chemistry analysis during the August 1972 event based on incoherent scatter measurements of ionization densities. Note the large decrease in electron loss rate near 80 km relative to quiet conditions and the increase near 60 km.

The effects on propagation of a PCA event of this magnitude are dramatic. Large absorption may completely wipe out ordinary HF communication, although the decrease in signal strength over a communication link is partly compensated for by a decrease in noise level. Absorption at riometer frequencies (~30 MHz) may be 10-20 dB above normal, corresponding to 100-200 dB at 10 MHz. An empirical relationship between proton flux and riometer 30 MHz absorption is quoted by Reid (1972)

$$J(>20 \text{ MeV}) = 60 \text{ A}^2 \qquad (2)$$

when J is the 2π omnidirectional flux in $cm^{-2}s^{-1}$ and A the absorption in desibels. Although it is derived for a particular event (February, 1965), (2) is nevertheless a useful approximate guide.

Although successful detailed modelling of the response of the lower ionosphere to solar proton events have been accomplished for a few selected cases (Reagan 1977, Swider et al. 1978), the models are not yet in general useful for prediction purposes. Empirical relations of the type quoted above are therefore valuable, and particularly at lower frequencies a number of studies have been carried out to establish the effects on propagation (Potemra et al. 1967, 1969, Egeland and Naustvik 1967, Åbom et al. 1969, Westerlund et al. 1969, Oelberman 1970, Field and Greifinger 1972).

In the lower frequency bands VLF (30-30 kHz) and LF (30-300 kHz) both phase and amplitude changes are observed on transpolar paths during PCA's (Westerlund et al. 1969). Amplitude changes, particularly for paths crossing the Greenland ice cap, seem to be erratic and difficult to predict, but the major systematic effect on all paths is a phase advance, corresponding to a lowering of the reflection height. VLF phase changes may be several cycles, and attenuation during the day may be greater than 30 dB. An example is shown in Figure 8 (Larsen 1977). Westerlund et al. (1969) have investigated the phase shift $\Delta\phi$ of VLF waves over transpolar paths as a function of the proton flux F. Theory predicts a linear relationship between the phase shift $\Delta\phi$ and ln (ln F). Figure 9 demonstrates that this assumption is reasonably accurate and also shows that the phase advance is significantly increased for paths across the Greenland icecap.

The phase shifts during PCA events are important for navigation systems such as Omega, and tests with a partially deployed Omega system show that errors in position fixes by as much as 10 km may occur (Swanson 1971). It should be noted that, due to the configuration of the earth's magnetic field, there is a marked longitudinal variation in the particle precipitation, the fluxes being greatest in the American sector.

Swanson (1974) has derived a probability distribution function of the phase perturbations induced at Omega frequencies (10.2 kHz) by solar proton events. Figure 10 shows the results for data averaged over a solar cycle, and compares these with SID data.

Figure 11 shows an example of the reflection height change for LF waves during a PCA (Larsen and Thrane 1977). These authors have studied the possible interference of Loran-C skywave and ground wave during PCA's. A drastic lowering of the reflection height may cause such interference, because the skywave arrives at the receiver at a point in time before the navigation information is extracted from the ground wave pulse.

5. MAGNETIC STORM EFFECTS IN THE F-REGION

Magnetic storms have a profound influence on the F-region, particularly at high latitudes. The critical frequency in the F2-layer may decrease significantly and the F-layer becomes thicker. The total electron content normally decreases. Figure 12 shows typical behaviour of N_mF_2 for strong and weak storms, for various latitudes (Matsushita 1959). F-region storm effects present many problems and are probably due to several different causes, such as heating causing thermal expansion of the atmosphere, storm induced composition changes, acceleration of the neutral atmosphere due to ion drag. Considerable progress has been made in recent years in understanding how energy is deposited in the ionosphere during a magnetic storm, and in particular how electric fields can influence composition, density and movement, both of ions and neutral atmospheric gases.

Models have been developed (Mayr and Hedin 1977, Roble 1977) to predict the effects on thermospheric circulation and composition of storm induced heating, and these show reasonable agreement with observations. Near the daytime F2-layer peak, observations during a storm show (Hedin et al. 1977; Prölss and von Zahn 1974, Chandra and Spencer 1976) that there is a close correlation between the electron density N_e and the ratio $[O]/[N_2]$. Examples are shown in Figures 13 and 14. The results fit with theoretical predictions that the ionosphere at these heights (≈200 km) is in photochemical equilibrium, the ion pro-

duction from atomic oxygen being balanced by charge transfer to molecular constituents. It is also clear from Hedin et al. (1977) that, at the same invariant latitude, the storm effects are different at different longitudes.

During storms it is well established that electric fields are a common feature of the high latitude ionosphere. Generally the magnitude of these fields are of the order 25-150 mV m^{-1}, but fields larger than 200 mV m^{-1} have been observed. It has been pointed out (Banks 1974) that such fields can significantly influence the ion composition and thereby the electron density in the E- and F-regions. Recently, Schunk et al. (1977) have estimated the effect of electric fields on the daytime high latitude ionosphere. Figure 15 shows that substantial decreases of E-region electron densities may occur. The effect is mainly due to the reactions $O^+ + N_2 \rightarrow NO^+ + N$ and $O_2^+ + O^2 \rightarrow O_2^+ + O$, the rates of which depend strongly on ion energy. The electric fields will increase these reaction rates through Joule heating and through the dependence of the reactions upon the relative speeds of ion and neutral gases. The ratio of atomic ion density to molecular ion density will decrease and electron loss rates increase as a consequence.

Much work remains to be done before an understanding of F-region storm effects, satisfactory from a prediction point of view, is reached. However, recent advances in theory and in observational evidence have uncovered several important mechanisms that seem to govern the state of the upper ionosphere during storms.

6. STORM EFFECTS IN THE LOWER IONOSPHERE

The magnetic storm effects in the lower ionosphere are caused by complex global patterns of energetic particle precipitation that cause enhanced ionization, as well as changes in loss rate and ion and neutral composition. Both increased radio wave absorption in the D-region and improved reflection properties from sporadic E-layers may result. We have already discussed PCA events caused by solar protons, arriving within hours of certain types of solar flares, and in this section we shall discuss the effects of electron precipitation. These depend strongly upon geomagnetic latitude, and also longitude, and may somewhat arbitrarily be divided into three classes; a) auroral absorption and E_S, b) mid-latitude afterstorm effects, and c) relativistic electron precipitation events.

6.1 Auroral Absorption

Auroral phenomena are often associated with radio blackouts. While the aurora itself is caused by soft electrons (1-10 keV), the enhanced absorption is caused by electrons with energies in excess of 10 keV penetrating into the D- and lower E-region. Although the general morphology of the auroral zone is well mapped on a statistical bases, the auroral structure is exceedingly complex, and anyone who has witnessed an auroral break-up will appreciate the difficulty in predicting its detailed behaviour. The auroral particle precipitation occurs in two zones as shown in the now classical Figure 16 by Hartz and Brice (1967), a diffuse zone with drizzle type precipitation and a zone with discrete, splash type precipitation. Figure 17 shows the occurrence pattern of auroral absorption (Hartz et al. 1963) expressed as the percentage of time the absorption exceeded 1 dB at 30 MHz. As will be seen the absorption has maximum occurrence rate along the auroral oval and shows a strong dependence on local geomagnetic time with greatest values in the morning hours, corresponding to the behaviour of the diffuse zone. In general auroral absorption at any one location will have time scales of hours and spatial extent of a few hundred kilometers. A great number of ionization density profiles have been measured during auroral events by rocket techniques. Figure 18 shows some examples with labels indicating the associated riometer absorption (Jespersen et al. 1968). The great variability in the profiles reflects the variability in time and space of the spectrum of precipitating particles. As discussed earlier (section 3) large ionization rates may also influence the ion chemistry in the lower ionosphere and change the ionization loss rates. These processes are not fully understood, which makes the prediction of the effect of a disturbance on radio wave propagation all the more difficult.

Radio communication may also be favoured in auroral conditions by formation of strongly reflecting E_S layers produced by soft particles not penetrating below 100 km. Figure 19 shows the percentage occurrence rates of E_S and illustrates that the time variation corresponds to the behaviour of the discrete auroral zone. This type of E_S ($fE_S > 7$ MHz) is thus most frequent at a time of day when absorption is least probable. A few examples will illustrate the effect of auroral zone disturbances upon propagation. Figure 20 (Veastad 1968) shows the occurrence rate of HF black-outs during a sunspot cycle for a path from North-Norway to Spitzbergen, and Figure 21 shows circuit behaviour during a particular disturbance from oblique incidence soundings (Folkestad 1968). The great variability is a striking feature of the latter figure.

Present standard prediction schemes are not well adapted to propagation conditions in polar regions. For example the CCIR "Bluedeck" does not include frequency and path length dependence of auroral absorption. Figure 22 shows an attempt at circuit evaluation and comparison with predictions for HF propagation over two paths in and to North-Norway. A digital signal was transmitted and the error rate counted. Less than 10% error rate was considered as acceptable. The test duration was 20 days during summer conditions, and the period included days with auroral absorption. Disturbed conditions were defined as periods with riometer absorption (30 MHz) greater than 0.2 dB. We note that for undisturbed conditions the agreement with predictions is reasonable, except for the lowest frequency, whereas there is a clear deterioration for disturbed conditions. Efforts are being made to improve predictions by including salient features of auroral absorption (P A Bradley private communication).

A large amount of work has been done to map auroral substorm behaviour, see for example Hargreaves 1969, Berkey et al. 1974. No method for reliable short term predictions has as yet been devised, but there are certain interesting possibilities. Hargreaves et al. (1974) have pointed out that an auroral absorption substorm is usually preceded by weak absorption observed first at high latitudes in the night sector and moving equatorwards. Such "precursors" may provide short time warning of the order of tens

of minutes of significant absorption events. Hargreaves (private communication) has also pointed out that absorption "spikes" often observed at the onset of an absorption event could be used for rapid detection and warning of propagation effects.

6.2 The mid-latitude storm after effect

It is well established that radio wave absorption at mid-latitudes may be enhanced a few days after the onset of a magnetic storm (Belrose and Thomas 1968). It also seems clear that one of the major causes is emergetic particle precipitation. Figure 23 shows an example of the morphology of precipitation of energetic electrons (>160 keV) measured in two polar orbiting satellites (Imhof et al. 1976). This storm after effect has also been studied in detail by Larsen et al. (1976) who used simultaneous observations of particle spectra in satellites and ground based observations of electron density to study the response of the lower ionosphere to the storm particles. Figure 24 shows the latitudinal variation of electron flux (>130 keV) before and after the storm, illustrating the enhanced precipitation down to lower latitudes after the storm. Figure 25 shows the corresponding values of electron loss rates at Ottawa. There is a strong variability in the height range 75-90 km, and no simple relation between the intensity of ion production and electron loss rate is evident from this study. One must conclude that even when a detailed particle spectrum is available and hence the ion production is known, the electron density profile and the radio propagation effects cannot yet be predicted with reasonable accuracy in the lower ionosphere. We obviously lack sufficient knowledge of the photochemistry of this region.

6.3 Relativistic electron precipitation events (REP)

Bailey and Pomerantz (1967) first noted a type of ionospheric disturbance affecting the very lowest part of the D-region causing radio wave absorption, enhanced VHF forward scatter and large phase changes of VLF waves. The disturbances are closely correlated with substorms. They occur at subauroral latitudes (L = 4.5-6) and are most frequent between 6 and 18 hours local time. Most events last from 1-6 hours, and the monthly number may be as large as 25. It is clear that the effects are caused by precipitation of relativistic electrons (Matthews and Simons 1973) with energies $\gtrsim$500 keV. Rosenberg et al. (1972) and Thorne and Larsen (1976) have studies such events. They conclude that substorm activity is a necessary condition for REP events, but that not all substorms lead to the intense precipitation causing REP's. Apparently the absolute intensity of the substorm is not a good indicator of whether or not a REP event will occur. An interesting feature is the absence of REP events in the early morning hours (local time) as observed in Alaska. Daytime events are often delayed by several hours relative to the onset of a substorm, whereas nighttime events are directly correlated with substorm activity. Thorne and Kennel (1971), Thorne (1974) suggest that REP events are triggered by ion cyclotron waves in the magnetosphere causing parasitic electron scattering. A definite test of this theory is still lacking, and the prediction of REP events and their effect on propagation can only be made on a statistical basis. Large absorption (>10 dB at 30 MHz) and large phase advances at VLF (for short paths 50-100 µs) are common features of REP events.

7. THE WINTER ANOMALY IN IONOSPHERIC ABSORPTION

At midile latitudes, 35-60°, ionospheric radio wave absorption in winter does not follow the simple solar zenith angle dependence to be expected from averaged summer observations. The general background of winter absorption is enhanced relative to summer values at the same zenith angles, and in addition days or groups of days occur in winter when HF-absorption is greatly enhanced and seriously affects radio communication. The consequenses for communication can be serious, since absorption values of 60 dB in excess of normal may occur on MF and HF circuits. The horisontal extent of a disturbance is of the order of 1000 km or more. The frequency of occurrence of such events increases with increasing latitude. No doubt this is partly due to the influence of particle precipitation, such as the storm after effects discussed earlier. However, it now seems clear that at least at the lower latitudes, the main winter anomaly effect is due to interactions of the ionosphere with the neutral atmosphere at and below ionospheric heights. This "meteorological type" of winter anomaly was recently studied during the "Wester Europe Winter Anomaly Campaign" conducted from Southern Spain during the winter 1975-76 (Offermann 1977). The enhanced absorption was due to increased electron densities in the height region 75-95 km. These enhanced electron densities were, however, not caused by increased ionizing radiation, in the form of solar electromagnetic radiation or energetic particles, but appeared to be due to at least three different factors (Thrane et al. 1978):

a) Enhanced density of mesospheric nitric oxide NO causing increased ionization by solar H-Lyman-α radiation.

b) Decreased electron loss rate in the range, 75-85 km. This decrease coincided with a depletion of heavy positive water cluster ions with large recombination rates.

c) Enhanced density of mesospheric excited molecular oxygen O_2 ($^1\Delta_g$) causing increased ionization by solar UV radiation.

The period of enhanced absorption in January 1976 was associated with wavelike structures giving marked deviation of the atmosphere from the reference atmosphere (CIRA 1972). Figure 26 shows the noon A3 absorption and Figure 27 shows rocket measurements of atmospheric temperature clearly demonstrating a temperature wave distorting the normal stratospheric- and mesospheric temperature profile (Offermann 1977, Becker et al. 1978). The disturbance could be traced all the way to the ground. The new results promise better understanding of ionosphere-atmosphere coupling and show the way towards possible prediction of such events. A further indication of the possible role of transport processes was given by Geller et al. (1976 who showed a connection between D-region electron densities at Urbana, Illinois and meteor radar drift observations. Drifts from the north was correlated with enhancements of electron density. Such observations could be explained by southward transport of nitric oxide produced by particle precipitation in the auroral zone.

1.0

1.1

1.25   1.4   1.6

18

16

20

22
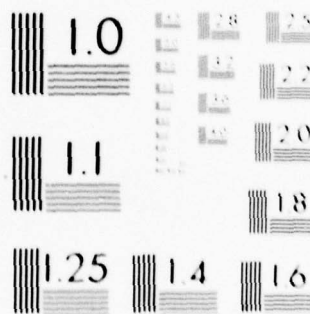
23

MICROCOPY RESOLUTION TEST CHART
NATIONAL BUREAU OF STANDARDS-1963-A

of minutes of significant absorption events. Hargreaves (private communication) has also pointed out that absorption "spikes" often observed at the onset of an absorption event could be used for rapid detection and warning of propagation effects.

6.2 The mid-latitude storm after effect

It is well established that radio wave absorption at mid-latitudes may be enhanced a few days after the onset of a magnetic storm (Belrose and Thomas 1968). It also seems clear that one of the major causes is emergetic particle precipitation. Figure 23 shows an example of the morphology of precipitation of energetic electrons (>160 keV) measured in two polar orbiting satellites (Imhof et al. 1976). This storm after effect has also been studied in detail by Larsen et al. (1976) who used simultaneous observations of particle spectra in satellites and ground based observations of electron density to study the response of the lower ionosphere to the storm particles. Figure 24 shows the latitudinal variation of electron flux (>130 keV) before and after the storm, illustrating the enhanced precipitation down to lower latitudes after the storm. Figure 25 shows the corresponding values of electron loss rates at Ottawa. There is a strong variability in the height range 75-90 km, and no simple relation between the intensity of ion production and electron loss rate is evident from this study. One must conclude that even when a detailed particle spectrum is available and hence the ion production is known, the electron density profile and the radio propagation effects cannot yet be predicted with reasonable accuracy in the lower ionosphere. We obviously lack sufficient knowledge of the photochemistry of this region.

6.3 Relativistic electron precipitation events (REP)

Bailey and Pomerantz (1967) first noted a type of ionospheric disturbance affecting the very lowest part of the D-region causing radio wave absorption, enhanced VHF forward scatter and large phase changes of VLF waves. The disturbances are closely correlated with substorms. They occur at subauroral latitudes (L = 4.5-6) and are most frequent between 6 and 18 hours local time. Most events last from 1-6 hours, and the monthly number may be as large as 25. It is clear that the effects are caused by precipitation of relativistic electrons (Matthews and Simons 1973) with energies ≳500 keV. Rosenberg et al. (1972) and Thorne and Larsen (1976) have studies such events. They conclude that substorm activity is a necessary condition for REP events, but that not all substorms lead to the intense precipitation causing REP's. Apparently the absolute intensity of the substorm is not a good indicator of whether or not a REP event will occur. An interesting feature is the absence of REP events in the early morning hours (local time) as observed in Alaska. Daytime events are often delayed by several hours relative to the onset of a substorm, whereas nighttime events are directly correlated with substorm activity. Thorne and Kennel (1971), Thorne (1974) suggest that REP events are triggered by ion cyclotron waves in the magnetosphere causing parasitic electron scattering. A definite test of this theory is still lacking, and the prediction of REP events and their effect on propagation can only be made on a statistical basis. Large absorption (>10 dB at 30 MHz) and large phase advances at VLF (for short paths 50-100 µs) are common features of REP events.

7. THE WINTER ANOMALY IN IONOSPHERIC ABSORPTION

At middle latitudes, 35-60°, ionospheric radio wave absorption in winter does not follow the simple solar zenith angle dependence to be expected from averaged summer observations. The general background of winter absorption is enhanced relative to summer values at the same zenith angles, and in addition days or groups of days occur in winter when HF-absorption is greatly enhanced and seriously affects radio communication. The consequenses for communication can be serious, since absorption values of 60 dB in excess of normal may occur on MF and HF circuits. The horisontal extent of a disturbance is of the order of 1000 km or more. The frequency of occurrence of such events increases with increasing latitude. No doubt this is partly due to the influence of particle precipitation, such as the storm after effects discussed earlier. However, it now seems clear that at least at the lower latitudes, the main winter anomaly effect is due to interactions of the ionosphere with the neutral atmosphere at and below ionospheric heights. This "meteorological type" of winter anomaly was recently studied during the "Wester Europe Winter Anomaly Campaign" conducted from Southern Spain during the winter 1975-76 (Offermann 1977). The enhanced absorption was due to increased electron densities in the height region 75-95 km. These enhanced electron densities were, however, not caused by increased ionizing radiation, in the form of solar electromagnetic radiation or energetic particles, but appeared to be due to at least three different factors (Thrane et al. 1978):

a) Enhanced density of mesospheric nitric oxide NO causing increased ionization by solar H-Lyman-α radiation.

b) Decreased electron loss rate in the range, 75-85 km. This decrease coincided with a depletion of heavy positive water cluster ions with large recombination rates.

c) Enhanced density of mesospheric excited molecular oxygen O_2 $(^1\Delta_g)$ causing increased ionization by solar UV radiation.

The period of enhanced absorption in January 1976 was associated with wavelike structures giving marked deviation of the atmosphere from the reference atmosphere (CIRA 1972). Figure 26 shows the noon A3 absorption and Figure 27 shows rocket measurements of atmospheric temperature clearly demonstrating a temperature wave distorting the normal stratospheric- and mesospheric temperature profile (Offermann 1977, Becker et al. 1978). The disturbance could be traced all the way to the ground. The new results promise better understanding of ionosphere-atmosphere coupling and show the way towards possible prediction of such events. A further indication of the possible role of transport processes was given by Geller et al. (1976 who showed a connection between D-region electron densities at Urbana, Illinois and meteor radar drift observations. Drifts from the north was correlated with enhancements of electron density. Such observations could be explained by southward transport of nitric oxide produced by particle precipitation in the auroral zone.

8. STRATOSPHERIC WARMINGS

The coupling between the ionosphere and stratosphere was first clearly demonstrated in studies of the correlation between ionospheric absorption and stratospheric warmings (Shapley and Beynon 1965) who showed that ionospheric absorption increased a few days after a temperature increase in the stratosphere. Stratospheric-mesospheric midwinter warmings are synoptic scale events associated with a reversal or "breakdown" of the polar circulation at altitudes at least as low as 30 km (Labitzke 1977). A major warming may result in temperature increases in the upper stratosphere and lower thermosphere of more that 50 K. The events occur in late winter and last for days or weeks. They are apparently forced from the troposphere, but no complete explanation has been given.

In view of the recent results from studies of the winter anomaly it seems clear that changes in the state of the neutral atmosphere, such as changes in composition and temperature, can influence ionospheric parameters. A better understanding of the coupling mechanisms may lead to reliable synoptic prediction of the lower ionosphere based partly on the meteorological situation at lower levels.

9. TRAVELLING IONOSPHERIC DISTURBANCES (TID)

Radio communications are sometimes disrupted by moving ionospheric irregularities that may alter the characteristics of the wave (phase, amplitude, polarization, direction of propagation) on time scales ranging from seconds to hours. Extensive studies have been made to identify the sources and map the behaviour of such travelling disturbances. A review of the results has been given by Georges (1967). He identifies three distinct types of travelling disturbances:

a) Very large disturbances retaining a wavelike structure over large distances. An example is shown in Figure 28. Such disturbances are closely correlated with magnetic storms, an almost one-to-one correspondence is observed between this kind of disturbance and storms with Kp indices greater than 5. The source is believed to be joule heating by the auroral electrojet. Typical speeds are >300 m/s and typical periods 30 minutes to more than one hour.

b) A second type of TID is the "medium scale" events which travel at speeds less than the speed of sound and have periods from 10 to 40 minutes. These TID's do not retain their shapes over a more than 100 km and are not well correlated with known geophysical phenomena. They have the characteristics of internal atmospheric waves and may originate in the lower atmosphere.

c) A third type of disturbance seems to be directly associated with severe weather systems such as large thunderstorms, and show oscillations of the order of 3 minutes.

Prediction for communication purposes of TID's would seem difficult until their behaviour is better understood. A possible exception are the very large disturbances that are clearly correlated with severe magnetic activity.

10. MAN-INDUCED IONOSPHERIC DISTURBANCES

Man may, inadvertently or on purpose, alter the state of the upper atmosphere and produce disturbances of importance for radio propagation. Such disturbances fall into three different categories.

a) Changes induced by heating the ionosphere from the ground by powerful radio waves.

b) Release of chemically active substances in the atmosphere that alter the composition and photochemical properties of the medium.

c) Nuclear detonations releasing ionizing radiation and producing shock waves that significantly change the state of the upper atmosphere.

Effects of all three kinds of disturbance have been observed and are now reasonably well understood. The first category includes the classical cross modulation, or Luxembourg effect, and the creation of irregularities or spread F conditions. Since appreciable power is needed for the "heating" transmitter, the affected areas have limited geographical extent, of the order of 100 km in the F-region (Bailey and Martyn 1937, Utlaut and Cohen 1971).

Releases of chemically active substances also have transient and limited effects unless very large amounts of material are released. For example an ionospheric effect was observed after the release of water into the ionosphere during the launch of Skylab (Mendillo et al. 1975). There is, however, the possibility that man's activity over longer periods may change the state of the upper atmosphere through releases of long lived species that are transported from the lower atmosphere to greater heights.

Undoubtedly nuclear explosions in the upper atmosphere have produced the strongest and most extensive changes in the propagation medium. Radiation from a nuclear charge has produced ionospheric effects such as black-outs, phase deviations and TID's over areas many thousands of kilometers in extent. With present day knowledge of the atmospheric response to radiation, effects of a known type of nuclear weapon discharged at a known height should be predictable with reasonable accuracy.

11. CONCLUSIONS

Geophysical disturbance effects in the upper atmosphere present a very complex and sometimes bewildering picture to the scientist as well as the user. Predictions of conditions relevant to radio communications have been greatly improved in recent years as far as short time forecasts of certain kinds of disturbances are concerned. However, our knowledge of the propagation medium is far from complete, and predictions of the response of the medium to an imposed stimuli such as particle precipitation, increased temperature etc are as yet bound to be uncertain and qualitative in nature. A picture is nevertheless emerging of the main physical mechanisms triggered by the disturbance sources, and the extensive efforts made in the field should result in usable prediction schemes in the future.

REFERENCES

Bailey, V.A. and D.F. Martyn (1934). Phil. Mag. $\underline{18}$, pp. 369.

Bailey, D.K. and M.A. Pomerantz (1965). Relativistic electron precipitation into the mesosphere at subauroral latitudes. J. Geophys. Res. $\underline{70}$, pp. 5823.

Bain, W.C. and E. Hammond (1975). Ionospheric solar flare effect observations. J. Atm. Terr. Phys. $\underline{37}$, pp. 573-574.

Banks, P.M., R.W. Schunk and W.J. Raitt (1974). NO^+ and O^+ in the high latitude F-region. Geophys. Res. Lett. $\underline{1}$, pp. 239-242.

Becker, M., J. Bäte, V.H. Friedrich, A. Loidl, D. Offermann, D.G. Papanikas, H.Schwentek and E.V. Thrane. Density and temperature profiles measured in the mesosphere and lower thermosphere during winter anomaly conditions. J. Atmos. Terr. Phys, to be published.

Belrose, J.S. and L. Thomas (1968). Ionization changes in the middle latitude D-region associated with geomagnetic storms. J. Atmos. Terr. Phys. $\underline{30}$, pp. 1397-1413.

Berkey, F.T., V.M. Driatskiy, K. Henriksen, B. Hultqvist, D.H. Jelly, T.I. Shuhuka, A. Theander and J. Ylimiemi (1974). A synoptic investigation of particle precipitation dynamics for 60 substorms in IQSY (1964-65) and IASY (1969). Planet. Space Sci. $\underline{22}$, pp. 255.

Chandra, S. and N.W. Spencer (1976). Thermosphere storms and related ionospheric effects. J. Geophys. Res. $\underline{81}$, pp. 5018-5026.

Deshpande, S.D. and A.P. Mitra (1972). Ionospheric effects of solar flares-III. The quantitative relationship of flare X-rays to SID's. J. Atmos. Terr. Phys. $\underline{34}$, pp. 243-253.

Desphande, S.D., S. Granguly, V.C. Jain and A.P. Mitra (1972). Ionospheric effects of solar flares V. The flare event of 30 January 1968 and its implications. J. Atmos. Terr. Phys. $\underline{34}$, pp. 267.

Donnelly, R.F. (1976). Solar flare X-ray and EUV emission; A terrestrial viewpoint. In: Physics of solar planetary environments. Proceedings of the International Symposium on Solar-Terrestrial Physics. Ed. D.J. Williams. American Geophysical Union, pp. 178-192.

Egeland, A. and E. Naustvik (1967). Influence of high-latitude disturbances on VLF propagation. Radio Science $\underline{2}$ (new series), pp. 659.

Field, E.C., C. Greifinger and K. Schwartz (1972). Transpolar propagation of long radio waves. J. Geophys. Res. $\underline{77}$, pp. 1264.

Folkestad, K. (1968a). Results from stepped frequency oblique soundings at high latitudes. In: Ionospheric Radio Communications, edited by K. Folkestad, Plenum Press, New York, pp. 279.

Geller, M.A., G.C. Hess and D. Wratt (1976). Simultaneous partial reflection and meteor radar wind observations at Urbana, Illinois, during the winter of 1974-1975. J. Atm. Terr. Phys. $\underline{38}$, pp. 287-290.

Georges, T.M. (1967). Ionospheric effects of atmospheric waves. ESSA Technical Report IER 57-ITSA 54, Boulder, Colorado.

Hargreaves, J.K. (1969). Auroral absorption of HF radio waves in the ionosphere: A review of results from the first decade of riometry. Proc. IEEE $\underline{57}$, pp. 1348.

Hargreaves, J.K., H.J.A. Chivers and W.I. Axford (1974). The development of the substorm in auroral radio absorption. J. Atmos. Terr. Phys. $\underline{23}$, pp. 905.

Hartz, T.R. (1968). The general pattern of auroral particle precipitation and its implications for high latitude communication systems. In: Ionospheric radio communications. Ed. K. Folkestad. Plenum Press, New York, pp. 9-32.

Hartz, T.R. and N.M. Brice (1967). Planet. Space Sci. $\underline{15}$, pp. 301.

Hartz, T.R., L.E. Montbriand and E.L. Vogan (1963). Canad. J. Phys. $\underline{41}$, pp. 581.

Hedin, A.E., P. Bauer, H.G. Mayr, G.R. Carignan, L.H. Brace, H.C. Brinton, A.D. Parks and D.T. Pelz (1977). Observations of neutral composition and related ionospheric variations during a magnetic storm in February 1974. J. Geophys. Res. $\underline{82}$, pp.3183-3189.

Imhof, W.L., T.R. Larsen, J.B. Reagan and E.E. Gaines (1977). Analysis of satellite data on precipitating particles in coordination with HLF propagation anomalies, LMSC-D560323, Lockheed Palo Alto Research Laboratory, Palo Alto, Ca., USA.

Jespersen, M. and B. Landmark (1968). Electron density observations during auroral absorption related to radio wave communication problems. In: Ionospheric Radio Communications. Ed. K. Folkestad, Plenum Press, New York, pp. 73-80.

Labtizke, K. (1977). Stratospheric-mesospheric mid-winter warmings. In: Dynamical and Chemical Coupling of Neutral and Ionized Atmosphere. Ed. B. Grandal and J.A. Holtet. Reidel Publ. Co., Dordrecht/Holland, pp. 17-34.

Larsen, T.R., J.B. Reagan, W.L. Imhof, L.E. Montbriand and J.S. Belrose (1976). A coordinated study of electron concentrations over Ottawa during disturbed conditions. J. Geophys. Res. 81, pp. 2200-2213.

Larsen, T.R. (1977). Omega accuracy in polar regions during ionospheric disturbances. In: AGARD Conf. Proc on "Propagation Limitations of Navigation and Posioning Systems", AGARD-CP-209, NATO-AGARD.

Larsen, T.R. (1979). Effects of D-region ionization on radio wave propagation. International Workshop on Solar-Terrestrial Predictions. Preprint 125 SEL, NOAA Boulder.

Larsen, T.R. and E.V. Thrane (1977). Ionospheric effects on Loran-C in polar regions. In: AGARD Conf. Proc. on "Propagation Limitations of Navigation and Positioning Systems", AGARD-AGARD.

Mathews, D.L. and D.J. Simons (1973). Observations of relativistic electron precipitation at L = 6. J. Geophys. Res. 78, pp. 7539-7542.

Matsushita, S. (1959). A study of the morphology of ionospheric storms. J. Geophys. Res. 64, pp. 305-321.

Mayr, H.G. and A.E. Hedin (1977). Significance of large-scale circulation in magnetic storm characteristics with application to AE-C neutral composition data. J. Geophys. Res. 82, pp. 1227-1234.

Mendillo, M., G.S. Hawkins and J.A. Klobuchar (1975). A sudden vanishing of the ionospheric F-region due to the launch of Skylab. J. Geophys. Res. 80, pp. 2217-2228.

Monthbriand, L.C. and J.S. Belrose (1972). Effective electron loss rates in the lower D-region during the decay of solar X-ray flare events. Radio Sci. 7, pp. 133-142.

Oelbermann, Jr, E.J. (1970). Solar particle effects on polar cap VLF propagation. J. Franklin Inst. 290, 281.

Offermann, D (1977). Some results from the European Winter Anomaly Campaign 1975-76. In: Dynamical and Chemical Coupling of Neutral and Ionized Atmosphere. Ed. B. Grandal and J.A. Holtet. Reidel Publ. Co., Dordrecth/Holland, pp. 235-252.

Potemra, T.A., A.J. Zmuda, C.R. Haave and B.W. Shaw (1967). VLF phase perturbations produced by solar protons in the event of February 5, 1965. J. Geophys. Res. 72, pp. 6077.

Potemra, T.A., A.J. Zmuda, C.R. Haave and B.W. Shaw (1969). VLF phase disturbances, HF absorption and solar protons in the events of August 28 and September 2, 1966. J. Geophys. Res. (Space Physics) 74, pp. 6444.

Prölss, G.W. and U. von Zahn (1974). ESRO 4 gas analyser results, 2. Direct measurements of changes in neutral composition during an ionospheric storm. J. Geophys. Res. 79, pp. 2535-2539.

Reagan, J.B. (1977). Ionization processes. In: Dynamical and Chemical Coupling of Neutral and Ionized Atmosphere. Ed. B. Grandal and J.A. Holtet. Reidel Publ. Co., Dordrecht/Holland, pp. 145-160.

Reid, G.C. (1972). A review of ionospheric radio propagation effects associated with solar proton events. In: Proceedings of COSPAR Symposium on Solar Particle Event of November 1969. Ed. James C. Ulwick. AFCRL-72-0474, pp. 201.

Risbeth, H. and O.K. Garriott (1969). Introduction to ionospheric physics. International Geophysics Series Volume 14, Academic Press.

Roble, R.G. (1977). Variations of the mean meridional circulation in the thermosphere. In: Dynamical and Chemical Coupling of Neutral and Ionized Atmosphere. Ed. B. Grandal and J.A. Holtet. Reidel Publ. Co., Dordrecht/Holland, pp. 217-234.

Rosenberg, T.J., L.J. Lanzerotti, D.K. Bailey and J.D. Pierson (1972). Energy spectra in relativistic electron precipitation events. J. Atmos. Terr. Phys. 34, pp. 1977.

Rowe, J.N., A.J. Ferraro, H.S. Lee, R.W. Kreplin and A.P. Mitra (1970). Observations of electron density during a solar flare. J. Atmos. Terr. Phys. 32, pp. 1609-1614.

Schunk, R.W., W.J. Ratts and P.M. Banks (1975). Effect of electric fields on the daytime high-latitude E and F-regions. J. Geophys. Res. 80, pp. 3121-3130.

Shapley, A.H. and W.J.G. Beynon (1965). Winter anomaly in ionospheric absorption and stratospheric warmings. Nature 206, pp. 1242.

Swanson, E. (1971). J. Inst. Navigation 18, pp. 168-175.

Swanson, E.R. (1974). Blunders caused by Omega propagation: SPA's and PCA's. Proc. 2nd Omega Symposium, 5-7 November 1974, Wash. D.C., pp. 202.

Swider, W., T.J. Keneshea and C.I. Foley (1978). An SPE-disturbed D-region model. Planet Space Sci. 26, pp. 883.

Thorne, R.M. (1974). A possible cause for dayside relativistic electron precipitation events. J. Atmos. Terr. Phys. 36, pp. 635.

Thorne, R.M. and C.F. Kennel (1971). Relativistic electron precipitation during magnetic storm main phase. J Geophys. Res. 76, pp. 4446.

Thorne, R.M. and T.R. Larsen (1976). An investigation of relativistic electron precipitation events and their association with magnetospheric substorm activity. J. Geophys. Res. 81, pp. 5501-5506.

Thrane, E.V., W. Bangert, D. Beran, M, Friedrich, B. Grandal, O. Hagen, A. Loidl, K. Spenner, H. Schwentek, K.M. Torkar and F. Ugletveit. Ion production and effective loss rate in the mesosphere and lower thermosphere during the Western Europe Winter Anomaly Campaign 1975-76. J. Atmos. Terr. Phys, to be published.

Utlaut, W.F. and R. Cohen (1971). Modifying the ionosphere with intense radio waves. Science 174, pp. 245-254.

Veastad, J.R. (1968). Survey of the user problems and existing communication facilities in the Norwegian Arctic. In: Ionospheric Radio Communications, edited by K. Folkestad, Plenum Press, New York, pp. 422.

Westerlund, S., F.H. Reder and C. Abom (1969). Effects of polar cap absorption events on VLF transmissions. Planet. Space Sci. 17, pp.1329.

Åbom, C., F.H. Reder and S. Westerlund (1969). Effects of polar cap absorption events on VLF transmissions. Planet. Space Sci. 17, pp. 1329.

Swanson, E. (1971). J. Inst. Navigation 18, pp. 168-175.

Swanson, E.R. (1974). Blunders caused by Omega propagation: SPA's and PCA's. Proc. 2nd Omega Symposium, 5-7 November 1974, Wash. D.C., pp. 202.
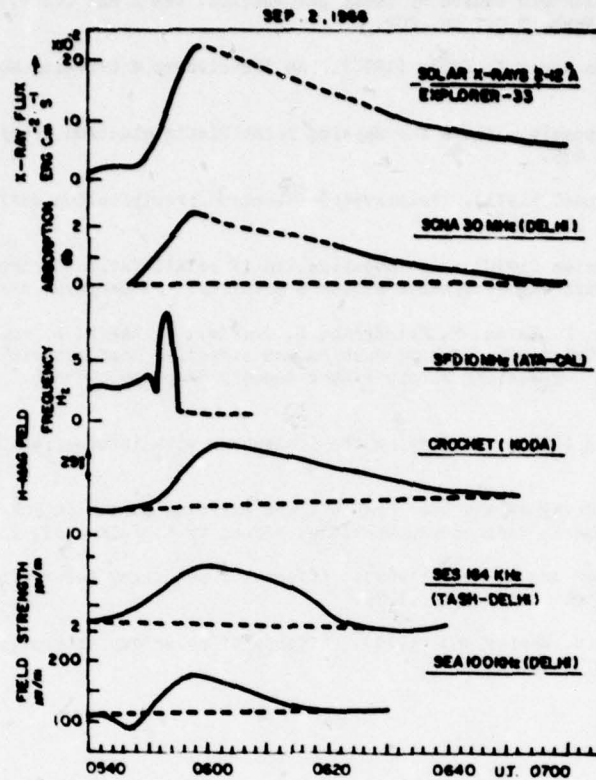
Figure 1   Time variation of X-ray flux and various SID's for a flare on Sept 2 1960
            (Desphande and Mitra 1972)
            SCNA   Sudden cosmic noise anomaly
            SFD   Sudden frequency deviation
            Crochet   Magnetic disturbance
            SES and SEA   Field strength changes of LF waves
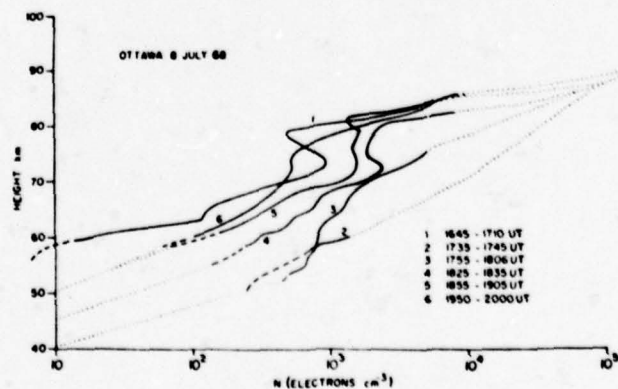
Figure 2   Electron density versus height profiles for a large flare on July 8 1969
            (Montbriand and Belrose 1972).
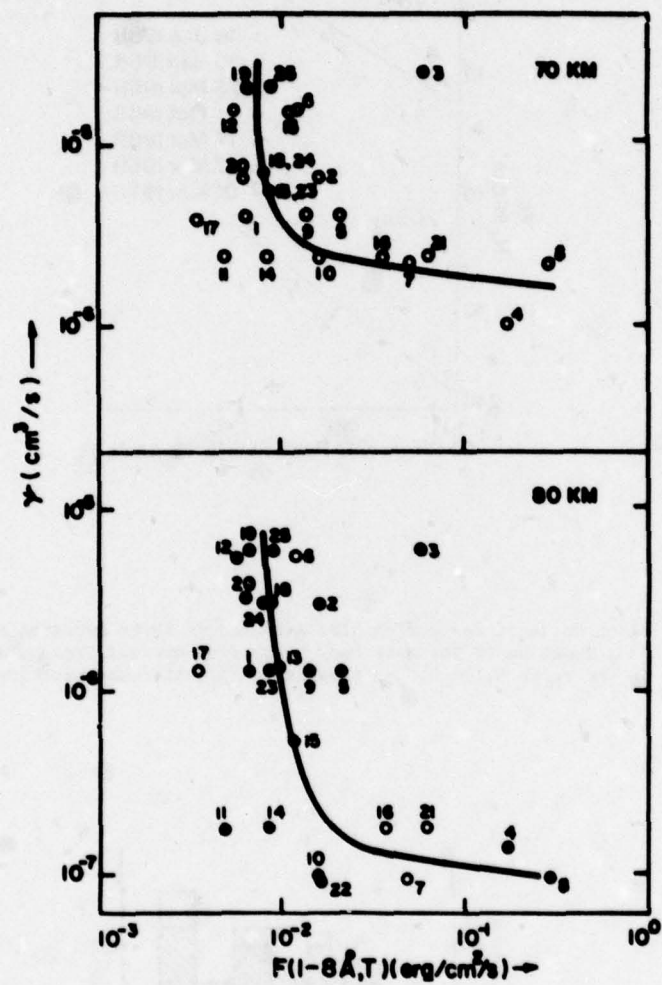
Figure 3   Effective recombination coefficient versus real flux in 0-8 A band for
flare - SCNA events for 80 and 70 km heights
(Desphande and Mitra 1972).
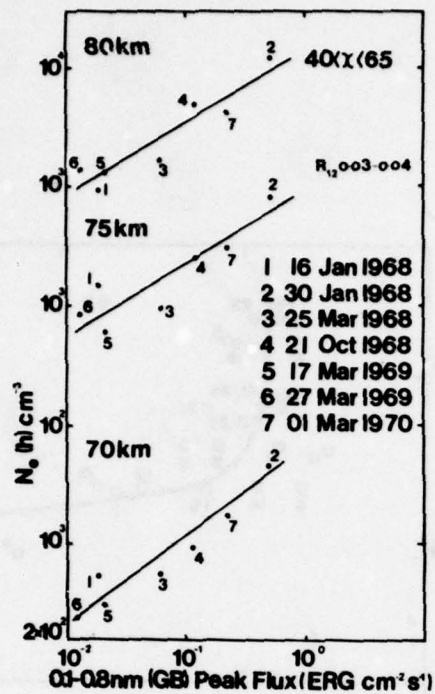
Figure 4   Electron densities during SIDs measured at three D-region heights and plotted as a function of the gray body X-ray flux derived from satellite measurements in the range 0.1 - 0.8 nm (Desphande, private communication).
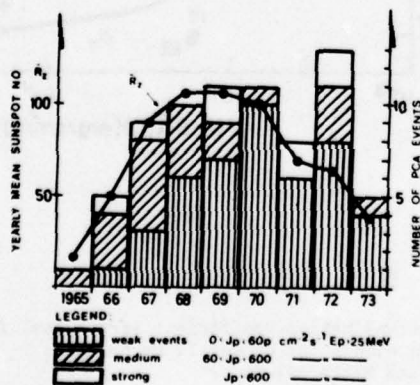
Figure 5   The occurrence rate of PCA during a sunspot maximum period. The sunspot number R_z is also shown (Westerlund, private communication).
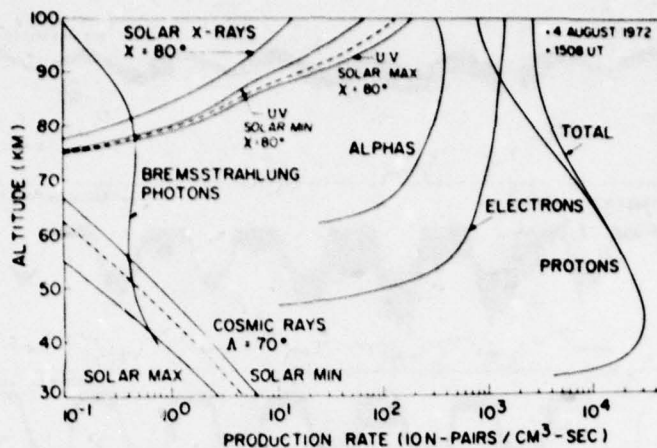
Figure 6   The contribution of the various solar particle, solar radiations, bremsstrahlung and cosmic rays to the total ion-par production in the August 1972 solar particle event (Reagan 1977).

a. 80 km   b. 70 km   c. 60 km
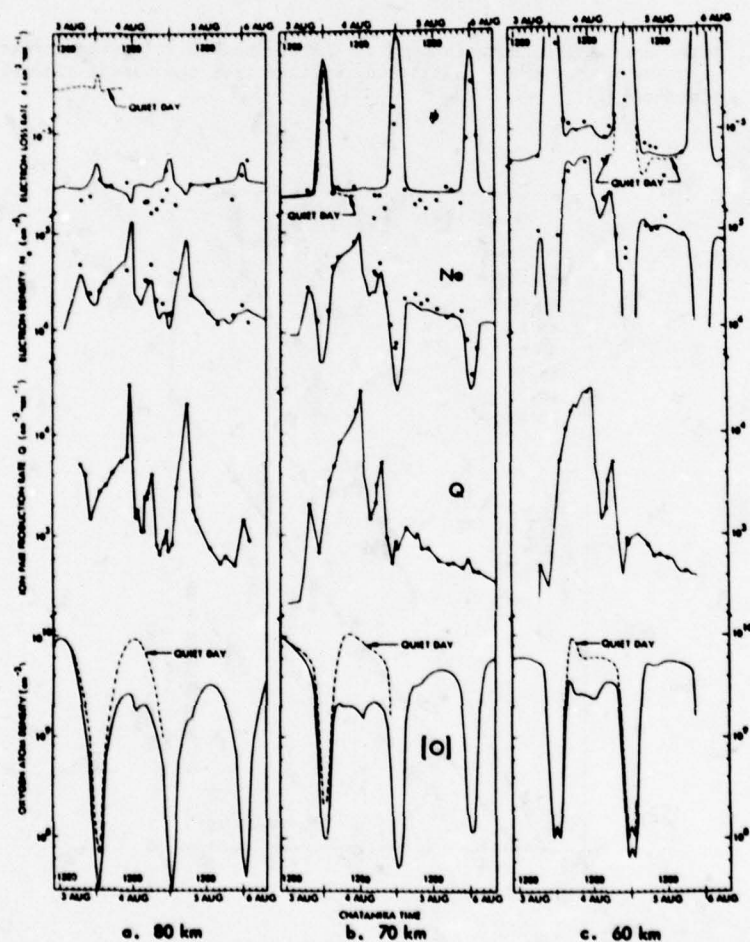
Figure 7   Some results of a neutral and ion chemistry analysis of the lower atmosphere at altitudes of 80, 70 and 60 km during the August 1972 solar particle event (Reagan 1977).
The points indicate observed values, the lines are derived from model calculations.
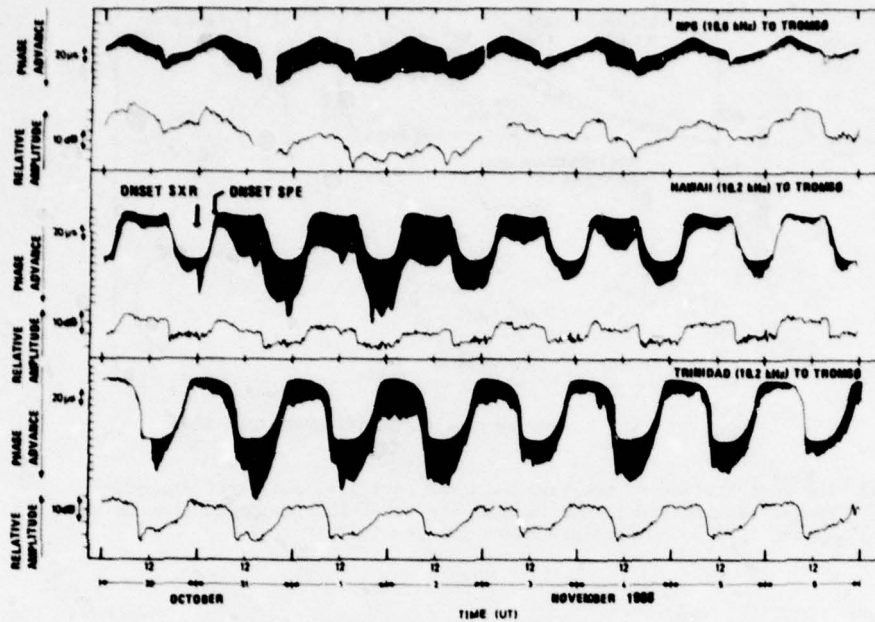
Figure 8   Phase and amplitude variations at VLF during PCA for paths across the polar cap. The shaded areas indicate deviations from the normal diurnal variation (Larsen 1977).
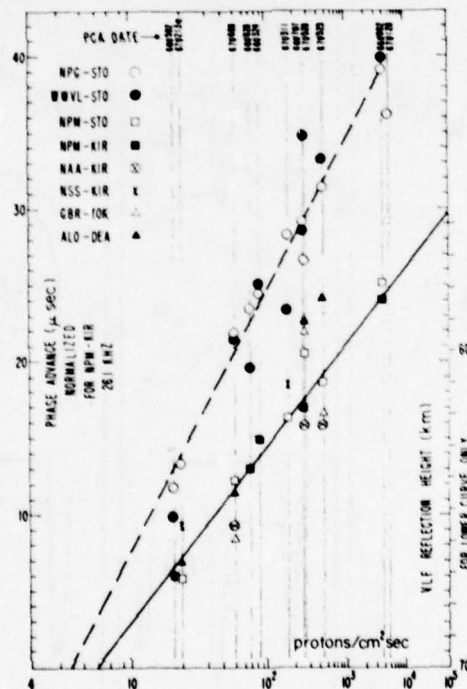
Figure 9   Daytime phase advance on high-latitude VLF circuits as a function of the flux of protons with energy greater than 25 MeV. Phase advances have been normalized to a frequency of 26.1 kHz and to a PCA-affected path portion of 5300 km. From Westerlund et al. (1969). The dashed line represents paths across 1000 km of Greenland icecap.
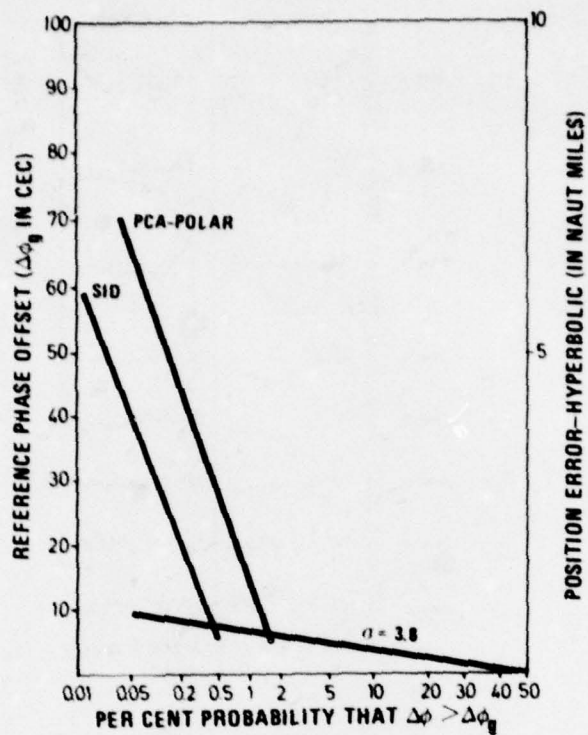
Figure 10 Per cent probability that phase offset at Omega frequencies exceed certain limits for PCA and SID conditions (Swanson 1974).
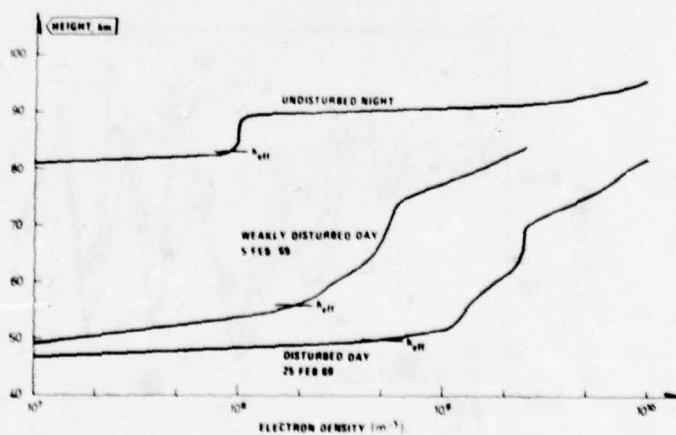
Figure 11 Typical electron density profiles for different D-region conditions ranging from undisturbed night to PCA. The reflection height h_{eff} at 100 kHz for medium length path is indicated for each profile (Larsen and Thrane 1977).
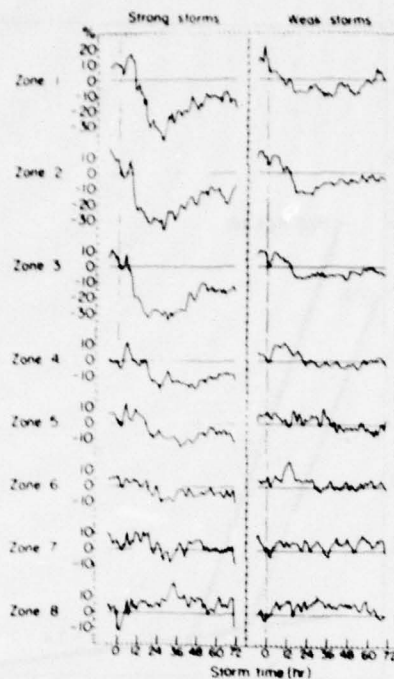
Figure 12 Dst variations of N_mF2 in each of eight latitude zones for strong and weak
magnetic storms with sudden commencements. The ordinate is the approximate
percentage deviation from the quiet day behavior versus storm time (in hours).
The zone number is shown in parenthesis between the applicable geomagnetic
latitudes: $60°$ (1) $55°$ (2) $50°$(3) $45°$ (4) $40°$ (5) $30°$ (6) $20°$ (7) $10°$ (8) -
$10°$ (Matsushita 1959).
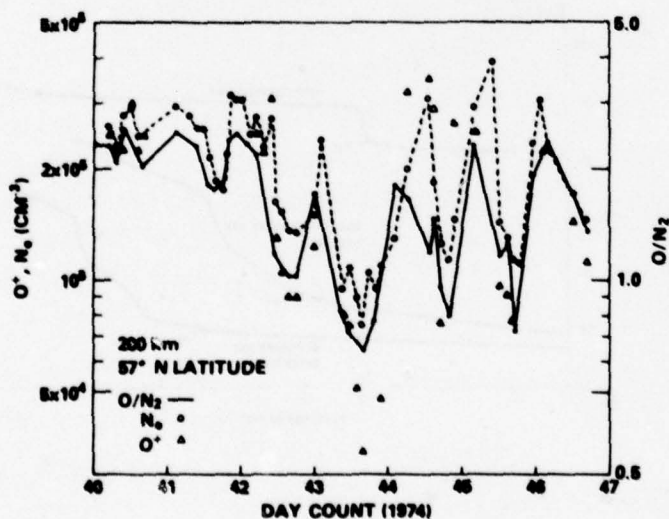
Figure 13 Temporal variation of the $[O]/[N_2]$ ratio, $[O^+]$, and N_e at 200 km ($57°$)
(Hedin et al. 1977).
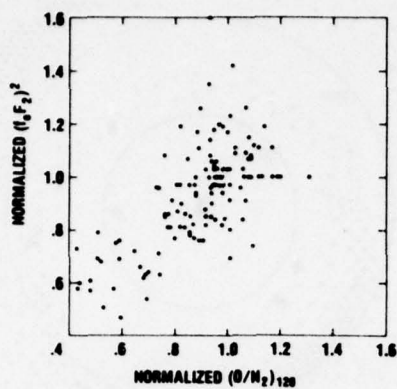
Figure 14 Plot of the square of the normalized foF2 frequency as a function of
the $[O]/[N_2]$ ratio at 120 km. Both are normalized by prestorm values on
day 40 1974 (Hedin et al. 1977).
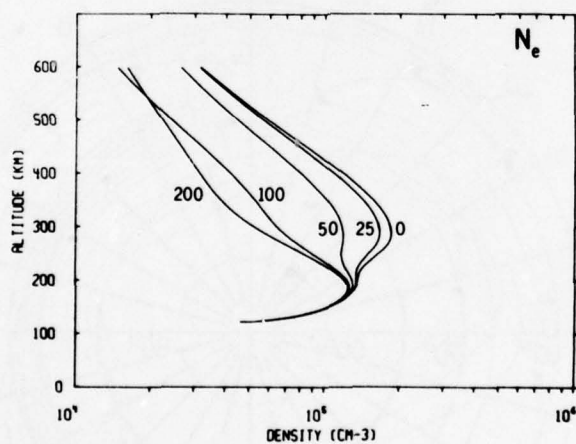
Figure 15 Altitude profiles of electron density for several effective electric
field strengths (mV m^{-1}) (Schunk et al. 1975).
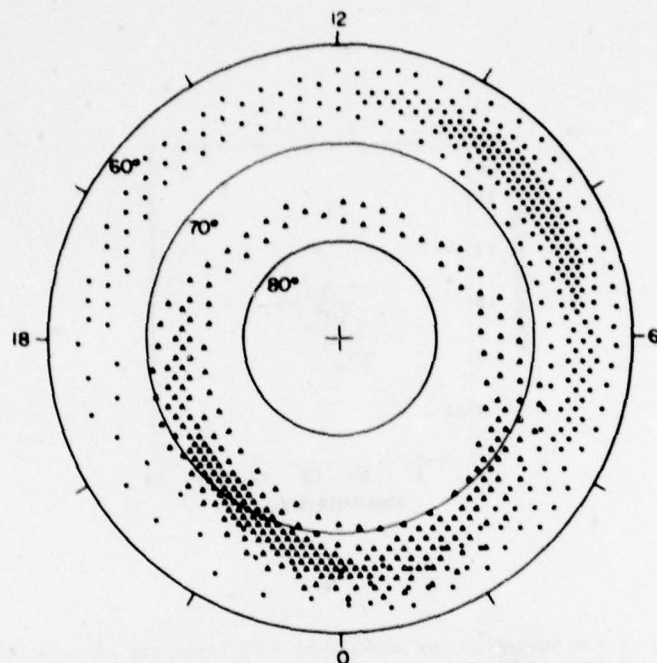
Figure 16 An idealized representation of the two main zones of auroral particle precipi-
tation in the northern hemisphere, where the average intensity of the influx
is indicated very approximately by the density of symbols and the coordinates
are geomagnetic latitude and geomagnetic time. The "discrete" events are rep-
resented by triangles (which closely correspond to the undisturbed "auroral
oval") and the "diffuse" events are indicated by the dots (Hartz and Brice
1967). (Geomagnetic time is local solar time measured with respect to geomag-
netic longitude.)
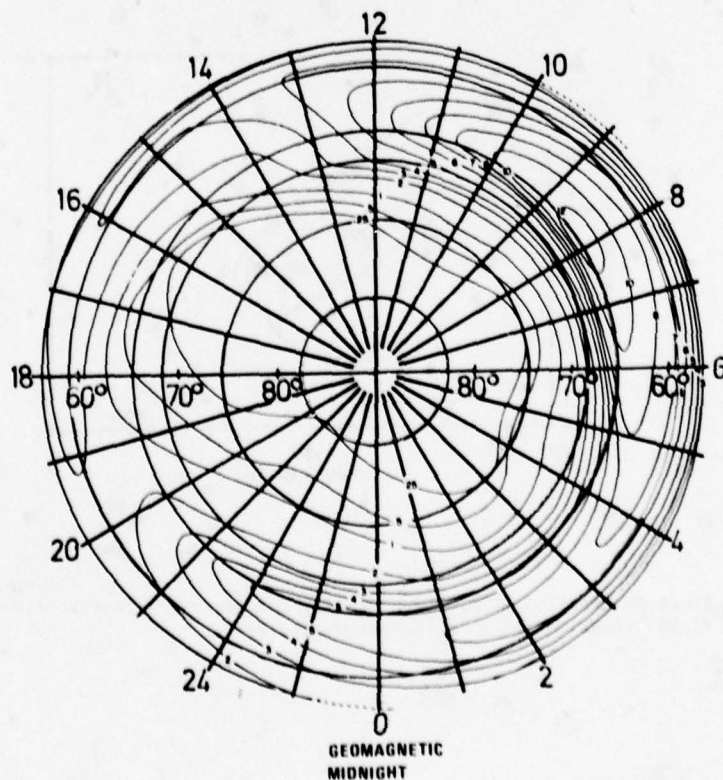
Figure 17 The percentage of the time that auroral radio wave absorption of 1.0 dB or
more occurred at 30 MHz. The data were obtained in the northern hemisphere
during the period 1959-1961, and are plotted as a function of geomagnetic
latitude and mean geomagnetic time. (After Hartz et al. 1963).
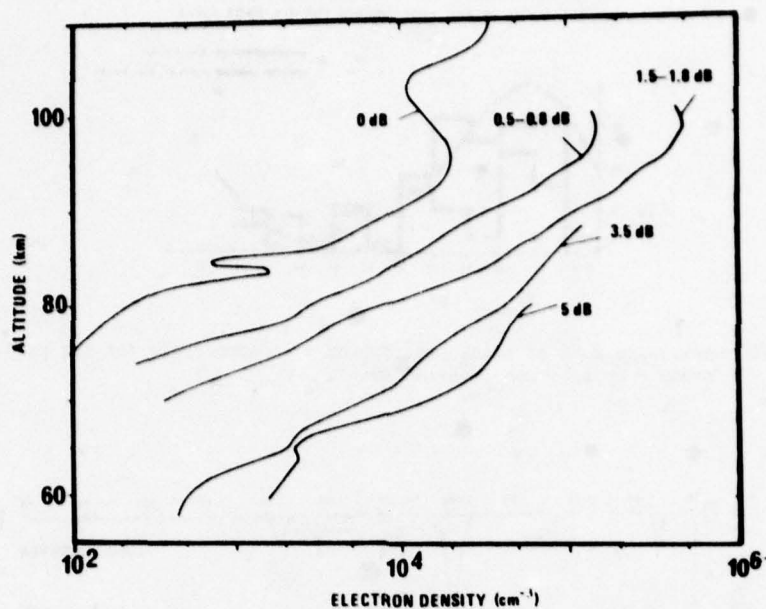
Figure 18 Average electron density profiles for different amounts of auroral absorption (Jespersen and Landmark 1968).
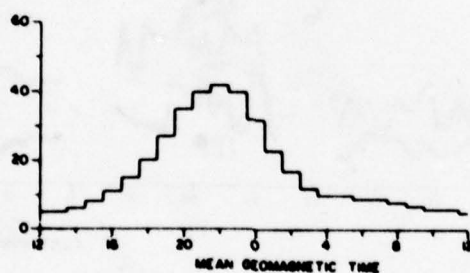
Figure 19 The diurnal variation in the percentage occurrence of sporadic E echoes that extend beyond 7 MHz on ionograms from auroral-zone stations: the data are the average of 5 years' data at Point Barrow (68.4°N), Churchill (68.7°N) and Ft-Chimo (69.6°N) (Hartz 1958).

1. NUMBERS OF BLACKOUTS AND PARTIAL BLACKOUTS IN
   ONE SUN SPOT CYCLE FOR THE HARSTAD-LONGYEARBYEN
   HF RADIO CIRCUIT.
2. THE CURVE OF SUN SPOT FIGURES FOR THE SAME CYCLE.
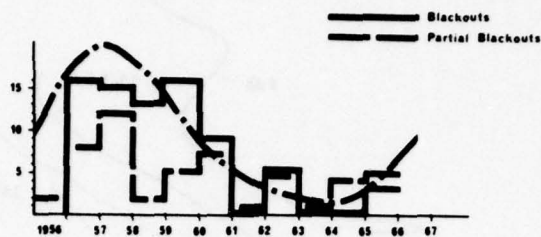
Figure 20   Occurrence rate of black outs during a sunspot cycle for the path North-
            Norway - Spitzbergen (Veastad 1968).
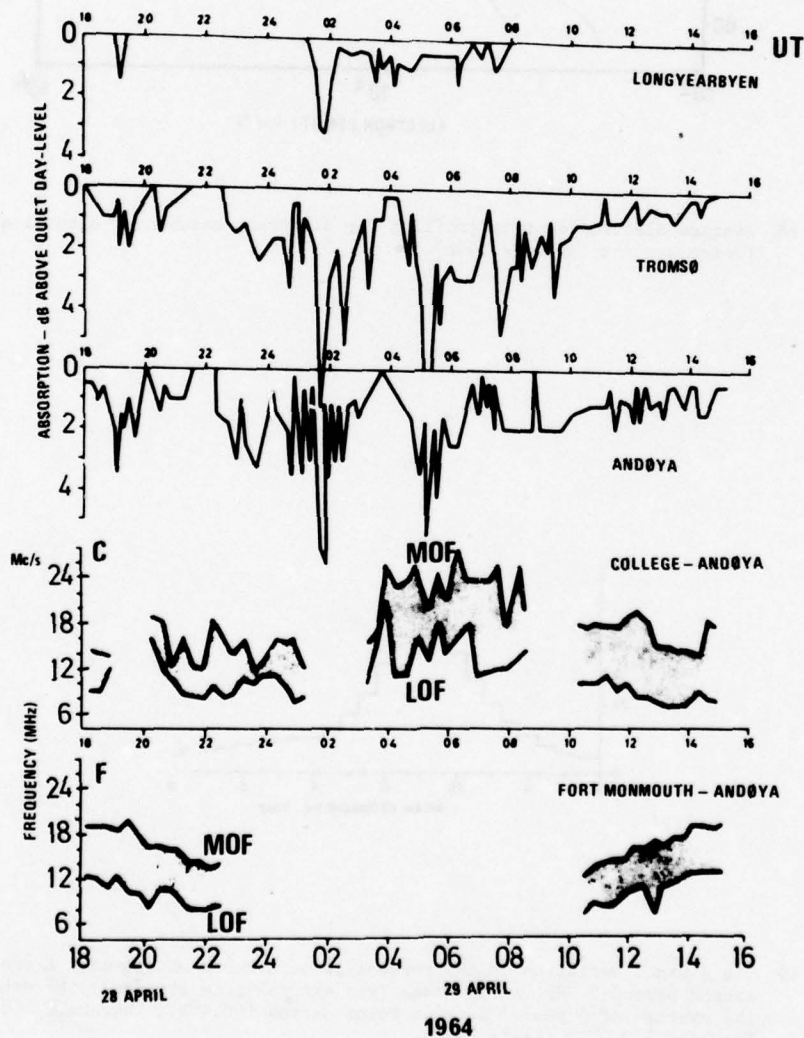
Figure 21   Circuit behaviour during auroral conditions compared with riometer absorption
            (Folkestad 1968).
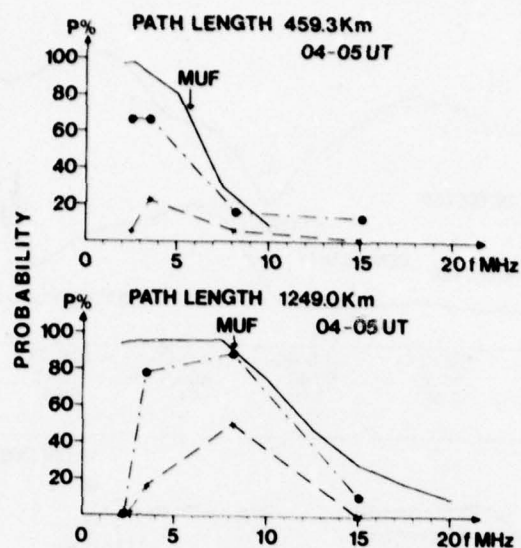
Figure 22 Comparison of HF predictions of probability of communication with measurements during quiet and auroral conditions
————— "Bluedeck" predictions
●–·–● Quiet conditions
x – – x Disturbed conditions
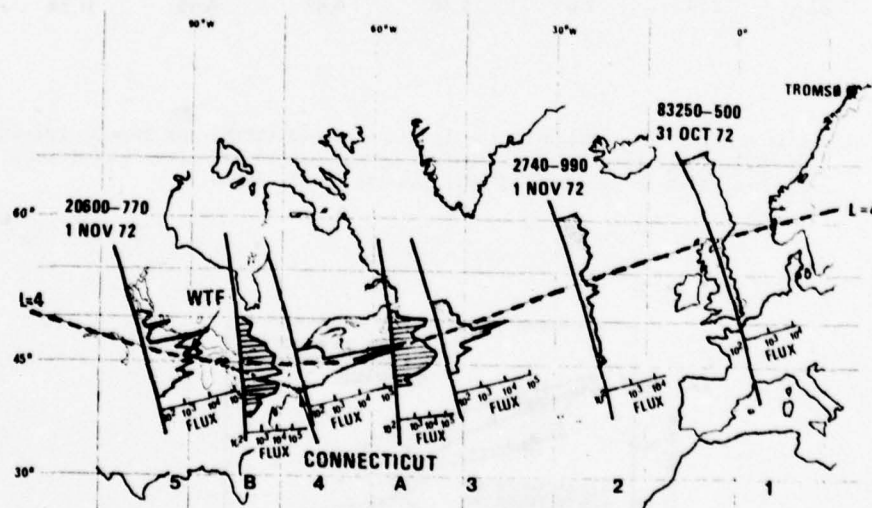
Figure 23 Schematic drawing of electron fluxes (E > 130 keV) for 7 satellite passes (Imhof et al. 1977).
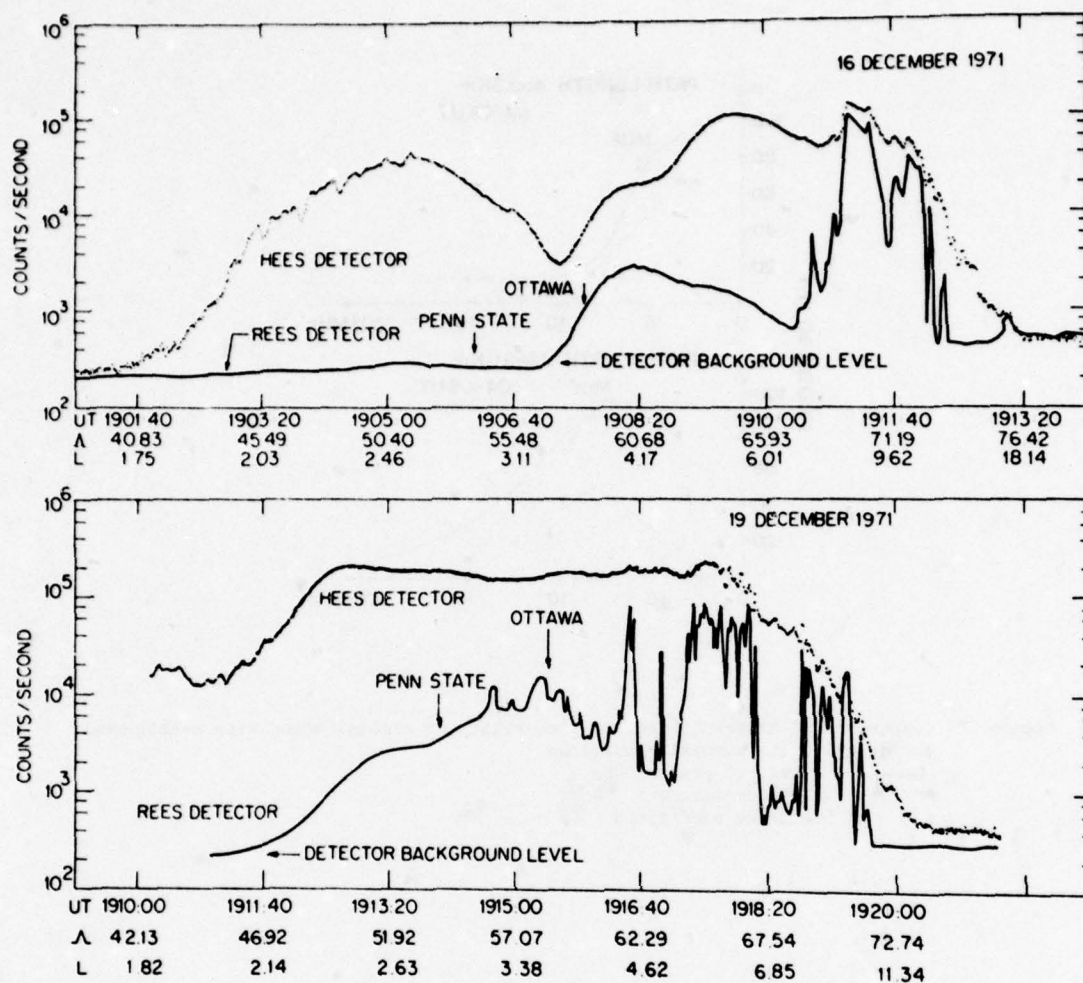
Figure 24 Latitudinal flux profiles of the locally-trapped (HEES) and locally-precipitating (REES) electrons > 130 keV before (upper panel) and after (lower panel) the magnetic storm of December 17 1971 (Larsen et al. 1976).
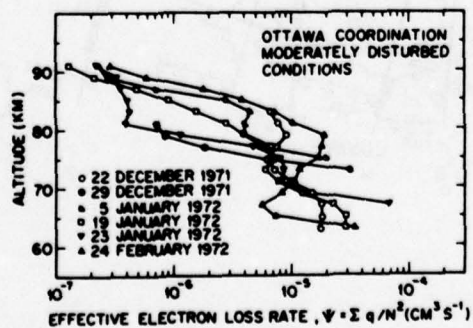
Figure 25 Effective electron loss rates, $\psi = \Sigma^q/N_e^2$ as a function of height for moderately disturbed conditions (Larsen et al. 1976).
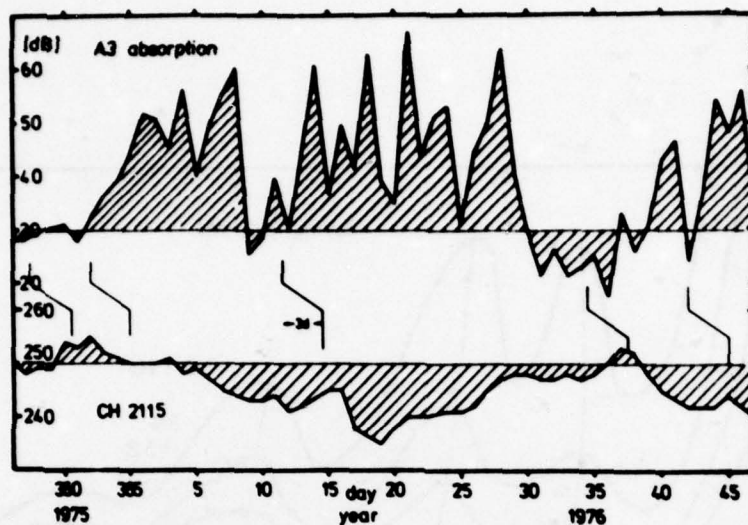
Figure 26   A3 absorption and infrared radiant fluxes (40-45 km) (ch 2115) during a period with winter anomaly conditions (Offermann 1977).
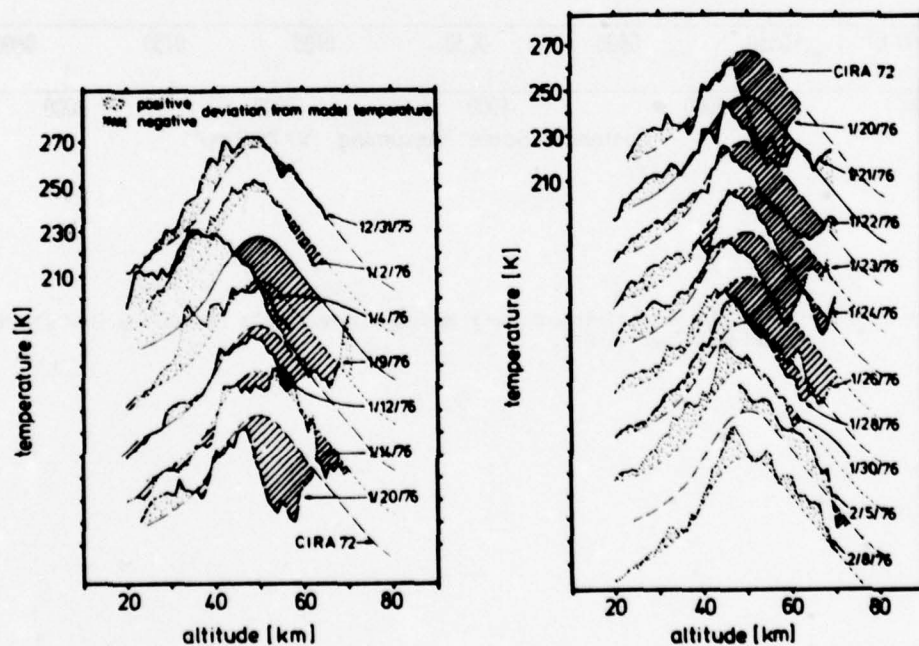
Figure 27   Rocket temperature measurements compared to CIRA 72 model profiles. Rocket flights are labelled by their dates (Offermann 1977).
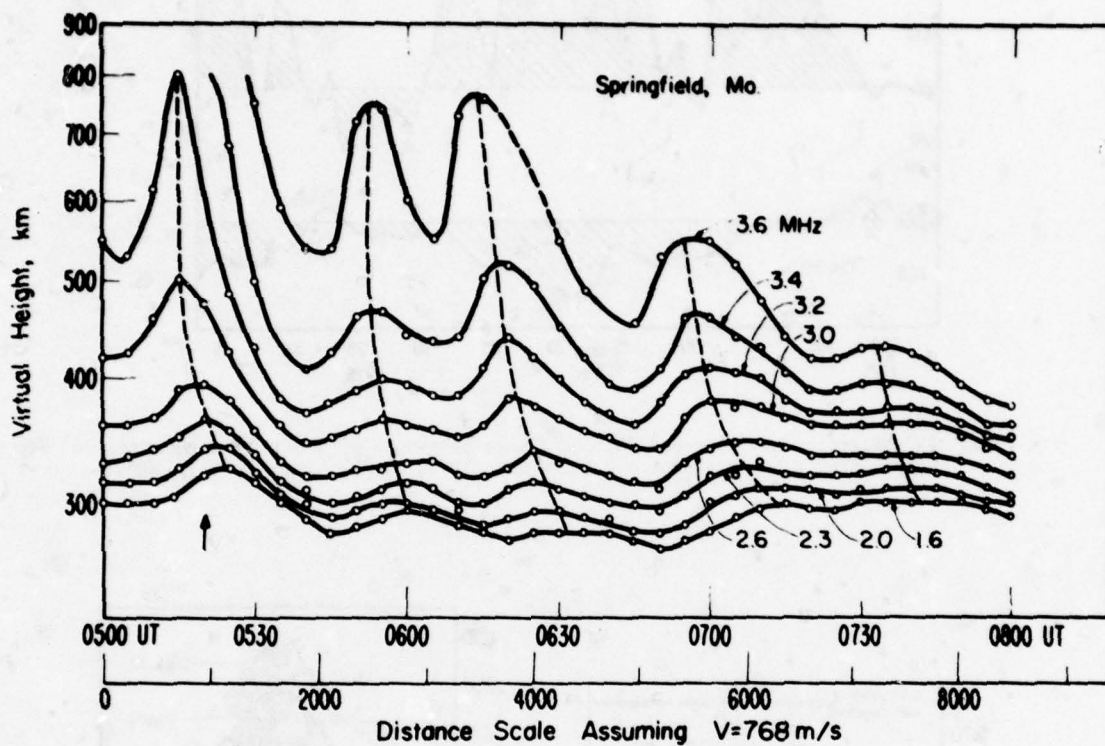
Figure 28 Virtual height variations observed during a large scale travelling ionospheric
disturbance (Georges 1967).

PROPAGATION AT MEDIUM AND HIGH FREQUENCIES, 2 :

LONG AND SHORT-TERM MODELS

by

P. A. Bradley
S.R.C., Appleton Laboratory, Ditton Park, Slough, Berks. SL3 9JX, U.K.

SUMMARY

Procedures for the long-term estimation of sky-wave signal strengths at MF and HF as proposed by the CCIR are discussed. At MF an empirical fit to past measured signal data is used. Particular consideration is given to modelling the increased losses at auroral latitudes and the excess polarisation-coupling loss on some low-latitude paths. Sea-gain-enhancement allowances are also presented. Models at HF are shown to involve a detailed representation of the state of the ionosphere, idealised height distributions of electron concentration, an approximate means of raypath determination and separate allowances for the different factors contributing to the transmission loss. The degree of agreement with observational data achieved is illustrated for both frequency bands.

CCIR models for atmospheric, man-made and galactic noise are reviewed and examples presented of computer-based calculations. The use of statistical day-to-day signal and noise variability statistics to provide system performance estimates at HF is indicated.

A brief review is given of short-term modelling approaches at HF involving real-time updates of long-term predictions and geophysical and ionospheric disturbance forecasting.

1. INTRODUCTION

In the companion text[1] the requirements are discussed for long-term and short-term models of signal propagation via the ionosphere and of noise reception characteristics. Long-term models are representative over time scales of a month or more; short-term models relate to current conditions in the light of day-to-day variability. At MF, long-term models are of use in system planning to determine necessary transmitter powers and preferred operating frequencies. Since this band is occupied for the most part by sound broadcasting, for which transmission schedules have to be published well in advance, there is little need for short-term prediction models, even if these were feasible. At HF long-term models are required for system design and network planning; short-term models have potential for frequency management.

There are many publications discussing prediction and modelling aspects of sky-wave radio propagation at MF and HF. These include earlier AGARD texts[2-4]. Here attention is paid to current international models for MF and HF services. Some aspects receiving further study at the present time are also mentioned.

2. LONG-TERM MODELS

2.1 Signal characteristics at MF

MF signals penetrate the lower ionosphere and are usually reflected from heights of 85-100 km, except over distances of less than 500 km by night when reflection may be from the F-region. Large amounts of absorption occur near the height of reflection and so daytime signals are very weak. Interest therefore centres largely on night-time sky-wave models for potential interference calculations, but there is also a need for signal-strength estimates in the twilight periods.

Some success has been obtained with a wave-hop prediction scheme[5] based on the results of ray tracing and absorption calculations for propagation via reference model ionospheres. This approach has merit for cases where non-standard transmitting antennas are involved, or for propagation paths leading to large polarisation-coupling losses. There are difficulties, however, in deriving representative values of absorption for all conditions, particularly at auroral latitudes, because of the extreme variability of the absorbing D-region of the ionosphere and the paucity of electron-concentration data from which the corresponding amounts of absorption can be deduced. The internationally preferred prediction model for general use at frequencies up to 1600 kHz for path lengths of 300-12000 km is therefore now based on an empirical fit to past measured field-strength data[6]. It is fortunate that broadcasting organisations pay particular attention to the monitoring of system performance. Hence, unlike the position at HF, a considerable quantity of such data exists, collected under standardised conditions for many years.

Measured night-time results have been grouped together independently of season to give annual median half-hourly field strengths for a reference transmitter power and for standardised transmitting and receiving antennas. Results have been examined as a function of distance, frequency, geographical region and path orientation. Although not surprisingly the measurements show appreciable scatter, it has been found possible to produce empirical curves of best fit in accord with expected general trends. Several sets of such curves have been proposed over the years.

The first propagation curves used were the so-called Cairo curves adopted by the CCIR in 1938[7]. One curve applies to N-S paths and the other to E-W paths. These curves were derived from measurements made in 1937 and 1938 at a frequency around 1 MHz on N-S paths on the American continent, on E-W paths across the North Atlantic and on paths between Europe and South America. The degree of match achieved by these curves is shown in Figure 1 where the ordinate scale relates to the reference conditions that have now been adopted to express the measured data. Also illustrated for comparison are curves given by empirical equations of Ebert[8] fitted to more recent measurements collected over European paths in campaigns organised by the European Broadcasting Union (EBU) and by the International Radio and Television Organisation (OIRT).

In particular the Ebert equations include a frequency dependence. Much controversy has centred on whether signal strengths are larger at the higher or lower frequencies of the band. It is now believed that for most paths there is more absorption at the higher frequencies, but the dependence is not large at low and middle latitudes. This is because the increased contribution to the absorption from the upper height ranges as the reflection height increases is compensated by the reduced absorption in all regions traversed.

In recent years a Working Party of the CCIR has re-analysed earlier measurements and combined results from these with later data, including those from geographic areas not previously included, to produce new curves. These are based on results for approximately 300 separate paths. With the inclusion of corrections to the curves for paths subject to certain additional factors such as above average polarisation-coupling loss or sea gain, the model thereby formed has general international acceptance[6].

E_o, the annual median sky-wave field strength measured by a loop antenna situated over ground of average conductivity and aligned in the vertical plane along the great-circle path to the transmitter at a time when night conditions have become established (from 6 hours after sunset to 2 hours before sunrise) is given as

$$E_o = V + G_S - L_P + A - 20 \log_{10} p - 10^{-3} K_R p \tag{1}$$

where E_o is measured in dB above 1 μV/m

V = transmitter cymomotive force, dB above a reference cymomotive force of 300 volts

G_S = sea-gain correction, dB

L_P = excess polarisation-coupling loss, dB

A = factor depending on latitude

p = slant-path propagation distance, km

and K_R = loss factor incorporating effects of ionospheric absorption, focusing, terminal losses, and losses between hops on multiple-hop paths.

V is related to the transmitter radiated power P_T(dB above 1 kW), G_V the transmitting antenna gain factor due to vertical directivity (relative to the radiation in the horizontal direction from a short vertical antenna) expressed in dB, and G_H the corresponding gain factor due to horizontal directivity in dB, by

$$V = P_T + G_V + G_H \tag{2}$$

G_S is the additional signal gain when one or both terminals are situated near the sea. Values adopted have been derived from theoretical considerations, but supported by some experimental evidence. G_S is a function of frequency, path length, distance from the coast and distance to the next section of land, measured in the great-circle path direction. It rises to a maximum of 10 dB for a single terminal for long paths when the terminal is on the coast and there is 100 km or more of sea in the receiver direction (Figure 2). Sea-gain allowances for the transmitting and receiving terminals are additive.

L_P is an allowance for the extra polarisation-coupling loss between vertically polarised transmitted and received signals that arises over low-latitude paths where the magnetic dip I is below 45°. This loss is particularly severe on E-W paths where the ordinary wave, which is stronger than the extraordinary wave, is essentially horizontally polarised. As deduced from detailed theoretical calculations, L_P is taken as being given by

$$L_P = 180 \ (36 + \theta^2 + I^2)^{-\frac{1}{2}} - 2 \ \text{dB/terminal} \tag{3}$$

θ is the path azimuth measured in degrees from the magnetic E-W direction such that $|\theta| \leq 90°$. L_P is evaluated separately for each terminal because of the different θ and I that may apply, and the two L_P values added. Figure 3 shows values of L_P calculated from eq. (3).

p is based on mirror reflection at a height h_r of 100 km for E modes and 220 km for F modes :

$$p = \sqrt{D^2 + h_r^2} \tag{4}$$

for a great-circle ground range D (km). F modes are assumed to occur for signals of wave frequency f (kHz) when

$$f > 350 + \left[(2.8D)^3 + 2.7 \times 10^7 \right]^{\frac{1}{3}} \tag{5}$$

The loss factor K_R is a function of frequency, geomagnetic latitude Φ and twelve-month smoothed sunspot number R_{12}:

$$K_R = K + 10^{-2} b R_{12} \tag{6}$$

with b = 4 for North American paths, 1 for Europe and Australia and 0 elsewhere. This expression takes account of the increased absorption for the higher levels of solar activity. K is referred to as the basic loss factor and is defined as

$$K = 3.2 + 0.19 \ f^{0.4} \ \tan^2 (\Phi + 3) \tag{7}$$

where f is the frequency in kilohertz and empirical rules depending on path length are provided giving an effective Φ in terms of the geomagnetic latitudes at the transmitter and receiver terminals. Φ is taken

as positive in the northern hemisphere. For $|\Phi| > 60°$ values of $\Phi = 60°$ for the northern hemisphere and of ~ 60° for the southern hemisphere are adopted. Figure 4 shows that K increases to a maximum in the auroral and polar zones where absorption is greatest. The dependence on frequency is only significant at the higher latitudes. It corresponds to an increase of absorption with increase of frequency, which is in the reverse sense to that found in the U.S.A. This aspect is under current investigation.

The factor A is a slowly-varying function of Φ given as

$$A = 106.6 - 2 \sin \Phi \qquad\qquad (8)$$

Use of eqs. (1), (4), (5), (7) and (8) leads to the propagation curves of Figure 5 for a frequency of 1 MHz and a cymomotive force of 300 V when G_S, L_p and R_{12} are all zero.

Sunrise and sunset reference times are taken at the ground at the mid-path position for D < 2000 km and at 750 km from the terminal where the sun sets last or rises first for longer paths. The median sky-wave field strength E_t at some other time t relative to these reference times is

$$E_t = E_o - L_t \qquad\qquad (9)$$

where L_t is a diurnal loss factor (see Figure 6).

For interference protection considerations it is important to be able to estimate sky-wave signal intensities other than annual median night-time values. The field strength exceeded for 10% of the total time on a series of nights in a given season, during short periods centred on a specific time is taken as being 8 dB greater than the median value derived from the above expressions, although it is noted that larger differences from the median may occur at the peak of the solar cycle. Seasonal variations in tropical latitudes are relatively small, but at temperate latitudes spring and autumn field strengths are the largest and summer field strengths the least. Suggested values for planning purposes are that the overall seasonal variation may be 15 dB at the lowest frequencies of the band, decreasing to about 3 dB at the upper frequencies. In Europe the median daytime field strength in winter is 25 dB less than the night-time value; in summer it is about 60 dB less. Further information on the day-to-day variability of measured field strengths is available[9].

Various sets of comparisons have been produced between measured and predicted field strengths and these have been used from time to time to effect changes to the prediction models. Figure 7 shows one set of comparisons produced in 1976 before the latest version of the model was adopted. Although not now valid in detail, it nonetheless gives an indication of the general range of accuracies achieved in different regions. Using the current model, Wang[10] has made a detailed study of North American path data. He finds that measured field strengths on N-S paths exceed those predicted by as much as 15 dB. Corresponding measurements for E-W paths give field strengths 10 dB less than predicted. Wang has produced a new model[11] in which the influence of solar activity is expressed by a parameter which depends not only on sunspot number but also on distance, frequency and geomagnetic latitude. Other models have been formulated to give a better match to the data in the different individual geographical regions. However, it is generally recognised that the loss of accuracy in using the present CCIR model is an acceptable price to pay for having a single prediction model of worldwide applicability. When applied to 266 paths for which individual results are available, the error in prediction has a standard deviation of 7 dB.

2.2 Signal characteristics at HF

2.2.1 Path MUF and FOT

Waves travel via the ionosphere at HF with reflection from the E, Es, F1 and F2 layers. The path MUF is defined as the highest frequency that can propagate between a pair of specified terminals via any ionospheric mode. It is a function of path length, geographic position and time. There are systematic variations with time-of-day, season and solar epoch, and also irregular day-to-day changes. Methods of prediction are restricted to determining smoothed monthly median values and to providing statistical parameters descriptive of the daily figures. Propagation by means of F2-, E- and F1 modes is allowed for, depending on the path length, but it is not usually appropriate to take account of Es-modes because of their generally intermittent occurrence and differing signal characteristics. The path MUF is taken as the highest MUF of any mode reflected from the different layers, so that it is necessary to first determine the separate F2-, E- and F1-MUF's, depending on the path length.

MUF's may be evaluated by ray-tracing procedures. However, a simpler alternative approach currently recommended by the CCIR and relying on empirical relationships makes use of the equation :

$$MUF - D = f_o \cdot M(D) \qquad\qquad (10)$$

where

MUF-D is the MUF for a single-hop mode reflected from a given ionospheric layer and propagated to ground distance D

f_o is the critical frequency of the layer

and   M (D) is known as the 'M' or 'MUF' factor for distance D.

There are three separate stages in the MUF determination process :

(i)   selection of procedures to define positions along the propagation path at which ionospheric information should be sought and to formulate appropriate single-hop path lengths D

(ii)   evaluation of f_o and M(D) for paths centred on these positions, and

(iii)   use of eq.(10)and where appropriate the comparison of MUF's for modes reflected from the different layers.

For paths shorter than 4000 km predictions are made for both an F2 mode and an E mode. Between 2000 km and 3400 km the F1 mode is also considered. For longer paths only an F2 mode is taken into account. For path lengths of 4000 km and less, calculations are based on single-hop propagation via the ionosphere given at the midpath position. With greater distances the so-called two-control-point procedure is used in which the path MUF is taken as the lower of the two MUF's for a 4000 km hop centred on locations 2000 km along the great circle from the transmitter and receiver. Although there is no rigorous basis for this approach and opinions are divided on its merits, its use is considered justifiable in many applications.

On the basis of transformation relationships from vertical to oblique propagation, standard MUF factors have been determined for reflection from the different layers. These factors depend principally on layer height. Curves showing representative factors as a function of distance for single-hop re-flection from the F2-, E- and F1- layers are given in Figure 8. Values are larger the lower the layer height and so are greatest for E-modes. A fixed MUF factor relationship is adopted for all E reflections since this layer maintains a nearly constant height. A family of MUF factor relationships parametric in smoothed sunspot number is used for F1-modes. These are consistent with F1-layer heights being signifi-cantly greater at sunspot maximum. The temporal and spatial changes of F2-layer heights are so complex that a more detailed treatment is needed for F2-modes. Families of MUF factor curves have therefore been defined which are parametric in the value for a 3000 km path, M(3000)F2.

Hence the kernel to the prediction procedure is the determination of values of foE, foF1, foF2 and M(3000)F2 for the appropriate locations and times. Numerical representations have been applied to past measured vertical-incidence ionosonde data[12] from many locations throughout the world where standardised recordings are made each hour of every day to provide predicted values of these ionospheric characteristics. The CCIR has produced an Atlas[13] giving monthly median estimates by means of charts, nomograms and computer-based formulations. foE is obtained from empirical expressions which assume a variation with latitude, time-of-day and season that depends on the solar-zenith angle χ. This angle is calculated readily. The solar-activity dependence is included by means of a multiplying factor in terms of R_{12} the smoothed sunspot number. foF1 obeys the empirical equation

$$foF1 = f_s \cos^n \chi \qquad (11)$$

where both f_s and n depend on geomagnetic latitude and R_{12}.

In the case of the F2-layer the Atlas contains printed world maps of the parameters EJF(ZERO)F2 and EJF(4000)F2 every two hours UT for each month of reference years with $R_{12} = 0$ and 100 (Figure 9). Estimates for other R_{12} are determined by linear interpolation or extrapolation between these figures. The nomograms provided with the Atlas give EJF(D)F2 in terms of EJF(ZERO)F2 and EJF(4000)F2 by means of an equivalent procedure to that described above. These two mapped parameters are related to foF2 and M(3000)F2, as given directly in the computer formulation, by

$$EJF(ZERO)F2 = foF2 + 0.5 \text{ MHz}$$

and $$EJF(4000)F2 = foF2 \times 1.1 \times M(3000)F2 \qquad (12)$$

There are separate computer formulations for foF2 and M(3000)F2 for every month of the two reference years. Each consists of orthogonal polynomial expressions in terms of geographic latitude λ, geographic longitude ϑ and Universal Time T. The general characteristic $\Omega(\lambda,\vartheta,T)$ is expressed as a time series :

$$\Omega(\lambda,\vartheta,T) = \sum_j [a_j(\lambda,\vartheta) \cos jT + b_j(\lambda,\vartheta) \sin jT] \qquad (13)$$

where the a's and b's give the latitude and longitude variations, being defined as :

$$a_j(\lambda,\vartheta) = \sum_k U_{2j,k} \cdot G_k(\lambda,\vartheta)$$

$$b_j(\lambda,\vartheta) = \sum_k U_{2j-1,k} \cdot G_k(\lambda,\vartheta) \qquad (14)$$

The U's are numerical coefficients and the G's are trigonometric functions of geographic longitude and a combined geographic and magnetic latitude parameter. Several tens of thousands of coefficients are in-volved in defining foF2, M(3000)F2 and the other ionospheric characteristics which are represented in this same way. These coefficients are contained on a special data tape.

The frequency of optimum traffic (FOT), known alternately as the optimum working frequency, is defined as the highest frequency that is likely to propagate at a given time between a specified pair of terminals via any ionospheric mode for 90% of the days. It is given in terms of the monthly median pre-dicted path MUF from a knowledge of day-to-day ionospheric variability. The E- and F1-layers experience relatively little variability from one day to another, and when these control the path MUF the FOT is taken as 0.95 of the MUF. For F2-modes F_ℓ, the ratio of the lower decile to median MUF, has been evaluated from a wide range of past signal measurements and tabulated as a function of solar epoch, season, local time and geographic latitude to provide a reference set of values[14].

A computer program, named MUFFY, has been developed at the Appleton Laboratory, Slough specifi-cally for the estimation of path MUF and FOT by the above CCIR procedures. The program carries out all

necessary calculations including path-length determination. Table I provides an illustration of the print-out.

Studies are in progress comparing the relative values of MUF given by this MUF factor procedure with those deduced from ray tracing. Some data are available produced as supplementary information in the first CCIR field-strength model (computer programs HFMLOSS and RIM1A) and in the Institute for Tele-communication Sciences, Boulder, procedure for system-performance assessment (program HFMUFES 3) - see Sections 2.2.2 and 2.4 respectively. Table II shows results for a short and a long path. There are differences between HFMLOSS and HFMUFES 3 because separate representations of foF2 are used. However both programs give enhanced MUF's when compared with MUFFY and there is some evidence that this is a general feature. Although for some applications these differences may not be regarded as too serious, there appears a need to re-examine existing MUF-factor relationships in comparison with ray-tracing results based on the best-available ionospheric models.

2.2.2 Signal strength

An interim computer-based signal-prediction procedure was developed by the CCIR in 1970[14] and a second procedure was produced in 1976[15]. The computer program for this second method is still in course of preparation. At the same time various participating organisations are attempting to formulate further improvements in the prediction technique. For the present, the CCIR recommends[16] that the first procedure should be used for all computer-based predictions at frequencies above 2 MHz until the computer program for the second procedure has been produced and the method tested. No manual signal-prediction model has yet been adopted by the CCIR, although several different procedures exist. Whilst user needs vary, the increasing availability of computing aids suggests that the principal requirement will be for a very simple manual method, albeit one including many approximations.

As noted in Section 2.1, two different approaches to sky-wave signal-intensity prediction are possible. One is to fit empirical equations to measured data for different paths, times and frequencies. The other is to estimate intensity in terms of a number of separate factors known to influence the signals. These factors may be given by expressions which have been deduced either from theory or measurement. Un-fortunately both approaches have limitations. The former is likely to be simpler but unless a large data base exists, trends must be inferred and are liable to error. The latter approach is conceptually more elegant and enables variations to be specified in a physically meaningful manner. However, there remains the possibility of error due to failure to allow for a significant term or to an inexact allowance. There is also a likelihood of devising a method which is over-complex and for which the accuracy achieved does not merit some of the complications that have been introduced. In view of the shortage of available and reliable measured signal data at HF, it is generally agreed in contrast to the position at MF that pre-diction methods should rely on allowances for the separate factors. Existing models differ in regard to what factors to include and what allowances to use for these.

HF prediction methods usually yield monthly medians of hourly smoothed field strengths and available receiver powers and their statistical day-to-day variations about these values. The separate-factor approach involves specifying models of the height distributions of electron concentration in terms of global representations of the standard vertical-incidence ionospheric characteristics discussed in Section 2.2.1. The raypaths of all propagation modes that can exist between the transmitter and receiver are determined using some form of ray tracing. The probabilities of mode occurrence (availabilities) are evaluated from estimates of the mode MUF's and their likely day-to-day variability. Signal strengths are given by computing the separate terms contributing to the transmission loss of each mode, with due allow-ance for the raypath angles involved. Different methods include those terms considered appropriate, but all allow for the most important factors which are generally agreed as transmitter power, transmitting and receiving antenna gains, spatial attenuation and ionospheric absorption. Data based on relative signal-intensity measurements[17], for which there are many more available than absolute measurements, give the likely day-to-day scatter in signal intensity about the predicted monthly-median values.

2.2.2.1 First CCIR procedure

In the first procedure the model of the vertical distribution of electron concentration consists of E and F-region segments with a parabolic height variation (Figure 10). The sporadic-E layer is in-cluded as an option. The F-region is taken as having a plasma frequency which is a maximum equal to foF2 at height hmF2; it becomes zero as the height is reduced by ymF2. The E-region is represented by a full parabola with maximum plasma frequency foE, height of maximum hmE = 110 km and semithickness ymE = 20 km. The sporadic-E layer is taken as a negligibly thin layer at a height of 110 km and of maximum plasma frequency foEs. The model is completely defined for any specified time and place, in terms of monthly median pre-dictions of the standard ionospheric characteristics[18] foF2, foE, foEs, M(3000)F2 and h'F.

hmF2 is given by an empirical equation based on M(3000)F2 :

$$hmF2 = \frac{1490}{M(3000)F2} - 176 - \Delta h, \text{ km} \tag{15}$$

where Δh is a correction factor for underlying ionisation, evaluated as

$$\Delta h = 30 \left[z \log_e \left(\frac{z+1}{z-1} \right) - 2 \right] \tag{16}$$

with $\quad z = 0.834 \dfrac{foF2}{foE}$

ymF2 is expressed in terms of h'F, the virtual height of the base of the F-region, by

$$ymF2 = hmF2 - (h'F - \Delta h) \tag{17}$$

To evaluate the propagation modes that exist between defined transmitter and receiver locations, raypaths are assumed to follow the great circle and are deduced from a single model of the vertical distribution of electron concentration taken as applying over the whole path. The values of the parameters of this model are given in terms of the average of the predicted ionospheric characteristics at up to five defined positions, depending on path length. For distances less than 2000 km, only the midpoint is considered. At other distances the separate positions are taken as

(i)   the mid-path point

(ii)   the E-region reflection point nearest the transmitter for the least possible number of hops

(iii)   the E-region reflection point nearest the receiver for that same number of hops

(iv)   the F-region reflection point nearest the transmitter for the least possible number of hops

(v)   the F-region reflection point nearest the receiver for that same number of hops.

Reflection points are taken to be at each mid-hop position and are estimated by assuming all hops have equal length not exceeding 2000 km in the case of E-modes or 4000 km for F-modes. When two points as defined above coincide they are awarded only a single weighting in evaluating the averages.

The modes which are examined depend on the transmitter-receiver separation. They include cases of single and multiple-hop reflection from the E, Es and F-layers, and also for paths exceeding 2000 km range, mixed modes involving reflection from the E or Es layers together with reflection from the F-layer. For the shorter paths (less than 2000 km) a search is made for the following modes : the least-order possible and the next-higher order E-modes, the least order and the next two higher-order possible F-modes. If desired, modes involving reflection from the Es-layer can be considered as an option for frequencies giving penetration of the regular E-layer, but the screening effect of the Es-layer is not taken into account.

For a mode to be possible at a given frequency the following conditions must be met and are tested :

(i)   the ray is reflected from the layer for the frequency and angle of elevation that apply

(ii)   The elevation angle exceeds a limiting minimum value which is specified. This can be non-zero to take account of terrain screening in undulating or mountainous regions

(iii)   in the case of reflection from the F-layer, screening by the E-layer does not occur.

For path lengths exceeding 2000 km, two mixed modes are also considered. One mixed mode consists of a single E (or Es) layer reflection and the least possible number of F-reflections. The other mixed mode consists of two E (or Es) reflections and the least possible number of F-reflections. Since a uniform ionosphere is assumed to exist over the whole path, no distinction is made in the order in which the separate mixed-mode reflections arise.

Oblique raypaths for a frequency f_{ob} are determined assuming plane-mirror reflection from a height h' equal to the virtual height for vertical-incidence propagation at an equivalent frequency f_v. From the well-known secant law

$$f_{ob} = f_v \cdot k \sec i \tag{18}$$

where i is the semi-vertex angle at height h' and k is a correction factor exceeding but close to unity, arising from earth and ionosphere curvature. k is given by an approximate empirical expression in terms of i, h' and the true height of reflection at vertical incidence for frequency f_v. For a specified hop length d and virtual height h'

$$\tan i = \sin \left(\frac{d}{2R} \right) / \left(1 - \cos \left(\frac{d}{2R} \right) + \frac{h'}{R} \right) \tag{19}$$

where R is the radius of the Earth.

Analytical equations are available for the true and virtual heights at vertical incidence. Iteration of eqs. (18) and (19) and the expression for k leads to a matched set of values. In particular, the elevation angle Δ is then given from

$$\tan \Delta = \cot \left(\frac{d}{2R} \right) - \frac{R}{R + h'} \cdot \operatorname{cosec} \left(\frac{d}{2R} \right) \tag{20}$$

In determining the hop length in the case of reflection from the F-layer, a separate allowance is made for the contribution due to ray bending which takes place in penetrating the E-layer on both the upward and downward legs of the path.

Iterative expressions involving the above equations are also used to determine the mode MUF and its associated elevation angle. In this case f_{ob} is assumed unknown and the procedure is based on the fact that at the MUF the term df_{ob}/df_v is zero. The path MUF is taken as the highest value of mode MUF for the different modes that are examined. Raypath parameters and MUF's evaluated in this way are monthly

median figures, since they are based on representations of the monthly median ionospheric characteristics. The distributions of daily MUF about the monthly median values are assumed to follow a chi-square law. Use is made of the reference tabular values, noted in Section 2.2.1, of F_ℓ, the ratio of the lower decile to the median MUF and also of corresponding values of F_u, the ratio of the upper decile to the median, to determine for each wave frequency and examined mode the fraction of days for which the mode can exist over the path. This is known, as already noted, as the availability. Since the day-to-day MUF variability of E-modes is very small, their availability is taken as either 0.99 or zero, depending on whether or not the median MUF exceeds the oblique-wave frequency. Reflection heights for sporadic-E modes do not vary greatly and so MUF variability is approximately the same as that of maximum plasma frequency. Hence availabilities are deduced in terms of f_v and foEs and use is again made of the chi-square law. Upper and lower decile foEs are taken from numerical representations similar to those for median foEs.

With those modes which can exist known and their associated elevation angles given, the next stage is to evaluate the corresponding signal intensities at the receiver. Monthly median values of mean available receiver power for the separate propagation modes are determined in terms of transmitter radiated power, transmitting and receiving antenna gains and the basic transmission loss.

$$P_r = P_t + G_t + G_r - L_b \tag{21}$$

where P_t = transmitter power (dBW)

P_r = received power (dBW)

G_t = transmitting antenna gain (decibels relative to an isotropic antenna)

G_r = receiving antenna gain (decibels relative to an isotropic antenna)

L_b = basic transmission loss (decibels)

The corresponding rms sky-wave field strengths E (dB>1μV/m) are given in terms of P_r by

$$E = P_r + 20 \log_{10} f + 107.2 \tag{22}$$

where f is the wave frequency in Megahertz.

For the estimation of basic transmission loss the spatial attenuation is taken to be that which would arise in free space at a distance equal to the mirror-reflection slant-path total length. Ionospheric absorption is given by an empirical equation derived from measured oblique-path signal data. It is taken as being a function of frequency, path obliquity, solar-zenith angle and smoothed sunspot number. Absorption on the separate hops is cumulative.

Multiple-hop ground-reflection losses are evaluated in terms of the ground-reflection coefficients for vertically and horizontally polarised waves. These depend on frequency, elevation angle and ground constants as deduced from a numerical world map of ground conductivity and relative dielectric constant. An additional term included in the basic transmission loss is known as the excess-system loss. This is intended to take account of losses not explicitly allowed for such as those due to polarisation effects, sporadic-E and auroral absorption effects. Reference values of excess-system loss in the range 9-29 dB adopted from measured signal data depend on midpath geomagnetic latitude and time of day, season and whether short or long-paths are involved. Corresponding reference values are also given of the upper and lower standard deviations of the day-to-day signal variability, to permit the estimation of the signal strengths exceeded for different fractions of the month. The probability that a given mode produces a mean available receiver power exceeding some specified required power (the dependability) is given as the product of the availability and the probability that it has the necessary strength.

Two computer programs are available from the CCIR to perform calculations in accordance with the above procedures : program HFMLOSS with a single output format and no allowance for antenna gain, and program RIM1A which is similar, but includes subroutines to calculate the gain of a selection of antennas and has three separate optional printout formats.

Table III illustrates the printout for HFMLOSS. Input data include transmitter radiated power and required available receiver power, assuming an isotropic lossless receiving antenna. For each hour there is a tabulation of the path MUF, and then for each frequency separately the following parameters are given :-

MODE	-	propagation mode with the greatest dependability
ANGLE	-	elevation angle (degrees) of the mode with the greatest dependability
DELAY	-	propagation time (millisec) of the mode with the greatest dependability
VIRT HT	-	equivalent mirror-reflection height (km) of the mode with the greatest dependability - This relates to F-layer reflection in the case of mixed modes
F. DAYS	-	availability of the mode with the greatest dependability
LOSS DB	-	transmission loss (dB) of the mode with the greatest available receiver power
DBU	-	rms sky-wave field strength (dB > 1 μV/m) of the mode with the greatest available receiver power
SIG DBW	-	greatest available receiver power from an isotropic lossless receiving antenna (dB > 1 watt) for the different modes
F. SIG	-	fraction of days that the mode with the greatest available power from an isotropic receiving antenna is present, for which the power exceeds the required power.

Since many HF circuits involve antennas with significant directivity at one or both terminals, there are particular advantages in taking account of this fact in the signal-strength predictions. The incorporation of allowances for transmitting and receiving-antenna gains leads not only to estimates of signal strength and system performance that are more directly applicable, but also ensures that the

strongest mode is accurately identified, since this can depend on the antennas used. In RIM1A, following procedures developed at the Institute for Telecommunication Sciences, Boulder, an array matrix of antenna gain as a function of frequency and elevation angle is formed for both the transmitting and receiving terminals. Table IV shows an abbreviated version of this matrix in the case of a stacked horizontal-dipole antenna of the type HR 4/4/1 (4 bays of 4 half-wave elements with a reflector screen. The elements are spaced half a wavelength apart in height and with the lowest element one wavelength above the ground). In the program, interpolation is made within array matrices of this type in terms of the computed raypath directions. RIM1A has four output formats - a short printout of MUF and FOT similar to that of program MUFFY, the antenna gain printout, a diagnostic printout indicating intermediate parameters in the calculations of use in special investigations, and a main printout illustrated in Table V. This last print-out is similar to that of HFMLOSS, except that additional information is included in the heading data to indicate the antenna types used, their dimensions and orientations, and the associated ground-reflection constants. Revised definitions of 'SIG DBW' and 'F. SIG' are :-

SIG DBW - greatest available receiver power from a receiving antenna of the type employed (dB > 1 watt) for the different modes

F. SIG - fraction of days that the mode with the greatest available power from a receiving antenna of the type employed is present, for which the power exceeds the required power.

The printout also includes the dependability (DEP.) of the mode with the greatest available power from a receiving antenna of the type employed (i.e. the product of F. SIG and F. DAYS).

For the purposes of testing the accuracy of HF signal prediction models, the CCIR has established a data bank of past measurements and has formulated standardised procedures for the collection, tabulation and analysis of future data[19]. A representative sample of the data already deposited for 16 paths with ranges of 450-16200 km has been studied. The measurements have been normalised to give the corresponding monthly median values of rms sky-wave field strength for 1 kW radiation from an isotropic transmitting antenna and compared with the model estimates indicated by HFMLOSS[20]. There is some evidence that the differences between predictions and measurements vary with time-of-day, season and path range with a greater tendency for the predicted intensities to exceed those which are measured by night and in the winter, also for discrepancies to be greater on the longer paths. However the dependences are not large by comparison with the scatter in the results. Figure 11 shows a combined histogram of differences for all hours, frequencies, months and circuits grouped together. The median discrepancy corresponds to a predicted field strength 3 dB greater than measured. 90% of the discrepancies are less than 20 dB.

2.2.2.2 Second CCIR procedure

The second procedure incorporates many features unchanged from the first procedure and others which differ only in detail. The principal changes arise in the form of the ionospheric model adopted and in aspects of the raypath determination, with the inclusion of focusing estimates and in the allowances for ionospheric absorption, polarisation-coupling loss, sporadic-E reflection and obscuration losses and above-the-MUF losses. These are described below. The excess-system loss concept is not retained.

The model height distribution of electron concentration is illustrated for comparison in Figure 10. As with the first method the E- and F2- regions have a parabolic form, but at intermediate (F1-region) heights there is a linear increase of electron concentration rather than a void. The frequency f_j at which the linear and parabolic segments meet is set as 1.7 foE. Tests have shown that this model provides an improved fit to measured ionospheric data. Agreement with results of true-height analysis applied to sample measured ionograms is shown in Figure 12. Again the model is completely specified in terms of the standard ionospheric characteristics which are predicted, but it is to be noted that for a given set of values of these characteristics, the inclusion of finite F1-region ionisation leads to a lowering in height of the F2-layer segment. The equations adopted for hmF2 and ymF2 are :

$$(i) \quad hmF2 \quad = \frac{1490}{M(3000)F2 + \Delta M} - 176 \quad , \quad km \tag{23}$$

$$with \quad \Delta M \quad = \frac{0.18}{x - 1.4} + \frac{0.096 (R_{12} - 25)}{150} \tag{24}$$

$$where \quad x \quad = \frac{foF2}{foE} \text{ or } 1.7, \text{ whichever is the larger}$$

$$(ii) \quad ymF2 \quad = hmF2 - h'F,F2 + \Delta h' \quad , \quad km \tag{25}$$

$$where \quad \Delta h' \quad = \left(\frac{0.613}{x - 1.33}\right)^{0.86} . \ (hmF2 - 104) \tag{26}$$

h'F,F2 is the minimum virtual height of reflection from the F2-layer. During the night it is equal to h'F. A numerical representation of h'F,F2 is available. ymF2 has a pre-set minimum value of 35 km and a maximum value of (hmF2 - hmE).

For the determination of raypaths a somewhat complicated method of iteration is incorporated in which the ionospheric model is generated repeatedly at different locations along the great circle between transmitter and receiver. Mid-hop position models are thereby derived and these differ for each hop. As in the first procedure, mirror reflection is assumed to occur from a height equal to the virtual height at an equivalent frequency for propagation at vertical incidence. This virtual height is readily given by analytical equations[21]. A separate reflection height is evaluated for each hop.

One particular feature of the procedure is that longitudinal ionisation tilts can be taken into account as an option using empirical equations relating the change in virtual height along the path to an equivalent plane mirror tilt ϵ_1. With ϵ_1 taken as positive in the sense illustrated in Figure 13, then for an upgoing raypath of elevation angle Δ_1, the downcoming raypath elevation angle is

$$\Delta_2 = \Delta_1 - 2\epsilon_1 \tag{27}$$

Plane mirror tilts of 3° or less are commonplace. Their influence on the ground-range span of a single-hop mode reflected from a height of 350 km is illustrated in Figure 14. Tilt effects become significant for elevation angles less than about 30° i.e. at ground ranges in excess of 1000 km. In particular, positive tilts cause rays launched at low angles to attain a perigee, rather than return to the ground after ionospheric reflection. Clearly the inclusion of tilts in the prediction model is important, but unfortunately it is not certain whether the tilts indicated from the numerical representations of the ionospheric characteristics are likely to be meaningful on average. Studies have shown[22] that the principal region of ray refraction extends typically over some 100-400 km depending on path obliquity, and that the scale size of the gradients given from the numerical maps greatly exceeds these values. This means that even if the predictions are generally accurate over a large distance, the indicated tilt in the region of ray refraction may be of the wrong sense (see Figure 15).

Spatial attenuation is that occurring in free space, together with a convergence correction. Raypath convergence focusing is allowed for by means of empirical equations derived from raypath calculations for sample ionospheric conditions. Horizon focusing, which arises principally on low-elevation paths, is given separately for E and F-modes as a function of elevation angle. It is taken as having a maximum value determined by ionospheric roughness of 9 dB (Figure 16). Other equations predict the antipodal focusing that occurs on very long paths.

Equations for the normal ionospheric absorption arising at low and middle latitudes are based principally on measured vertical-incidence data and on the results of ray calculations for sample model ionospheres. This is in contrast to the first prediction method where oblique-path measurements are used. It is to be noted that the absorption experienced in traversing a thin slab of ionisation is directly proportional to the product of the electron concentration, the collision frequency and the slab thickness, and inversely proportional to the refractive index. The important advantages of this second procedure are :

(i) the variation with frequency includes, through the multiplicative term φ_n (Figure 17), an allowance for the change in height of reflection and for the different refractive indices at different heights; also for the way these depend on path obliquity

(ii) latitude and seasonal variations indicated by the measurements are included independently from the diurnal variation (Figure 18). In the first prediction method position and time changes are combined via the assumed solar zenith-angle dependence

(iii) finite absorption is predicted at night-time.

Explicit allowances are included for auroral absorption arising at high latitudes from precipitating-particle induced ionisation. The absorption is taken as resulting from two separate sources of particles (Figure 19). For each there is a gaussian variation with latitude and time-of-day about the maximum value. Longitudinal and seasonal dependences are included. Important solar-cycle changes in the intensities, positions and widths of the auroral absorption zones are also modelled in the representation.

When an upgoing wave is incident on the ionosphere it leads to the excitation of an ordinary (O) and an extraordinary (X) wave. These two waves have different but related polarisations which change as they progress, may be regarded as propagating independently within the ionosphere, and are subject to different amounts of absorption. The polarisation of a wave radiated from a transmitting antenna depends on the antenna configuration and the wave direction and frequency; likewise for the wave polarisation to which a receiving antenna responds. Waves travel through free space with unchanged polarisation but the power coupling between incident or emergent waves and the O and X-waves at the base of the ionosphere depends on their relative polarisations. In the second prediction method this coupling is explicitly calculated using the magnetoionic expressions for wave polarisation. In particular these require a knowledge of the wave and Earth's magnetic-field directions. The X-wave absorption is also estimated and the resultant received power from the O and X-waves thereby deduced.

Improved understanding of the properties of sporadic-E ionisation now permits the inclusion of allowances for reflection from and transmission through this layer. These allowances are based on oblique-path measurements at HF and VHF. Es-modes are assumed to be mirror reflected from a height of 110 km and the resulting reflection loss is given as an empirical function of distance, mode order, and the ratio of wave frequency to foEs (Figure 20). Other equations give the obscuration loss of transmitted waves in terms of this ratio and elevation angle. Sporadic-E obscuration losses suffered by F-modes are calculated separately for each leg of each hop. The obscuration loss for a single traverse of the Es layer, L_q, is given as :

$$L_q = -10 \log_{10} (1 - R^2) \quad , \quad dB \tag{28}$$

where
$$R = \frac{1}{1 + 10 \left(\dfrac{f}{foEs \cdot \sec i_{110}} \right)^8} \tag{29}$$

f is the wave frequency in megahertz and i_{110} is the zenith angle of the oblique ray at a height of 110 km.

Strong signals are often received at frequencies above the predicted MUF, not just because of prediction errors. The predicted values are monthly median figures so that for half the days the iono-

sphere can support higher frequencies. Other reasons are that significant signal contributions arise via sidescatter paths and from sporadic-E modes. It has also been suggested that the regular F-layer is composed of separate patches of ionisation each with its own MUF. This would mean that the number of patches supporting wave reflection falls with increase of frequency, no single frequency giving as abrupt cut-off. A single empirical allowance for these separate effects based on measured data is included in the transmission loss expression. This takes the form of an above-the-MUF loss term L_m which increases with increase of frequency. It is 0 dB at the MUF and has a value of 20 dB for a frequency of 1.4 times the MUF. The expression used for L_m is

$$L_m = 130 \left(\frac{f}{MUF} - 1 \right)^2 \quad , \quad dB \tag{30}$$

2.3 Noise

In every radio system, background noise is the limiting factor to satisfactory signal reception. This includes atmospheric noise from thunderstorms, man-made noise, galactic noise, other radio transmissions and receiver noise. At MF and HF it is rare to find receiver noise dominant and galactic noise is usually only important in quiet locations at the upper frequencies of the HF band. Models for estimating atmospheric and galactic noise were adopted by the CCIR in 1963[23] and those for man-made noise were presented in 1974[24]. Their use is recommended[25].

2.3.1 Atmospheric noise

The electromagnetic radiation from an estimated 1800 thunderstorms active throughout the world on any given occasion provides a background of atmospheric noise. This may be specified statistically in terms of parameters which are descriptive of its intensity and time structure. Whilst there are undoubtedly some applications requiring the characterisation of the time durations of different bursts of noise and of the intervals between successive bursts, very little information concerning this exists at present. Measurements of atmospheric noise over a period of many years have been made at a number of locations in different regions of the world. The most extensive series of measurements are those provided by the network of up to 16 stations sponsored since 1958 by the U.S. Institute for Telecommunication Sciences. This network gives values of mean noise power, mean noise and in some cases also the mean logarithm of the noise. From these combined parameters it is possible to determine empirically the noise amplitude-probability distribution, and in particular to assess the fraction of time that the noise exceeds any specified threshold. Since well-established and generally applicable trends in the year-to-year changes in atmospheric noise have not been found, data collected prior to 1962 have been grouped without regard for solar epoch. These results form the basis of standard atmospheric-noise models.

CCIR Report 322 presents geographical maps of median values of 1 MHz mean noise power for each of three seasonal groupings (summer, winter, equinoxes) and four-hourly periods of the 24-hours. An example of one such map is given in Figure 21. These maps have been produced from a harmonic fit to the measured data. Noise powers are expressed in terms of the noise figure F_a, defined as

$$F_a = 10 \log_{10} \left(\frac{P_n}{kT_o b} \right) \tag{31}$$

with P_n = mean available receiver power

k = Boltzmann's constant = 1.38×10^{-23} Joules per Kelvin

T_o = reference temperature, taken as 288 K

and b = effective receiver noise bandwidth, Hz.

Hence the mean noise power P_n in decibels > 1 watt is given as

$$P_n = F_a + 10 \log_{10} b - 204.0 \tag{32}$$

By interpolation between the data for the different seasons and by combining those for the different time periods, F_{am}, the median value of mean noise power for a frequency of 1 MHz has been represented numerically by Zacharisen and Jones[26]. They have expressed this parameter separately for each month in units of F_a as a function of geographic latitude λ, geographic longitude θ and Universal Time T by a series of the form

$$F_{am}(\lambda, \theta, T) = p_1(\lambda, \theta) + \sum_{i=1}^{2} \left(p_{2i}(\lambda, \theta) \sin iT + p_{2i+1}(\lambda, \theta) \cos iT \right) \tag{33}$$

where $$p_r(\lambda, \theta) = P_{1,r}(\lambda) + \sum_{j=1}^{10} \left(P_{2j,r}(\lambda) \sin j\theta + P_{2j+1,r}(\lambda) \cos j\theta \right) \tag{34}$$

and $$P_{s,t}(\lambda) = \sum_{k=1}^{10} A_{s,k,t} \sin^k \lambda \, \cos^s \lambda \tag{35}$$

The A's are numerical coefficients, of which 960 are used for each monthly representation.

The data in CCIR Report 322 give F_{am} at other frequencies in terms of the values for 1 MHz (Figure 22). Numerical representations of the different frequency variations that apply have been formulated by Lucas and Harper[27] :

$$F_{am} = A + B\left[F_{am}\right]_{1MHz} \tag{36}$$

where A and B are each seventh-order polynomials of a simple power function of the frequency. Separate sets of 14 coefficients have been generated for each seasonal-time period representation.

Day-to-day variability of mean noise power about the seasonal-time period median value is given in terms of the upper and lower decile deviations, D_u and D_ℓ respectively, in decibels (Figure 23). Lucas and Harper[27] have also produced empirical representations of these factors by fitting fifth-order polynomials of the logarithm of the frequency and generating separate coefficients for each seasonal-time period. These representations are interpreted as indicating the decile deviations from the monthly median values of hourly mean noise power. Since the representations yield values that generally differ from the noise measurements at a given frequency and location, a measure of the errors introduced in their formulation is provided by the standard deviations of the differences from F_{am}, D_u and D_ℓ, referred to as $\sigma_{F_{am}}$, σ_{D_u} and σ_{D_ℓ} respectively. These quantities are of use in assessing model accuracies and the likelihood that an estimated system performance based on the model will be achieved; they also have been represented by fifth-order polynomials of the logarithm of the frequency. Sample data are shown in Figure 23.

The noise measurements were recorded using short vertical grounded-monopole antennas and it is assumed that the above models formulated from these data are also valid for other types of antenna. Related to the noise figure F_a is the corresponding rms noise field strength E_n. For a lossless monopole

$$E_n = F_a - 65.5 + 20 \log_{10} f + 10 \log_{10} b \tag{37}$$

where E_n is expressed in dB $>1\mu$ V/m, f is the frequency in megahertz and b the receiver power bandwidth in kilohertz. In CCIR Report 322 the mean noise field strength is expressed as a deviation V_{dm} from the rms noise field strength. V_{dm} for a bandwidth of 200 Hz has also been mapped as a function of frequency and time period (Figure 23).

The variation of V_{dm} with bandwidth is illustrated in Figure 24. A family of reference cumulative amplitude probability distributions of the noise envelope has been produced and is shown in Figure 25. The curves are normalised to E_n and are parametric in the value of V_{dm}. Numerical representations of these data are available[28]. Hence it is possible to estimate for any location, frequency, time and receiver bandwidth, the probability that a specified threshold field strength will be exceeded.

2.3.2 Man-made noise

Man-made noise arises from unintentional radiation from a wide range of sources including corona discharge from power lines, rotating machinery, motor-car ignition systems, neon and fluorescent lights, hospital therapy equipment and microwave heating devices. At HF most man-made noise is incident via the ground wave, but additional noise is undoubtedly propagated via the ionosphere. Man-made noise is extremely variable with location and time, so that although many measurements exist, it is not possible to predict intensities with great accuracy.

In some circumstances, such as for example with a receiving site near a busy main road, or close to power lines, the noise may be determined by one specific source or type of source. In other circumstances it arises as the composite effect of a large number of independent contributors. At present it is not possible to make a distinction between these cases in the modelling. There is, however, some evidence of a correlation of likely intensities with degree of urbanisation, and the CCIR now proposes four basic man-made noise power curves for business, residential, rural and quiet rural areas[24] (Figure 26). Business areas are defined as the core centres of large cities and residential areas as the residential sections of large cities as well as the suburban areas of large population centres. Rural areas are defined as small communities and farms. The curves follow the relationship for the noise power F_{am} :

$$F_{am} = A - 27.7 \log_{10} f \tag{38}$$

where f is the frequency in megahertz and A is a constant for each curve.

The CCIR has not yet adopted representative values of the day-to-day variability of man-made noise. Table VI gives upper and lower decile values D_u and D_ℓ quoted by Barghausen et al.[17] for the different receiver sites and ranges of frequency.

2.3.3 Galactic noise

Galactic noise is noise incident from extra-terrestrial sources. It includes black-body 'thermal' cosmic noise and solar noise. For communication-system performance modelling where interest centres on broadband characteristics, a gradual variation with frequency is assumed and any discrete radiation bands are ignored. Results of Cottony and Johler[29] have been adopted by the CCIR in Report 322 as reference values independent of time and location (Figure 22). These fit the relationship (Lucas and Haydon[30]) :

$$P_n = -165 - 9.555 \log_e \left(\frac{f}{3}\right) \tag{39}$$

where P_n is the mean noise power in decibels > 1 watt for a 1 Hz bandwidth and f is the frequency in

megahertz.

Values given by the above equation relate to reception on a lossless half-wave horizontal dipole antenna one quarter-wavelength above a perfect ground plane and in the absence of ionospheric screening. Undoubtedly noise powers from directional antennas will differ from these figures to some extent and, particularly at frequencies below about 10 MHz, ionospheric screening of the more obliquely incident noise components is to be expected. In general, galactic noise is uniformly incident from all directions but the ionosphere acts as a filter, permitting only those components within a vertical cone to be transmitted. The size of the cone is reduced at the lower frequencies and the greater the ionisation present. Received galactic noise therefore changes with ionospheric conditions, but in system planning it is usual to base calculations on its unscreened and maximum intensity. Ionospheric screening is likely to give rise to some day-to-day variability of the received noise. In CCIR Report 322 it is proposed that the figure $D_u = D_\ell = 2$ dB should be adopted.

A computer program, named NOISEY, has been produced at the Appleton Laboratory, Slough to compute the intensities of the different sources of noise for a given location and month. Input data include a specification of the receiver noise power bandwidth and either the type of site (business, residential, rural or quiet rural) or the estimated man-made noise power at a frequency of 3 MHz. An example of the program printout is given in Table VII. In addition to the data provided as input, this indicates for each frequency and hour the monthly median values of mean power arising from atmospheric ATM, man-made MAN and galactic GAL sources (expressed in dB > KTb) together with their resultant, RES. Also quoted are the resultant power in dB > 1 watt within the receiver bandwidth and the corresponding rms field strength, RES DBU in dB > 1 μV/m.

System performance at HF

The type and quantity of information to be conveyed over a proposed radio circuit determine the modulation system and necessary receiver bandwidth. The next step in the circuit design is to specify the wanted signal/noise power ratio at the receiver. Reference minimum signal/noise ratios judged to give satisfactory reception for different services are available[31].

So far, attention has been paid principally to monthly median conditions and ways have been described of estimating monthly median signal/noise ratio. At present there are no accepted CCIR procedures for system-performance determination but a number of schemes originally developed in the U.S.A. are now in widespread use. An important monthly median system performance parameter is the LUF or lowest usable frequency. Since in general at HF signal intensity falls with reduction of frequency, principally because of the greater ionospheric absorption, and because this change is more rapid than for the noise, signal/noise ratio is reduced at the lower frequencies. The LUF is the lowest frequency for which the monthly median signal/noise ratio equals that which is wanted. The LUF may be specified for a particular propagation mode, or for the circuit as a whole via any mode.

Two other important parameters that have been introduced to quantify system performance by taking account statistically of day-to-day variations are the reliability and the service probability. Again these may relate to a single mode or to the circuit as a whole. The reliability of a mode is defined as the probability that this mode shall be present and that its signal/noise power ratio equals or exceeds the wanted value. Means of evaluation of the availability have already been discussed in Section 2.2.1. The day-to-day distribution of signal/noise ratio is estimated similarly from the monthly median signal/noise ratio by combining the day-to-day variabilities of the signals and noise, assuming these to be uncorrelated, and by again assuming that some distribution such as the chi-square law holds. Thereby the probability that a specified signal/noise ratio will be equalled or exceeded is given. On the assumption that the day-to-day ionospheric changes influencing mode support are not correlated with those giving rise to changes in signal/noise ratio, the mode reliability is then taken as the product of the mode availability and the probability that the mode provides a specified signal/noise ratio. Whilst undoubtedly there is some correlation between daily variations of the ionospheric support of different modes, and likewise in their relative signal strengths, a means of allowing for this has yet to be found.

Table VIII shows examples of the range of combined circuit availabilities for two modes with separate availabilities Q_1 and Q_2 and different degrees of correlation. When the modes are uncorrelated the availability is Q given as

$$Q = 1 - (1 - Q_1)(1 - Q_2) \tag{40}$$

There are difficulties in deriving a single value for the circuit availability because this requires both the specification and evaluation of some parameter indicative of the correlation between the modes and also a means of determining the day-to-day spatial variability of the ionosphere at the separate mode reflection positions. At present it is usual to take the circuit availability as equal to the largest of the separate mode availabilities, and likewise for the reliabilities.

Since reliability is the product of the availability which falls with increase of frequency and the probability of achieving a required signal/noise power ratio which is greater the higher the frequency, there is some frequency for which the reliability is a maximum. This frequency may be regarded as an alternative best frequency to the OWF as already defined. However, unlike the OWF, it is to be noted that the frequency of greatest reliability is system sensitive and is lowered the greater the transmitter power or the less the required signal/noise power ratio.

Table IX is an example of a computer printout from the program HFMUFES 3 developed by the Institute for Telecommunication Sciences, Boulder, which includes the estimation of circuit reliability. Input data are similar to those from program RIM1A (see Section 2.2.2.1) except that a required signal/noise mean power must be specified. For each frequency there are tabulated :

        MODE   - propagation mode with the greatest reliability
        ANGLE   - elevation angle (degrees) of the mode with the greatest reliability

F. DAYS   - availability of the mode with the greatest availability
DBU   - rms sky-wave field strength (dB > 1 μV/m) of the mode with the greatest reliability
S/N DB   - monthly median signal/noise mean power ratio in 1 Hz bandwidth (dB) for the signal mode with the greatest available receiver power, when present
REL   - product of the availability of the mode with the greatest availability and the probability that the mode with the greatest available receiver power when present provides a monthly median signal/noise mean power ratio exceeding that required.

An alternative definition of LUF used in HFMUFES 3 is the lowest frequency giving a specified required reliability rather than a specified signal/noise ratio. Table X shows a second printout from this program of FOT and LUF formulated as :

FOT   - highest frequency with an availability of 0.9
LUF   - lowest frequency for which the monthly median signal/noise mean power ratio for the signal mode with the greatest available receiver power when present exceeds that required for the fraction of occasions defined on input as the required circuit reliability.

All parameters used in the reliability predictions are somewhat uncertain, and a standard error may be ascribed to each. The terms involved include the uncertainty in the predictions of the monthly median noise and signal powers, and of the standard deviations of the noise and signal day-to-day variations. The total uncertainty variance, found by adding the appropriate individual uncertainty variances may be used to define an uncertainty distribution giving the probability that a required reliability is achieved. This is known as the service probability. Table XI from program HFMUFES 3 is similar to Table IX, except that in place of REL there is S. PROB - probability that the required circuit reliability will be achieved.

So far, the concern has been entirely with system-performance parameters depending on signal and noise intensities. Mention should also be made of signal multipath distortion. By combining predictions for different modes, the probability of multipath can be estimated. Multipath is defined as existing when two or more modes are jointly present having a difference in signal powers of less than some specified amount and a difference in group-path times exceeding a given figure. Predictions of multipath involve a simple extension of the procedures described.

Multipath is indicated in the sample printout from HFMUFES 3. Other computer programs providing estimates of system-performance parameters include HFMUFES 4 and IONCAP (Institute for Telecommunication Sciences, Boulder) and APPLAB 2 (Appleton Laboratory, Slough). In this last program, multipath considerations include an allowance for the high-angle ray present at frequencies close to the MUF.

The excess group path of the high-angle ray relative to the low-angle ray (ΔP) depends on the ratio of the wave frequency (f) to the mode MUF (f_m) and on the hop ground range (d_1), except that this excess reaches a minimum for hop ground ranges of 2000-2500 km and there is little change out to the limiting distance for a single-hop mode. With ΔP and d_1 in kilometres :

$$\Delta P = \frac{850,000}{d_1} \sqrt{1 - \frac{f}{f_m}} \qquad (41)$$

for $d_1 \leqslant 1500$ km. At greater ranges, values for $d_1 = 1500$ km apply approximately. The excess attenuation of the high-angle ray, relative to that of the corresponding low-angle ray, ΔL, is taken as

$$\Delta L = 0.1 \ \Delta P \qquad (42)$$

where ΔL is expressed in decibels and ΔP in kilometres.

3. SHORT-TERM SIGNAL PROPAGATION MODELS AT HF

Short-term models for frequency management are directed towards assessing the best frequency to use with an existing system in the light of the prevailing ionospheric conditions of the time. Therefore the requirement is to use system-performance predictions of the form already described, but with the forecast ionosphere replaced by a more accurate representation. King and Slater[32], and Rush et al.[33] have studied the day-to-day variability of different ionospheric characteristics. They conclude that the greatest fractional variations in the E and F regions arise in foF2. Therefore a useful improvement in modelling capability would be achieved if it were possible to use near real-time values of foF2 and to retain monthly-median estimates of the other ionospheric characteristics. Hence effort has centred on deducing foF2. Although forecasts can sometimes be made of solar-disturbance effects leading to enhanced D-region ionisation, models of daily absorption are not feasible at the present time.

Procedures involving vertical-incidence sounders at one of the path terminals to measure foF2 directly have only limited use because from such measurements it is possible to infer values at other locations separated only by short distances. Rush and Miller[34] have shown that at mid-latitudes the correlation of daily departures of foF2 from the monthly median values at different point separations depends markedly on path orientation, time-of-day and season. The correlation at a fixed Universal Time extends over a greater distance in the E-W direction than for N-S paths, despite the change in local time along the paths in the former case. Typically the correlation falls to a value of 0.7 in a distance of about 2000 km for E-W paths and 1000 km for N-S paths. Suggestions have been made that foF2 values at different locations should correlate better if they are compared at the same local time, and the possibility merits further study. This would mean that measured data could be used to provide better forecasts of conditions on westerly than easterly paths.

Oblique forward sounders and backscatter sounders have hitherto conventionally been used operationally with varying but generally limited success as direct probes of propagation conditions in support of point-

to-point radio systems. They can also be employed with appropriate processing algorithms to infer iono-spheric structure as described in a separate lecture of this present series. However the complexity of such systems and analysis procedures makes these unattractive as adjuncts to conventional commercial tele-communications facilities.

Two approaches then remain : to use past foF2 data or to find other parameters that can be measured and on which foF2 depends. Rush and Gibbs[35] have compared the accuracy of forecasts of daily foF2 in terms of observed monthly median models with those deduced from weighted means of the preceding past days. Figure 27 is an example from their published results. They found that on average for a series of locations and times the use of a previous five-day period value gives estimates that are comparable or better than from the observed monthly median. This means they are to be preferred to using predicted monthly median figures. Nevertheless they conclude that an uncertainty of the order of 0.5 MHz exists at all times and that when attempts are made to extrapolate results to remote locations where measured data are not available, errors are likely to be prohibitive.

Interest centres on the identification of precursors of solar disturbances responsible for changes in the ionosphere and in the Earth's magnetic field. A review of solar-terrestrial relations and short-term ionospheric forecasting has been presented by Cook and McCue[36]. Optical, X-ray and radio emissions from the sun are observed daily at a number of ground-based sites and also aboard satellites. Ionospheric disturbances following solar flares occur either in close time succession and last for several hours, or begin 24-36 hours later and last for several days. The former arise from enhanced X-ray, ultraviolet and high-energy particle radiation, while the latter are associated with lower-energy particles.

Various attempts have been made to correlate daily foF2 values with indices of solar and magnetic activity. The 10.7 cm solar flux and the extreme ultraviolet flux producing the ionosphere are well correlated, so that monthly median foF2 varies in a systematic manner with monthly median flux. McNamara[37] has compared daily flux and foF2 values. He finds that during magnetically quiet periods daily and 60-day average flux values are equally good in predicting hourly foF2 a day ahead.

Barghausen et al.[17] extended their long-term prediction procedure by including models for the re-gression of foF2 with planetary magnetic activity index Kp. Different reference regression relationships have been generated as a function of midpath geomagnetic latitude, local time, season and smoothed sunspot number. Unfortunately, however, the operational use of the procedure with Kp approximated by the local magnetic-activity index K has proved of only limited success. Eccles and King (private communication) have shown that daily foF2 for Lindau correlates better with Kp if a time lag is introduced between the magnetic change and the ionospheric response. Figure 28 shows examples in which the correlation coefficient was - 0.2 and - 0.1 without a lag, but became around - 0.7 for a lag of 24-36 hours. The improvement in the dependence of the daily foF2 values on Kp when the optimum lag is used is illustrated in Figure 29. Whilst there are clearly difficulties in deriving the morphology of the optimum time lag, the approach appears promising and to merit further study.

4.   CONCLUSIONS

The current state-of-the art in long-term models for sky-wave signal-strength estimation at MF and HF, noise and system-performance assessment is reviewed. Areas where additional work is needed are mentioned and it is evident that further changes to the models are likely to be proposed in the future. These may well concentrate on model simplifications rather than improvements in accuracy.

The position regarding short-term models of HF sky-wave propagation is discussed with regard to methods of estimating the ionospheric characteristic foF2. Further studies are called for and these should be directed towards the formulation of new procedures which, even if not yielding quantitatively accurate estimates, may prove of value in disturbance forecasting. For some practical radio systems, however, the development of improved operational channel-sounding procedures may be a more attractive line to pursue.

5.   REFERENCES

1. BRADLEY, P. A. (1979) Propagation at medium and high frequencies, 1 : Practical radio systems and modelling needs in 'Aerospace propagation media modelling and prediction schemes for modern communications, navigation and surveillance systems', AGARD Lecture Series 99 (this volume).

2. AGARD (1978) Recent advances in radio and optical propagation for modern communications, navigation and detection systems. Lecture Series 93.

3. AGARD (1968) Radio wave propagation. Lecture Series XXIX.

4. AGARD (1970) Ionospheric Forecasting. Conference Proceedings 49 Ed. V. Agy.

5. KNIGHT, P. (1973) MF propagation : a wave-hop method for ionospheric field-strength prediction. BBC Engineering, 100, 22-34, BBC, London.

6. CCIR (1978) Prediction of sky-wave field strength between 150 and 1600 kHz. Recommendation 435-3, Documents of XIVth Plenary Assembly, International Telecommunication Union, Geneva.

7. CCIR (1938) Documents of the Cairo International Conference on Radio communications, 1, 425-433, International Telecommunication Union, Geneva.

8. EBERT, W. (1962) Ionospheric propagation on long and medium waves. EBU Review, Part A, 71-73, EBU Technical Centre, Brussels.

9. CCIR (1978) The accuracy of predictions of sky-wave field strength in Bands 5 (LF) and 6 (MF). Report 432-1, Documents of XIVth Plenary Assembly, International Telecommunication Union, Geneva.

10. WANG, J. C. H. (1975) A comparative study of medium frequency sky-wave field strength prediction methods. FCC Report RS 75-07, NTIS, PB 245564, Springfield, Va.

11. WANG, J. C. H. (1977) Predictions of medium frequency sky-wave field strength in North America, IEEE Trans. Broadcasting, BC-23, 43-49.

12. JONES, W. B., GRAHAM, R. P. and LEFTIN, M. (1969) Advances in ionospheric mapping by numerical methods. ESSA Tech. Report ERL 107-ITS 75, U.S. Government Printing Office, Washington.

13. CCIR (1966) CCIR atlas of ionospheric characteristics. Report 340, Documents of XIth Plenary Assembly, International Telecommunication Union, Geneva.

14. CCIR (1970) CCIR interim method for estimating sky-wave field strength and transmission loss at frequencies between the approximate limits of 2 and 30 MHz. Report 252-2, Documents of XIIth Plenary Assembly, International Telecommunication Union, Geneva.

15. CCIR (1978) Second CCIR computer-based interim method for estimating sky-wave field strength and transmission loss at frequencies between 2 and 30 MHz. Supplement to Report 252-2, Documents of XIVth Plenary Assembly, International Telecommunication Union, Geneva.

16. CCIR (1978) Estimating sky-wave field strength and transmission loss at frequencies greater than 2 MHz. Recommendation 533, Documents of XIVth Plenary Assembly, International Telecommunication Union, Geneva.

17. BARGHAUSEN, A. F., FINNEY, J. W., PROCTOR, L. L. and SCHULTZ, L. D. (1969) Predicting long-term operational parameters of high-frequency sky-wave telecommunication systems. ESSA Tech. Rept. ERL 110-ITS 78, U.S. Government Printing Office, Washington.

18. PIGGOTT, W. R. and RAWER, K. (1972) URSI Handbook of ionogram interpretation and reduction. Report UAG-23, World Data Center for solar-terrestrial physics, NOAA, Boulder, Colorado.

19. CCIR (1978) Measurement of sky-wave signal intensities at frequencies above 1.6 MHz. Report 253-3, Documents of XIVth Plenary Assembly, International Telecommunication Union, Geneva.

20. CCIR (1978) Comparisons between observed and predicted sky-wave field strength and transmission loss at frequencies between 2 and 30 MHz. Report 571-1, Documents of XIVth Plenary Assembly, International Telecommunication Union, Geneva.

21. CCIR (1978) CCIR atlas of ionospheric characteristics. Supplement 3 to Report 340, Documents of XIVth Plenary Assembly, International Telecommunication Union, Geneva.

22. BRADLEY, P. A. (1978) Ionospheric data requirements for better techniques of HF sky-wave field strength and system performance prediction. URSI International Symposium on Radio Waves and the Ionosphere, Helsinki.

23. CCIR (1963) World distribution and characteristics of atmospheric radio noise. Report 322, Documents of Xth Plenary Assembly, International Telecommunication Union, Geneva.

24. CCIR (1978) Man-made radio noise. Report 258-3. Documents of XIVth Plenary Assembly, International Telecommunication Union, Geneva.

25. CCIR (1978) Use of data on radio noise. Recommendation 372-2, Documents of XIVth Plenary Assembly, International Telecommunication Union, Geneva.

26. ZACHARISEN, D. H. and JONES, W. B. (1970) World maps of atmospheric noise in universal time by numerical mapping. OT/ITS Resch. Rept. 2, U.S. Government Printing Office, Washington.

27. LUCAS, D. L. and HARPER, J. D. (1965) A numerical representation of CCIR Report 322 high frequency (3-30 Mc/s) atmospheric radio noise data, National Bureau of Standards Tech. Note 318, U.S. Government Printing Office, Washington.

28. AKIMA, H. (1972) A method of numerical representation for the amplitude-probability distribution of atmospheric radio noise. OT/ITS Resch. and Eng. Rept. 27, U.S. Government Printing Office, Washington.

29. COTTONY, H. V. and JOHLER, J. R. (1952) Cosmic radio noise intensities in the VHF band. Proc. IRE, 40 (9), 1053-1060.

30. LUCAS, D. L. and HAYDON, G. W. (1966) Predicting statistical performance indexes for high frequency ionospheric telecommunication systems. ESSA Tech. Report IER 1 - ITSA 1, U.S. Government Printing Office, Washington.

31. CCIR (1978) Bandwidths, signal-to-noise ratios and fading allowances in complete systems. Recommendation 339-4, Documents of XIVth Plenary Assembly, International Telecommunication Union, Geneva.

32. KING, J. W. and SLATER, A. J. (1973) Errors in predicted values of foF2 and hmF2 compared with the observed day-to-day variability. Telecommunication Journal, 40, (12), 766-770.

33. RUSH, C. M., MILLER, D. and GIBBS, J. (1974) The relative daily variability of foF2 and hmF2 and their implications for HF radio propagation. Radio Science, 9, 749-756.

34. RUSH, C. M. and MILLER, D. (1973) A three-dimensional ionospheric model using observed ionospheric parameters. AFCRL Tech. Rep. 73-0567. Defense Documentation Center, Alexandria, Va.

35. RUSH, C. M. and GIBBS, J. (1973) Predicting the day-to-day variability of the midlatitude ionosphere for application to HF propagation predictions. AFCRL Tech. Rep. 73-0335, 2-9. Defense Documentation Center, Alexandria, Va.

36. COOK, F. E. and McCUE, C. G. (1975) Solar-terrestrial relations and short-term ionospheric forecasting, Radio and Electronic Engineer, 45, 11-30.

37. McNAMARA, L. F. (1976) The correlation of individual values of foF2 and M(3000)F2 with the solar 10.7 cm flux under magnetically quiet conditions. Ionospheric Prediction Service (Australia), Series R No. 30.

38. HARTZ, T. R. and BRICE, N. M. (1967) The general pattern of auroral particle precipitation. Planet. Space Sci., 15, 301-329.

6.   ACKNOWLEDGEMENTS
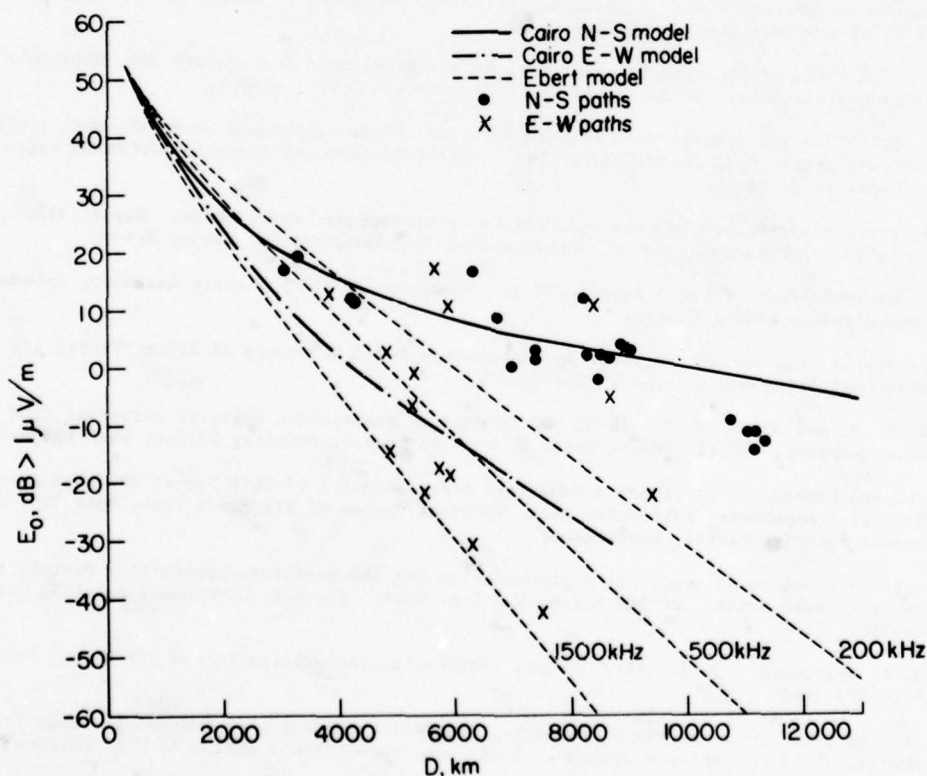
Figure 1   Comparison of measured and predicted annual median night-time MF sky-wave field strengths, E_o (from CCIR Recommendation 435-3)
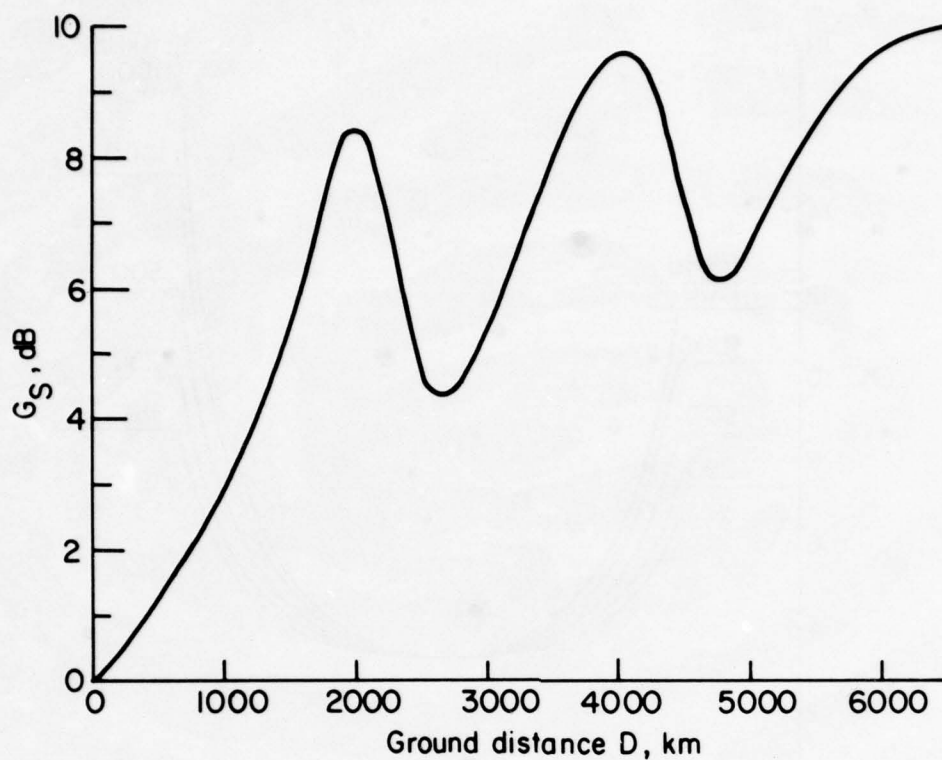
Figure 2   Sea gain G_s at MF for a single terminal on the coast and uninterrupted sea in the receiver direction (from CCIR Recommendation 435-3)
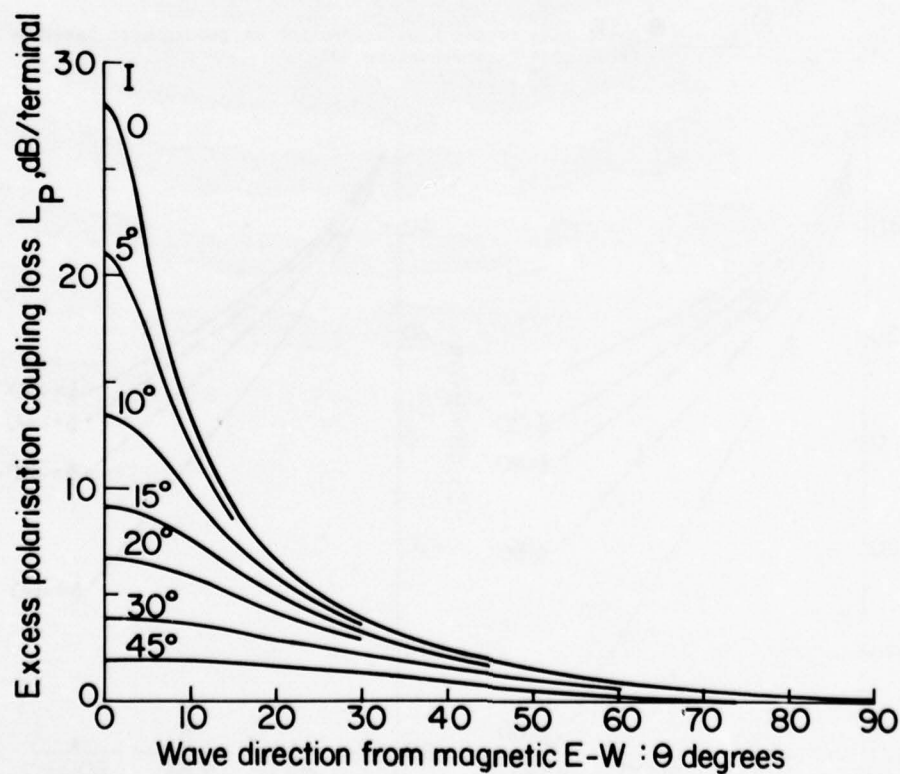
Figure 3   Excess polarisation-coupling loss L_p for single terminal (from CCIR Recommendation 435-3)
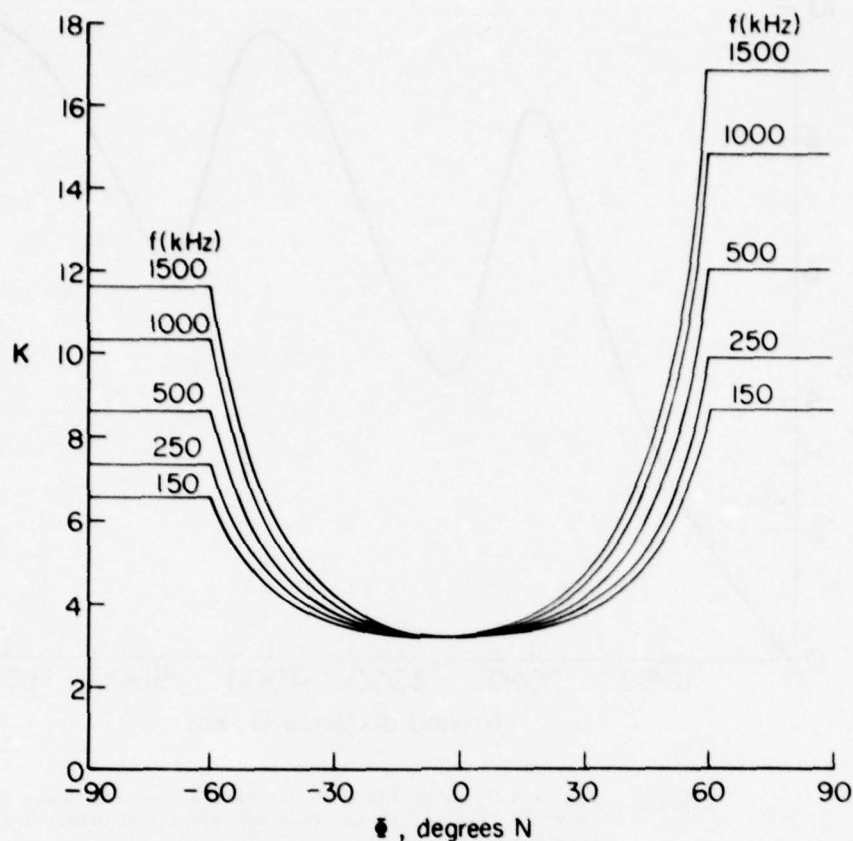
Figure 4   Basic loss factor K as a function of geomagnetic latitude Φ
(from CCIR Recommendation 435-3)
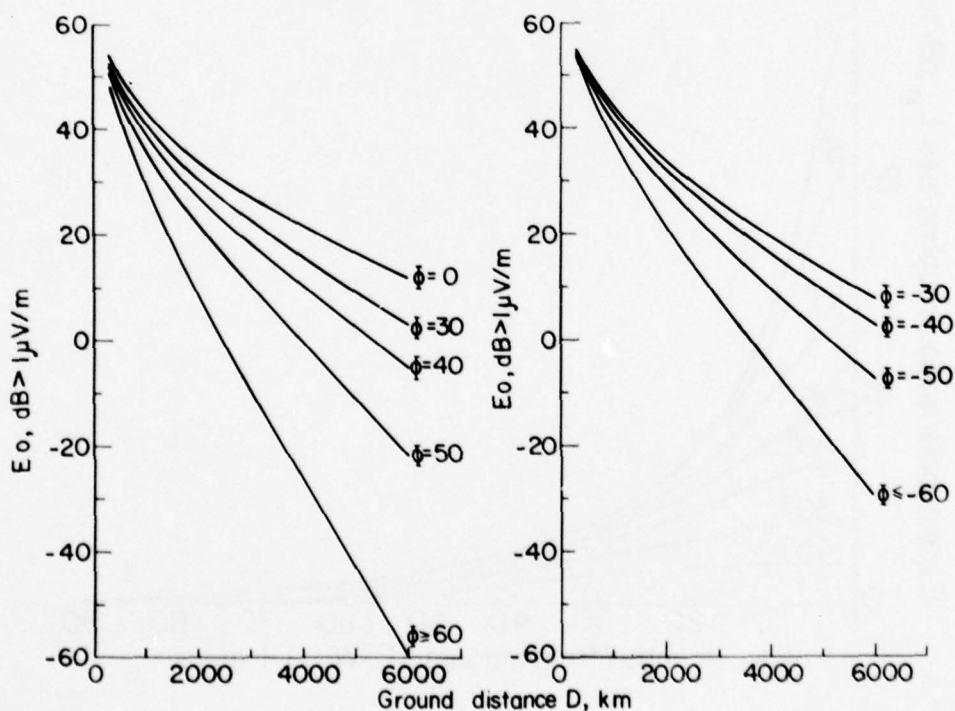
Figure 5   Night-time sky-wave field strengths E_0 at 1 MHz given by
CCIR model for different geomagnetic latitudes Φ and cymomotive
force of 300 V with G_s, L_p and R_{12} all zero (from CCIR
Recommendation 435-3)
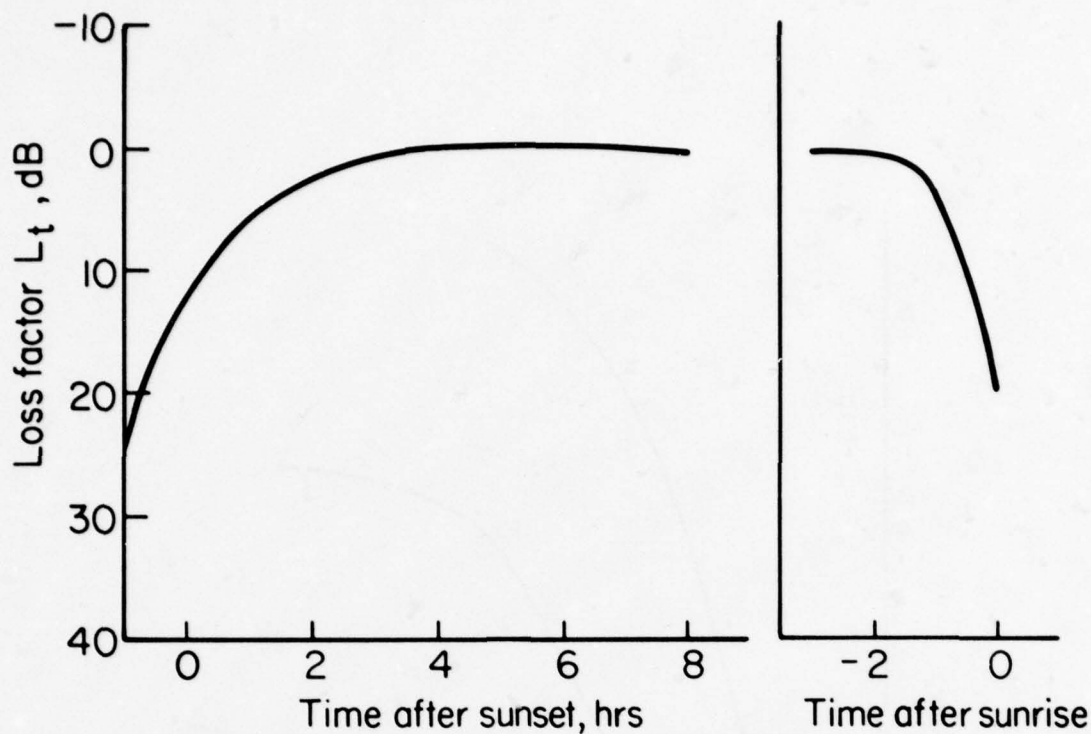
Figure 6   Diurnal loss factor L_t (from CCIR Recommendation 435-3)

Predicted-measured field strength , dB
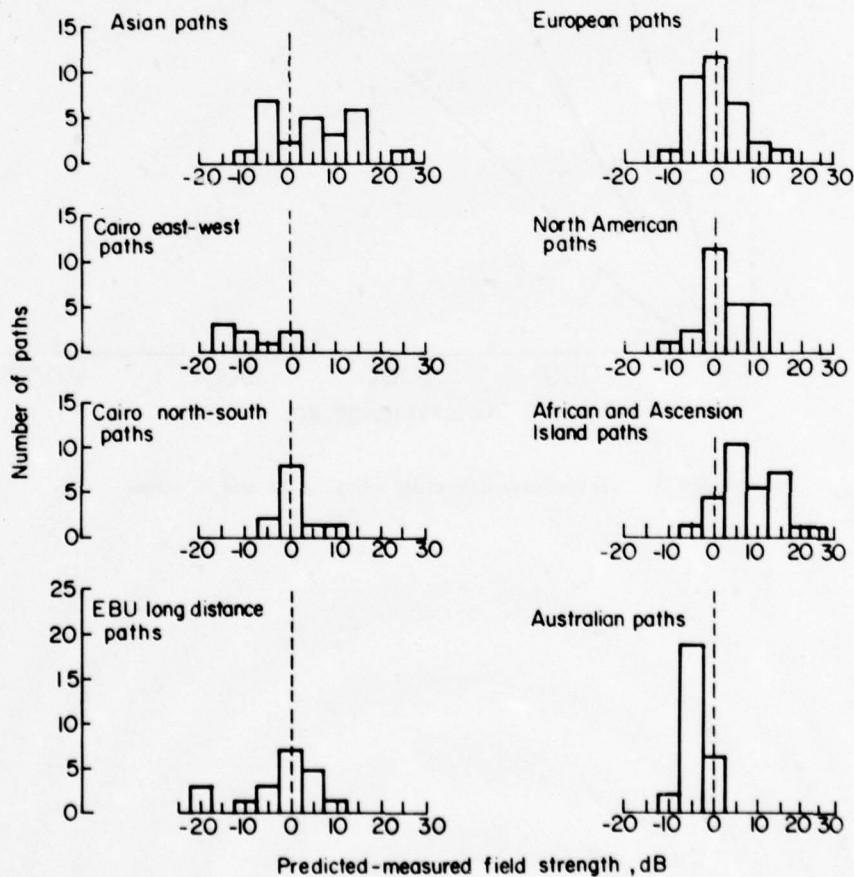
Figure 7   Histograms of prediction discrepancies at MF for 1976 CCIR model
(from CCIR Report 431-1 (Rev. 76))
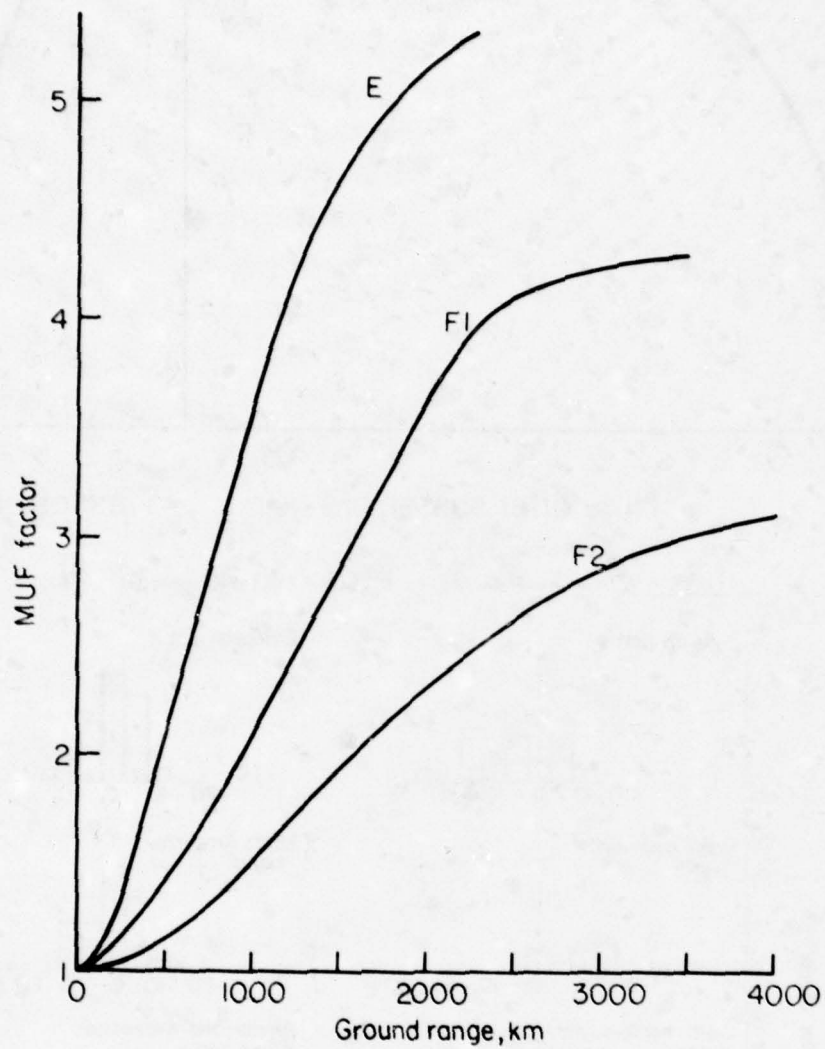
Figure 8   MUF factors for single-hop E, F1 and F2 modes
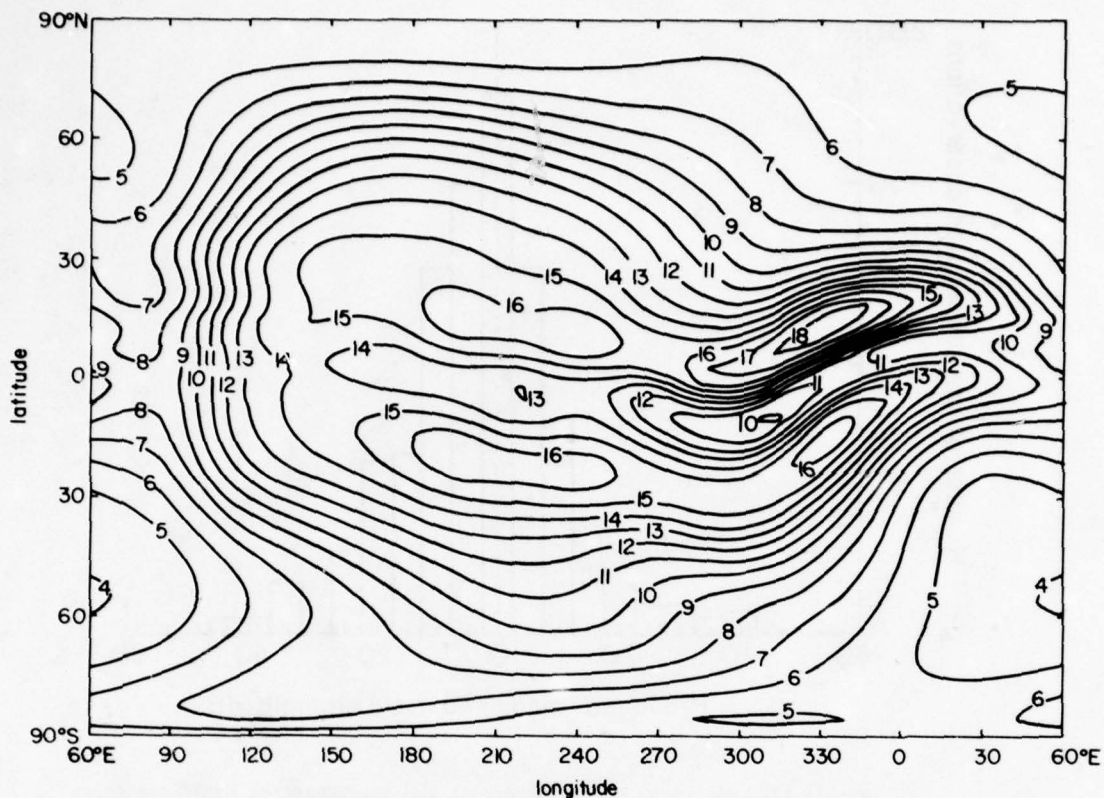
Figure 9   Predicted median EJF(ZERO)F2, MHz for 00 h UT in March 1958
(from CCIR Report 340)
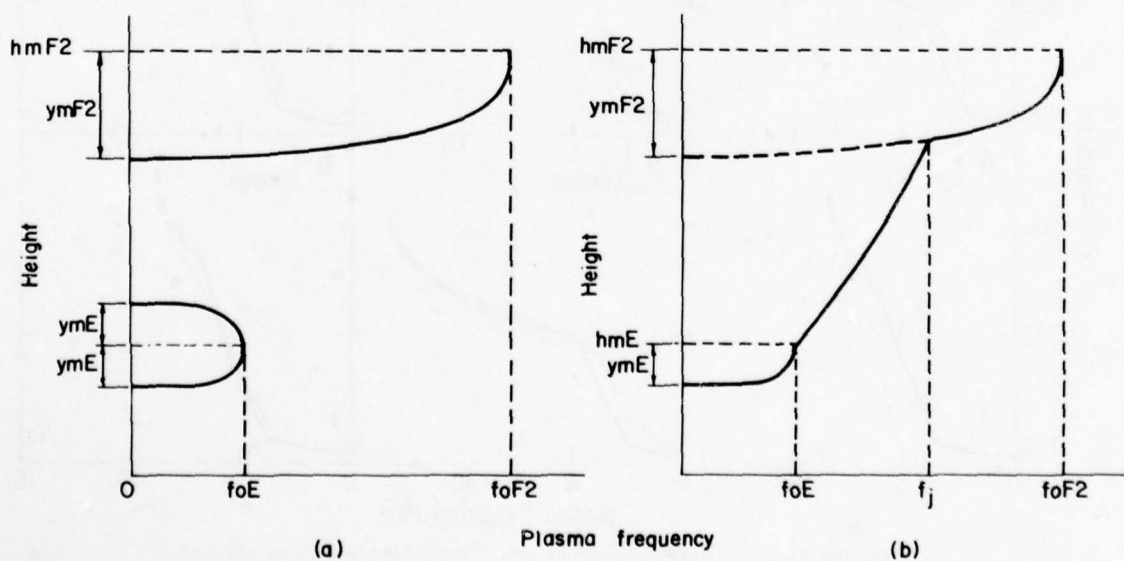
Figure 10   Models of height distribution of electron concentration

(a) First CCIR procedure
(b) Second CCIR procedure
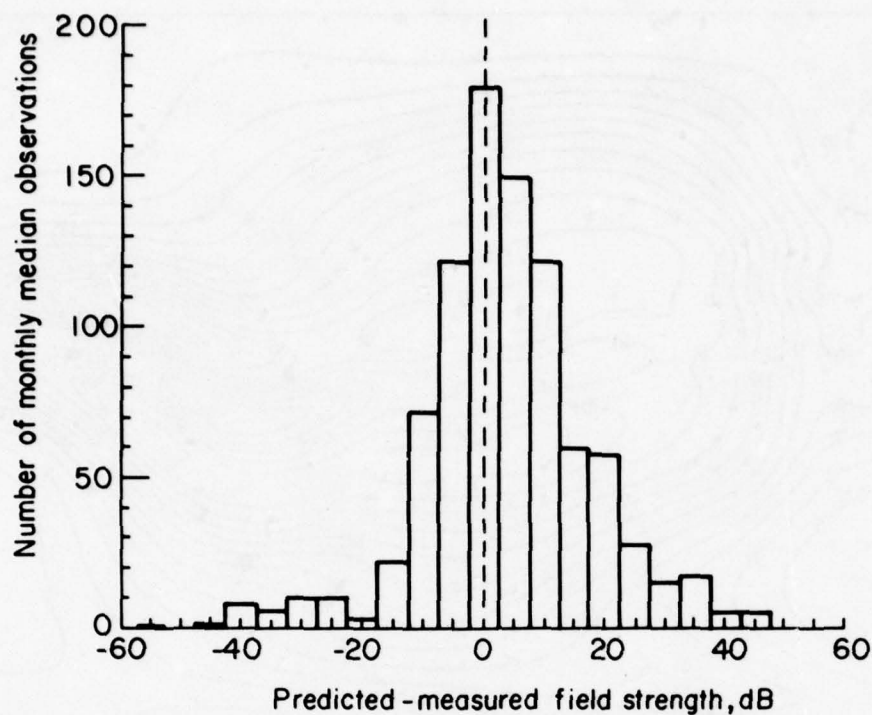
Figure 11   Histogram of signal prediction discrepancies at HF for first
CCIR procedure   (from CCIR Report 571-1)
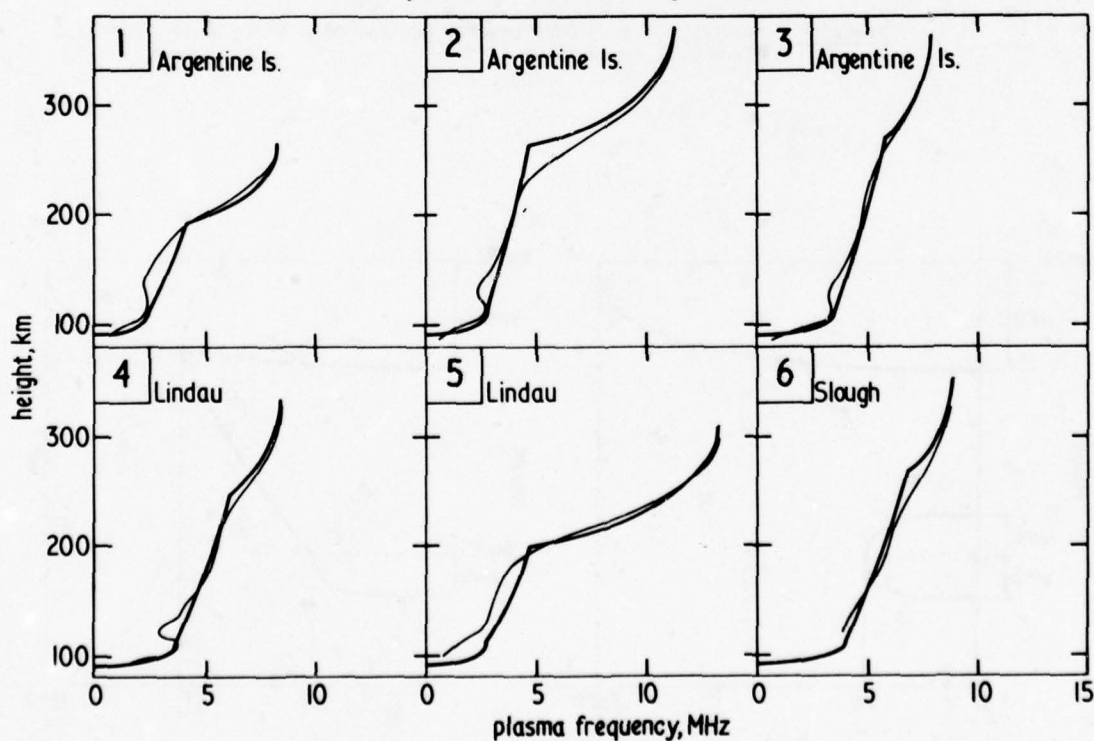
Figure 12   Comparison of model and true-height analysis electron-
concentration profiles for range of sample occasions

1. Argentine Islands 1645 LT 29 September 1968
2. Argentine Islands 0530 LT 17 December 1968
3. Argentine Islands 1330 LT 31 December 1967
4. Lindau   1550 LT 21 July 1958
5. Lindau   1430 LT 10 December 1958
6. Slough   1200 LT 27 July 1957
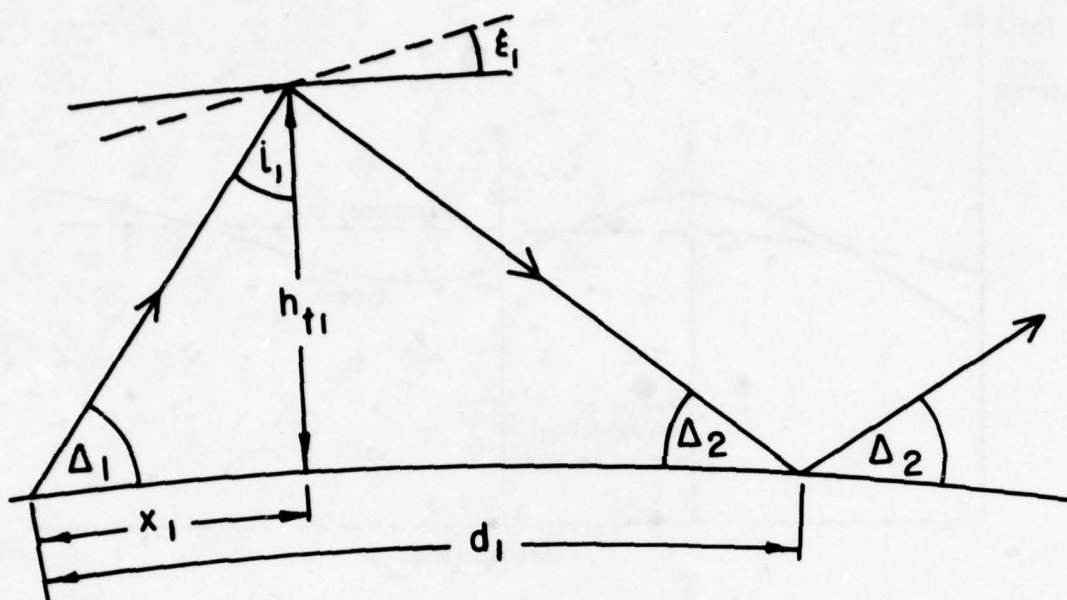
Figure 13   Ray-hop geometry for reflection from a plane tilted mirror
(from Supplement to CCIR Report 252-2)
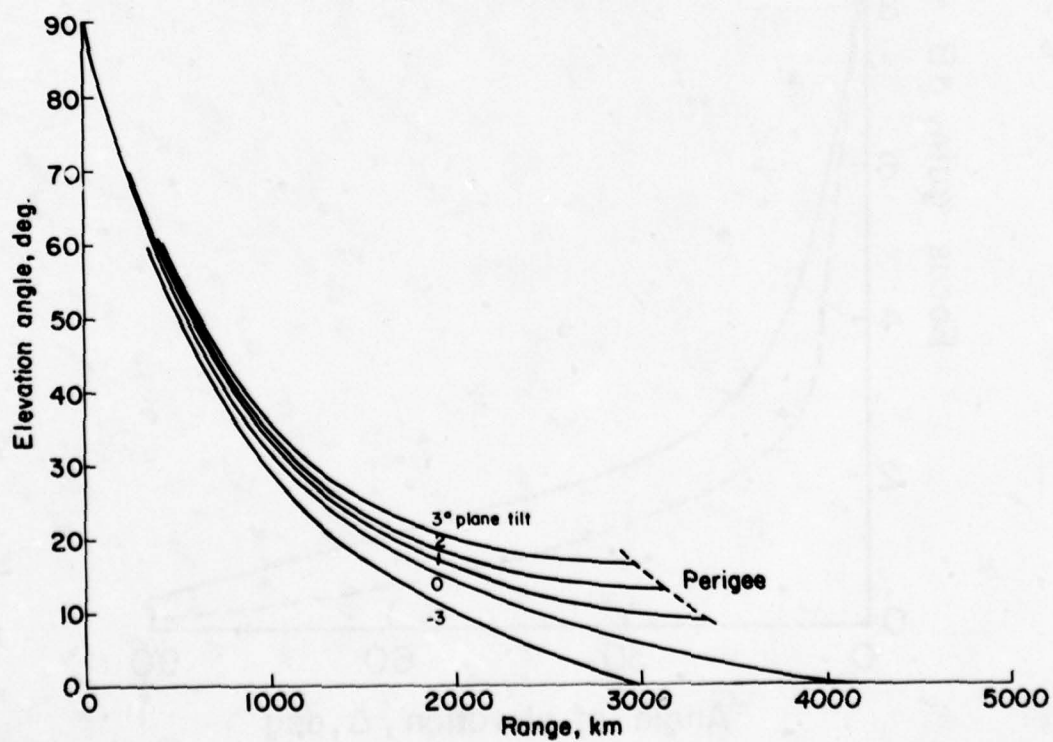
Figure 14   Ground range for reflection from plane tilted mirror
at height of 350 km
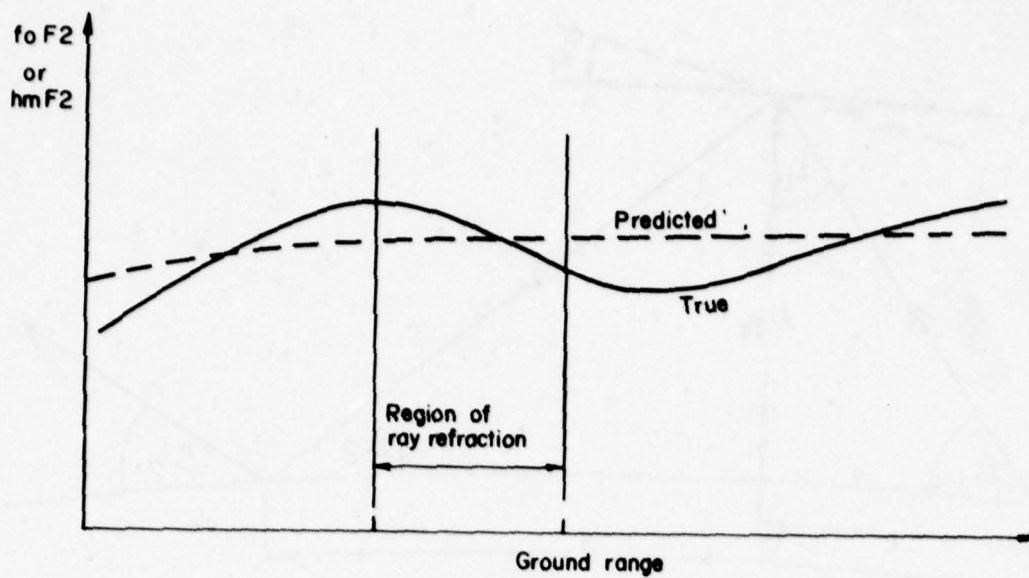
Figure 15   True and predicted ionospheric tilts
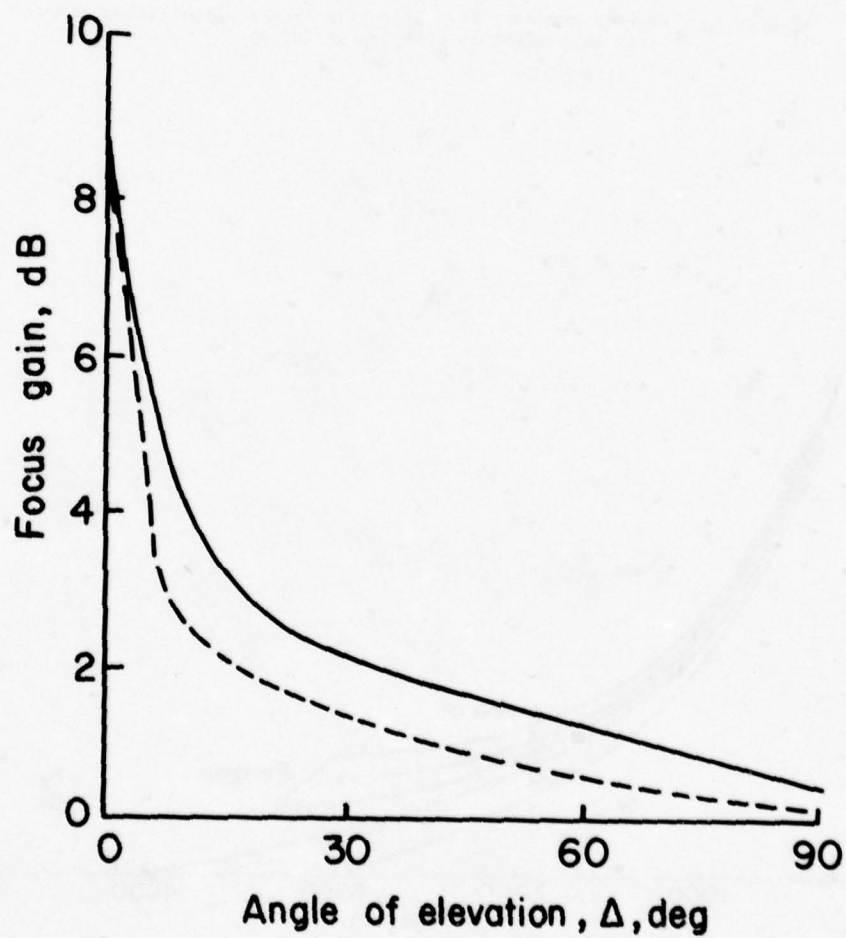
Figure 16   Horizon focus gain (from Supplement to CCIR Report 252-2)

——————— F modes

- - - - E modes
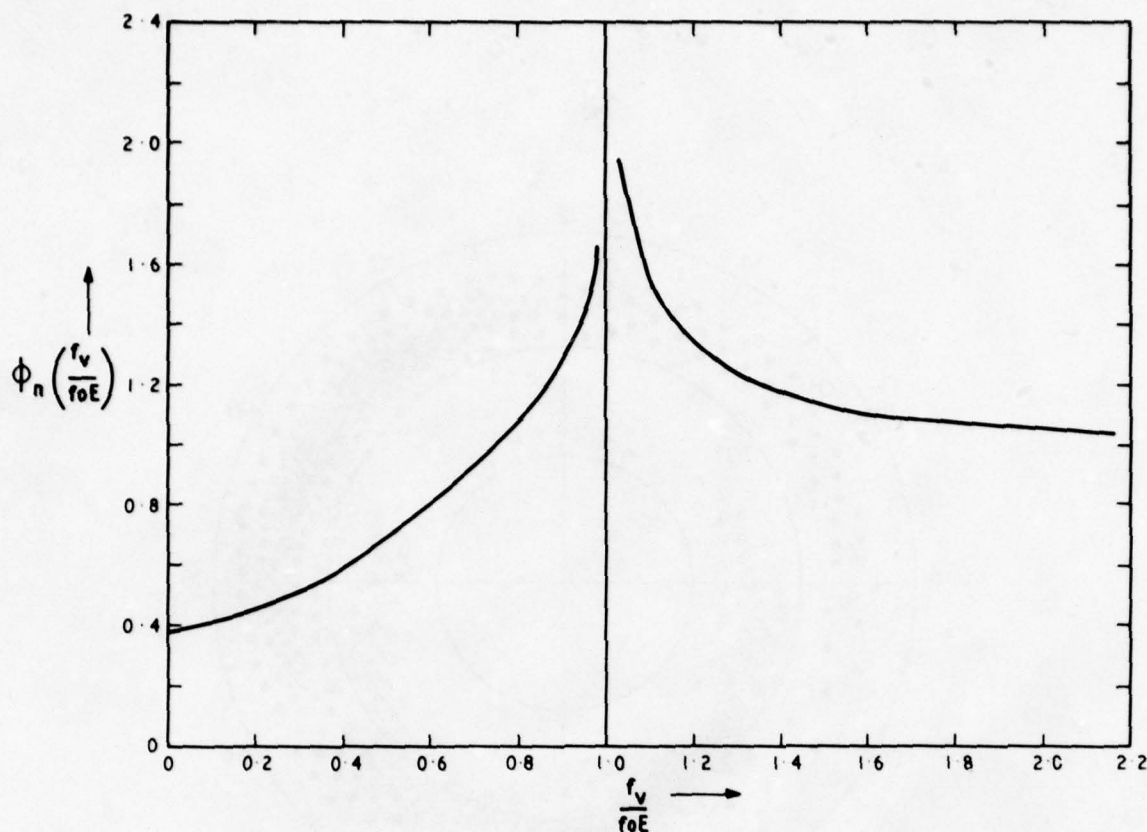
Figure 17   Absorption factor φ_n for equivalent vertical-incidence
frequency f_v (from Supplement to CCIR Report 252-2)
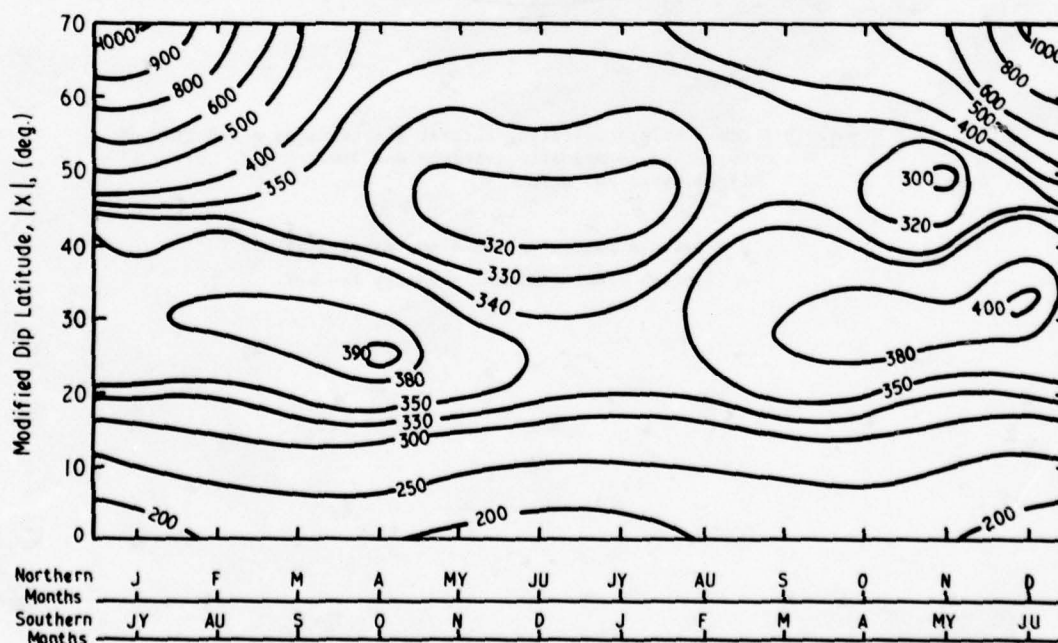
Figure 18   Absorption factor A_T for an overhead sun and a smoothed sunspot
number of zero (from Supplement to CCIR Report 252-2)

$$X = \arctan \frac{I}{\sqrt{\cos \lambda}}$$

where I = magnetic dip in radians and λ = geographic latitude
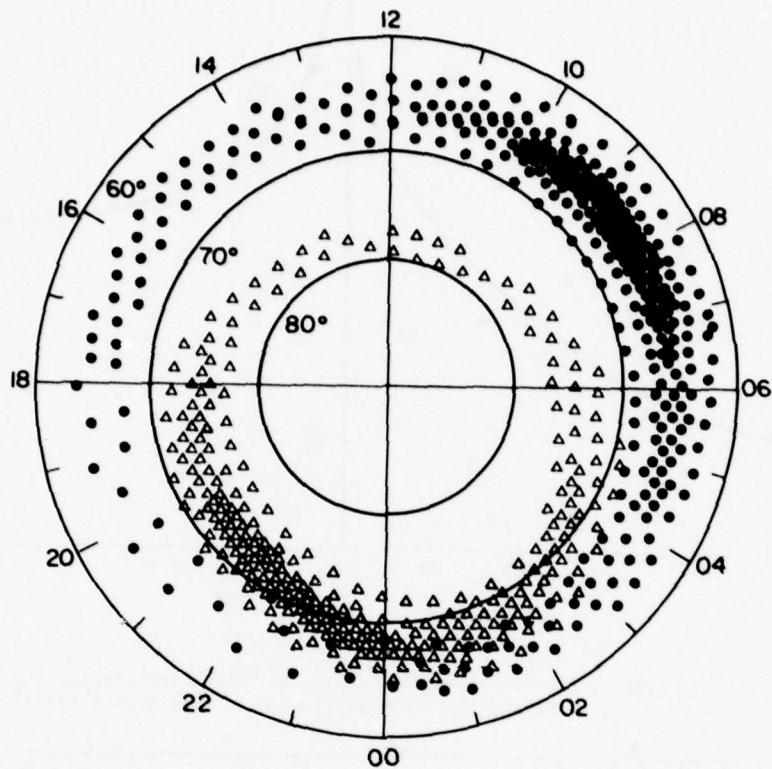
Figure 19   Zones of precipitating auroral electrons as a function of
corrected geomagnetic latitude and time
(from Hartz and Brice[38])

   •   drizzle precipitation - energy tens of keV

   Δ   splash precipitation - energy few keV
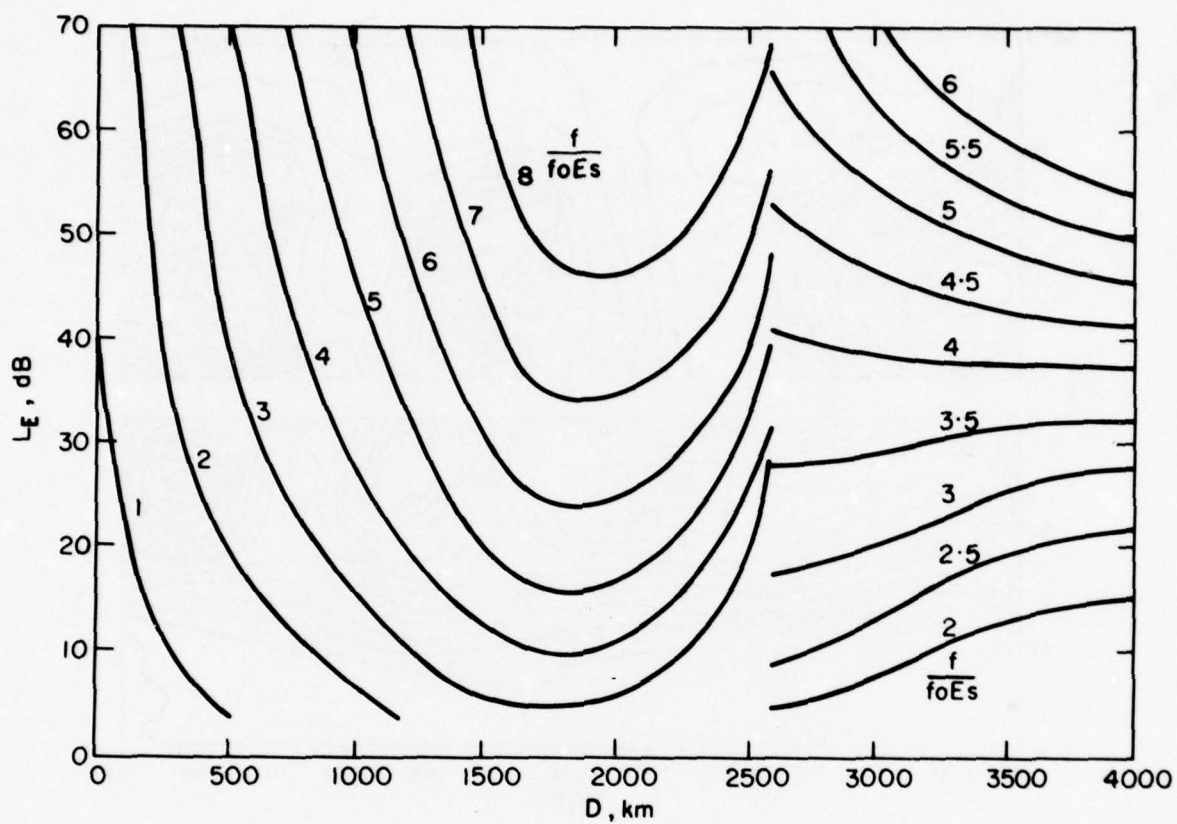
Figure 20   Sporadic-E reflection loss, L_r
(from Supplement to CCIR Report 252-2)

Curves relate to a single hop for ground range
D < 2500 km and to two hops for greater distances
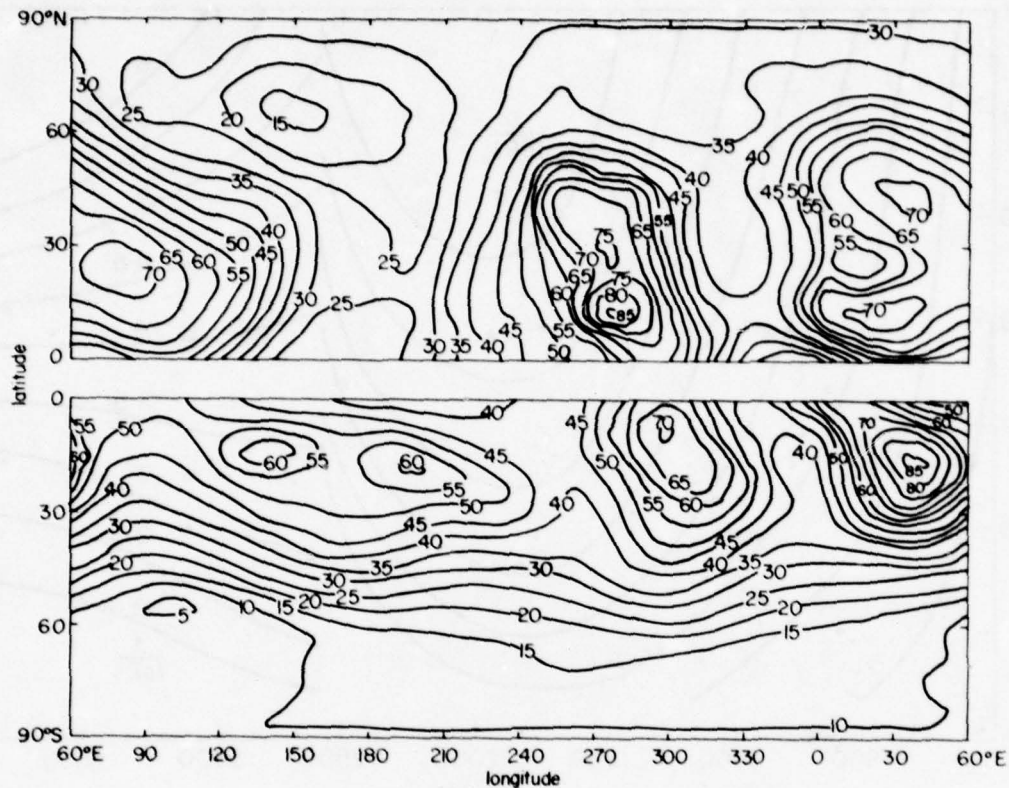
Figure 21 F_{am}, expected atmospheric noise mean power at 1 MHz in summer at 12-16 h local time, dB above $KT_o b$ where T_o is the reference temperature of 288 K (from CCIR Report 322)
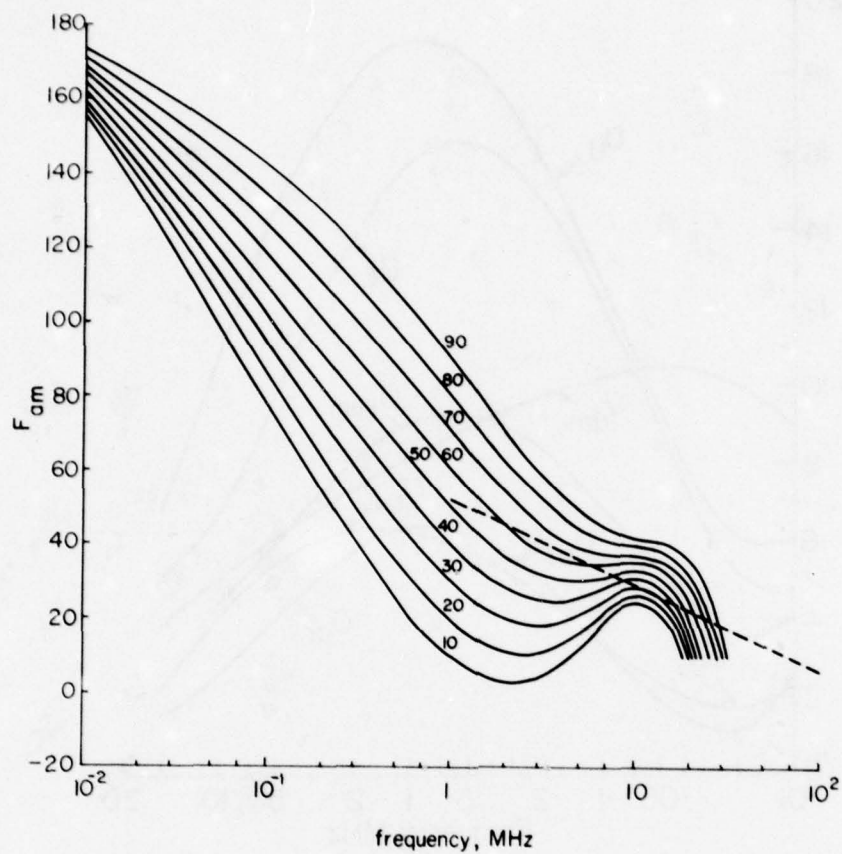
Figure 22   Expected variation of atmospheric noise mean power with
frequency in summer at 12-16 h local time
(from CCIR Report 322)

- - - - - expected galactic noise in the absence of
ionospheric screening
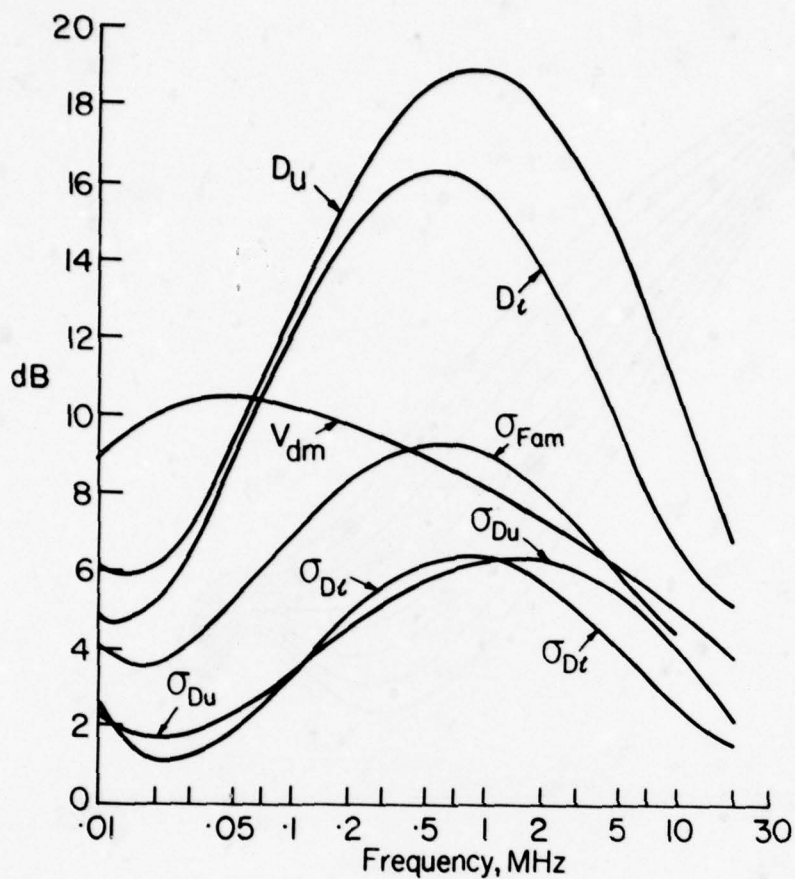
Figure 23   Parameters of atmospheric noise envelope in summer at 12-16 h local time (from CCIR Report 322)

D_u = upper decile deviation of daily mean noise powers from seasonal median

D_ℓ = lower decile deviation of daily mean noise powers from seasonal median

$\sigma_{F_{am}}$ = standard deviation of differences of measurements from mapped F_{am}

σ_{D_u} = standard deviation of differences of measurements from mapped D_u

$\sigma_{D\ell}$ = standard deviation of differences of measurements from mapped D_ℓ

V_{dm} = deviation of mean from rms noise field strength
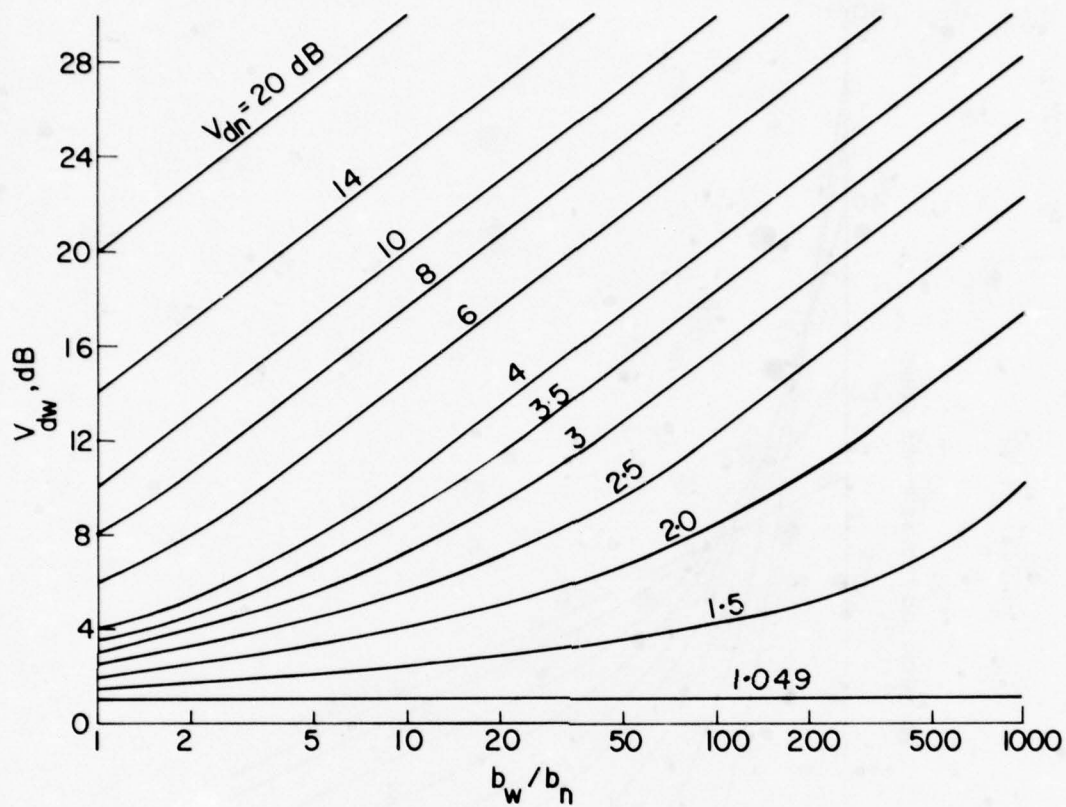
<u>Figure 24</u>   Dependence of rms/average ratio of atmospheric noise envelope
V_d on bandwidth b (from CCIR Report 322)

V_{dw} for wider bandwidth b_w is given in terms of V_{dn} for
narrower bandwidth b_n
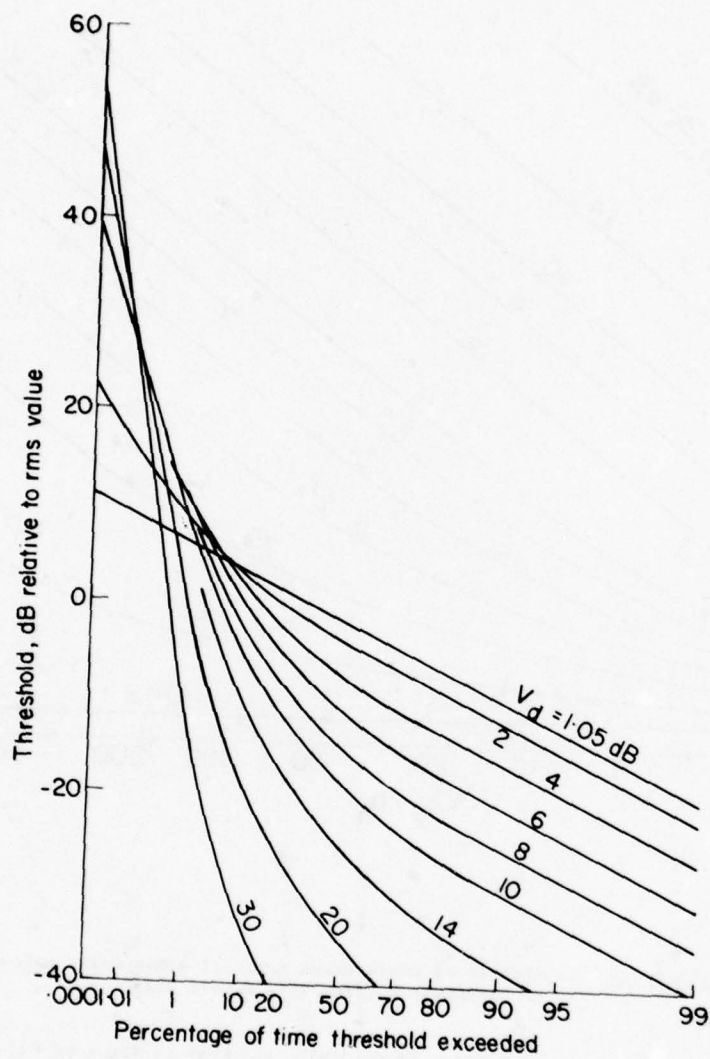
Figure 25 Amplitude probability distributions of atmospheric noise envelope
(from CCIR Report 322)
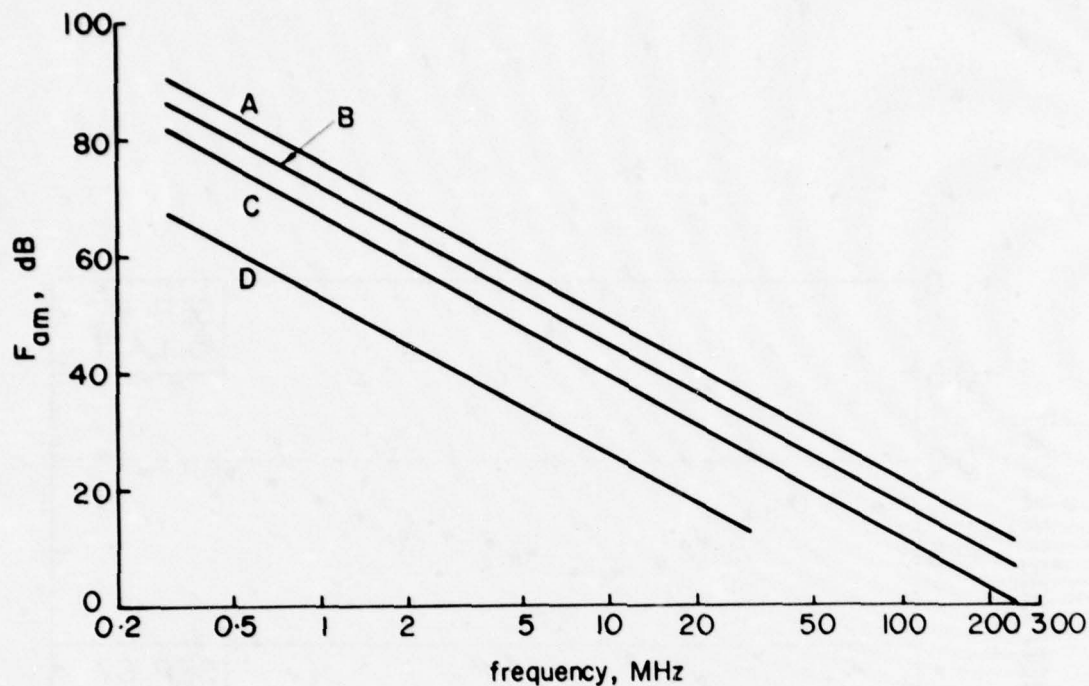
Figure 26   Mean values of man-made noise power at receiver for a short
vertical lossless grounded monopole antenna situated in
different areas (from CCIR Report 258-3)

A   business
B   residential
C   rural
D   quiet rural
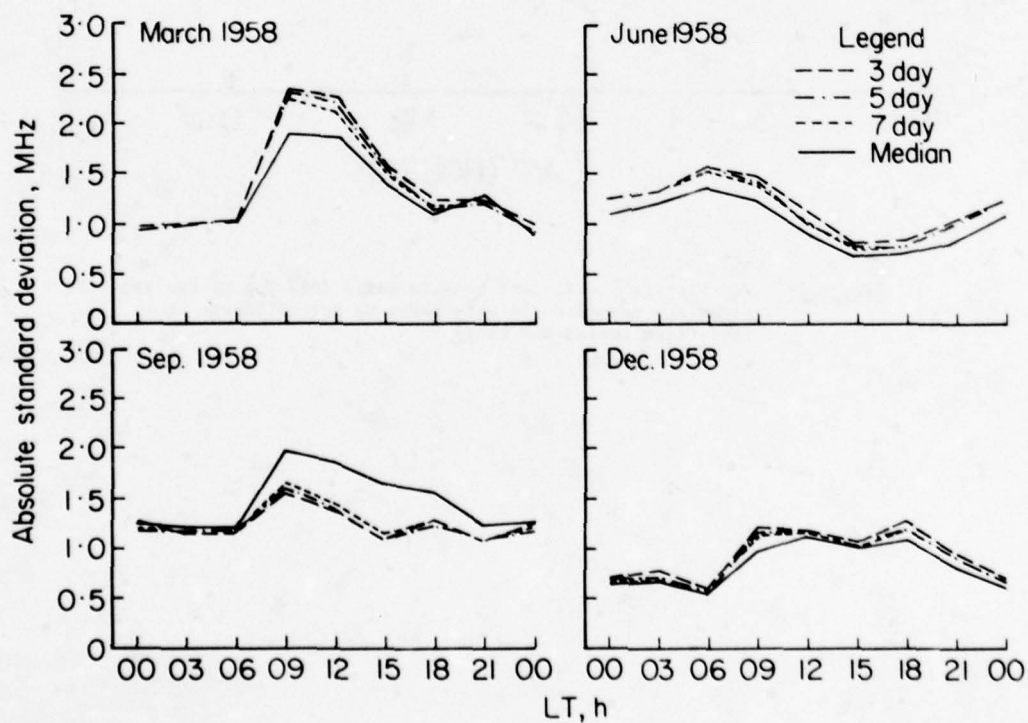
Figure 27   Errors in estimates of daily values of foF2 at Slough using monthly
median and weighted means of past days measurements (from Rush and
Gibbs[35])
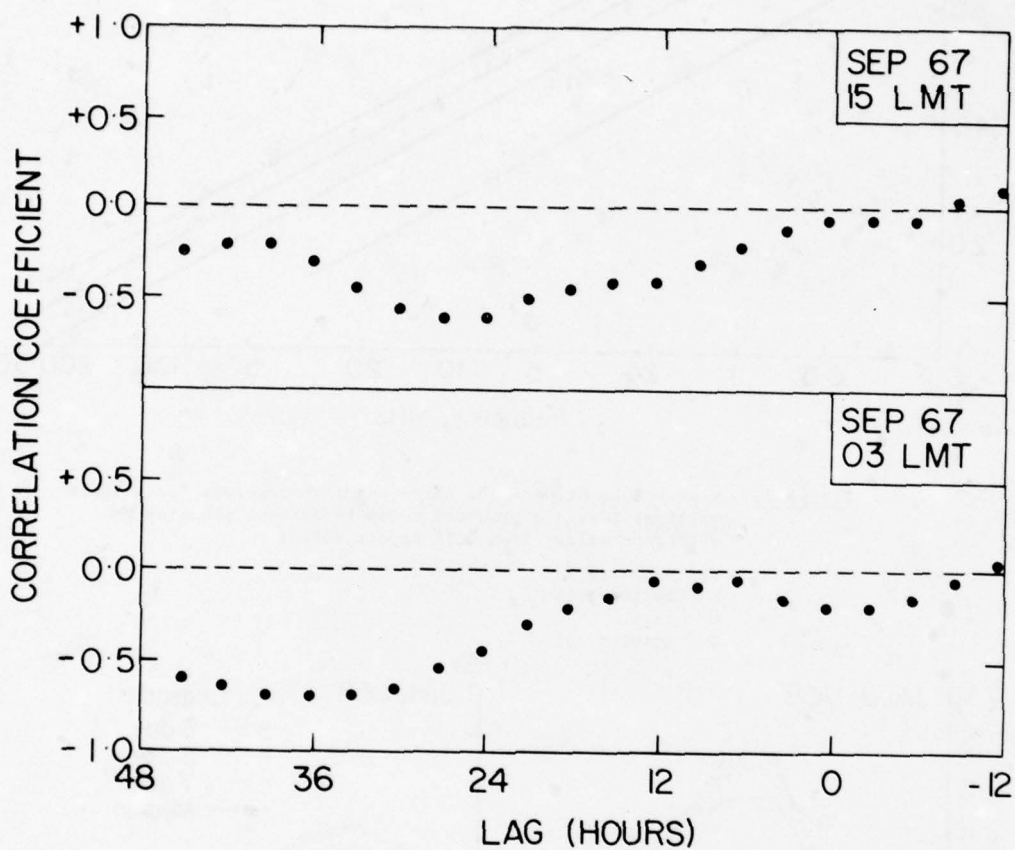
Figure 28   Correlation coefficient between daily foF2 for Lindau and planetary magnetic activity index Kp for different time lags (from Eccles and King)
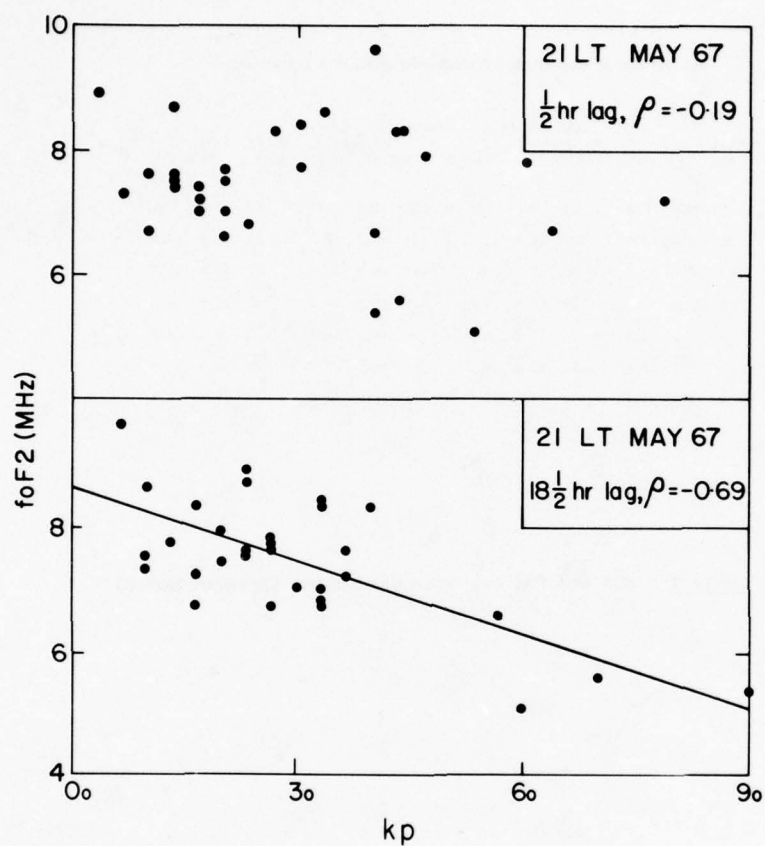
Figure 29   Example of improvement in regression of foF2 for Lindau with Kp when optimum time lag is introduced (from Eccles and King)

MUF AND FOT DETERMINATION IN ACCORDANCE WITH CCIR REPORT 340-3

			JUNE 1979			SUNSPOT NO. 143.0					
LONDON			TO BOULDER				AZIMUTHS		MILES	KM	
51.50N		0.17W		40.03N	105.27W	306.97	40.51		4679.1	7530.0	

UT	MUF	FOT	UT	MUF	FOT	UT	MUF	FOT	UT	MUF	FOT
01	17.4	13.9	07	14.1	10.7	13	15.2	11.3	19	17.2	13.8
02	16.7	13.3	08	13.1	9.9	14	15.5	11.5	20	17.4	13.9
03	16.0	12.3	09	12.6	9.6	15	15.8	12.1	21	17.6	14.1
04	15.5	11.9	10	12.9	9.8	16	16.1	12.4	22	18.1	14.5
05	15.0	11.6	11	13.8	10.2	17	16.5	12.7	23	18.6	14.9
06	14.9	11.4	12	14.7	10.9	18	16.9	13.0	24	18.0	14.4

<u>Table I</u>   MUF and FOT computer prediction (program MUFFY)

Table II   Values of the MUF deduced by different procedures

(i)   Short-path example : Sydney to Adelaide (range 1160 km) March, $R_{12} = 125$

UT, h	MUF, MHz		
	MUF-factor method MUFFY	Ray-tracing method	
		HFMLOSS/RIM1A	HFMUFES 3
00	15.3	17.1	18.5
01	15.7	17.2	18.7
02	15.9	17.2	18.6
03	15.8	17.0	18.2
04	15.5	16.7	17.8
05	15.4	16.5	17.6
06	15.2	16.6	17.6
07	15.1	16.6	17.5
08	14.7	16.3	17.0
09	13.8	15.4	16.1
10	12.5	13.9	14.6
11	11.3	12.4	13.1
12	10.6	11.6	12.3
13	10.4	11.3	12.1
14	10.1	11.1	11.9
15	9.7	10.6	11.5
16	9.3	10.1	11.0
17	8.8	9.5	10.3
18	8.1	8.9	9.4
19	7.8	8.7	9.1
20	8.7	9.9	10.5
21	10.9	12.6	13.4
22	13.2	15.2	16.4
23	14.7	16.7	18.0

(ii) Long path : Geneva to New York (range 6210 km) January, $R_{12} = 40$

UT, h	MUF, MHz		
	MUF-factor method MUFFY	Ray-tracing method	
		HFMLOSS/RIM1A	HFMUFES 3
00	8.4	10.0	9.4
01	8.2	9.7	9.3
02	8.3	9.9	9.4
03	8.6	10.3	9.7
04	9.0	10.1	9.7
05	7.6	8.6	8.2
06	5.9	7.4	7.1
07	6.6	8.8	8.4
08	6.9	9.2	9.1
09	7.7	9.6	9.3
10	9.6	10.9	10.3
11	12.9	13.7	12.9
12	17.6	18.1	17.4
13	22.3	22.6	22.0
14	25.0	25.5	24.9
15	25.0	25.5	24.4
16	23.6	23.7	22.5
17	21.0	20.9	19.8
18	17.4	17.4	16.6
19	14.0	14.5	13.8
20	11.6	12.6	11.6
21	10.1	11.3	10.3
22	9.1	10.5	9.6
23	8.6	10.2	9.5

```
                              1
                       JUNE 1979      SUNSPOT NUMBER 143.0
  LONDON           TO  BOULDER                 AZIMUTHS      MILES     KM.
  51.50N -  0.17W     40.03N - 105.27W      306.97   40.51  4679.1   7530.0
  MINIMUM ANGLE  0.0 DEGREES   POWER= 100.00KW   REQ.SIG. -105.0 DBW
                          FREQUENCIES IN MHZ
  UT    MUF  2.0  3.0  5.0  7.5 10.0 12.5 15.0 17.5 20.0 25.0 30.0
```

UT	17.2												
04	2F	7F	5F	3F	2F	2F	2F	2F	2F	2F	-	-	MODE
	4.9	31.1	20.5	9.7	1.9	1.6	1.8	2.4	4.9	4.9	-	-	ANGLE
	26.7	30.7	28.1	26.6	26.0	26.0	26.1	26.2	26.7	26.7	-	-	DELAY
	463	312	313	315	319	329	344	369	463	463	-	-	VIRT HT
	.50	.99	.99	.99	.99	.98	.93	.78	.45	.10	-	-	F. DAYS
	153	187	175	159	152	151	151	152	153	154	-	-	LOSS DB
	29	-24	8	12	23	26	28	29	29	29	-	-	DBU
	-103	-137	-125	-109	-102	-101	-101	-102	-103	-104	-	-	SIG.DBW
	.58	.0	.0	.29	.66	.69	.68	.65	.58	.55	-	-	F. SIG

UT	14.6												
08	2F	6F	4F	2F	2F	2F	2F	2F	2F	-	-	-	MODE
	5.3	23.9	14.3	2.2	0.9	1.2	2.0	5.3	5.3	-	-	-	ANGLE
	26.7	28.7	27.0	25.9	25.9	26.0	26.2	26.7	26.7	-	-	-	DELAY
	478	287	289	291	302	322	356	478	478	-	-	-	VIRT HT
	.50	.99	.99	.99	.99	.95	.79	.44	.8	-	-	-	F. DAYS
	161	296	252	194	175	166	162	160	160	-	-	-	LOSS DB
	20	-133	-85	-22	0	11	17	20	22	-	-	-	DBU
	-111	-246	-202	-144	-125	-116	-112	-110	-110	-	-	-	SIG.DBW
	.29	.0	.0	.0	.0	.12	.24	.30	.33	-	-	-	F. SIG

UT	16.0												
12	2F	4E	4E	7F	4F	3F	3F	2F	2F	2F	-	-	MODE
	6.1	1.2	1.2	27.4	15.1	9.8	10.8	3.7	6.1	6.1	-	-	ANGLE
	26.8	25.4	25.4	29.5	27.1	26.6	26.8	26.3	26.8	26.8	-	-	DELAY
	481	90	91	281	288	309	358	373	481	481	-	-	VIRT HT
	.50	.99	.99	.96	.94	.89	.62	.63	.33	.11	-	-	F. DAYS
	167	704	560	315	232	197	182	170	165	163	-	-	LOSS DB
	14	-541	-393	-143	-57	-20	-3	11	17	20	-	-	DBU
	-117	-654	-510	-265	-182	-147	-132	-120	-115	-113	-	-	SIG.DBW
	.0	.0	.0	.0	.0	.0	.0	.0	.1	.9	-	-	F. SIG

UT	19.0												
16	2F	4E	4E	4E	7F	4F	4F	3F	2F	2F	-	-	MODE
	7.6	1.2	1.2	1.2	34.5	17.7	19.5	13.8	7.6	7.6	-	-	ANGLE
	26.9	25.4	25.4	25.4	32.3	27.6	28.2	27.4	26.9	26.9	-	-	DELAY
	481	90	90	91	398	335	399	417	481	481	-	-	VIRT HT
	.50	.99	.99	.99	.80	.86	.48	.47	.54	.24	-	-	F. DAYS
	171	925	724	484	271	220	200	182	171	168	-	-	LOSS DB
	11	-762	-557	-313	-96	-43	-21	-1	11	15	-	-	DBU
	-121	-875	-674	-434	-221	-170	-150	-132	-121	-118	-	-	SIG.DBW
	.0	.0	.0	.0	.0	.0	.0	.0	.0	.0	-	-	F. SIG

UT	19.8												
20	2F	4E	4E	6F	4F	3F	2F	2F	2F	2F	-	-	MODE
	5.8	1.2	1.2	22.8	13.6	8.4	2.2	1.5	2.3	5.8	-	-	ANGLE
	26.8	25.4	25.4	28.3	26.8	26.3	25.9	25.9	26.1	26.8	-	-	DELAY
	487	90	91	261	270	279	281	305	346	487	-	-	VIRT HT
	.50	.99	.99	.99	.99	.99	.99	.94	.78	.48	-	-	F. DAYS
	166	715	568	316	240	203	180	173	168	166	-	-	LOSS DB
	17	-552	-401	-145	-66	-26	0	8	14	18	-	-	DBU
	-116	-665	-518	-266	-190	-153	-130	-123	-118	-116	-	-	SIG.DBW
	.3	.0	.0	.0	.0	.0	.0	.0	.0	.3	-	-	F. SIG

UT	19.5												
24	2F	4E	5F	3F	2F	2F	2F	2F	2F	2F	-	-	MODE
	5.1	1.3	20.2	9.3	1.5	0.9	1.0	1.5	2.4	5.1	-	-	ANGLE
	26.7	25.4	27.9	26.4	25.9	25.9	26.0	26.1	26.2	26.7	-	-	DELAY
	472	92	286	289	292	301	315	335	369	472	-	-	VIRT HT
	.50	.99	.99	.99	.99	.99	.93	.73	.43	-	-	-	F. DAYS
	157	346	235	194	169	162	159	157	157	157	-	-	LOSS DB
	26	-183	-69	-23	6	15	20	23	25	26	-	-	DBU
	-107	-296	-185	-144	-119	-112	-109	-107	-107	-107	-	-	SIG.DBW
	.41	.0	.0	.0	.0	.20	.35	.41	.43	.41	-	-	F. SIG

<u>Table III</u>   Signal strength computer prediction (program HFMLOSS)
without allowance for antenna gain

ANTENNA POWER GAIN - FREQUENCIES IN MEGAHERTZ - ELEVATION ANGLE IN DEGREES - ITR = 1

FREQUENCY RANGE	ANTENNA TYPE	NR	HEIGHT	LENGTH	ANGLE	OFFAZIM	EX(1)	EX(2)	EX(3)	EX(4)	CONDUCT.	DIELECT.
2.0 TO 30.0	CURTAIN	6	-1.000	-0.500	4.000	6.971	4.000	-0.501	-0.500	-0.250	0.010	30.00

Angle	2	3	4	5	6	7	8	10	12	14	16	18	20	22	24	26	28	30	
90	-10.0	-10.0	-10.0	-10.0	-10.0	-10.0	-10.0	-10.0	-10.0	-10.0	-10.0	-10.0	-10.0	-10.0	-10.0	-10.0	-10.0	-10.0	
88	-10.0	-10.0	-10.0	-10.0	-10.0	-10.0	-10.0	-10.0	-10.0	-10.0	-10.0	-10.0	-10.0	-10.0	-10.0	-10.0	-10.0	-10.0	
86	-10.0	-10.0	-10.0	-10.0	-10.0	-10.0	-10.0	-10.0	-10.0	-10.0	-10.0	-10.0	-10.0	-10.0	-10.0	-10.0	-10.0	-10.0	
84	-10.0	-10.0	-10.0	-10.0	-10.0	-10.0	-10.0	-10.0	-10.0	-10.0	-10.0	-10.0	-10.0	-10.0	-10.0	-10.0	-10.0	-10.0	
82	-10.0	-10.0	-10.0	-10.0	-10.0	-10.0	-10.0	-10.0	-10.0	-10.0	-10.0	-10.0	-10.0	-10.0	-10.0	-10.0	-10.0	-10.0	
80	-10.0	-10.0	-10.0	-10.0	-10.0	-10.0	-10.0	-10.0	-10.0	-10.0	-10.0	-10.0	-10.0	-10.0	-10.0	-10.0	-10.0	-10.0	
78	-10.0	-10.0	-10.0	-10.0	-10.0	-10.0	-10.0	-10.0	-10.0	-10.0	-10.0	-10.0	-10.0	-10.0	-10.0	-10.0	-10.0	-10.0	
76	-10.0	-10.0	-10.0	-10.0	-10.0	-10.0	-10.0	-10.0	-10.0	-10.0	-10.0	-10.0	-10.0	-10.0	-10.0	-10.0	-10.0	-10.0	
74	-9.9	-10.0	-10.0	-10.0	-10.0	-10.0	-10.0	-10.0	-10.0	-10.0	-10.0	-10.0	-10.0	-10.0	-10.0	-10.0	-10.0	-10.0	
72	-7.4	-7.6	-7.7	-7.8	-7.9	-7.9	-8.0	-8.1	-8.1	-8.2	-8.2	-8.2	-8.3	-8.3	-8.3	-8.3	-8.3	-8.3	
70	-5.5	-5.7	-5.8	-5.9	-6.0	-6.0	-6.1	-6.2	-6.2	-6.3	-6.3	-6.4	-6.4	-6.4	-6.4	-6.4	-6.4	-6.5	E
68	-4.2	-4.4	-4.5	-4.6	-4.6	-4.7	-4.8	-4.9	-4.9	-5.0	-5.0	-5.1	-5.1	-5.1	-5.1	-5.2	-5.2	-5.2	L
66	-3.6	-3.7	-3.8	-3.9	-4.0	-4.1	-4.1	-4.2	-4.3	-4.4	-4.4	-4.5	-4.5	-4.5	-4.6	-4.6	-4.6	-4.6	E
64	-3.9	-4.0	-4.1	-4.1	-4.2	-4.3	-4.4	-4.5	-4.6	-4.6	-4.7	-4.7	-4.8	-4.8	-4.8	-4.9	-4.9	-4.9	V
62	-5.7	-5.6	-5.6	-5.7	-5.8	-5.8	-5.9	-6.0	-6.1	-6.2	-6.2	-6.3	-6.3	-6.4	-6.4	-6.4	-6.5	-6.5	A
60	-10.0	-10.0	-9.8	-9.6	-9.6	-9.5	-9.5	-9.5	-9.6	-9.6	-9.6	-9.7	-9.7	-9.7	-9.8	-9.8	-9.8	-9.8	T
58	-10.0	-10.0	-10.0	-10.0	-10.0	-10.0	-10.0	-10.0	-10.0	-10.0	-9.9	-9.8	-9.7	-9.6	-9.6	-9.5	-9.5	-9.4	I
56	-4.1	-4.2	-4.2	-4.1	-4.0	-3.9	-3.8	-3.7	-3.5	-3.4	-3.3	-3.3	-3.2	-3.2	-3.1	-3.1	-3.1	-3.1	O
54	1.7	1.5	1.4	1.4	1.4	1.4	1.4	1.5	1.5	1.6	1.6	1.7	1.7	1.7	1.7	1.7	1.8	1.8	N
52	5.3	5.2	5.1	5.0	5.0	5.0	5.0	5.0	5.0	5.0	5.0	5.1	5.1	5.1	5.1	5.1	5.1	5.1	
50	7.8	7.6	7.6	7.5	7.4	7.4	7.4	7.4	7.4	7.4	7.4	7.4	7.4	7.4	7.4	7.4	7.4	7.4	A
48	9.3	9.2	9.1	9.0	8.9	8.9	8.9	8.9	8.9	8.9	8.8	8.8	8.8	8.8	8.8	8.8	8.8	8.8	N
46	10.0	9.9	9.8	9.7	9.7	9.6	9.6	9.6	9.5	9.5	9.5	9.5	9.5	9.5	9.5	9.5	9.5	9.5	G
44	9.9	9.8	9.7	9.6	9.6	9.5	9.5	9.4	9.4	9.4	9.3	9.3	9.3	9.3	9.3	9.3	9.3	9.3	L
42	8.8	8.7	8.6	8.5	8.5	8.4	8.4	8.3	8.3	8.2	8.2	8.2	8.2	8.2	8.2	8.1	8.1	8.1	E
40	6.4	6.3	6.2	6.2	6.1	6.0	6.0	5.9	5.9	5.8	5.8	5.8	5.8	5.7	5.7	5.7	5.7	5.7	
38	2.0	2.0	1.9	1.9	1.8	1.7	1.7	1.6	1.5	1.5	1.4	1.4	1.4	1.3	1.3	1.3	1.3	1.3	I
36	-6.9	-6.8	-6.7	-6.7	-6.8	-6.9	-7.0	-7.1	-7.1	-7.2	-7.2	-7.3	-7.3	-7.4	-7.4	-7.4	-7.4	-7.4	N
34	-10.0	-10.0	-10.0	-10.0	-10.0	-10.0	-10.0	-10.0	-10.0	-10.0	-10.0	-10.0	-10.0	-10.0	-10.0	-10.0	-10.0	-10.0	
32	-9.5	-9.6	-9.7	-9.7	-9.7	-9.7	-9.7	-9.6	-9.6	-9.6	-9.5	-9.5	-9.5	-9.5	-9.5	-9.4	-9.4	-9.4	D
30	-10.0	-10.0	-10.0	-10.0	-10.0	-10.0	-10.0	-10.0	-10.0	-10.0	-10.0	-10.0	-10.0	-10.0	-10.0	-10.0	-10.0	-10.0	E
28	-1.8	-1.9	-2.0	-2.0	-2.0	-2.1	-2.1	-2.1	-2.1	-2.1	-2.1	-2.1	-2.1	-2.1	-2.1	-2.1	-2.1	-2.1	G
26	5.6	5.5	5.5	5.4	5.4	5.4	5.3	5.3	5.3	5.3	5.3	5.3	5.3	5.3	5.3	5.3	5.3	5.3	R
24	9.4	9.3	9.3	9.2	9.2	9.2	9.1	9.1	9.1	9.1	9.0	9.0	9.0	9.0	9.0	9.0	9.0	9.0	E
22	10.9	10.8	10.8	10.7	10.7	10.7	10.7	10.6	10.6	10.6	10.5	10.5	10.5	10.5	10.5	10.5	10.5	10.5	E
20	10.1	10.1	10.0	10.0	9.9	9.9	9.9	9.8	9.8	9.8	9.7	9.7	9.7	9.7	9.7	9.7	9.7	9.7	S
18	5.1	5.1	5.0	5.0	5.0	4.9	4.9	4.8	4.7	4.7	4.7	4.6	4.6	4.6	4.6	4.5	4.5	4.5	
16	-2.5	-2.5	-2.4	-2.3	-2.2	-2.0	-1.9	-1.7	-1.6	-1.5	-1.4	-1.3	-1.3	-1.2	-1.2	-1.1	-1.1	-1.1	
14	12.0	12.0	11.9	11.9	11.9	11.9	11.9	11.9	11.9	11.9	12.0	12.0	12.0	12.0	12.0	12.0	12.0	12.0	
12	17.4	17.3	17.3	17.3	17.3	17.3	17.3	17.3	17.3	17.3	17.3	17.3	17.3	17.3	17.3	17.3	17.3	17.3	
10	20.2	20.2	20.1	20.1	20.1	20.1	20.1	20.1	20.1	20.1	20.1	20.1	20.1	20.1	20.1	20.1	20.1	20.1	
8	21.4	21.3	21.3	21.3	21.3	21.3	21.3	21.3	21.2	21.2	21.2	21.2	21.2	21.2	21.2	21.2	21.2	21.2	
6	21.1	21.1	21.1	21.0	21.0	21.0	21.0	21.0	21.0	21.0	21.0	21.0	21.0	21.0	21.0	21.0	21.0	21.0	
4	19.1	19.1	19.1	19.0	19.0	19.0	19.0	19.0	19.0	19.0	19.0	19.0	19.0	19.0	19.0	19.0	19.0	19.0	
2	14.0	13.9	13.9	13.9	13.9	13.9	13.9	13.9	13.9	13.9	13.9	13.9	13.9	13.9	13.9	13.9	13.9	13.9	
0	-10.0	-10.0	-10.0	-10.0	-10.0	-10.0	-10.0	-10.0	-10.0	-10.0	-10.0	-10.0	-10.0	-10.0	-10.0	-10.0	-10.0	-10.0	
	2	3	4	5	6	7	8	10	12	14	16	18	20	22	24	26	28	30	

FREQUENCIES IN MEGAHERTZ

Table IV   Antenna-gain tabulation (program RIM1A)

1

JUNE 1979   SUNSPOT NUMBER 143.0

LONDON		TO	BOULDER		AZIMUTHS	MILES	KM.
51.50N -	0.17W	40.03N -	105.27W	306.97	40.51	4679.1	7530.0

MINIMUM ANGLE 0.0 DEGREES   POWER= 100.00KW   REQ.SIG.-105.0 DBW

	FREQUENCY RANGE	ANTENNA TYPE	NR	HEIGHT	LENGTH	ANGLE	OFFAZIM	CONDUCT	DIELECT
TX	2.0 TO 30.0	CURTAIN	6	-1.000	-0.500	4.000	6.971	0.010	30.000
RX	2.0 TO 30.0	VERTICAL	2	0.000	2.500	0.000	0.000	0.010	30.000

FREQUENCIES IN MHZ

UT	MUF	2.0	3.0	5.0	7.5	10.0	12.5	15.0	17.5	20.0	25.0	30.0	

04   17.2

	2.0	3.0	5.0	7.5	10.0	12.5	15.0	17.5	20.0	25.0	30.0	
	2F	4E	5F	3F	3F	3F	3F	2F	2F	2F	-	MODE
	4.9	1.3	20.5	9.7	9.0	9.2	10.0	2.4	4.9	4.9	-	ANGLE
	26.7	25.4	28.1	26.6	26.5	26.6	26.8	26.2	26.7	26.7	-	DELAY
	463	92	313	315	322	335	357	369	463	463	-	VIRT HT
	.50	.99	.99	.99	.99	.95	.80	.78	.45	.10	-	F. DAYS
	141	205	174	149	145	143	141	145	141	141	-	LOSS DB
	49	-32	3	32	40	43	44	46	49	49	-	DBU
	-91	-155	-124	-99	-95	-93	-91	-95	-91	-91	-	SIG.DBW
	.92	.0	.0	.75	.85	.90	.92	.86	.92	.92	-	F. SIG
	.46	.0	.0	.75	.85	.85	.74	.67	.42	.9	-	DEP.

08   14.6

	2.0	3.0	5.0	7.5	10.0	12.5	15.0	17.5	20.0	25.0	30.0	
	2F	6F	4F	2F	3F	3F	3X	2F	2F	-	-	MODE
	5.3	23.9	14.3	2.2	8.1	9.1	6.8	5.3	5.3	-	-	ANGLE
	26.7	28.7	27.0	25.9	26.4	26.6	26.3	26.7	26.7	-	-	DELAY
	478	287	289	291	307	335	372	478	478	-	-	VIRT HT
	.50	.99	.99	.99	.97	.85	.66	.44	.8	-	-	F. DAYS
	149	297	252	189	172	160	156	148	146	-	-	LOSS DB
	40	-124	-75	-8	12	26	32	41	43	-	-	DBU
	-99	-247	-202	-139	-122	-110	-106	-98	-96	-	-	SIG.DBW
	.70	.0	.0	.0	.1	.31	.48	.71	.75	-	-	F. SIG
	.35	.0	.0	.0	.1	.27	.32	.31	.6	-	-	DEP.

12   16.0

	2.0	3.0	5.0	7.5	10.0	12.5	15.0	17.5	20.0	25.0	30.0	
	2F	4E	4E	7F	5F	3F	3F	2F	2F	2F	-	MODE
	6.1	1.2	1.2	27.4	20.9	9.8	10.8	3.7	6.1	6.1	-	ANGLE
	26.8	25.4	25.4	29.5	28.2	26.6	26.8	26.3	26.8	26.8	-	DELAY
	481	90	91	281	333	309	358	373	481	481	-	VIRT HT
	.50	.99	.99	.96	.86	.89	.62	.63	.33	.11	-	F. DAYS
	153	705	560	324	232	185	169	161	151	148	-	LOSS DB
	35	-532	-383	-143	-48	0	16	30	38	41	-	DBU
	-103	-655	-510	-274	-182	-135	-119	-111	-101	-98	-	SIG.DBW
	.58	.0	.0	.0	.0	.0	.0	.20	.66	.74	-	F. SIG
	.29	.0	.0	.0	.0	.0	.0	.13	.22	.8	-	DEP.

16   19.0

	2.0	3.0	5.0	7.5	10.0	12.5	15.0	17.5	20.0	25.0	30.0	
	2F	4E	4E	4E	6F	5F	4F	3F	2F	2F	-	MODE
	7.6	1.2	1.2	1.2	26.6	25.1	19.5	13.8	7.6	7.6	-	ANGLE
	26.9	25.4	25.4	25.4	29.5	29.4	28.2	27.4	26.9	26.9	-	DELAY
	481	90	90	91	321	399	399	417	481	481	-	VIRT HT
	.50	.99	.99	.99	.89	.66	.48	.47	.54	.24	-	F. DAYS
	155	926	725	485	279	219	196	173	155	152	-	LOSS DB
	33	-753	-548	-304	-95	-36	-12	12	32	36	-	DBU
	-105	-876	-675	-435	-229	-169	-146	-123	-105	-102	-	SIG.DBW
	.51	.0	.0	.0	.0	.0	.0	.0	.48	.61	-	F. SIG
	.25	.0	.0	.0	.0	.0	.0	.0	.26	.14	-	DEP.

20   19.8

	2.0	3.0	5.0	7.5	10.0	12.5	15.0	17.5	20.0	25.0	30.0	
	2F	4E	4E	6F	4F	3F	3F	3F	3X	2F	-	MODE
	5.8	1.2	1.2	22.8	13.6	8.4	8.3	9.5	7.4	5.8	-	ANGLE
	26.8	25.4	25.4	28.3	26.8	26.3	26.4	26.6	26.4	26.8	-	DELAY
	487	90	91	261	270	279	294	336	380	487	-	VIRT HT
	.50	.99	.99	.99	.99	.99	.94	.72	.59	.48	-	F. DAYS
	151	716	568	316	237	191	175	164	160	151	-	LOSS DB
	38	-542	-392	-134	-53	-5	12	22	27	38	-	DBU
	-101	-666	-518	-266	-187	-141	-125	-114	-110	-101	-	SIG.DBW
	.62	.0	.0	.0	.0	.0	.0	.12	.29	.62	-	F. SIG
	.31	.0	.0	.0	.0	.0	.0	.9	.17	.30	-	DEP.

24   19.5

	2.0	3.0	5.0	7.5	10.0	12.5	15.0	17.5	20.0	25.0	30.0	
	2F	4E	5F	3F	3F	3F	3F	3F	2F	2F	-	MODE
	5.1	1.3	20.2	9.3	8.1	8.1	8.7	10.0	2.4	5.1	-	ANGLE
	26.7	25.4	27.9	26.4	26.4	26.4	26.5	26.8	26.2	26.7	-	DELAY
	472	92	286	289	295	306	324	359	369	472	-	VIRT HT
	.50	.99	.99	.99	.99	.99	.94	.70	.73	.43	-	F. DAYS
	144	346	235	183	166	156	150	147	149	144	-	LOSS DB
	46	-173	-58	-2	19	30	36	39	43	46	-	DBU
	-94	-296	-185	-133	-116	-106	-100	-97	-99	-94	-	SIG.DBW
	.76	.0	.0	.0	.3	.45	.64	.71	.66	.76	-	F. SIG
	.38	.0	.0	.0	.3	.45	.60	.50	.49	.33	-	DEP.

Table V   Signal strength computer prediction (program RIM1A) with inclusion of antenna-gain allowance

	frequency (MHz)	D_u and D_ℓ (dB)
Business	≤ 10 10 - 20 ≥ 20	4 6 7
Residential	≤ 10 10 - 20 ≥ 20	6 9 12
Rural	≤ 10 10 - 20 ≥ 20	10 7 4
Quiet rural	≤ 10 10 - 20 ≥ 20	10 7 4

Table VI   Upper and lower decile values of the day-to-day variability of man-made noise, D_u and D_ℓ

ESTIMATED MEAN NOISE POWERS

BOULDER   JUNE

40.03 N   254.73 E

RX POWER BANDWIDTH   3000 HZ   MAN-MADE NOISE TYPE   RURAL

FREQUENCIES IN MHZ

UT	2.0	3.0	5.0	7.5	10.0	12.5	15.0	17.5	20.0	25.0	30.0		
0000	62.1	56.8	51.9	48.6	45.6	42.0	37.8	32.7	27.0	13.8	-1.0	ATM	DB.KTB
	58.9	54.0	47.9	43.0	39.5	36.8	34.6	32.8	31.2	28.5	26.3	MAN	DB.KTB
	42.9	39.0	34.1	30.2	27.5	25.4	23.6	22.1	20.9	18.7	17.0	GAL	DB.KTB
	63.8	58.7	53.4	49.7	46.6	43.3	39.6	36.0	32.9	29.1	26.8	RES	DB.KTB
	-105.4	-110.5	-115.9	-119.6	-122.6	-126.0	-129.6	-133.3	-136.4	-140.2	-142.4	RES	DBW
	7.8	6.2	5.3	5.1	4.6	3.2	1.1	-1.2	-3.1	-5.0	-5.7	RES	DBU
0400	71.4	66.3	59.4	52.5	46.2	40.0	34.0	28.1	22.3	10.6	-1.4	ATM	DB.KTB
	58.9	54.0	47.9	43.0	39.5	36.8	34.6	32.8	31.2	28.5	26.3	MAN	DB.KTB
	42.9	39.0	34.1	30.2	27.5	25.4	23.6	22.1	20.9	18.7	17.0	GAL	DB.KTB
	71.7	66.5	59.7	53.0	47.1	41.8	37.5	34.3	32.0	28.6	26.8	RES	DB.KTB
	-97.6	-102.7	-109.5	-116.2	-122.2	-127.4	-131.7	-134.9	-137.2	-140.2	-142.4	RES	DBW
	15.7	14.0	11.6	8.5	5.0	1.7	-1.0	-2.8	-4.0	-5.1	-5.7	RES	DBU
0800	76.3	70.9	63.1	54.6	46.5	38.7	31.3	24.2	17.4	4.7	-7.4	ATM	DB.KTB
	58.9	54.0	47.9	43.0	39.5	36.8	34.6	32.8	31.2	28.5	26.3	MAN	DB.KTB
	42.9	39.0	34.1	30.2	27.5	25.4	23.6	22.1	20.9	18.7	17.0	GAL	DB.KTB
	76.4	71.0	63.3	54.9	47.4	41.0	36.5	33.7	31.7	28.9	26.8	RES	DB.KTB
	-92.8	-98.2	-106.0	-114.3	-121.9	-128.2	-132.7	-135.6	-137.5	-140.3	-142.4	RES	DBW
	20.4	18.5	15.2	10.4	5.3	0.9	-2.0	-3.5	-4.3	-5.1	-5.7	RES	DBU
1200	56.9	53.7	50.3	45.9	40.5	34.7	28.6	22.6	16.8	5.6	-5.3	ATM	DB.KTB
	58.9	54.0	47.9	43.0	39.5	36.8	34.6	32.8	31.2	28.5	26.3	MAN	DB.KTB
	42.9	39.0	34.1	30.2	27.5	25.4	23.6	22.1	20.9	18.7	17.0	GAL	DB.KTB
	61.1	57.0	52.3	47.8	43.2	39.1	35.9	33.5	31.7	29.0	26.8	RES	DB.KTB
	-108.2	-112.3	-116.9	-121.5	-126.0	-130.1	-133.4	-135.7	-137.5	-140.3	-142.4	RES	DBW
	5.1	4.5	4.3	3.2	1.2	-1.0	-2.6	-3.7	-4.3	-5.1	-5.7	RES	DBU
1600	31.8	28.2	28.1	30.2	31.0	29.9	26.9	22.3	16.3	1.9	-14.1	ATM	DB.KTB
	58.9	54.0	47.9	43.0	39.5	36.8	34.6	32.8	31.2	28.5	26.3	MAN	DB.KTB
	42.9	39.0	34.1	30.2	27.5	25.4	23.6	22.1	20.9	18.7	17.0	GAL	DB.KTB
	59.0	54.1	48.1	43.4	40.3	37.9	35.6	33.5	31.7	28.9	26.8	RES	DB.KTB
	-110.2	-115.1	-121.1	-125.8	-128.9	-131.3	-133.6	-135.7	-137.5	-140.3	-142.4	RES	DBW
	3.0	1.7	0.0	-1.1	-1.7	-2.2	-2.9	-3.7	-4.3	-5.1	-5.7	RES	DBU
2000	42.4	36.6	33.3	33.8	34.5	33.9	31.5	27.5	22.0	7.6	-9.5	ATM	DB.KTB
	58.9	54.0	47.9	43.0	39.5	36.8	34.6	32.8	31.2	28.5	26.3	MAN	DB.KTB
	42.9	39.0	34.1	30.2	27.5	25.4	23.6	22.1	20.9	18.7	17.0	GAL	DB.KTB
	59.1	54.2	48.2	43.7	40.9	38.8	36.6	34.2	32.0	29.0	26.8	RES	DB.KTB
	-110.2	-115.0	-121.0	-125.6	-128.3	-130.4	-132.6	-135.0	-137.2	-140.3	-142.4	RES	DBW
	3.1	1.7	0.1	-0.9	-1.1	-1.3	-1.9	-3.0	-4.0	-5.1	-5.7	RES	DBU

Table VII   Noise computer prediction (program NOISEY)

Q_1	Q_2	Q		
		positive correlation	no correlation	negative correlation
.50	.40	.50-.70	.70	.70-.90
.90	.50	.90-.95	.95	.95-1.00

Table VIII   Circuit availability with two modes present

```
                                  1
                  JUNE 15, 1979    10 CM FLUX 186.     (SSN 143.)
     LONDON        TO BOULDER                 AZIMUTHS    MILES      KM
     51.50N -   0.17W   40.03N - 105.27W    306.97   40.51   4679.1   7530.0
                        MINIMUM ANGLE  0.0 DEGREES
     XMTR  2.0 TO 30.0     CURTAIN    H  -1.00 L  -0.50 A   4.0 OFF AZ   7.0
     RCVR  2.0 TO 30.0     VERTICAL   H   0.00 L   2.50 A   0.0 OFF AZ   0.0
     POWER= 100.00KW  3 MHZ NOISE=-150.0DBW  TIME= 90 PERCENT  REQ.S/N=55.0DB
     MULTIPATH POWER TOLERANCE= 6.0 DB    MULTIPATH DELAY TOLERANCE=0.50 MS.
                        FREQUENCIES IN MHZ
     UT   MUF  2.0  3.0  5.0  7.5 10.0 12.5 15.0 17.5 20.0 25.0 30.0

     04   16.7  K(0)MUF=(20.5)   K(5)MUF=(13.1)
          2F    -    -   3F   3F   3F   3F   2F   2F   2F    -    -  MODE
          4.9   -    -   9.2  8.6  9.0 10.0  2.5  4.9  4.9   -    -  ANGLE
          .50   -    -   99  .99  .98  .92  .73  .37  .4     -    -  F. DAYS
          48.   -    -   33.  40.  44.  46.  42.  48.  48.   -    -  DBU
          75.   -    -   56.  66.  73.  76.  75.  75.  74.   -    -  S/N DB
          .47   -    -   .54  .84  .92  .89  .69  .35  .4    -    -  REL.
          .6    -    -    -    -    -    -    -   .1    -    -    -  MP PROB

     08   14.7  K(0)MUF=(18.0)   K(5)MUF=(11.5)
          2F    -    -    -    -   3F   3X   2F   2F    -    -    -  MODE
          5.3   -    -    -    -   9.0  5.6  5.3  5.3   -    -    -  ANGLE
          .50   -    -    -    -   95  .79  .44  .8     -    -    -  F. DAYS
          37.   -    -    -    -   20.  25.  38.  40.   -    -    -  DBU
          67.   -    -    -    -   49.  60.  67.  68.   -    -    -  S/N DB
          .39   -    -    -    -   .27  .53  .35  .6    -    -    -  REL.
          .6    -    -    -    -   .31  .4    -    -    -    -    -  MP PROB

     12   16.1  K(0)MUF=(18.9)   K(5)MUF=(13.2)
          2F    -    -    -    -   3F   2F   2F   2F    -    -    -  MODE
          5.8   -    -    -    -  10.0  3.1  5.8  5.8   -    -    -  ANGLE
          .50   -    -    -    -   .78  .64  .34  .12   -    -    -  F. DAYS
          31.   -    -    -    -    9.  21.  33.  38.   -    -    -  DBU
          59.   -    -    -    -   42.  53.  61.  64.   -    -    -  S/N DB
          .32   -    -    -    -   .6   .28  .24  .9    -    -    -  REL.
          .8    -    -    -    -    -   .12  .4    -    -    -    -  MP PROB

     16   19.0  K(0)MUF=(19.0)   K(5)MUF=(19.0)
          2F    -    -    -    -    -   3F   3X   2F    -    -    -  MODE
          7.0   -    -    -    -    -  13.3  7.8  7.0   -    -    -  ANGLE
          .99   -    -    -    -    -   .99  .99  .26   -    -    -  F. DAYS
          32.   -    -    -    -    -   10.  17.  34.   -    -    -  DBU
          60.   -    -    -    -    -   43.  50.  61.   -    -    -  S/N DB
          .62   -    -    -    -    -   .12  .34  .17   -    -    -  REL.
           -    -    -    -    -    -    -   .5    -    -    -    -  MP PROB

     20   20.2  K(0)MUF=(24.5)   K(5)MUF=(15.8)
          2F    -    -    -    -    -   3F   3F   2F   2F    -    -  MODE
          5.6   -    -    -    -    -    -   8.8 12.9  4.2  5.6   -  ANGLE
          .50   -    -    -    -    -    -   .95  .81  .53  .5    -  F. DAYS
          35.   -    -    -    -    -    -   17.  24.  32.  40.   -  DBU
          61.   -    -    -    -    -    -   49.  55.  58.  66.   -  S/N DB
          .32   -    -    -    -    -    -   .28  .41  .31  .4    -  REL.
          .5    -    -    -    -    -    -    -    -    -   .6    -  MP PROB

     24   19.5  K(0)MUF=(23.5)   K(5)MUF=(14.8)
          2F    -    -    -    -   3F   3F   3F   2F   2F   2F    -  MODE
          5.1   -    -    -    -   7.9  8.5  9.9  2.3  5.1  5.1   -  ANGLE
          .50   -    -    -    -   .99  .99  .93  .73  .43  .4    -  F. DAYS
          44.   -    -    -    -   23.  32.  37.  35.  44.  46.   -  DBU
          69.   -    -    -    -   53.  63.  68.  68.  69.  72.   -  S/N DB
          .40   -    -    -    -   .45  .68  .71  .57  .33  .3    -  REL.
          .10   -    -    -    -    -    -    -    -   .3   .7    -  MP PROB
```

Table IX   Signal/noise ratio and reliability computer prediction
          (program HFMUFES 3)

```
                        1
             JUNE 15, 1979    10 CM FLUX 186.   (SSN 143.)
    LONDON       TO  BOULDER            AZIMUTHS    MILES     KM.
    51.50N -   0.17W   40.03N - 105.27W   306.97   40.51   4679.1   7530.0
                    MINIMUM ANGLE  0.0 DEGREES
    XMTR  2.0 TO 30.0     CURTAIN    H -1.00 L  -0.50 A   4.0 OFF AZ   7.0
    RCVR  2.0 TO 30.0     VERTICAL   H  0.00 L   2.50 A   0.0 OFF AZ   0.0
    POWER= 100.00KW  3 MHZ NOISE=-150.0DBW  TIME= 90 PERCENT  REQ.S/N=55.0DB
    MULTIPATH POWER TOLERANCE= 6.0 DB    MULTIPATH DELAY TOLERANCE=0.50 MS.

      UT  FOT  LUF    UT  FOT  LUF    UT  FOT  LUF     UT  FOT  LUF

      01  15.0   -    07  12.0   -    13  15.3   -     19  15.9   -

      02  14.3  10.7  08  11.1   -    14  17.5   -     20  16.2   -

      03  13.3   8.8  09  10.6   -    15  18.9   -     21  16.4   -

      04  12.9   8.8  10  10.8   -    16  19.0   -     22  16.2   -

      05  12.6   -    11  11.2   -    17  17.9   -     23  15.9   -

      06  12.6   -    12  12.5   -    18  16.0   -     24  15.6   -
```

Table X   FOT and LUF computer prediction (program HFMUFES 3)
      - required reliability not satisfied at any frequency

```
                        1
             JUNE 15, 1979    10 CM FLUX 186.   (SSN 143.)
    LONDON       TO  BOULDER            AZIMUTHS    MILES     KM.
    51.50N -   0.17W   40.03N - 105.27W   306.97   40.51   4679.1   7530.0
                    MINIMUM ANGLE  0.0 DEGREES
    XMTR  2.0 TO 30.0     CURTAIN    H -1.00 L  -0.50 A   4.0 OFF AZ   7.0
    RCVR  2.0 TO 30.0     VERTICAL   H  0.00 L   2.50 A   0.0 OFF AZ   0.0
    POWER= 100.00KW  3 MHZ NOISE=-150.0DBW  TIME= 90 PERCENT  REQ.S/N=55.0DB
    MULTIPATH POWER TOLERANCE= 6.0 DB    MULTIPATH DELAY TOLERANCE=0.50 DB
                         FREQUENCIES IN MHZ
    UT  MUF   2.0  3.0  5.0  7.5 10.0 12.5 15.0 17.5 20.0 25.0 30.0

    04  16.7   K(0)MUF=(20.5)    K(5)MUF=(13.1)
        2F      -    -   3F   3F   3F   3F   2F   2F   2F   -    -   MODE
        4.9     -    -  9.2  8.6  9.0 10.0  2.5  4.9  4.9   -    -   ANGLE
         .50    -    -  .99  .99  .98  .92  .73  .37  .4    -    -   F. DAYS
        48.     -    -  33.  40.  44.  46.  42.  48.  48.   -    -   DBU
        75.     -    -  56.  66.  73.  76.  75.  75.  74.   -    -   S/N DB
         .35    -    -  .8   .37  .65  .72  .49  .25  .2    -    -   S. PROB
         .6     -    -   -    -    -    -    -   .1    -    -    -   MP PROB

    08  14.7   K(0)MUF=(18.0)    K(5)MUF=(11.5)
        2F      -    -    -   3F   3X   2F   2F    -    -    -    -   MODE
        5.3     -    -    -  9.0  5.6  5.3  5.3    -    -    -    -   ANGLE
         .50    -    -    -  .95  .79  .44  .8     -    -    -    -   F. DAYS
        37.     -    -    -  20.  25.  38.  40.    -    -    -    -   DBU
        67.     -    -    -  49.  60.  67.  68.    -    -    -    -   S/N DB
         .9     -    -    -  .0   .6   .8   .2     -    -    -    -   S. PROB
         .6     -    -    -    -   .31  .4    -    -    -    -    -   MP PROB

    12  16.1   K(0)MUF=(18.9)    K(5)MUF=(13.2)
        2F      -    -    -    -   3F   2F   2F   2F    -    -    -   MODE
        5.8     -    -    -    - 10.0  3.1  5.8  5.8    -    -    -   ANGLE
         .50    -    -    -    -  .78  .64  .34  .12    -    -    -   F. DAYS
        31.     -    -    -    -  9.   21.  33.  38.    -    -    -   DBU
        59.     -    -    -    -  42.  53.  61.  64.    -    -    -   S/N DB
         .0     -    -    -    -  .0   .0   .1   .0     -    -    -   S. PROB
         .8     -    -    -    -    -   .12  .4    -    -    -    -   MP PROB

    16  19.0   K(0)MUF=(19.0)    K(5)MUF=(19.0)
        2F      -    -    -    -    -   3F   3X   2F    -    -    -   MODE
        7.0     -    -    -    -    - 13.3  7.8  7.0    -    -    -   ANGLE
         .99    -    -    -    -    -  .99  .99  .26    -    -    -   F. DAYS
        32.     -    -    -    -    -  10.  17.  34.    -    -    -   DBU
        60.     -    -    -    -    -  43.  50.  61.    -    -    -   S/N DB
         .2     -    -    -    -    -  .0   .0   .0     -    -    -   S. PROB
          -     -    -    -    -    -    -   .5    -    -    -    -   MP PROB

    20  20.2   K(0)MUF=(24.5)    K(5)MUF=(15.8)
        2F      -    -    -    -    -   3F   3F   2F   2F    -    -   MODE
        5.6     -    -    -    -    -  8.8 12.9  4.2  5.6    -    -   ANGLE
         .50    -    -    -    -    -  .95  .81  .53  .5     -    -   F. DAYS
        35.     -    -    -    -    -  17.  24.  32.  40.    -    -   DBU
        61.     -    -    -    -    -  49.  55.  58.  66.    -    -   S/N DB
         .1     -    -    -    -    -  .0   .0   .0   .0     -    -   S. PROB
         .5     -    -    -    -    -    -    -   .6    -    -    -   MP PROB

    24  19.5   K(0)MUF=(23.5)    K(5)MUF=(14.8)
        2F      -    -    -    -   3F   3F   3F   2F   2F   2F    -   MODE
        5.1     -    -    -    -  7.9  8.5  9.9  2.3  5.1  5.1    -   ANGLE
         .50    -    -    -    -  .99  .99  .93  .73  .43  .4     -   F. DAYS
        44.     -    -    -    -  23.  32.  37.  35.  44.  46.    -   DBU
        69.     -    -    -    -  53.  63.  68.  68.  69.  72.    -   S/N DB
         .6     -    -    -    -  .0   .4   .7   .6   .4   .1     -   S. PROB
         .10    -    -    -    -    -    -    -   .3   .7    -    -   MP PROB
```

Table XI   Signal/noise ratio and service probability computer
      prediction (program HFMUFES 3)

PROPAGATION OF LONG RADIO WAVES IN THE EARTH'S ENVIRONMENT

by

E V Thrane
Norwegian Defence Research Establishment
P O Box 25 - N-2007 Kjeller
Norway

SUMMARY

A brief review is given of the characteristics of radio waves with frequencies below 300 kHz. First the antenna problem is discussed, then the propagation of the long waves in the waveguide formed by the earth's surface and the lower ionosphere is treated. Some of the most important computational methods available for predicting phase and amplitude of long waves are briefly described. The penetration of long waves into the sea is of importance for submerged vessels, and the physical principles of such penetration will be given some attention. At present, the most important application of long waves is probably for navigation purposes. The major VLF and LF navigation systems in use will be described and their accuracy and limitations discussed.

1. INTRODUCTION

The history of man's practical use of radio waves begins with communication at low frequencies, and the existence of the ionosphere was first inferred from the behaviour of low frequency signals propagating over long distances. Even though technical advances now allows generation and detection of coherent electromagnetic waves through the entire frequency spectrum up to and including visible light, the long radio waves are still important, and their useful properties are being exploited.

In this lecture we shall discuss the propagation of radio waves with frequencies below 300 kHz and some of their applications for navigation and communication purposes. This frequency range is normally divided into several parts:

Low frequency waves (LF)	30 kHz - 300 kHz
Very low frequency waves (VLF)	3 kHz - 30 kHz
Extremely low frequency waves	3 Hz - 3 kHz
Ultra low frequency waves (ULF)	<3 Hz

The waves in each subrange have their specific, interesting and useful properties. For example, VLF and ELF waves can propagate to large distances with little attenuation and high phase stability, and ELF and ULF waves penetrate the sea to appreciable depths.

Both the conducting layers in the upper atmosphere and the earth's surface play decisive roles in the propagation of waves below 300 kHz, and we shall discuss the influence of these boundaries, both separately and taken together to form a waveguide.

2. ANTENNAS AND GROUND WAVE PROPAGATION

2.1 Antennas

Since the free space wavelengths in the frequency range we are dealing with change from 1 km at 300 kHz to 100 000 km at 3 Hz, it is obvious that all antennas must be electrically small, that is with physical dimensions which are small compared to one wavelength. The design of antennas in this frequency range is a very difficult problem, both in theory and in practice, and we cannot go into great detail here. The problems are treated by Watts (1967).

A useful, simple concept of an electrically small antenna is a short vertical wire with one end on a perfectly conducting flat plane, Figure 1. Our main concern is the vertical electric field produced by such an antenna as a function of distance d along the earth's surface. This field can be expressed as

$$E_z(t) = -\frac{1}{2\pi\epsilon_0} \left[\int \frac{M(t')\,dt}{d^3} + \frac{M(t')}{c_0 d^2} + \frac{d}{dt}\frac{M(t')}{c_0 d} \right] \tag{1}$$

where $M(t) = I(t) \times h_e$

I – antenna current

h_e – effective height of antenna

c_0 – free space velocity of light

$t' = t - d/c_0$

$h_e = \frac{\int I\,dh}{I}$ $d \gg h_e$

We note that the total field consists of three terms:

a)   The electrostatic term produced simply the the separation of stationary charge in the conducting system, that is, the time integral of charge times the effective height

b)   The induction term produced by the current flow

c)   The radiation term produced by the time rate of change of current

If we apply an alternating current $I = I_o \, e^{i\omega t}$ to the antenna, we obtain

$$E_z(t) = \frac{I_o h_e}{2\pi\epsilon_0} \left[\frac{-i}{\omega d^3} + \frac{1}{c_0 d^2} + \frac{i\omega}{c_0^2 d} \right] e^{i\omega t'} \tag{2}$$

Similarly the tangential magnetic field is given by

$$H_\phi(t) = \frac{i_o h_e}{2\pi} \left[\frac{1}{d^2} + \frac{i\omega}{c_0 d} \right] e^{i\omega t'} \tag{3}$$

We note that the electrostatic field decays very rapidly with distance d, this term will only dominate for $d/\lambda < 0.1$. For $d = \lambda$ the magnitude of the induction and radiation terms are equal, and thus for distances $d > \lambda$ the radiation field will dominate and both the electric and magnetic fields will decay as $1/d$. This means that only the radiation term need be considered for most practical communication purposes at LF and in the upper part of the VLF band, whereas the induction term will be important at ELF, and in the lower part of the VLF band.

The simple antenna model we are considering will have a polar diagram such that a wave launched at an elevation angle ψ will have an amplitude $E_\psi = E_o \cos \psi$, where E_o is the "free space reference field", that is, the vertical field of the wave launched tangentially along the conducting plane. The vertical component of E_ψ will be $E_{z,\psi} = E_o \cos^2 \psi$ (Figure 2).

The power flow per unit area from the antenna is given by the Poynting vector $\mathrm{Re}|\vec{E} \times \vec{H}| = E_{z,\psi} H_\phi$. Introducing the impedance of free space $Z_o = E_{z,\psi}/H_\phi$ and integrating over the hemisphere above the conducting plane at a distance d

$$P_r = \frac{4\pi d^2}{G} \frac{E_{z,o}^2}{Z_0} \tag{4}$$

where   G - gain of the antenna relative to an isotropic radiator

This gain is $G = 3$ for our simple case and $Z_o = 120 \, \pi\Omega$.

Introducing these numbers and putting $E_{z,o}$ equal to the radiation term in Equation (2.2) we obtain for the radiated power

$$P_r = I^2 \, 160 \, \pi^2 \left(\frac{h_e}{\lambda} \right)^2 \tag{5}$$

The radiation resistance is

$$R_o = \frac{P_r}{I^2} = 160 \, \pi^2 \left(\frac{h_e}{\lambda} \right)^2 \qquad h_e < 0.1 \, \lambda \tag{6}$$

We note that the radiation resistance, and hence the power radiated decreases rapidly with increasing wavelength.

Although a short vertical wire is a useful conceptual model for a VLF-LF transmitter antenna, in actual practice an antenna is often a very complex and expensive structure. As an example Figure 3 shows the biggest antenna at VLF in existence. The effective height h_e of such an antenna is often determined experimentally by measuring the electric field at a distance d in the radiation zone.

Another useful quantity is the radiation efficiency of an antenna, defined as

$$\eta_a = R_r / R_a \tag{7}$$

where $R_a = R_r + R_e$

R_e - antenna loss resistance

For the large antenna shown in the figure the radiation efficiency is 70%.

2.2 Ground wave propagation

Having discussed the antenna, our next step is to consider ground wave propagation, that is, propagation in the absence of an ionosphere. A realistic approach to this problem at low and very low frequencies must take into account earth curvature and the finite conductivity of soil or sea. The problem is mathematically quite complex, and we shall not go into detail, but only illustrate some general properties of ground wave propagation.

Propagation of radio waves along the earth's surface was treated theoretically as early as 1907 by Zennick. Treatments by Sommerfeld, Van der Pol, and others followed. Norton (1936, 1937, 1941) developed working formula suitable for numerical computations. To give an impression of the properties of the waves we shall consider some computations made by Wait and Howe (1956) for distances up to 2500 km. These authors assume a short vertical dipole on a spherical earth of radius a and conductivity σ. They find that the vertical electric field at a distance d from the transmitter can be approximated by

$$E = \frac{-i\mu\omega I h_e \; e^{-i\bar{k}d}}{2\pi d} \left[1 - \frac{i}{d} - \frac{1}{k^2 d^2} \right] W \qquad (8)$$

Here
$k = 2\pi/\lambda_o$ where λ_o = free space wavelength

$\bar{k} = k(1+\frac{1}{3}akf)$ where f is a factor that takes into account refraction in the neutral atmosphere (not the ionosphere)

$W = W(k,a,d,\sigma)$ is a residue series

Figure 4a-d show the amplitude and phase of the ground wave for several frequencies and ground conductivities. We note that the attenuation increases with increasing frequency and decreasing ground conductivity, and that the phase lag beyond a certain distance increases with frequency and decreasing conductivity.

2.3 The lower ionosphere

At distances beyond a few hundred km the ground wave from a LF or VLF transmitter will no longer necessarily dominate over the signal reflected from the ionosphere, and a knowledge of the properties of the lower ionosphere becomes essential in order to estimate the phase and amplitude of the waves. For most practical applications only the ionosphere below 110 km is of interest here, but propagation through the ionosphere into the magnetosphere is possible for VLF waves and will be mentioned later. The region between 50 and 110 km above the earth's surface is a very interesting one, characterized by very rapid changes of atmospheric properties with height. The air density decreases from about $2 \cdot 10^{16}$ cm^{-3} at 50 km to about $2 \cdot 10^{12}$ cm^{-3} at 110 km. The temperature decreases with height from about 259 K at 50 km to 150 K at 85 km, and then increases to 300 K at 110 km. The electron density, on the other hand, increases from normal daytime values of less than 10 cm^{-3} at 50 km to more than 10^5 cm^{-3} at 110 km. Thus the degree of ionization is very low throughout the region ($\simeq 10^{-15}$ at 50 km, $\simeq 10^{-7}$ at 110 km) and collisions between electrons and neutral molecules and between ions and neutrals are important. The atmosphere below 100 km appears to be in a state of turbulent mixing so that the relative abundance of the major atmospheric constituents does not change with height. At 100 km or slightly above there is an abrupt transition called the turbopause from the turbulent regime to a region where diffusive equilibrium prevails, and each gas is distributed with its own scale height. The photochemistry of the lower ionosphere is very complex and characterized by the important role played by some minor constituents with very small concentrations, such as nitric oxide and water vapour.

The most important sources of ionization in the lower ionosphere are solar ultraviolet radiation, x-rays, and energetic particle precipitation. It is convenient to distinguish between the undisturbed ionosphere, characterized by regular seasonal and diurnal variations, and the ionosphere during various kinds of disturbances, caused by irregular changes in the flux of ionizing radiation. The disturbed ionosphere has been discussed in detail in a previous lecture, and we shall only deal with the quiet D-region here.

Figure 5 shows estimates of ion production based on solar and atmospheric measurements during undisturbed conditions, and for two different solar zenith angles (Thrane, 1972). We note that the picture is fairly complex. In the upper part solar ultraviolet (102.5 nm, 97.7 nm) and x-rays (0.4 - 14.0 nm) ionize all atmospheric constituents. At lower heights, the solar radiation of 121.6 nm very efficiently ionizes a minor constituent NO to produce an appreciable ion density. At the very lowest part of the region cosmic rays, that is, extremely energetic particles from the galaxy, give a small but stable contribution to the ion production. We also note the important changes caused by changes in solar elevation. During an undisturbed night there is a very small remnant of ion production caused by scattered light, and of course, by cosmic rays.

The primary ions that are produced are O_2^+, N_2^+ and also NO^+. Through a charge transfer N_2^+ will rapidly convert to O_2^+ so that O_2^+ and NO^+ are the main primary ions. In recent years it has been discovered that the primary ions, in the presence of water vapour, can convert to complex cluster ions of the form $H^+(H_2O)_n$. Electrons can also attach to neutral molecules to form negative ions (Johannessen, 1974).

The ionization balance in the lower ionosphere can be described by a simple continuity equation

$$\frac{dN^+}{dt} = q - L \qquad (9)$$

where   q – production

L – loss rate of positive ions with concentration N^+

Under undisturbed conditions $q = =(h,\chi)$ where h is the height and χ the solar zenith angle.

The loss term is given by

$$L = \alpha_D N_e N^+ + \alpha_i N^- N^+ = \psi N_e^2 \tag{10}$$

where N_e and N^- are the electron and negative ion densities

$N^+ = N_e + N^-$ and α_D and α_i are recombination coefficients

ψ is an effective recombination rate, often used in the literature. Figure 6 shows some examples of $\psi(h)$ in the D-region, compiled for undisturbed conditions. The change in ψ from a value of about 10^{-6} cm^3 s^{-1} below 85 km to a value of $5\cdot10^{-7}$ at greater heights is thought to be due mainly to a change in ion composition from a lower regime where cluster ions dominate. The cluster ions recombine more rapidly than the primary ions. Conditions favourable for the formation of cluster ions are: low temperature, weak ion production and small concentration of atomic oxygen, which species effectively inhibit cluster ion formation. These conditions are not fulfilled in the higher regime.

The continuity equation is normally written in terms of the electron density N_e, because the free electrons with their small mass have greater influence on the propagation of radio waves than do the heavy ions. However, under some conditions it has been shown that the concentration of ions are important for ELF and VLF propagation. Figures 7 and 8 show typical night- and daytime $N_e(h)$ profiles for undisturbed conditions.

2.4 Ionospheric propagation of waves below 300 kHz

The principles of HF propagation in the ionosphere have been discussed in previous lectures. It is important to realize that these principles cannot always be directly applied to propagation of waves with frequencies below 300 kHz. The reason is simply that HF waves have wavelengths from 100 m to 10 m, which are small compared to the scale of the ionospheric layers, whereas LF, VLF and ELF waves have wavelengths comparable to or much greater than the vertical ionospheric structure. For HF waves, the ionosphere may in most cases be treated as a slowly varying medium where the principles of geometric optics apply. This approximation is often not valid for LF and VLF waves.

It is nevertheless useful to introduce the subject by considering some simple magnetoionic formula (Ratcliffe, 1959). We define a complex refractive index $n = \mu - i\chi$ and remind the reader that propagation in a horisontally stratified medium may be described by Snell's law, $n(h) \sin \theta = \sin\theta_I$. A wave incident from below the ionosphere with a wavenormal at an angle θ_I to the vertical, will at, a height h where the refractive index is $n(h)$, be refracted at an angle θ to the vertical. Reflection ($\sin \theta = 1$) occurs at a level where $n(h) = \sin \theta_I$, that is $n(h) = 0$ at vertical incidence.

For propagation in an ionospheric plasma without magnetic field and with no collisions, we have

$$n^2 = 1 - X, \quad X = \frac{\omega_N^2}{\omega^2} \tag{11}$$

where ω_N – plasma frequency of the wave

$$\omega_N = \frac{N_e e^2}{\epsilon_0 m_e}$$

A wave of angular frequency ω propagating vertically in an ionosphere where ω_N^2, and therefore X, increases with height, will be reflected at the level where $n^2 = 0$ and $X = 1$. It is useful to plot a dispersion diagram (Figure 9) showing the real part of the refractive index $\mu^2(X)$. Beyond $X = 1$, $\mu = 0$ and no propagation is possible.

We now introduce the earth's magnetic field through the parameter $Y = \omega_H/\omega$ where ω_H is the electron gyrofrequency. For waves with frequencies below 300 kHz, $Y > 1$, and for propagation very nearly along the magnetic field lines (vertical propagation at high latitudes) the dispersion is sketched in Figure 10. Note that there are three branches, two corresponding to waves reflected at $X = 1$ and $X = 1+Y$ respectively, and one corresponding to a wave with large refractive index propagating only at levels where $X > 1$.

In a realistic ionosphere we must include the effects of collisions. Inclusion of collisions will smear out the sharply defined reflection levels in Figure 10, and the branches may be joined as indicated in Figure 11. Here there is one branch that corresponds to a weak reflection near $X = 1$ and a reflection near $X = 1+Y$, while the other branch represents a wave that can travel beyond both $X = 1$ and $X = 1+Y$. This wave can thus penetrate the ionosphere and is called the whistler wave.

For a wave of frequency 100 kHz the condition $X = 1$ corresponds to an electron density of $N_e = 124$ cm^{-3}, whereas $X = 1+Y$ corresponds to $N_e \approx 1900$ cm^{-3}. Referring to the electron density profiles in Figures 7 and 8, we see that we should expect reflections to occur at low heights, even during an undisturbed night. The exception is, as already mentioned, the whistler wave. This wave component has some peculiar properties. After penetration of the ionosphere it will be guided along the earth's magnetic field lines to the opposite hemisphere. On its way through the magnetospheric plasma, the wave suffers frequency dispersion and a signal pulse from a broadband source such as a lightning flash will arrive at the opposite

hemisphere as a whistling tone with steadily falling pitch. Unfortunately we shall not have time to go further into this matter here.

It should be emphasized again that our simple discussion of the Appleton-Hartree formulae for the refractive index of a low frequency wave can only give a very rough picture of what happens to such a wave inside the ionosphere. In practice quite sophisticated methods must be used to study the propagation of waves in and below a medium which changes significantly within a distance smaller than a wavelength. We shall briefly discuss two such methods here, the "full wave" ray theory and the "mode" theory. The first of these deals with the problem of computing the reflection coefficient of a wave incident upon a horisontally stratified ionosphere. The field at a distance from the transmitter is then calculated as a sum of the ground wave and waves reflected one or more times from the ionosphere and the ground (see Figure 12). Experience shows that this method is useful up to distances of 100-1500 km. In this region only the ground wave and the first and possibly the second hop skywave need be considered. Beyond 1500 km too many skywaves must be added for the method to be practical. The second method, the "mode" theory, treats the space between the earth and the ionosphere as a waveguide. It can be shown that many waveguide modes are excited by the transmitter, but that at large distances, that is beyond about 1000 km, only one or possibly two modes need be considered. The full wave ray theory and the mode theory are thus complementary, each has its range of distances and frequencies in which it is useful.

The two types of approach just mentioned will serve to illustrate the problem, however, there are a number of ways in which the behaviour of long waves may be predicted (Swanson 1977). The most sophisticated methods may be termed "Full wave waveguide" and include detailed structure and inhomogeneities in the ionosphere as well as the earth's surface (Pappert et al 1967, Galejs 1972). Other methods use empirical relations between observable quantities, such as phase and amplitude as functions of solar zenith angle and time and space coordinates, to describe the phenomena without involving physical parameters (Swanson 1977).

2.4.1 The full wave solution

The principle of the "full wave" theory is as follows (Pitteway 1965, Budden 1961):

a) Assume a coordinate system with the z-axis vertical and the y-axis along the magnetic meridian. A plane wave whose wave normal has direction cosines (l, m, n) is incident upon an ionosphere that only changes in the z-direction. Combining Maxwell's equations with the constitutive relations of the medium it is possible to show that the electric and magnetic field components of the wave satisfy a set of differential equations of the form

$$\vec{e}' = -ik\,T\,\vec{e} \qquad (12)$$

Here $\vec{e}$ is a column vector

$$\vec{e} = \begin{vmatrix} E_x \\ E_y \\ H_x \\ H_y \end{vmatrix} \qquad (13)$$

and derivation is with respect to height z. k is the wave number and T is a four by four matrix whose elements contain the wave direction cosines and the properties of the medium, that is, the earth's magnetic field and the electron density and collision frequency. Snell's law is introduced by writing $\partial/\partial x = -ikl$ and $\partial/\partial y = -ikm$ in all field quantities so that time and horisontal spatial variations are described by a factor $\exp[i\omega t - ik(lx+my)]$. Equation (12) is equivalent to four first order linear differential equations.

b) Find a solution that satisfies the differential equations at some height. For example at some great height there are only upgoing waves since the energy is incident from below.

c) Integrate the equations analytically or numerically downwards through the ionosphere to give the height variation of the wave field, and form the solution below the ionosphere.

d) Separate this solution into upgoing and downcoming waves and find the reflection coefficients and polarizations.

A solution to the wave equation found in this manner is called a "full wave" solution. Analytical solutions can only be found in a few simple cases, but with modern computers numerical solutions can be found rapidly by a step by step integration for an ionosphere with an arbitrarily specified height variation. An example is shown in Figure 13. For a particular electron density profile, shown at the top of the figure, two solutions corresponding to the two magneto-ionic components have been found. The figure gives a snapshot of the wavefields at a particular instant. We note that one component has a fairly well defined reflection level and a standing wave pattern produced by almost equally strong up- and downgoing waves. The other solution has only a weak downgoing wave, and part of the energy is coupled into the whistler mode that penetrates the ionosphere.

Another example of computed wavefields is shown in Figure 14 and demonstrates the lowering of the reflection level as the angle of incidence increases. Note also that the reflection process becomes more and more gradual, and at grazing incidence there is little meaning to the term reflection height inside the ionosphere. This illustrates why simple ray theory breaks down for the long waves.

Now in order to find the total wavefield on the ground at a given distance from a transmitter, the skywave reflected from the ionosphere must be combined with the ground wave, taking properly into account their relative phases. The correct procedure would of course be to perform a full wave calculation for each component of an angular spectrum of plane waves reflected from the ionosphere. However, this cumber-

some procedure may be circumvented by using Fermat's principle to find the wave that has the shortest optical path from transmitter to receiver, and then do a full wave integration for that wave only (Bain and May 1967). The result of such a computation is shown in Figure 15, which depicts the vertical electric field versus distance for a day time ionospheric model. Skywave and groundwave combine to produce an interference pattern called a Hollingworth pattern. Beyond 700 km the two hop skywave should be included to give a correct estimate of the total field. The positions of the maxima and minima in the Hollingworth pattern will change with the ionospheric model and measurements of the positions of such minima and maxima may be used to determine an effective reflection height of the ionospheric layers, although such a height may have little physical significance.

Extensions of the ray "hop" theory have also been made by Johler (1970), Berry and Herman (1971) and Bjøntegaard (1974).

2.4.2 The mode theory

The basic principle of the mode theory is illustrated in Figure 16 (Davies 1965, Wait 1970). The ground and ionosphere are, as a first approximation, thought of as plane, perfect conductors a distance h apart and a vertical dipole in the plane $z = 0$ is the source. An observer on the ground a distance from the source will see the signal arriving from the dipole plus a series of images in the ground and the ionosphere. The signals from the images in the ionosphere are in phase in the direction making an angle β with the vertical when

$$2h \cos \beta = 2h\, C_n = n\lambda \tag{14}$$

For a given value of n

$$\cos \beta = C_n = \frac{n\lambda}{2h}$$

where n is an integer, the mode order.

Similarly, the ground images will add up at an angle $\pi-\beta$ and the composite wwave will travel parallel to the plane $z = 0$ with a phase velocity $c/\sin \beta = c/S_n$.

Consider the wave directed broadside, that is $\beta = 90^\circ$, $n = 0$. We imagine the wave to originate in a line source with an effective uniform current I_a. Since the images occur as pairs of dipoles of length s and current I and since they are separated by distances 2h we find

$$I_a = 2\, \frac{s}{2h}\, I \tag{15}$$

The vertical field E_z from such a line current is given by (Wait 1960)

$$E_z = \frac{1}{4}\, \mu_0\, \omega\, I_a H_0^{(2)}(kr) = \frac{1}{4}\, \mu_0\, \omega\, \frac{I_s}{h} H_0^{(2)}(kr) \tag{16}$$

Here $H_0^{(2)}(kr)$ is the Hankel function of the second kind with argument kr. r is the distance from the transmitter along the ground.

For large distances equation (16) reduces to $(r \gg \lambda)$

$$E_z = \frac{1}{2} \left(\frac{\mu_0}{\epsilon_0}\right)^{1/2} \frac{I_s}{h} (\lambda r)^{-1/2}\, e^{i\frac{\pi}{4}}\, e^{-ikr} \tag{17}$$

This field corresponds to the mode obtained by putting $n = 0$ in equation (14), and is called the zero order mode. The field for the higher order modes are obtained by first finding the field from a pair of dipole images at distances 2nh above and below the ground

$$E_{zn} = 2 \frac{\mu_0 \omega I_s}{4h}\, S_n^2\, H_0^{(2)}(kr\, S_n) \tag{18}$$

and then summing over all n

$$E_z = \frac{\mu_0 \omega I_s}{2h} \sum_{n=0}^{\infty} \zeta_n S_n^2\, H_0^{(2)}(kr\, S_n) \tag{19}$$

$$(\zeta_0 = 1,\ \zeta_n = 2)$$

In the case $r \gg \lambda$ this expression also reduces to a simple expression.

We have so far assumed that both ground and ionosphere are perfect conductors with reflections coefficients $R = +1$. In practice the ionosphere at large distances may behave as if it had a reflection coefficient $R = -1$. In this case the contributions from the ionospheric images alternates in sign corresponding to a phase change of π. Thus

$$2h \cos \beta = (n - \frac{1}{2}) \lambda \tag{20}$$

and there is no zero order mode.

The electric field will be

$$E_z = \frac{\mu_0 \omega I_s}{2h} \sum_{n=1}^{\infty} S_n^2 H_0^{(2)} (kr S_n)$$

(21)

The field patterns along the direction of propagation are shown in Figure 17 for the first and second order mode. The patterns will change as indicated depending upon the sign of the ionospheric reflection coefficient. In both cases it may be shown that at large distances only one mode need be considered, which gre greatly simplifies the computations.

From Figure 16 we see that the wavelength along the direction of propagation is

$$\lambda_g = \frac{\lambda}{\sin \beta}$$

Combining this with equation (14) we obtain

$$(\frac{1}{\lambda_g})^2 = \frac{1}{\lambda^2} - (\frac{n}{2h})^2$$

(22)

For $\lambda < 2h/n$, λ_g is imaginary and the wave is evanescent. There exists, therefore, a minimum cutoff frequency below which waves will not propagate

$$f_n = \frac{nc}{2h}$$

(23)

For n = 1 and an ionospheric height of 75 km $f_0 = 2$ kHz. Obviously, below this frequency only the zero order mode can propagate. An approximate formula for the vertical electric field of this mode is given below (Rowe 1974). The source is here assumed to be a horizontal line current of strength I and length L and would apply to a horizontal lightning stroke or a horizontal antenna, but the propagation characteristics would not change significantly if the source was a vertical current.

$$|E_{za}| = \frac{|I|Lf}{2h_i} (\frac{2\pi\mu_0}{c_o \sigma_e})^{1/2} (\frac{1/a}{\sin r/a}) e^{-\alpha r} \cos \theta$$

(24)

Here

h_i = effective ionospheric height

v = phase velocity

σ_e = earth conductivity

a = earth radius

r = distance along curved earth

θ = angle between source current and direction of propagation

α = attenuation factor

The attenuation factor α for ELF is very small. Figure 18 shows some measured values for day and nighttime conditions (Davis 1975). For frequencies of 45-75 Hz values in the range 0.4 - 2.5 dB/Mm have been measured for different ionospheric conditions.

Mode theory is a powerful tool in the study of long wave propagation, particularly over large distances. The theory has been modified and extended to take into account imperfectly conducting boundaries, earth curvature, and even the change with height of the ionospheric parameters. Figure 19 shows some experimental and calculated attenuation rates in the VIF-range. As will be seen, typical values are 1-2 dB/Mm. For ELF waves the attenuation is even less, in the range 0.5 - 1.5 dB/Mm. The attenuation rate and phase stability depend upon effective ionospheric height and upon the ground. In particular the Greenland ice cap greatly increases the attenuation of waves propagating across it.

Figure 20 shows the dependence of attenuation rate and phase velocity of the first order mode upon ionospheric height. It will be appreciated that a lowering of the effective height caused by an ionospheric disturbance may significantly alter the phase and amplitude of the long waves.

2.5 Penetration of long waves into the sea

The need for navigation and communication for submerged vessels has renewed the interest in radio waves with frequencies near and below 10 kHz, since such waves can penetrate sea water to some extent. The refractive index, n = c/v, is very large for radio waves in sea water. Thus the phase velocity v of the waves is much smaller than the free space velocity of light c. The problem of communicating with a submarine is illustrated in Figure 21. The radio waves are refracted steeply into the water. A series of articles on the problem can be found in IEEE No 4 (1974).

We treat the problem of penetration of a radio wave into the sea by assuming a plane boundary z = 0 between air and sea water. The wave is travelling along the boundary in the direction of the positive x-axis, see Figure 21, with an angle of incidence θ_1. The total field above the surface $\vec{E}_a$ is the sum of an incident and a reflected wave. We shall use indices a and b for field quantities above and below the surface.

Sea water is a good electrical conductor. The refractive index of an electromagnetic wave travelling in this medium may be written

$$n_s^2 = \frac{\epsilon_s}{\epsilon_0} - i\frac{\sigma_s}{\epsilon_0\omega}$$

(25)

Typical numerical values are $\epsilon_s/\epsilon_0 = 81$ and $\sigma_s = 4$ mho m^{-1}. For a frequency of $f = 100$ Hz we thus obtain

$$n_s^2 = (81 - i\,7.2\cdot10^8)$$
$$n_s \approx 1.9\cdot10^4\,(1-i)$$

(26)

Because the real part of the refractive index squared is small compared to the imaginary part, we may write

$$|n_s| = \left(\frac{\sigma_s}{\epsilon_0\omega}\right)^{1/2}, \quad n_s \approx \left(\frac{\sigma_s}{2\epsilon_0\omega}\right)^{1/2}(1-i)$$

(27)

$$|n_s| = 27\,000 \quad \text{for} \quad f = 100\,\text{Hz}$$

Because of the very large values of the refractive index in the sea, an ELF or VLF wave travelling in air along the surface of the sea will be refracted at the air-sea boundary and travel almost vertically into the sea water, regardless of the angle of incidence. This can be demonstrated by applying Snell's law to the air-sea boundary.

$$\sin\theta_I = \text{Re}\{n_s\}\sin\theta_R$$

(28)

where θ_I and θ_R are angles of incidence and refraction respectively, and the refractive index in air is assumed to be $n_{air} = 1$. For the limiting case of grazing incidence, $\theta_I = 90°$, and for $f = 100$ Hz we find $\text{Re}\{n_s\} \approx 27\,000$ and $\theta_R = 0.002°$. In a real case a wave travelling in the earth-ionosphere waveguide will have a wavefront which has a forward tilt near both boundaries. Thus the wave described by Equation (24) will, in addition to the dominating vertical electric field E_{za}, have a small electric field component E_{xa} in the direction of propagation. It is this component that gives rise to an electromagnetic wave travelling nearly vertically into the sea. The magnetic wavefield will be tangential to the boundary both in the air and below the surface.

We now estimate the field strength and attenuation rate of the wave penetrating into the sea. Based on the above discussion we assume that the wave is travelling in the direction of negative z, with its electric field along the x-axis. The wave may therefore be described by

$$E_{xb} = E_{xbo}\,c^{in_s\omega z/c}$$

(29)

where n_s is the refractive index and E_{xbo} is the electric field just below the surface.

We insert the approximate value of n_s given by Equation (27) and find

$$E_{xb} = E_{xbo}\,c^{i\left(\frac{\sigma_s\omega}{2\epsilon_0 c^2}\right)^{1/2}z}\,c^{\left(\frac{\sigma_s\omega}{2\epsilon_0 c^2}\right)^{1/2}z}$$

(30)

Since z is negative, the last factor gives an attenuation rate. We note that the amplitude has fallen to a value E_{xb}/e at a depth

$$\delta_s = |z_s| = \left(\frac{2\epsilon_0 c^2}{\sigma_s\omega}\right)^{1/2} = \frac{1}{(\pi f\sigma_s\mu_0)^{1/2}}$$

(31)

where f is the wave frequency and $c = (\mu_0\epsilon_0)^{-\frac{1}{2}}$.

The depth δ_s is called the skin depth. At $f = 100$ Hz, $\delta_s \approx 25$ m. The phase velocity of the wave is

$$v_{ph} = \frac{c}{\text{Re}\{n_s\}} = \frac{c}{(\sigma_s/2\epsilon_0\omega)^{1/2}}$$

(32)

and the wavelength

$$\lambda_s = v_{ph}/f = \frac{c/f}{(\sigma_s/2\epsilon_0\omega)^{1/2}} = \left(\frac{4\pi}{\sigma_s f\mu_0}\right)^{1/2} = \left(\frac{4\pi\lambda_0}{\sigma_s c\mu_0}\right)^{1/2}$$

(33)

where λ_0 is the free space wavelength.

The attenuation at a depth $z = -\lambda_s$ is from (30) and (31)

$$|E_{xb}| = |E_{xbo}|\,e^{-2\pi} = 1.86\cdot10^{-3}\,|E_{xbo}|$$

(34)

This is equivalent to an attenuation rate of 55 dB per wavelength, and the wave is thus very rapidly absorbed in the medium.

We may therefore conclude that in order to reach a submerged vessel, the radio waves must travel in air to a point directly above the vessel, and then propagate vertically downwards, to the ship. Communication over long distances in sea water will be impossible.

Our next step is to estimate the magnitude of $E_{x_{bo}}$, that is the electric field just below the surface of the sea, from the knowledge of E_{za} the vertical electric field of the wave in air just above the surface. We assume that in air E_{za} is given by Equation (24) at a distance r from the transmitter. We further assume that the horizontal magnetic field H_{ya} is related to E_{za} through

$$H_{y_a} = -\frac{1}{SZ_0} E_{z_a} \qquad Z_0 = (\frac{\mu_0}{\epsilon_0})^{1/2} \qquad S = \sin\theta_1 \approx 1 \tag{35}$$

where the subscript a refers to fields just above the boundary. Since the magnetic field must be continuous across the boundary, the field just below the surface is

$$H_{y_b} = H_{y_a} \tag{36}$$

We again assume that the wave below the surface travels along the negative z-axis with its electric field along the x-axis as given by Equation (29). Maxwell's equation gives

$$\nabla \times \vec{E} = -\mu_0 \frac{\partial \vec{H}}{\partial t} = -i\mu_0 \omega \vec{H} \tag{37}$$

where $\partial/\partial t = i\omega$ is assumed.

In our case $\partial/\partial x = \partial/\partial y = 0$

$$\frac{\partial E_{x_b}}{\partial z} = -i\omega\mu_0 H_{y_b} \tag{38}$$

and from Equation (29)

$$\frac{\partial E_{x_b}}{\partial z} = i n_s \frac{\omega}{c} E_{x_b} = -i\omega\mu_0 H_{y_b} \tag{39}$$

This yields

$$E_{x_b} = -\frac{c\mu_0}{n_s} H_{y_b} = -\frac{Z_0}{n_s} H_{y_b} \tag{40}$$

Just below the surface we have from (35) and (40)

$$E_{x_{bo}} = -\frac{Z_0}{n_s} H_{y_a} = \frac{1}{n_s} E_{z_a}$$

and from (27)

$$|E_{x_{bo}}| = (\frac{\epsilon_0 \omega}{\sigma_s})^{1/2} |E_{z_a}| \tag{41}$$

Combining this expression with (30) and (31) we find

$$|E_{x_b}| = (\frac{2\pi f\epsilon_0}{\sigma_s})^{1/2} e^{(\pi f \sigma_s \mu_0)^{1/2} z} |E_{z_a}| \tag{42}$$

From Equation (42) we can estimate the horizontal electric field $|E_{x_b}|$ at a depth d = -z below the surface when the vertical electric field $|E_{za}|$ above the surface is known. It is convenient to introduce numerical values at this stage. Assuming the conductivity $\sigma_s = 4$ mho m^{-1} we obtain

$$|E_{x_b}|/|E_{z_a}| = 3.727 \cdot 10^{-6} \sqrt{f} \; e^{-3.974 \cdot 10^{-3} \sqrt{f} d} \tag{43}$$

Figure 22 shows the ratio $|E_{x_b}|/|E_{za}|$ as a function of depth for several frequencies in the range 10 Hz to 10 kHz. Curves for 100 kHz and 1 MHz have also been added for comparison.

We note that at a particular depth there seems to be an optimum frequency that gives the greatest field strength. Differentiating (43) with respect to f, we find this optimum frequency as

$$f_{opt} = 6.332 \cdot 10^4 / d^2 \tag{44}$$

Table 1 summarizes some properties of long waves in air and water. From a practical point of view, waves at 10 kHz may probably be useful down to heights of 15-20 m, whereas 100 kHz waves probably cannot be detected at depths greater than the amplitude of normal ocean waves.

FREQUENCY f		10 Hz	100 Hz	1 kHz	10 kHz	100 kHz	1 MHz
REFRACTIVE INDEX	μ_{sea}	60 000	19 000	6 000	1 900	600	190
	μ_{air}	1	1	1	1	1	1
WAVELENGTH	λ_{sea}	500 m	158 m	50 m	16 m	5 m	1.6 m
	λ_{air}	30 000 km	3 000 km	300 km	30 km	3 km	300 m
SKIN DEPTH δ_s		80 m	25 m	8 m	2.5 m	0.8 m	0.25 m

Table 1   Important parameters for electromagnetic waves propagating in air and seawater
(σ_s = 4 mho m^{-1})

2.6   <u>The noise environment</u>

Signals must of course be detected through a background of noise, and a knowledge of the natural as well as the man-made noise environment is essential. The noise environment in the low frequency region consists of noise from three kinds of sources:

a)   <u>Atmospheric noise</u>. This noise is generated by electrical discharges in the atmosphere. A lightning flash is an extremely strong, short-lived current that produces a broad noise spectrum with a peak around 10 kHz. Throughout the world the average discharge rate is about 100 per second, but the noise sources are concentrated in three areas, the thunderstorm centres in Central Africa, South America and in South-East Asia. There is of course a distinct seasonal and diurnal variation in the intensity of these sources, and because of the low attenuation the sources will contribute to the noise background over the whole globe.

b)   <u>Noise generated in the magnetosphere</u>. This noise is generated through the interaction of particles in the solar wind with the magnetospheric plasma, and penetrates the ionosphere in the whistler mode. Hiss, dawn chorus, are such noise sources.

c)   <u>Man-made noise</u>. Such noise is created by powerlines and electrical machinery. As will be appreciated, there are significant peaks in the noise spectrum at 50 Hz and 60 Hz. Long power lines are efficient antennas in the ELF range.

Concerning detection of long waves under the sea surface it should be noted that atmospheric noise arriving from distant sources will refracted at the sea surface in the same way as signals from a transmitter. The signal-to-noise ratio below the surface should therefore not be significantly different from that above.

3   PRINCIPLES OF VLF AND LF NAVIGATION SYSTEMS

We have discussed the propagation of waves below 300 kHz in some detail. It is clear that, particularly in the lower part of the frequency range, the waves can propagate to large distances with little attenuation. The ionosphere clearly has important influence on the propagation, but the signals are nevertheless much less sensitive to changes in the ionosphere than HF waves. Since the long waves are reflected below 100 km they are of course not influenced at all by the great variability of the F-region. The lower ionosphere at middle and low latitudes is very stable and has a systematic and predictable diurnal variation. At high latitudes severe disturbances may occur, but whereas HF communication is often completely disrupted under such conditions, the long waves reflected off the bottom of the ionosphere will be less severely affected and may even have their signal strengths increased.

The small attenuation and the great phase stability make the long waves attractive for communication, timing and navigation purposes. Of course, the small available bandwidth at low frequencies limits the usefulness for communication, but a fair number of VLF transmitters are in use throughout the world. One of the best known is perhaps the Rugby transmitter in England which operates on 16 kHz. Wherever high reliability is required for low data rates, such transmissions are of importance.

Navigation, both at sea and in the air, is perhaps the area where the long waves are most useful today.

Several navigation systems based upon long waves have been developed. In this section we will very briefly describe the principles of the three most important systems, Omega, Decca and Loran C, (Burgess 1977). The next section will discuss the propagational limitations of these systems.

Two different principles are used for long wave navigation, one depends upon measurements of phase differences between continuous waves, the other upon measured time differences between pulsed signals from several transmitters. The first principle is called hyperbolic navigation and is illustrated in Figure 23. Here A and B represent two navigation transmitters joined by a baseline AB. The two transmitters radiate synchronous signals at the same frequency but in a time-sharing mode. A receiver capable of detecting the phase difference between the signals from the two transmitters will measure such a difference at all points away from the normal in the midpoint of the baseline. The locus of all points having the same phase difference is a hyperbola, or rather a family of hyperbolas, since we realize that there must be an inherent

ambiguity of 2π in the phase determination. The area between two hyperbolas is called a "lane", and the width of a lane along the baseline is half of the transmitted wavelength. If we now use a third station together with, say, station A, we obtain another family of hyperbolas that cross the first one. Thus if we by other means have obtained a coarse "fix" or position so that we know which two lanes we are in, an accurate position can be obtained. The accuracy of a "fix" will of course depend on the geometry of the position relative to the transmitters. Wherever the hyperbola's cross at small angles poor resolution results. If the ship or aircraft starts out from a known position, it can navigate by counting the number of lanes through which it is passing, and as long as it does not lose track of the three necessary transmitters it will always know its position.

Both Omega and Decca employ the principle of hyperbolic navigation, whereas Loran-C uses pulsed signals.

3.1 The Omega system

The Omega system is a worldwide navigational aid operating in the band between 10 and 14 kHz. At present eight stations provide near global coverage. A fully implemented, permanent system is expected to be in operation in the near future. Detailed descriptions of the system are given by Swanson (1977) and references therein. The eight stations (see Figure 24) provide very long base lines, and transmit a series of frequencies in a time multiplex format. The basic navigation frequencies are 10.2, 11 1/3 and 13,6 kHz, but each station has additional unique frequencies that may be used for navigation by distance measurements based on a cycle counting technique. Omega may be used in different modes:

a) Using a single frequency, lines of position (lop) at the baseline with ambiguities of 15 km (10.2 kHz) are provided

b) Combining several frequencies, lop's of ambiguity 45 km (10.2 and 13.6 kHz) and 135 km (10.2 and 11 1/3 kHz) may be obtained

c) Differential Omega uses monitoring stations to correct for propagational variations within a few 100 km of the user.

In mode a) typical accuracies are 1-3 km, in mode b) lane identification is eased, whereas mode c) may give improved accuracy of 0.5 - 1 km in limited areas. Omega accuracy is limited by the propagation characteristics of the ionosphere-earth waveguide.

3.2 The Decca system

The Decca system operates on frequencies in the range 70 to 100 kHz. It is a hyperbolic CW system designed for high accuracy at medium range. About 50 Decca chains have been installed throughout the world, each chain consisting of one master and two or three slave stations.

The master and slave stations transmit on different frequencies, which are converted in the receiver to a single frequency for phase comparison. Navigation depends upon the ground waves, and because of the phase stability of the ground wave, very accurate positioning can be obtained. The wave reflected from the ionosphere is heavily absorbed at these frequencies, at steep incidence during the day. However, beyond a few hundred km the ionospheric reflection becomes stronger, and because the ground wave at 100 kHz is fairly rapidly attenuated, interference between ground and skywaves may occur and reduce the accuracy of the system. The range of the Decca system is therefore only of the order of 300 - 400 km, and will vary with ionospheric conditions. Accuracies of about 100 m may be obtained for pure ground wave propagation. For ionospheric propagation to greater distances the difference in the reflecting properties of the ionosphere within the frequency range may be a problem.

3.3 The Loran-C system

Loran-C is a very accurate navigation system using pulsed radio signals with a carrier frequency of 100 kHz. A chain of stations may consist of a "master" and two or more "slaves" and may cover a geographical region with a radius of up to 2000 km. An example is the existing chain in the North Atlantic with a master station at Færøy Islands and slaves at Jan Mayen, Iceland and North Norway. The pulses transmitted from stations in the chain are synchronized with great precision, and the user determines his position by measuring the time delay between signals received from different stations. The great advantage of the Loran-C is that the ground wave pulse, because it arrives first at the receiver, can normally be separated from the skywave. Accuracies of position determination of 150 m up to distances of 1800 km are quoted as typical in the literature (Potts 1972). Each station transmits pulses in a coded pattern that ensures correct identification and prevents interference.

4. INFLUENCE OF THE PROPAGATION MEDIUM UPON THE ACCURACY OF VLF AND LF NAVIGATION SYSTEMS

As we have seen both the state of the ionosphere and the properties of the earth's surface influence the accuracy of the long wave navigation systems. The ionosphere has characteristic regular and irregular variations in time and space, and the condition of the terrain and sea will change with position, but also to some extent with time. To what extent is it possible to predict and to correct for such changes?

4.1 The influence of the earth's surface

The velocity of a radio wave along the earth's surface will depend upon the value of the soil or water's refractive index, or conductivity, but also upon the contours of the terrain along the ray path. The conductivity should be known, not only on the surface, but down to the skin depth in the soil (see Equation (31). The most dramatic effect of anomalous ground conductivity is observed for VLF waves crossing the Greenland icecap (see Figure 9 in Thrane (this volume)). For the Omega system, a spatial theory developed by Swanson (1971), takes into account the effect of ground conductivity. The propagation paths are divided into segments and the phase delay estimated for each segment using coefficients describing the properties of the soil and ionosphere. In daytime and evening the phase velocity of the waves decreases monotonically with decreasing ground conductivity, down to a conductivity of 10^{-4} mho m^{-1}. For smaller ground conductivities a rapid increase in phase velocity is predicted. For certain paths anomalous phase variations are still unexplained, and may be due to the effects of stratified irregular ground (Swanson 1977). The errors for Omega signals from North Dakota received in Europe and the Mediterranean are about 18 centicycles, or five standard deviations.

The effects of irregular terrain contours on Loran-C signals have been studied by, for example Johler (1977). Figure 25 illustrates the effect of a hill upon the phase of the ground wave. In this case a disturbance of the order of 0.5 μs, corresponding to 150 m, is introduced. Obviously if better accuracy is required, detailed modelling of the terrain in the area of interest is necessary.

4.2 Modelling of the regular ionospheric variations

For the Omega system modelling of the regular diurnal and seasonal variation are included in the phase correction tables used with the system. A diurnal function is defined (Swanson 1977) which gives the transition from stable night conditions to daytime conditions (see Figure 26). The propagation path is divided into segments and for each segment the phase delay is computed using the diurnal weighting function. The total delay over a long path is then found by summing incremental delays over all segments. Except in the rapid transition periods near sunrise and sunset, the diurnal function is a good predictor of relative phase variation.

4.3 Influence of disturbances on navigation accuracy

The different types of ionospheric disturbances have been treated in some detail in a previous lecture. In this section we shall show a few examples of the influence of disturbances on Omega and Loran-C. Larsen (1977) has discussed results from 300 000 hourly observations of Omega signals at high latitudes. From his work we show Figure 27 which demonstrates the occurrence distributions of phase offsets during solar x-ray flares. In 1968 the flare effects on Omega had a mean duration of individual events of ≈55 minutes, with a standard deviation of ≈30 minutes. Mean phase deviation was ≈23 centicycles, which translates into a positional error of about 4 km under favourable system geometry. Figure 28 shows the phase offset during a solar proton event (PCA). During 1968-70 13 solar proton events gave a mean maximum phase offset of 38 centicycles, corresponding to a positional error of ≈7 km. The largest observed phase offset was 60 centicycles.

Loran-C signals may also be influenced by disturbances. Larsen and Thrane (1977) have demonstrated that interference between ground wave and skywave under certain conditions may cause navigation errors. Figure 29 shows schematically the Loran-C pulse as transmitted, and as received in the presence of noise and skywaves. The time delay of the received ground wave is measured at the third swing in the pulse, 30 μs after the start of the signal. Even though the ground wave will always arrive before the skywave, there is a possibility that a strong skywave pulse arrives less than 30 μs later than the ground wave pulse, causing interference at the sampling point. This situation may arise when the ground wave suffers large delay across poorly conducting or irregular ground, and when the skywave reflection height is significantly lowered during a disturbance. For propagation over poorly conducting land, Figure 30 shows time differences between received ground wave and skywave, versus distance, for various ionospheric reflection heights. Table 2 shows computational results for three ionospheric models. The distances given indicate roughly where interference may occur. For each ionospheric model and each type of ground, the largest distance listed indicate the zone near the transmitter where interference between ground wave and skywave cannot occur.

CONDITIONS	EFFECTIVE REFLECTION HEIGHT	SEA ($\sigma = 4$ mho m^{-1})		LAND ($\sigma = 10^{-3}$ mho m^{-1})	
		DISTANCE WHERE $\Delta t = 30$ μs	DISTANCE WHERE $E_{skw} = E_{grw}$	DISTANCE WHERE $\Delta t = 30$ μs	DISTANCE WHERE $E_{skw} = E_{grw}$
UNDISTURBED NIGHT	83 km	∞	400 km	∞	200 km
WEAKLY DIS-TURBED DAY	66 km	1400 km	1050 km	800 km	590 km
SEVERELY DIS-TURBED DAY	50 km	770 km	950 km	590 km	350 km

Table 2   The table gives the distances for which the propagation time delay between the groundwave and skywave equals 30 μs; the computations are made for three ionospheric electron density profiles and two values of ground conductivity. Also given are the distances for which the groundwave and skywave have equal amplitude.

At distances beyond 2000 km the skywave will normally dominate, and positioning accuracy depends upon the stability of the ionosphere. At 2000 km a 10 km height change in the ionosphere may give a phase change of 20 μs corresponding to a position error of 6 km. In extreme cases the reflection height at 100 kHz may change as much as 30 km during strong solar proton events.

References

Bain, W.C. and B.R. May (1967), D-region electron density distributions from propagation data. Proc. IEEE 114, 1593-1597.

Berry, L.A. and J.E. Herman (1971), A wave hop program for an anisotropic ionosphere, OT/ITS Res. Rept. 11, April 1971.

Bjøntegaard, G. (1974), Deduction of daytime electron density profiles from VLF measurements over a middle latitude path during quiet conditions, J. Atmos. Terr. Phys. 36, 693.

Budden, K.G. (1961), Radio waves in the ionosphere, Cambridge University Press.

Burgess, B. (1977), A review of radio navigation systems and some related propagation influences. AGARD Conference Proc. No. 209, 9-1.

Davies, K. (1965), Ionospheric Radio propagation, Nat Bureau of Standards, Monograph 80.

Davis, J.R. (1974), ELF propagation irregularities on northern and mid-latitude paths. In: ELF-VLF Radio Wave Propagation, Ed. J Holtet, Reidel Publ. Co, 263.

Galejs, J. (1972), Terrestrial propagation of long electromagnetic waves, Pergamon Press p. 362.

IEEE Com-22, 4 (1974).

Johannessen, A. (1974), Investigation of the positive ion composition in the upper mesosphere and lower thermosphere during daytime, NDRE Report 64, Norwegian Defence Research Establishment.

Johler, J.R. (1970), Spherical wave theory for MF, LF and VLF propagation, Radio Science 5, 1429-1443.

Johler, J.R. (1977), Prediction of ground wave propagation time anomalies in the Loran-C signal transmission over land. AGARD Conference Proceedings No. 209, 12-1.

Larsen, T.R. (1977), Omega accuracy in polar regions during ionospheric disturbances. AGARD Conference Proceedings No. 209, 18-1.

Larsen, T.R. and E.V. Thrane (1977), Ionospheric effects on Loran-C in polar regions. AGARD Conference Proceedings No. 209, 14-1.

Mechtly, E.A. and L.G. Smith (1968), Growth of the D-region at sunrise, Journ. Atmos. Terr. Phys. 30, 363-369.

Norton, K.A. (1936), Proc. IRE 24, 1367.

Norton, K.A. (1937), Proc. IRE 25, 1203.

Norton, K.A. (1941), Proc. IRE 29, 623.

Pappert, R.A., E.E. Gossard and I.J. Rothmuller (1967), A numerical investigation of classical approximations used in VLF propagation. Radio Science 2, 387-400.

Pitteway, M.L.V. (1965), The numerical calculation of wave-fields, reflection coefficients and polarizations for long radio waves in the lower ionosphere, Phil. Trans. Roy. Soc. 257, 219-271.

Potts, C.E. (1972), Precise time and frequency dissemination via the Loran-C system, Proc. IEEE 60, 530-539.

Ratcliffe, J.A. (1959), Magneto-ionic theory, Cambridge University Press.

Rowe, H.E. (1974), IEEE Com-22, 371.

Smith, L.G. (1970), A sequence of rocket observations of nighttime sporadic E, J. Atmos. Terr. Phys. 32, 1247-1257.

Swanson, E.R. (1971), Omega, Navigation 18, 168-175.

Swanson, E.R. (1977), Propagation effects on Omega, AGARD Conference Proc. No. 209, 15-1.

Thrane, E.V. (1972), On the diurnal and seasonal variations of the D- and E-regions above Kjeller. In: Ed. K. Folkestad, Magnetosphere-Ionosphere Interactions, pp. 29-38, Oslo University Press.

Wait, J.R. (1970), Electromagnetic waves in stratified media, Pergamon Press.

Wait, J.R. and H.H. Howe (1956), Amplitude and phase curves for ground wave propagation in the band 200 cycles per second to 500 kilocycles, National Bureau of Standards, Circular 574, Boulder, Colo, USA.

Wait, J.R. and K.P. Spies (1964), Characteristics of the earth-ionosphere waveguide for VLF radio waves. NBS Technical Note No. 300, US Dept. of Commerce.

Watts, A.D. (1967), VLF radio engineering, Pergamon Press.
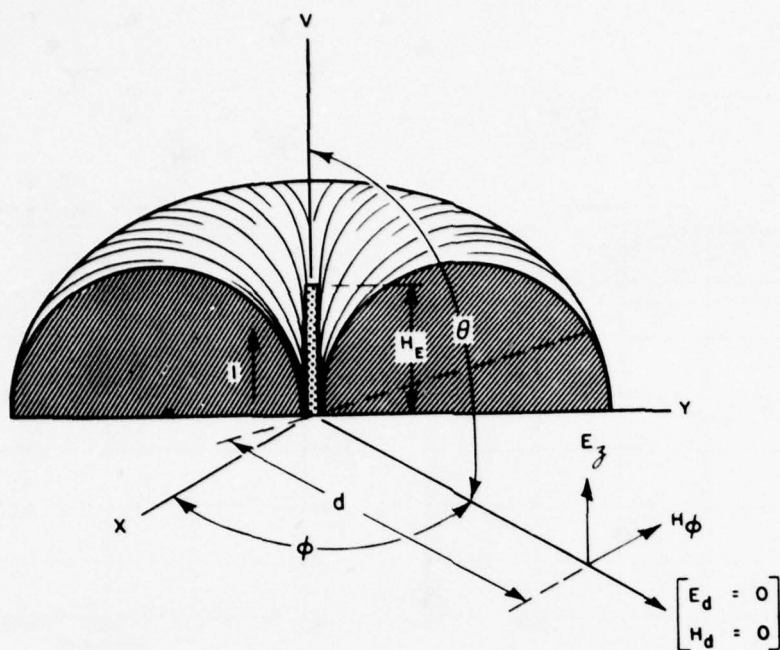
Figure 1   A simple antenna model.
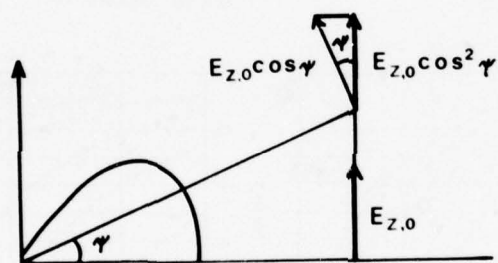
Figure 2   The polar diagram for the simple antenna.
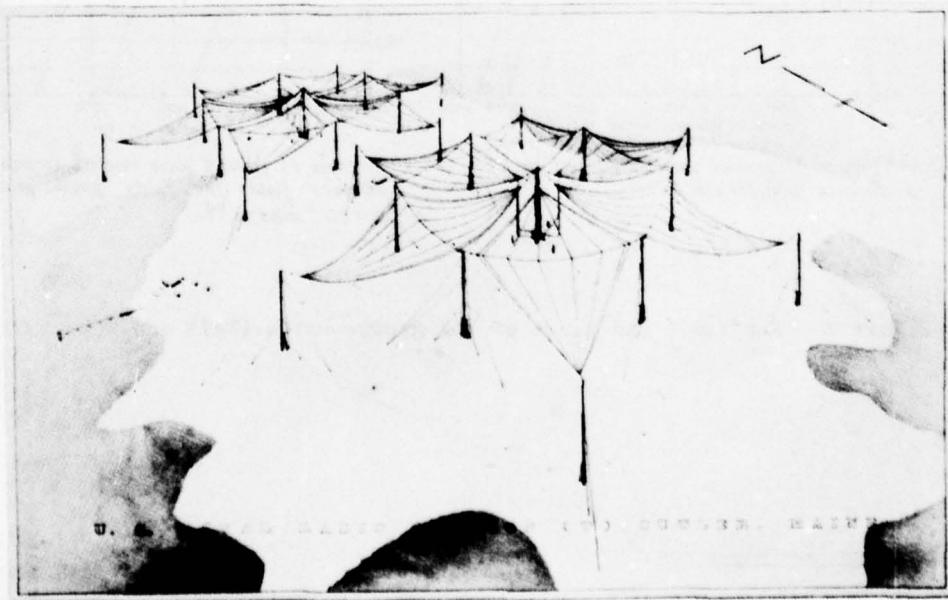
Figure 3   A large VLF antenna installation
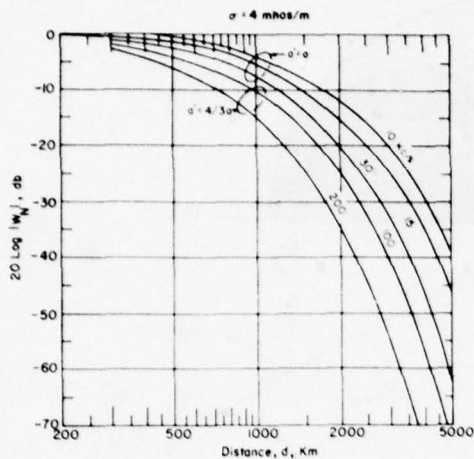
a) Magnitude of ground wave field relative to inverse distance field, for sea
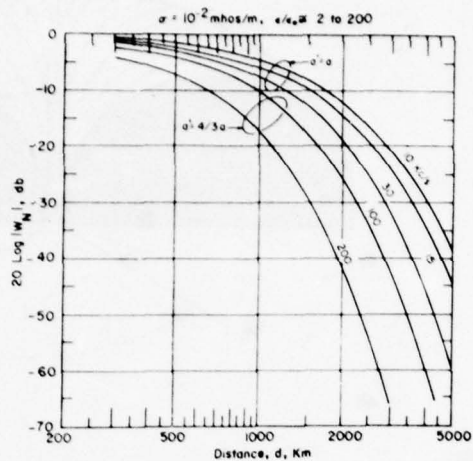
b) Magnitude of ground wave relative to inverse distance field, for fairly good ground $\sigma = 10^{-2}$ mho m^{-1}
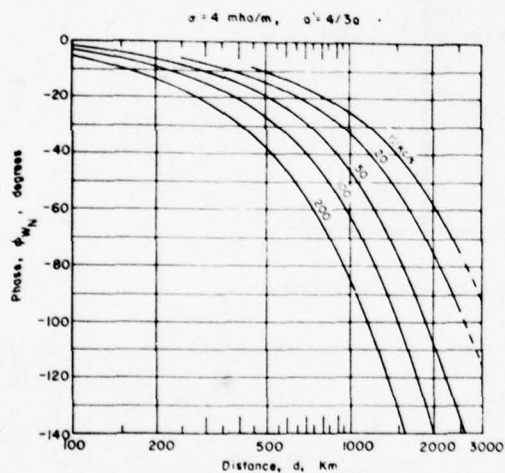
c) Phase of ground wave relative to inverse distance field, for sea
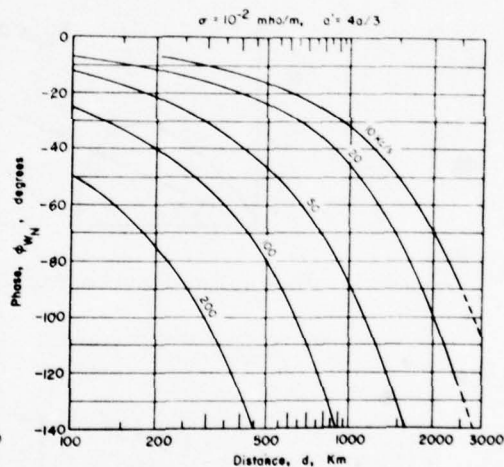
d) Phase of ground wave relative to inverse distance field, for fairly good ground $\sigma = 10^{-2}$ mho m^{-1}

Figure 4   Amplitude and phase of VLF ground waves. (Wait and Howe, 1972)
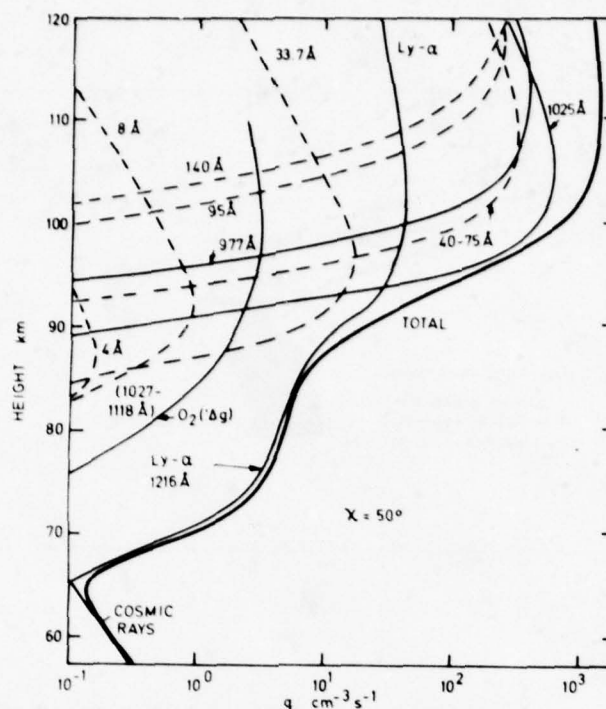
a) Solar zenith angle = 50°
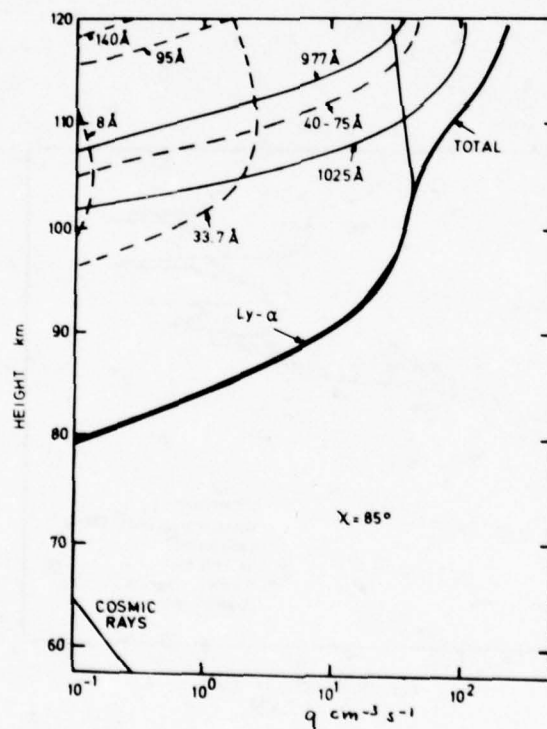
b) Solar zenith angle = 85°

Figure 5   Estimates of ion production during sunspot minimum
undisturbed conditions.
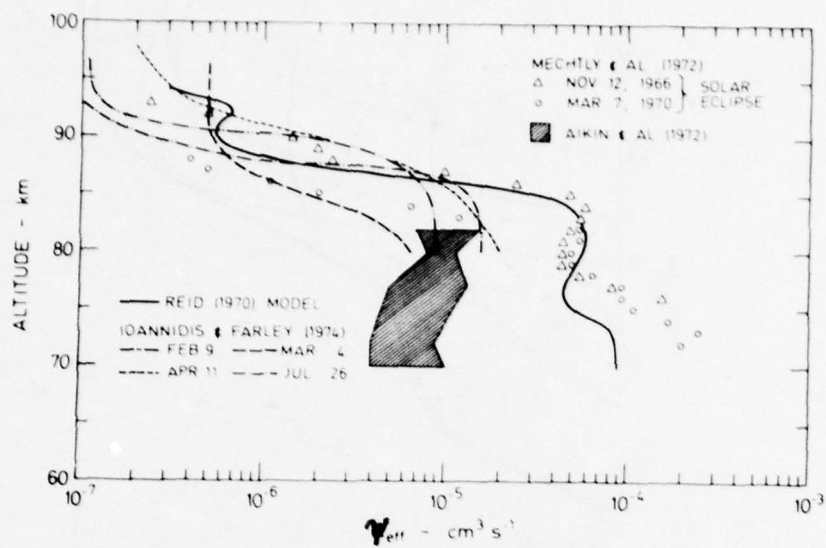
Figure 6   A compilation of ionospheric determinations of ψ during undisturbed conditions (Johannessen, 1974)
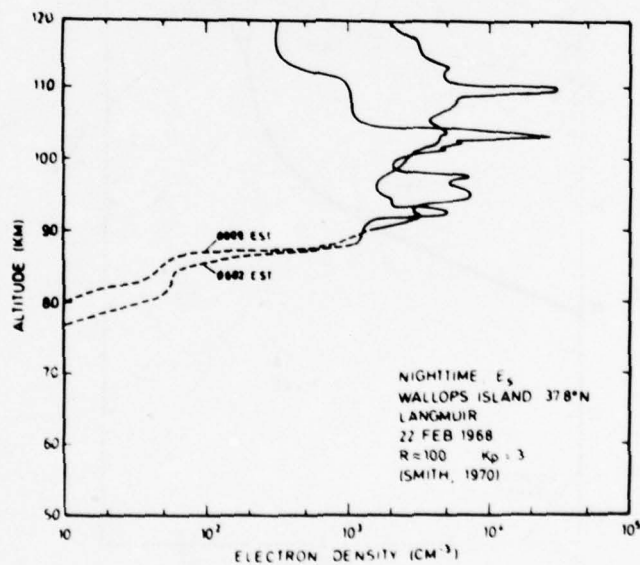
Figure 7   Electron density profiles for undisturbed night conditions.
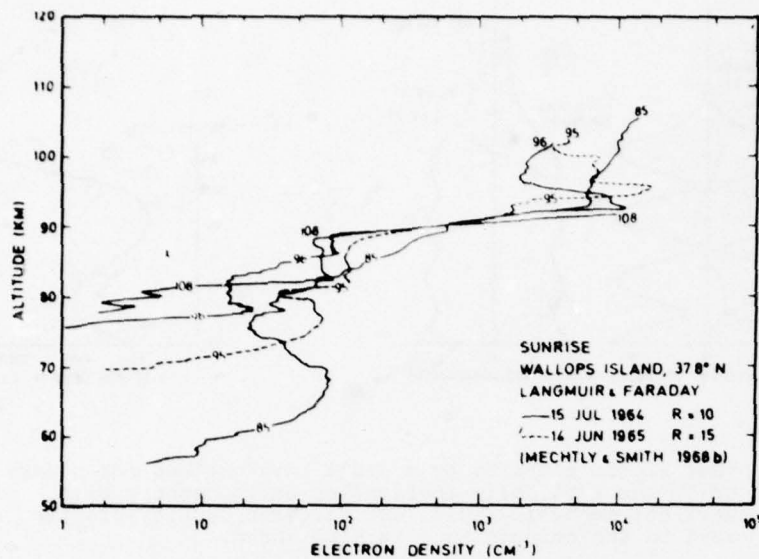
Figure 8   Electron densities for undisturbed daytime conditions.
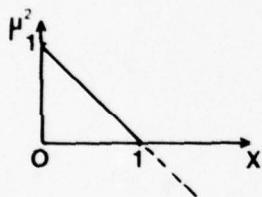
Figure 9   Dispersion diagram—
no magnetic field,
no collisions.
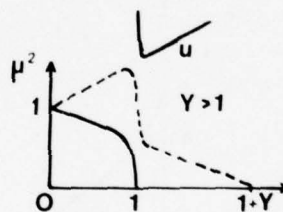
Figure 10   Dispersion diagram
including magnetic
field.
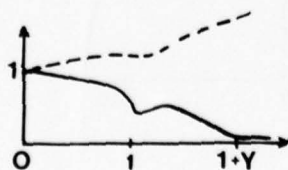
Figure 11   Dispersion diagram
including magnetic
field and collisions.
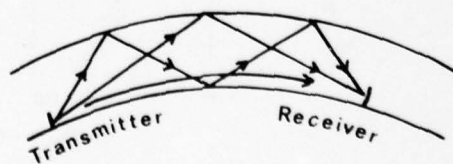
Figure 12   Illustrating esti-
mates of field
strength by adding
ground wave and
skywaves.
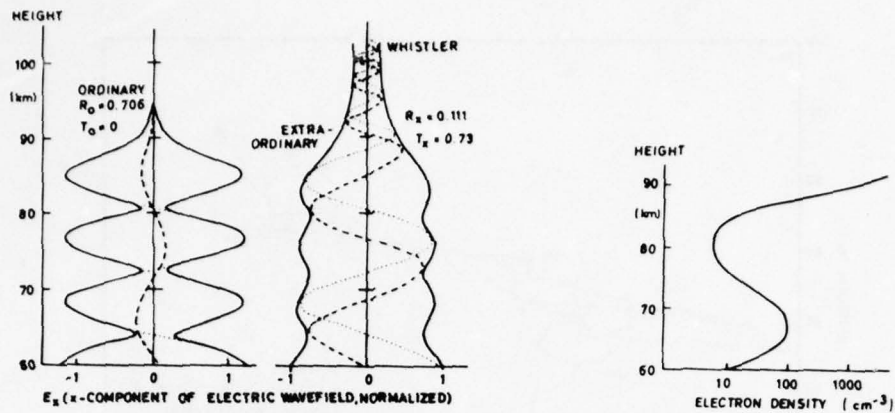
Figure 13   Wave fields computed by a "full wave" method for a wave of 18 kHz vertically incident on an ionosphere with vertical magnetic field. The electron density profile used in the computations is also shown.

——— Modulus of field, ... Real part, - - - imaginary part

R and T are reflection and penetration coefficients.
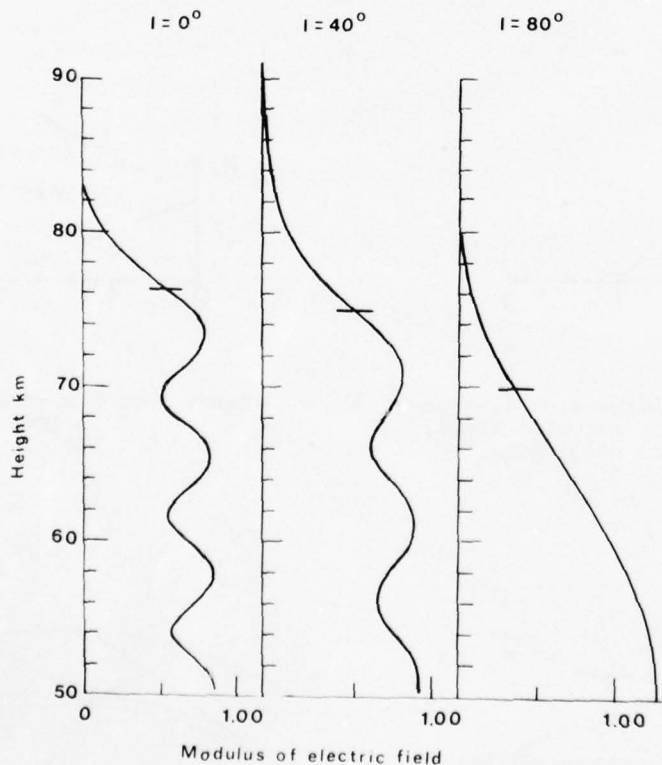
Figure 14   Modulus of electric as a function of height for a wave of 18 kHz incident on an exponential electron density profile at three angles of incidence: I = 0°, I = 40°, I = 80°. The horisontal bars indicate the "triangulation height" of reflection.
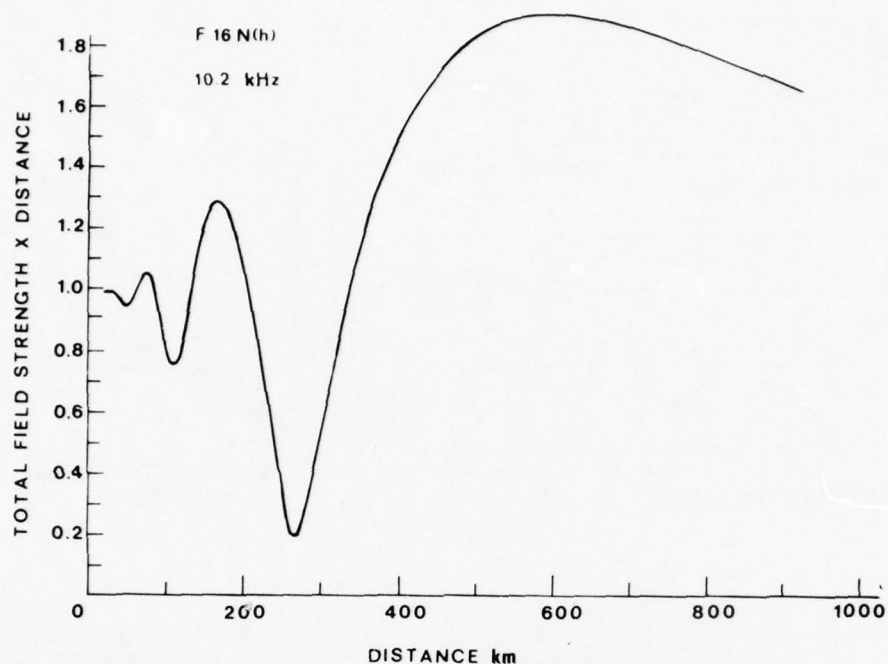
Figure 15   Vertical electric field x distance for the sum of ground
wave and skywave. Computations were made for a moderately
disturbed auroral ionospheric D-region, at 10,2 kHz.
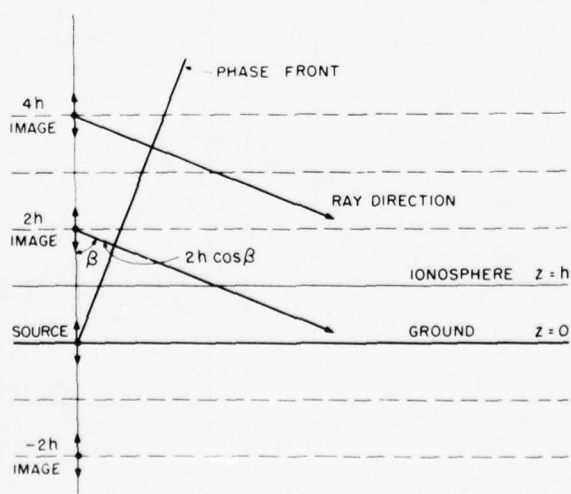
Figure 16   Illustrating the principle of mode theory.(Davies,1965)
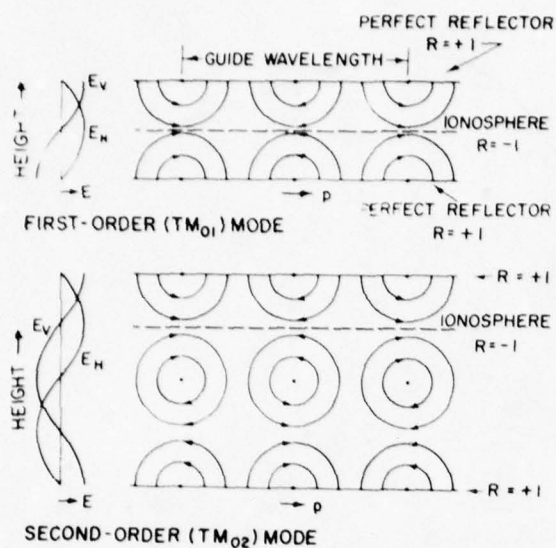
Figure 17   E-field patterns for first
and second order modes in
an idealized earth-ionosphere
waveguide (Davies, 1965).
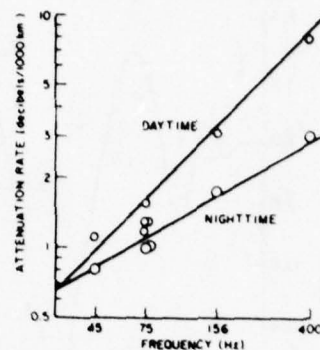
Figure 18   Measured values of ELF
attenuation rates.
(Davis, 1974)
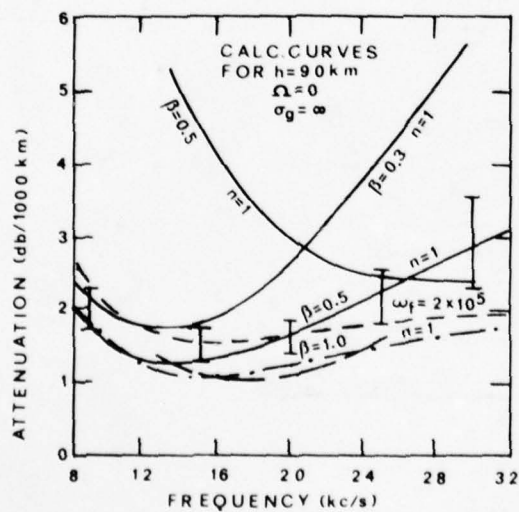
Figure 19   Examples of measured and
calculated VLF attenuation
rates for nighttime con-
ditions(Wait and Spies,1964)
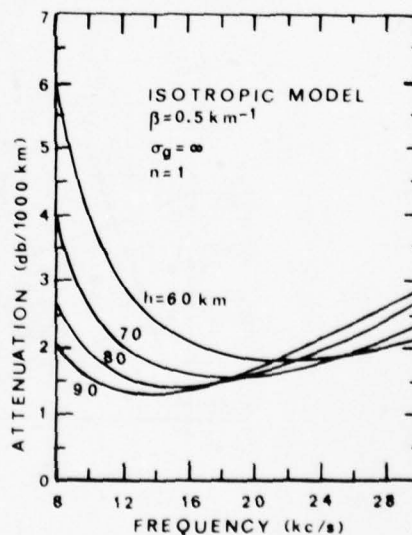
Figure 20   VLF attenuation rates
computed for different
ionospheric heights.
(Wait and Spies,1964)
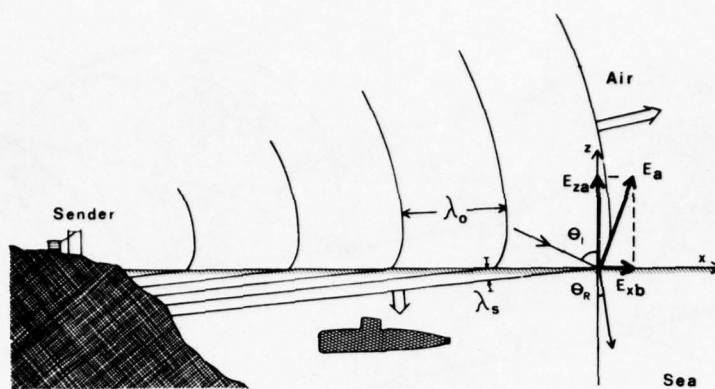
Figure 21   Illustrating the propagation of long waves into the sea.
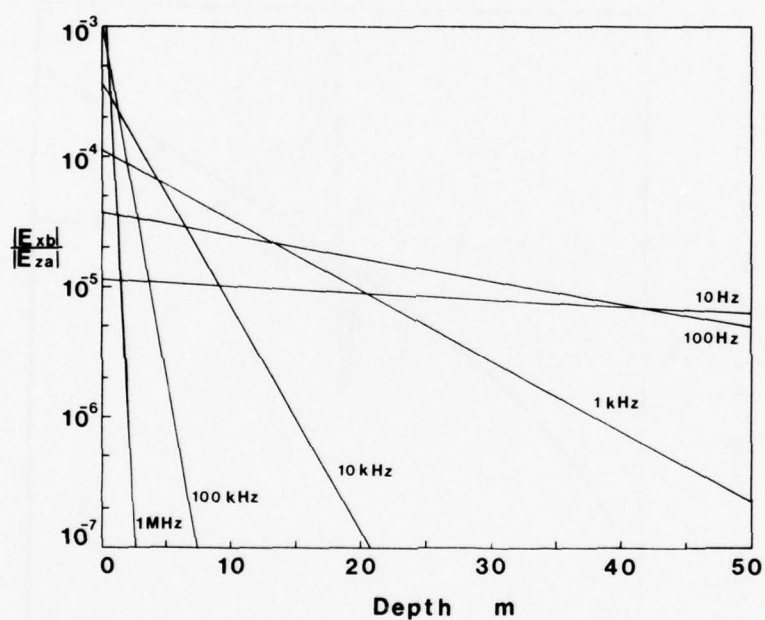
Figure 22   Ratio of electric wavefield below the surface to
wavefield above the surface for several frequencies.

$$\Delta\phi \quad k(r_1 - r_2)$$

A,B   baseline
R   receiver
$\Delta\phi$ phase difference

Single hyperbolic pattern
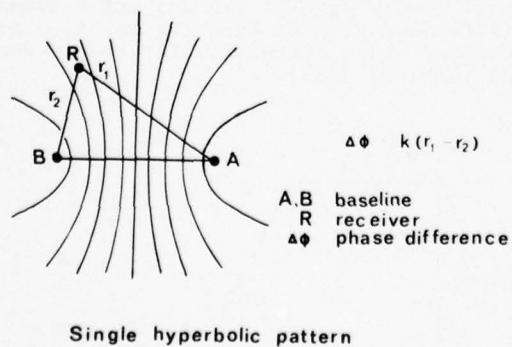
Figure 23   The principle of hyperbolic navigation.
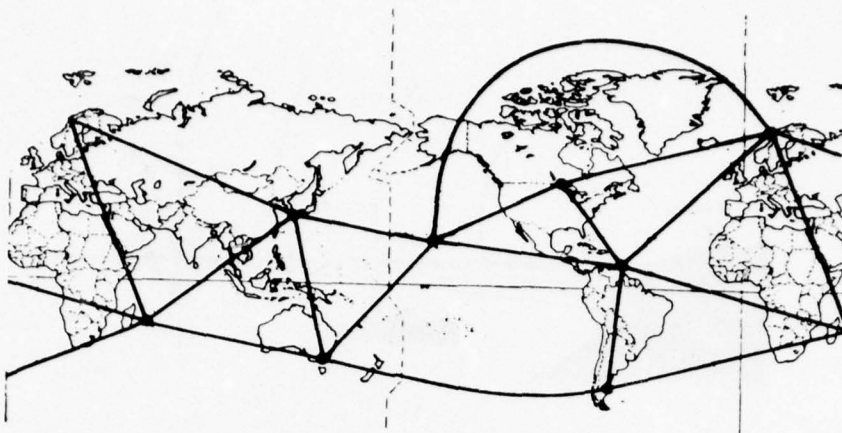
Figure 24   Planned complete Omega navigation system.
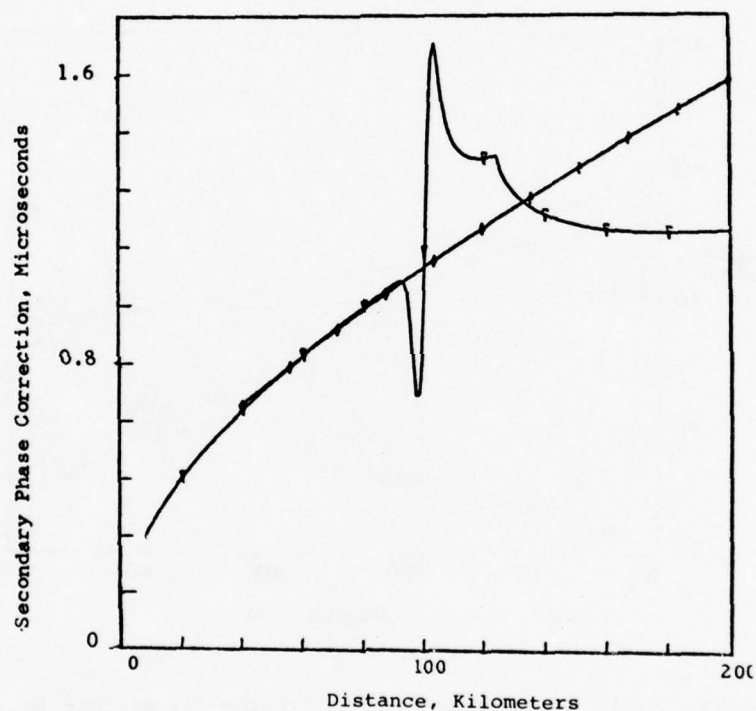
Figure 25   Secondary phase correction as a function of distance
from a Loran-C transmitter, depicting the effect of
a hill 1000 m high at 100 km, and a seawater expanse
at distances greater than 125 km. Also given is the
secondary phase correction for smooth homogeneous
land (Johler, 1977).
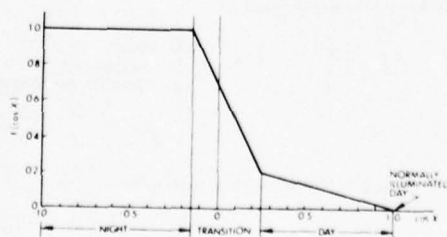
Figure 26   The diurnal function for weighting phase velocities
at Omega frequencies.(Swanson,1977)

SXR-EFFECTS ON OMEGA
PROPAGATION AT 10.2 kHz

+ A-C at Ny Ålesund

△ A-B at Oslo 1968
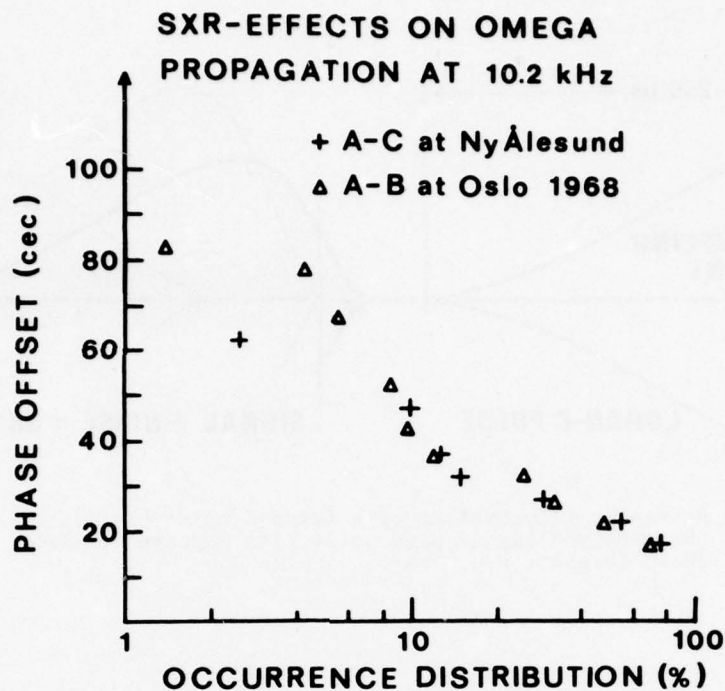
Figure 27   Omega phase difference offset for Norway minus Hawai
(A - C) and Norway minus Trinidad (A - B) measured at
Spitzbergen during solar X-ray flares in 1968.
(Larsen,1977)
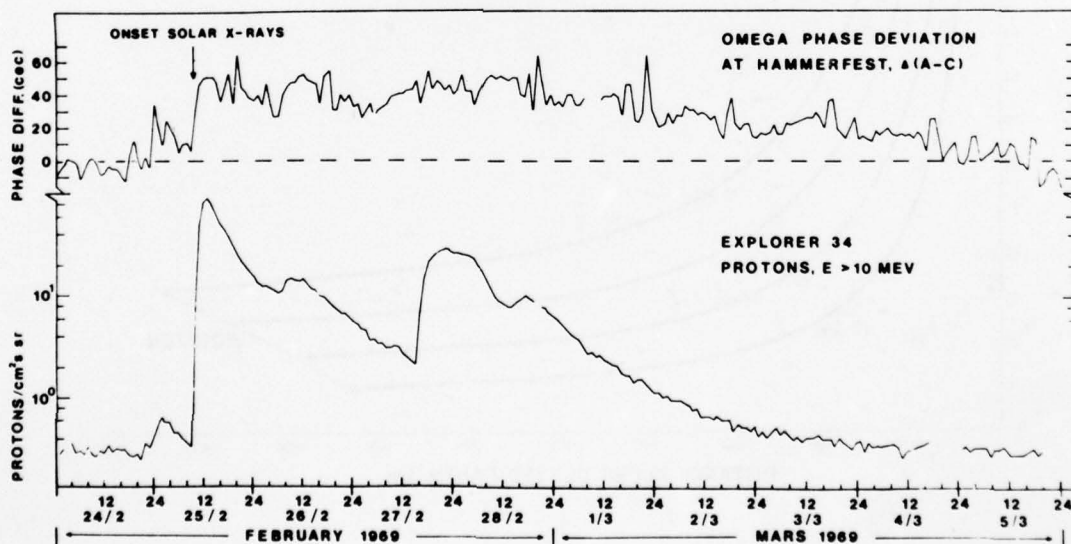
Figure 28   Omega phase difference offset for Norway minus Hawai
(10.2 kHz) received in Hammerfest during a solar
proton event in February-March 1969, compared with
fluxes of energetic solar protons (> 10 MeV).
(Larsen, 1977)
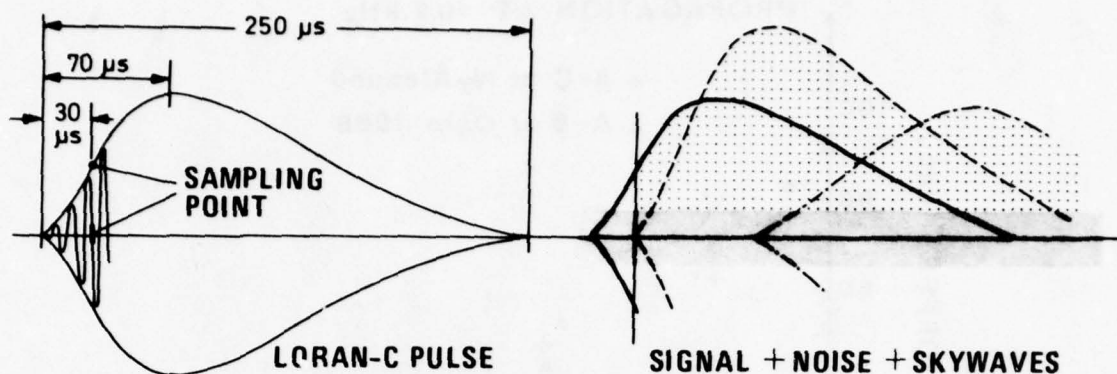
Figure 29   Schematic illustration of a Loran-C pulse (left).
            The received signal plus noise plus skywave is also
            shown (right).
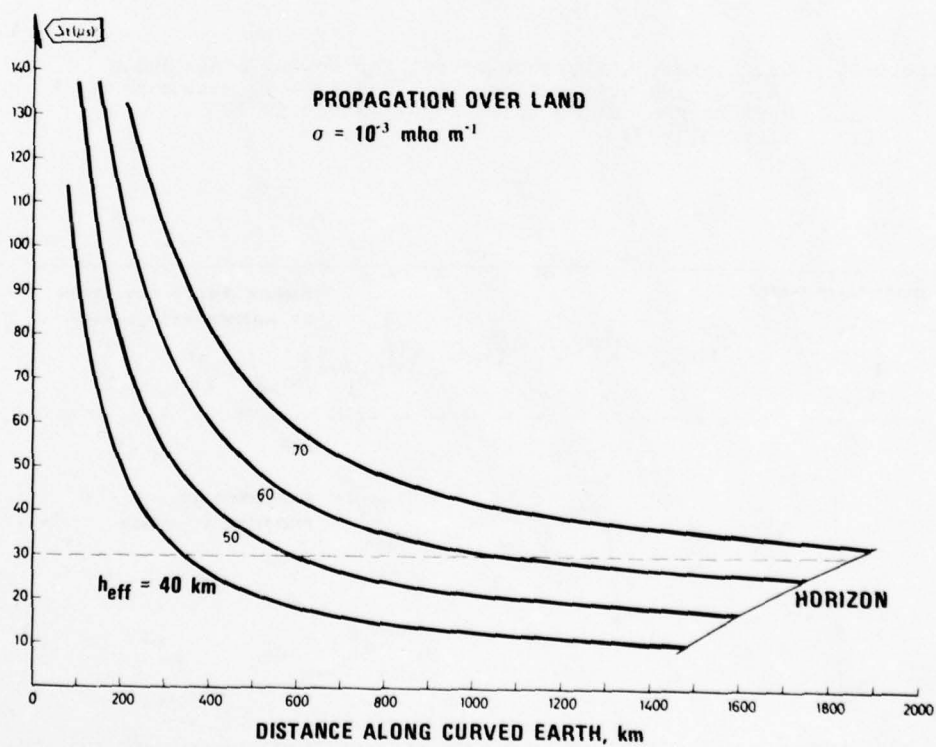
Figure 30   Difference in propagation time (in us) between ground
            wave and skywave, versus distance along the Earth for
            different values of effective ionospheric reflection
            height.

BIBLIOGRAPHY

Aerospace Propagation Media Modelling

This Bibliography with Abstracts has been prepared to support AGARD Lecture Series No. 99 by the Scientific and Technical Information Branch of the U. S. National Aeronautics and Space Administration, Washington, D. C., in consultation with the Lecture Series director, Dr. Haim Soicher.

BIBLIOGRAPHY

The below-listed documents are considered major references that emcompass all subject matters. (They are not listed in the special sections delineated above.)

1. AGARD Conference Proceeding No. 49 on "Ionospheric Forecasting," Ed. V. Agy, Jan. 1970, 472p. Presented at the Avionics Panel 15th Tech. Symp., Quebec, 2-5 Sept. 1969.

2. AGARD Conference Proceeding No. 183 on "Optical Propagation in the Atmosphere," May 1976, 625p. Presented at the Electromagnetic Wave Propagation Panel Symp., Lyngby, Denmark, 27-31 Oct. 1975.

3. AGARD Conference Proceeding No. 238 on "Operational Modelling of the Aerospace Propagation Environment," Ed. H. Soicher, November 1978, 275p. Presented at the Electromagnetic Wave Propagation Panel Meeting, Ottawa, Canada, 24-28 April 1978.

SECTION 1

RADIO PROPAGATION

1a. Media Characterization

Solution of the ray equation for an inhomogeneous dispersive spherically-stratified medium by the perturbation method

A/GUSEV. V. D.; B/KHURI. A. B/(Moskovskii Gos.darstvennyi Universitet. Moscow. USSR) Moskovskii Universitet. Vestnik. Seriia III - Fizika. Astronomiia. vol. 16. May-June 1975. p. 289-293. In Russian.

ABS:The ray equation is solved to the second approximation by the perturbation method for a spherically-stratified linear model of the ionosphere. On the basis of this solution. variations in the arrival angles of a wave and the average direction of its emergence from the ionosphere are calculated for the case of random isometric Gaussian inhomogeneities. The obtained results are analyzed in comparison with results for a plane-stratified medium. 75/06/00 76A10703

Numerical calculation of electromagnetic waves in an isotropic multilayered medium

A/NAGANO. I.; B/MAMBO. M.; C/HUTATSUISHI. G. C/(Kanazawa University. Kanazawa. Japan) Radio Science. vol. 10. June 1975. p. 611-617.

ABS:An improved matrix method of calculating the solutions of wave equations in a horizontally stratified anisotropic medium is described. An inhomogeneous medium is divided into a number of thin horizontal and homogeneous slabs. The solutions of a differential equation with constant coefficients in each slab are connected by applying the boundary conditions. and the wave fields are given as the power-series expansion of wave fields. In calculating the wave fields. a matrix is divided into two matrices for two independent solutions. and the Gram-Schmidt orthogonalizing process is applied to prevent numerical swamping. Comparisons are made between this and other full-wave methods regarding step size and computer time. and this method is found to be more efficient than the full-wave method. especially at high-frequency wave fields. The magnetoionic modes separated from the resultant wave are shown for a model ionosphere. 75/06/00 75A42354

HF and UHF propagation studies of the mid-latitude ionosphere

A/HARTMANN. G. K. A/(Max-Planck-Institut fuer Aeronomie. Lindau ueber Northeim. West Germany) European Geophysical Society Annual Meeting. 2nd. Trieste. Italy. Sept. 23-26. 1974. Paper. 35 p.

ABS:Attention is concentrated on the main trough region of the mid-latitude ionosphere. Examples are given of particularly interesting results obtained by different ground based techniques. including bottomside ionosondes. swept frequency backscatter systems and incoherent scatter

Approximate boundary conditions for the electromagnetic field on the surface of an isotropic medium

A/PAPOUSEK. W. A/(Graz. Technische Universitaet. Graz. Austria) Acta Physica Austriaca. vol. 45. no. 3-4. 1976. p. 277-290. In German.

ABS:The approximate concept of the constant surface impedance provides an approach for the study of the electromagnetic field in the layer in which the radiation source is located. taking into account the earth-air-ionosphere model used for a description of the propagation of long electromagnetic waves. The considered concept makes it possible to replace the continuity conditions for the layer interfaces by boundary conditions which can be represented by a simple mathematical vector relation. Explicit expressions are derived for the surface impedances of arbitrary magnetic fields. 76/00/00 76A40047

Contribution to the theory of the propagation of VLF waves within a plane anisotropic inhomogeneous waveguide model for an arbitrary direction of the geomagnetic field

A/LEDINEGG. E.; B/PAPOUSEK. W.; C/SCHNIZER. B. C/(Graz. Technische Universitaet. Graz. Austria) Archiv fuer Elektronik und Uebertragungstechnik. vol. 30. July.Aug. 1976. p. 303-311. In German. 76/08/00 76A39115

Electromagnetic wave propagation between earth and ionosphere in a spherical. anisotropic. nonhomogeneous waveguide model

A/LEDINEGG. E.; B/PAPOUSEK. W.; C/SCHNIZER. B. C/(Graz. Technische Universitaet. Graz. Austria) Acta Physica Austriaca. vol. 44. no. 3-4. 1976. p. 293-313. In German.

ABS:The reported investigation makes use of a conductivity approximation. employed by Monteath (1951). to study the propagation of EM waves in the VLF band. The propagation of a vertical dipole excitation in a homogeneous waveguide are explored and the derivation of an integral equation in connection with the study of the inhomogeneous-waveguide problem is discussed. A description is given of the iterative solution of the integral equation and an expression representing the field is obtained. 76/00/00 76A33025

radars. Satellite-to-ground propagation experiments are then reviewed; these include scintillation and radio holography studies, together with total electron content studies by Faraday rotation, differential phase (dispersive Doppler) and differential group delay methods. HF propagation studies provide a good way of investigating the motion of the trough (and hence of studying the plasmapause), the interchange of ionization between the ionosphere and the plasmasphere, magnetic storm effects, gravity waves, and effects of practical importance in radio communications and navigation systems. 74/09/00
75A26594

Chatanika model of the high latitude ionosphere for application to HF propagation prediction

A/VONDRAK, R. R.; B/SMITH, G.; C/HATFIELD, V. E.; D/TSUNODA, R. T.; E/FRANK, V. R. SRI International Corp., Menlo Park, Calif.

ABS:Electron density measurements made with the incoherent-scatter radar at Chatanika, Alaska have been used to obtain a synoptic model of the high-latitude ionosphere. This Chatanika model is a modification of the RADC-POLAR model developed by Elkins and coworkers for use in raytracing codes for HF propagation prediction. Because the existing RADC model was derived from a larger and more geographically extensive data base than that used in this study, many of its features have been retained in the new model. The major modification made was an improved specification of the auroral E-layer and the altitude interval between the E and F regions. This region sometimes acts as a duct in which HF signals may travel for great distances without traversing the D region, where most absorption occurs.
AD-A053154 RADC-TR-78-7 78/01/00 78N26359

Ionospheric reflection and absorption properties of normal modes at ELF

A/PAPPERT, R. A.; B/SHOCKEY, L. R. Naval Ocean Systems Center, San Diego, Calif. (EM Propagation Div.)

ABS:As an aid to better understanding ELF propagation in the earth-ionosphere waveguide, full-wave ELF modal height gains are analyzed as regards regions of reflection and absorption. Frequencies in the Schumann and Seafarer bands are discussed for representative day/night, ambient and disturbed ionospheres. Enhancement of the earth-ionosphere waveguide attenuation due to Sporadic E layering is discussed and the origin of the enhancement clarified.
AD-A049778 NOSC/IR-772 77/09/15 78N21702

INVERT: A computer program for obtaining D-region electron density profiles from VLF reflection coefficients

A/MORFITT, D. G.; B/SHELLMAN, C. H. Naval Ocean Systems Center, San Diego, Calif. (Electromagnetic Propagation Div.)

ABS:INVERT is a FORTRAN computer program designed to study the feasibility of obtaining electron density distributions of the D-region of the ionosphere. These electron density profiles would be derived from measurements of ionospheric reflection coefficients. The radio propagation frequencies would be limited to the VLF band, particularly 3-20 kHz. This report contains a discussion of the analytical approach taken in INVERT, a FORTRAN listing of the program, instructions for using the program and some sample calculations using simulated data. The program has not been used with real data.
AD-A050256 NOSC/IR-782 77/11/30 78N20699

Wideband satellite observations

A/RINO, C. L.; B/FREMOUW, E. J.; C/LIVINGSTON, R. C.; D/COUSINS, M. D.; E/FAIR, B. C. SRI International Corp., Menlo Park, Calif.

ABS:The Wideband Satellite (P76-5) was launched on 22 May 1976 and data have been recorded at three receiving stations since that time. The unique nature of the Wideband signals (coherent transmissions covering VHF to S-band) and the geophysically interesting locations of the receiving stations (covering auroral and equatorial latitudes) have led to a number of new and significant results. These results pertain to both scintillation phenomenology and the physics of striation formulation. This report presents the results of the first year of Wideband operations; work described previously in detailed bimonthly progress reports is only summarized here. Emphasis is placed on aspects not previously described, including: (1) evidence for a geometrical scintillation enhancement due to east-west sheet-like irregularity structures in the auroral zone; (2) spaced-receiver measurements of the diffraction pattern anisotropy and apparent drift motion; (3) total electron content measurements of the paleward boundary of the ionospheric trough; (4) characteristics of equatorial scintillations, particularly the gigahertz scintillation that develop during extremely active periods; and (5) results from the equatorial scintillation campaign conducted in Peru during March 1977. Using the Wideband data base with theoretical work and systems analysis, it should be possible to develop a self-consistent model relating a simple parameterization of the irregularity structure and strength to the observed phase and amplitude scintillation.
AD-A048801 DNA-4399F AD-E300071 77/06/00 78N18282

Plasmaspheric signal time-delay effects in satellite
navigation systems
A/SOICHER. H. Army Electronics Command. Fort Monmouth.
N. J. (Communications/Automatic Data Processing Lab.)
In AGARD Propagation Limitations of Navigation and
Positioning Systems 9 p (SEE N77-22068 13-04)

ABS:Since delay time modeling efforts to date have been
based on total electron count obtained by the Faraday
rotation technique. the plasmaspheric delay is not
compensated for and thus comprises a source of error. In an
effort to determine the magnitude of this error.
observations of plasmaspheric content were performed at a
midlatitude station. an auroral station and a station in
the vicinity of the geomagnetic equatorial anomaly.
Diurnal. day-to-day. and latitudinal variations of the
contents were observed. The ratio of the
plasmaspheric-to-ionospheric contents varied substantially
from day to night. 77/02/00 77N22070

Proceedings of Symposium on the Effect of the Ionosphere on
Space Systems and Communications Naval Research Lab..
Washington. D. C.   Symp. held at Arlington. Va.. 20-22
Jan. 1975

ABS:Papers primarily dealing with ionospheric
scintillation are presented. Topic areas include: High
altitude morphology: spectra of amplitude and phase
scintillation; amplitude and fade statistics for equatorial
scintillations; holographic radio camera technique for
studying ionospheric inhomogeneities; electron and ion
density studies; Faraday rotation and angle of arrival
measurements; and solar cycle variations of the total
electron content at low latitude.
AD-A008939 75/00/00 75N30714

1b. Propagation Phenomena
and Simulation

Multiple scattering effects in electromagnetic wave propagation through a medium containing precipitation
A/UZUNOGLU, N. K.; B/EVANS, B. G. B/(Essex. University. Colchester, England) Journal of Physics A - Mathematical and General. vol. 11. Apr. 1978. p. 767-776.
ABS:The general scattering problem of vector electromagnetic waves from a stochastic medium containing particles with random size, orientation and position distributions is formulated and solved in terms of a generalised dyadic average scattering amplitude. The independence approximation used in the solution is verified by considering the results of an exact solution to the scattering from two spheres as a function of their displacement. The specific case of a rain-filled medium and propagation in the centimetre and millimetre wave regions is considered. The general theory is applied in order to derive a more generalised form of the Van de Hulst propagation equation for the coherent field in such a medium. Conditions are then formulated for multiple scattering to be negligible and numerical examples presented covering the frequency range up to 100 GHz which show that indeed the effects of multiple scattering are negligible for the raindrop medium. 78/04/00 78A32799

High-frequency reflection and transmission coefficients for a semi-infinite plasma medium with gradual boundary
A/HIZAL, A. A/(Middle East Technical University. Ankara, Turkey) Journal of Physics D - Applied Physics. vol. 11. Feb. 21, 1978. p. 261-269. Research supported by the University of Birmingham.
ABS:High-frequency power reflection and transmission coefficients of horizontally polarized waves are calculated for an opaque sporadic E-layer as a function of the edge profile, the edge thickness and the electron density. The inhomogeneous edge layer is treated by numerical integration of the full-wave equations for the total tangential fields. The behavior of the curves presented for the normal and the oblique incidence of waves are explained by considering the total reflection phenomena in the inhomogeneous layer. The results indicate that the reflection and transmission coefficients depend significantly on the edge-profile and that the thickness of the edge should decrease with the electron density in order to explain the observed very high order of dependence of the power reflection coefficient on the electron density. 78/02/21 78A29460

Wave propagation in an anisotropic three-layer model
A/HEBENSTREIT, H. A/(Graz. Technische Universitaet. Graz, Austria) Acta Physica Austriaca. vol. 48. no. 2. 1978. p. 131-150. In German.
ABS:The present paper is concerned with the propagation of VLF-waves between earth and ionosphere; the ionosphere is regarded as rendered electrically anisotropic by a static uniform vertical magnetic field. With help of the reflection-matrix method field distributions of a vertical electrical dipole are calculated and exact solutions are obtained in form of integral representations. Their integration leads to mode series and integrals along the branch cuts. The contributions of these branch cuts are found to be negligible for large distances. The analytic expressions are evaluated numerically for various physical and geometrical parameters and the influence of the anisotropy is studied. 78/00/00 78A26640

Plane wave pulse propagation through random media
A/HONG, S. T.; B/SREENIVASIAH, I.; C/ISHIMARU, A. C/(Washington. University. Seattle. Wash.) IEEE Transactions on Antennas and Propagation. vol. AP-25. Nov. 1977. p. 822-828.
ABS:The theory of plane wave pulse propagation through a random medium, under the forward-scattering assumption is presented. Since pulse propagation characteristics are determined by two-frequency mutual coherence function gamma, a set of normalized curves is given for gamma for different propagation parameters (operating frequency, propagation distance, turbulence strength or density of scatterers, etc.). From the curves one can obtain the coherence bandwidth of a wave for a variety of situations. A received pulse form due to an input delta function is given in a normalized form which is applicable to the whole range of strong fluctuation. The results are applied to optical pulse propagation in dense clouds. It is shown that the high data rate optical pulse communication through clouds may be limited due to a narrow coherence bandwidth of the order of megahertz. A good agreement between the theoretical prediction and the available experimental data has been demonstrated for both the received pulse shapes and the pulse durations of an optical pulse in clouds. 77/11/00 78A13963

Scintillation correlation at different wavelengths
A/RUFENACH, C. L. A/(NOAA. Space Environment Laboratory. Boulder, Colo.) Journal of Geophysical Research. vol. 81. May 1, 1976. p. 2419-2422.
ABS:Scintillation cross-correlation coefficients at two radio wavelengths are investigated on the basis of a shallow-modulated phase screen for several different spectral descriptions of the scattering medium. For the

1.0

1.1

1.25 1.4 1.6

2.8 2.5

3.2 2.2

3.6

4.0 2.0

1.8

MICROCOPY RESOLUTION TEST CHART

NATIONAL BUREAU OF STANDARDS-1963-A

A transionospheric communication channel model
A/FREMOUW, E. J.; B/HESSING, A. R.; C/RINO, C. L.; D/HATFIELD, V. E. Stanford Research Inst., Menlo Park, Calif.

ABS: This report presents the final results of a three-year contract to develop a signal-statistical model of the transionospheric radio communication channel, building on a previously existing model for first-order signal statistics. The objectives of the contract work were as follows: (1) to test and improve the first-order statistical model; (2) to extend the model to second-order statistical quantities in the temporal, spatial, and spectral domains; (3) to free the model from restriction to cases of weak, single scatter; and (4) to calibrate and iteratively test the morphological description of ionospheric structure that underlies the model. The foregoing objectives have been met, and the research results have been committed to two computer codes for performing systems-oriented, signal-statistical calculations. The more extensive of the two codes, IONSCNT, contains the morphological model and a two-component propagation routine that permits calculation of both focusing and diffractive-scatter effects. Mode 1 of IONSCNT provides calculation of intensity and phase scintillation indices and other first-order, signal-statistical parameters as functions of frequency, observing geometry, or other relevant variables from a user-selected set of ionospheric state parameters. Mode 2 of IONSCNT extends the Mode 1 results to second-order statistics for cases to be selected by the user.
AD-A055272 RADC-TR-78-88 78/04/00 78N32318

Applications guide for propagation and interference analysis computer programs (0.1 to 20 GHz)
A/JOHNSON, M. E.; B/GIERHART, G. D. Institute for Telecommunication Sciences, Boulder, Colo.

ABS: Ten computer programs useful in estimating the service coverage of radio systems operating in the frequency band from 0.1 to 20 GHz are reported. These programs were used to obtain a wide variety of computer-generated microfilm plots such as transmission loss versus path length and the desired-to-undesired signal ratio at a receiving location versus the distance separating the desired and undesired transmitting facilities. Emphasis was placed on the types of outputs available and the input parameter requirements. The propagation model used with these programs is applicable to air/ground, air/air, ground/satellite, and air/satellite paths. It can also be used for ground-to-ground paths that are line-of-sight or smooth earth.
AD-A053242 FAA-RD-77-60 78/03/00 78N27314

relevant simplification, a sufficiently large outer-scale dimension. It is argued that the normalized correlation coefficient is primarily dependent on spectral shape and wavelength separation and is independent of anisotropy and outer-scale dimension. Ionospheric and interplanetary scintillation measurements are compared with this result. 76/05/01 76A33077

Effects of ionospheric irregularities on radio waves. I - Phase path changes
A/ROBINSON, I.; B/DYSON, P. L. B/(La Trobe University, Bundoora, Victoria, Australia) Journal of Atmospheric and Terrestrial Physics, vol. 37, Nov. 1975, p. 1459-1467. Research supported by the Australian Research Grants Committee. 75/11/00 76A12508

An assessment of the magnitude of the F-region absorption on HF radio waves using realistic electron density and collision frequency models
A/RUSH, C. M.; B/ELKINS, T. J. B/(USAF, Cambridge Research Laboratories, Bedford, Mass.) ITU Telecommunication Journal, vol. 42, Aug. 1975, p. 476-488.

ABS: The amount of absorption on HF oblique transmissions due to the F-region is studied using realistic electron density and collision frequency models. It is seen that the F-region absorption for modes near the MUF for paths of 2000 to 3000 km rarely exceeds 1.0 to 2.0 dB, and the F-region absorption is significant only when the radio wave suffers severe dispersion and retardation. 75/08/00 75A41416

Theory of the terrestrial propagation of VLF electromagnetic waves
A/WAIT, J. R. A/(Cooperative Institute for Research in Environmental Sciences, Boulder, Colo.) In: ELF-VLF radio wave propagation; Proceedings of the Advanced Study Institute, Spatind, Norway, April 17-27, 1974. (A75-34751 16-46) Dordrecht, D. Reidel Publishing Co., 1974. p. 129-146; Discussion, p. 146, 147.

ABS: A model for the propagation of VLF waves in the earth-ionosphere waveguide is proposed. First, ground wave propagation over an airless spherical earth without any ionosphere is considered, then the model is extended to include waves reflected from the ionosphere. By suitably summing the rays, a modal representation for the total field is obtained. Extensive use is made of impedance concepts in formulating the propagation equations. The model includes such effects as coupling between TM and TE modes, earth-detached modes, and mode conversion phenomena. 74/00/00 75A34762

Active-R bandpass filter design using hybrid-pi transistor
model
A/ROTH. L. C.. Missouri Univ.. Rolla.   (Dept. of
Electrical Engineering.)
ABS:A design procedure is developed for a bandpass
filter utilizing five bipolar transistors and no external
capacitors. Base resistors of a three-stage amplifier are
used to set a third-order open-loop pole at a location
given in terms of the center frequency and bandwidth of the
filter. A feedback resistor, also given in terms of the
center frequency and bandwidth, is then used to move the
poles to the final location. A test circuit is constructed
and compared with a computer simulation. Limitations of the
circuit are discussed.
AD-A053144   78/03/20   78N26378

Simulation and measurement of high frequency ionospheric
channels. Time- and frequency-dispersive properties of HF
sky-wave propagation paths can be modeled for use in
adapting signal format and signal processing algorithms for
communication system development
A/SAILORS. D. B.; B/HILL. J. R.   Naval Ocean Systems
Center. San Diego. Calif.
ABS:The report presents literature search of HF channel
simulators. describes the Watterson model and its
limitations. and discusses distortion of ionospherically
propagated signals due to ionospheric refraction.
Significant dispersion occurs if the half-bandwidth exceeds
pie/(delta TAO/delta f) to the 1/2 power. where (delta
TAO/delta f) to the 1/2 power (in s/Hz) is the ionogram
slope at center frequency. For 100 kHz bandwidth.
dispersion is significant (delta TAO/delta f) to the 1/2
power exceeds 3.14 X 10 to the -4th ms/kHz. its measurement
requiring 62.8 microsec. resolution. Recommendations: For
bandwidths above 2.5 kHz at night and 12 kHz during the
day. add frequency dispersion correction filters to the
Watterson simulator tap delay lines. To achieve required
time delay resolution. use a complementary-sequence or
modulated-pulse oblique sounder system. For the
microprocessor or minicomputer controlled receiver. provide
an atomic time-frequency standard and interfaces for
terminal. CRT display. magnetic tape recorder. and
auxiliary devices. When measuring modem performance
capabilities with a channel simulator. take a 'single and
multiple distortions' approach. Use the Jones ray-tracing
program to obtain the frequency dispersion relationships
needed for applying corrective filters to the Watterson
model: relate results to channel-caused system distortions.
Use a suggested approach if too many delay line taps would
be needed.
AD-A043364 NOSC/TR-111   77/04/22   78N10371

Ionospheric range error correction in precision radar
systems by adaptive probing of the propagation medium
A/ALLEN. R. S.; B/DULONG. D. D.; C/GROSSI. M. D.;
D/K'IZ. A. H.   E/(Regis College. Weston. Mass.);
C/(Raytheon Co.. Sudbury. Mass.); D/(Raytheon Co..
Sudbury. Mass.)   Air Force Geophysics Lab.. Hanscom AFB.
Mass.   In AGARD Propagation Limitations of Navigation and
Positioning Systems 16 p (SEE N77-22068 13-04)
ABS:A real time adaptive scheme for ionospheric range
error correction in precision UHF radars is based on the
use of a model of the monthly median ionosphere constructed
from existing worldwide climatology and on updating and
correcting this model with real-time dual frequency
measurements of the columnar electron content. The
space-time cell in which the dual frequency correction
maintains its validity is so large that a single dual
frequency sample taken along a direction that cuts across
the volume monitored by the radar as rarely as once every
half hour still suffices. This requires that the adopted
ionospheric model. while the solar cycle progresses.
correspondingly becomes more and more sophisticated in such
features as its reproduction of horizontal gradients.
77/02/00   77N22074

Present status of the RRI slant-path absorption model
(SLAM) computer program
A/KOPPEL. D.   Riverside Research Inst.. New York.
ABS:A computer program (SLAM) is described which
calculates the attenuation by air of microwave and
submillimeter radiation. Besides the horizontal attenuation.
the vertical attenuation from various levels down to the
ground and out into space is calculated for a fixed
frequency. The line profile and atmospheric model can be
selected from among several. Comparison is made with other
calculations. and with experiments. Possibilities for
improving the program are discussed.
AD-A027215 RRI-T-2/306-3-14   76/01/23   77N14320

Modeling of transionospheric radio propagation
-A/FREMOUW. E. J.; B/RINO. C. L.   Stanford Research
Inst.. Menlo Park. Calif.
ABS:This is the final quarterly technical report on a
one-year contract to extend and improve an existing
empirical model for worldwide behavior of ionospherically
imposed radio-wave scintillation. The objectives of the
project were (1) to improve the accuracy of model-based
calculations of the intensity-scintillation index and (2)
to develop a capability for full description (from the
point of view of engineering applications) of the
first-order. complex-signal statistics that characterize
the transionospheric radio comunication channel. The
stated objectives of the just-completed project were

A method for determining the field strength distribution of a tropospheric scatter communications link
A/BALAZS. A. J. Air Force Inst. of Tech. Wright-Patterson AFB. Ohio. (School of Engineering.)
ABS:A method is developed for determining the on and off path field strengths for a typical tropospheric scatter communications link. The earth is assumed to be smooth and homogeneous over the entire path. A spherically symmetric atmospheric model is used. Meteorological conditions which affect tropospheric communications are discussed as well as a method for determining the refractive index from meteorological charts. A field source representation is developed which can be easily adapted to specific site facilities. The overall field problem is developed in four parts: the direct field. the reflected field. the diffracted field and the scattered field.
AD-A008710 GE/EE/74-39   74/12/00   75N31313

Proceedings of Symposium on the Effect of the Ionosphere on Space Systems and Communications. Naval Research Lab.. Washington. D. C. Symp. held at Arlington. Va.. 20-22 Jan. 1975
ABS:Papers primarily dealing with ionospheric scintillation are presented. Topic areas include: High altitude morphology; spectra of amplitude and phase scintillation; amplitude and fade statistics for equatorial scintillation; holographic radio camera technique for studying ionospheric inhomogeneities; electron and ion density studies; Faraday rotation and angle of arrival measurements; and solar cycle variations of the total electron content at low latitude.
AD-A008939   75/00/00   75N30714

A deterministic propagation model for the rough earth
A/CASTELLINI. N. R. Army Electronics Command. Fort Monmouth. N. J.
ABS:The paper develops a deterministic mathematical model for the prediction of the field generated at any point by radio wave propagated over the rough earth. The model considers all wave paths associated with surface discontinuities and identifies those that contribute to a first order approximation. It accounts for the effects of refraction. reflection and diffraction and gives formulas for the terminal field and for the reflection coefficient.
AD-A003840 ECOM-4280   74/11/00   75N26232

Predicting long-term operational parameters of high-frequency sky-wave telecommunication systems
A/BARGHAUSEN. A. F.; B/FINNEY. J. W.; C/PROCTOR. L. L.; D/SCHULTZ. L. D. Institute for Telecommunication Sciences. Boulder. Colo.
ESSA-TR-ERL-110-ITS-78   69/05/00   70N24144

accomplished by starting with the scintillation model developed by Fremouw and Rino (1973). adding a geomagnetic-activity dependence for the behavior of scintillation-producing ionospheric irregularities. and substituting a more accurate and general scattering theory for that of Briggs and Parkin (1963) used in the earlier model. The results of those efforts have been implemented in two computer programs. The first. entitled RFMOD. contains the main elements of the scattering theory. the morphological model for ionospheric irregularity strength and other parameters. and subroutines for calculating the geometry and other relevant quantities from user-specified inputs.
AD-A023197 RADC-TR-76-35   76/02/00   76N31390

Some expansions for an electromagnetic wave propagating through a spherically symmetric refracting medium
A/GIBSON. L. R. Naval Surface Weapons Center. Dahlgren. Va.
ABS:Three expansions are derived for an electromagnetic wave propagating through a spherically symmetric refracting medium. The first enables one to compute the phase path length for any vacuum zenith angle when a model for the index of refraction is given. The second enables one to compute the refracted zenith angle corresponding to any vacuum zenith angle. The third enables one to compute the various order effects that the refracting medium has on the received frequency. Although the three expansions are valid for any spherically symmetric refracting medium. they are particularly useful for a wave propagating through the ionosphere because of the fact that they split the terms according to increasing powers of inverse transmitter frequency and therefore. converge rapidly for signals of 150 mhz or higher. A satellite simulation computer program was developed and the first two expansions checked for consistency. It was found that they disagreed the most at large zenith angles. The difference. however. was less than 0.0003% at 85 deg. In addition. the third expansion was used to find the various order contributions to the received frequency. For small zenith angles around 5 deg. the second order contribution (second order in the expansion parameter; third order in inverse frequency) was only about 0.001 as great as the first order and at large zenith angles around 85 deg. the second order contribution was about 0.01 as great as the first order. The transmitter frequency was taken to be about 150 Mhz.
AD-A013216 NSWC/DL-TR-3344   75/06/00   76N13369

1c. System Performance

Developments in propagation and systems analysis for the OMEGA Navigation System

A/MORRIS, P. M. A/(U.S. Coast Guard, Washington, D.C.) (Canadian Symposium on Navigation, 2nd, Ottawa, Canada, Nov. 18, 1975.) Canadian Aeronautics and Space Journal, vol. 22, Mar.-Apr. 1976, p. 102-111.

ABS:Some efforts in signal-propagation and systems analysis conducted by the U.S. Coast Guard's OMEGA Navigational System Operations Detail are discussed. The development and utilization of three full-wave propagation-prediction models are described along with several prediction techniques and two models used in conjunction with full-wave signal calculations for S/N prediction schemes. Semiempirical propagation-correction models are outlined, and the formulation and compilation of signal coverage diagrams are reviewed. An OMEGA system-availability analysis and an error analysis are also considered. 76/04/00 76A33568

Scattering of a code-modulated radio signal and associated multipath range errors

A/MARGERUM, E. A.; B/ROHDE, F. W. Army Engineer Topographic Labs., Fort Belvoir, Va.

ABS:To account for range errors obtained when a code-modulated radio signal is used to make range measurements in a scattering environment, a mechanism termed 'carrier cancellation' is proposed. This allows for destructive interference between several nearly direct path signals, leaving the possibility for a weaker signal that has traveled over a longer path to predominate. A mathematical formulation of the phenomenon is given, and the equations derived are used for a computer simulation of the effects. The results of the simulation confirm that the proposed mechanism represents a viable explanation of the observed range errors.

AD-A047824 ETL-0125 77/01/00 78N17279

Performance prediction for short-range troposcatter links

A/DANIEL, L. D. Air Force Inst. of Tech., Wright-Patterson AFB, Ohio. (School of Engineering.)

ABS:Existing models which characterize the performance of troposcatter channels fail to give adequate results for short paths (less than 150 miles). In the paper, one such model, developed by Bello to predict the delay power spectrum of the channel, was modified by treating the scatter-angle exponent as a function of path length rather than a constant. This modification indicated that a first-order relationship between scatter-angle exponent and path length accurately modeled the available data from six short-range troposcatter systems. Use of the empirical relationship results in significantly improved Bello model

performance predictions for the paths analyzed. This modified model accurately predicted the performance of a medium length (168 mile) path, indicating that the modification may be valid for paths greater than 150 miles. AD-A019811 GE/EE/75-22 75/12/00 76N25460

Message receipt probabilities

A/HARDEBECK, T. M.; B/KAMM, J. M., JR. Air Force Weapons Lab., Kirtland AFB, N. Mex.

ABS:A method for evaluating digital communication systems performance is given. This method involves calculating the probability that a formatted message transmitted by the system is correctly received. Communication systems which employ radio wave propagation are susceptible to degradation of the propagated signal. Degradation of the signal occurs even in normal conditions because of various disturbances to the medium through which the signal passes. Nuclear detonation, far more so, produce severe disturbances. There are mathematical models incorporated in computer codes which assist in rapid calculation of various quantities used to describe degradation. These quantities include: signal absorption and signal to noise ratio. For the commander, these quantities do not answer the main question, which is, will the system perform its mission. This report is an attempt to bridge the gap between the output of the system codes and the data required for command decisions. To do this, the probability of receiving a correct message is calculated. This message probability is an easily understood measure of system performance upon which command decisions can be based.

AD-A017852 AFWL-TR-75-172 75/11/00 76N21376

Performance evaluation of data modems for the aeronautical satellite channel

A/DUNCOMBE, C. B.; B/SALWEN, H. B/(Proteon Associates, Inc.) Transportation Systems Center, Cambridge, Mass.

ABS:The modems tested included a high performance DPSK modem, a high performance CPSK modem, two hybrid voice/data modems, and a lower performance CPSK modem. Data performance results are presented in the form of probability of bit error versus signal to noise density and signal to multipath ratios with Doppler spread as a parameter. Some tests were conducted with a hard limiting IF processor in cascade with the channel simulator to simulate satellite characteristics. The characteristics of the aeronautical satellite channel simulator are also described.

AD-A017085 DOT-TSC-FAA-75-13 FAA-RD-75-150 75/09/00 76N21373

Proceedings of Symposium on the Effect of the Ionosphere on Space Systems and Communications. Naval Research Lab.. Washington, D. C. Symp. held at Arlington, Va., 20-22 Jan. 1975

ABS:Papers primarily dealing with ionospheric scintillation are presented. Topic areas include: High altitude morphology; spectra of amplitude and phase scintillation; amplitude and fade statistics for equatorial scintillations; holographic radio camera technique for studying ionospheric inhomogeneities; electron and ion density studies; Faraday rotation and angle of arrival measurements; and solar cycle variations of the total electron content at low latitude.
AD-A008939   75/00/00   75N30714

Propagation effects at radio frequencies on satellite navigation systems
A/PISACANE. V. L.; B/FEEN. M. M. Applied Physics Lab.. Johns Hopkins Univ.. Silver Spring. Md.

ABS:The report discusses the effects of the neutral and ionized atmosphere on radio frequency signals used in satellite navigation systems. Knowledge of the signal velocity along the transmission path is necessary to properly interpret the navigation measurements. A technique for taking into account the influence of the neutral atmosphere on radio frequency signals is discussed. The algorithm is based on modeling of the refractive index as a function of surface temperature, pressure, and humidity. Several techniques for accounting for the effects of the ionized atmosphere at VHF and UHF are considered. Recent results are presented on the development of corrective algorithms that could be used operationally by navigators. The techniques developed are based on real-time prediction of the atmospheric electron density distribution.
AD-784378 APL-TG-1243   74/05/00   75N10747

Corrections for tropospheric range error
A/ALTSHULER. E. E. Air Force Cambridge Research Labs.. L. G. Hanscom Field. Mass. (Microwave Physics Lab.)

ABS:Satellite systems like the 621B have been proposed for air traffic control and navigation. Such systems are designed to provide aircraft position and velocity data based on time delay measurements of propagation between the aircraft and a network of satellites. Since the index of refraction of the troposphere is greater than unity, radiowaves propagate through the troposphere slower than through freespace and the time delay is therefore longer. Range error corrections calculated from various models of index of refraction generally require the use of numerical methods and a large capacity high speed computer. This paper presents a simple empirical expression for range error for elevation angles above 5 degrees. The CRPL Reference Atmosphere 1958 was the model used. A simple regression line that yields range error corrections within 1 percent of the values obtained by means of more sophisticated techniques was derived.
AD-731170 AFCRL-71-0419 AFCRL-ERP-369   71/07/27
72N15600

SECTION 2

OPTICAL PROPAGATION

1a. Media Characterization

An integral representation for eigenfunctions of linear ordinary differential operators
A/SYMES. W. Wisconsin Univ. - Madison. (Mathematics Research Center.)
ABS:This paper generalizes an integral representation formula for eigenfunctions of Sturm-Liouville operators, known as the Volterra transformation operator in the theory of the inverse scattering problem, to higher-order differential operators. A specific fourth-order initial value problem is considered whose solutions are expressed as an inverse-Laplace-Borel transform.
AD-A054543 MRC-TSR-1824 78/01/00 78N29832

Fast Poisson solvers on general two dimensional regions for the Dirichlet problem
A/SHIEH. A. S. L. Wisconsin Univ., Madison. (Mathematics Research Center.)
ABS:It is shown that by using the simplest construction of discrete dipoles. the operation count for solving the Dirichlet problem of Poisson's equation by the capacitance matrix method does not exceed constant times n-squared log n. $n = 1/h$ for certain first and second order schemes of interpolating boundary conditions.
AD-A054539 MRC-TSR-1820 78/01/00 78N29830

Estimation and identification for modeling dynamic systems
A/MENDEL. J. M. University of Southern Calif., Los Angeles. (Dept. of Electrical Engineering.)
ABS:Systems are modelled in order to understand and explain them better and as a prelude to action. The study has been aimed at two problem areas: multi-stage modelling estimation and identification algorithms for dynamic systems, and state estimation and a parameter identification for a new class of models -- causal functional equations -- which describe wave propagation in layered media systems. The first problem is concerned with developing estimation algorithms both for parameter and state estimation that are recursive in the dimension of the parameter vector or state vector. The second problem is concerned with developing whole new theories of state estimation and parameter identification for a new class of equations which is referred to as causal functional equations. Eight new papers were submitted or accepted for publication.
AD-A053583 AFOSR-78-0767TR 78/03/27 78N29826

Estimation and detection of Lie groups
A/LO. J. T. H. Maryland Univ., Baltimore. (Div. of Mathematics and Physics.)
ABS:A new approach developed in recent years for nonlinear estimation and detection is the employment of the differential geometric techniques. In this report, this approach is surveyed and the ideas of rolling without slipping and the exponential Fourier densities are discussed in great detail. Some new results on estimation on general compact Lie groups are also included.
AD-A053633 MRR-77-11 AFOSR-78-0734TR 77/10/00 78N29821

Applications of hybrid and digital computation methods in aerospace-related sciences and engineering
A/HUANG. C. J.; B/MOTARD. R. L. Houston Univ., Tex. (Coll. of Engineering.)
ABS:The computing equipment in the engineering systems simulation laboratory of the Houston University Cullen College of Engineering is described and its advantages are summarized. The application of computer techniques in aerospace-related research psychology and in chemical. civil. electrical. industrial. and mechanical engineering is described in abstracts of 84 individual projects and in reprints of published reports. Research supports programs in acoustics. energy technology. systems engineering. and environment management as well as aerospace engineering.
NASA-CR-157364 78/07/00 78N29820

The finite element method applied to a class of time-dependent nonlinear partial differential equations
A/MAZHAR. Z. Waterloo Univ. (Ontario). (Dept. of Mechanical Engineering.)
ABS:The finite element - Galerkin approximation is utilized for the solution of a class of time-dependent partial differential equations. Among the types of partial differential equations considered are unsteady linear/nonlinear heat conduction and also diffusion of a concentration in a fluid flow. A considerable number of problems are solved and compared with the available finite difference and/or variational and/or analytical solutions. Some interesting observations are also discussed parallel to the solution procedure and presentation of results. The highly sparse algebraic systems of equations are solved by means of the Gauss-Seidel iteration method. Based on the available literature and the observations had. the efficiency of the Gauss-Seidel method for this type of problems is also discussed. Triangular idealization and linear elements are used throughout the formulation. A computer program is also presented. in which. with some minor changes. higher order elements can also be utilized.
TN-21 77/05/00 78N29819

Runge-Kutta formulas with extended regions of stability
A/SEPEHRONOORI. K. Texas Univ.. Austin.
ABS:The development of Runge-Kutta formulas with special
properties is described. These formulas have limited
storage requirements and are suitable for the integration
of large systems of ordinary differential equations.
Furthermore. the coefficients of these formulas can be
chosen such that the methods are appropriate for the
integration of systems that possess certain ill-conditioned
stability properties. These Runge-Kutta formulas can be
used in conjunction with the method of lines for solving
partial differential equations arising in a number of
fields of applied mathematics. 77/00/00
78N29818

The Bohl transformation and oscillation of linear
differential systems
A/GOFF. S. Massachusetts Univ.. Amherst.
ABS:The (scalar) Bohl transformation is generalized for
the purpose of answering questions for self-adjoint matrix
systems. A comparison-type theorem for one of the
self-adjoint matrix systems is established. 78/00/00
78N29817

Optical modelling of the atmosphere
A/MCCLATCHEY. R. A.: B/SZLBY. J. E. A.: C/GARING. J.
S. Air Force Cambridge Research Labs.. L. G. Hanscom
Field. Mass. In AGARD Opt. Propagation in the Atmosphere
21 p (SEE N76-29815 20-46)
ABS:Optical atmospheric modelling requires both the
knowledge of the physical properties of the atmosphere as
well as the spectroscopic properties of the gases and
particulates of which it is composed. The atmospheric
absorption line parameter compilation system is discussed
and requirements for such a data compilation are indicated.
The line-by-line transmittance calculation technique is
described. indicating the capability of this technique for
use in laser propagation studies as well as low spectral
resolution applications. The LOWTRAN computer model is
presented together with an indication of its limitations.
76/05/00   76N29816

2b. Propagation Phenomena
and Simulation

Laser beam propagation model with a hydrodynamic treatment
of the transmission medium.
  A/MAHER, W. E. A/(Boeing Scientific Research
Laboratories. Seattle, Wash.) (Optical Society of America
and Institute of Electrical and Electronics Engineers,
Conference on Laser Engineering and Applications,
Washington, D.C., June 2-4, 1971.) Applied Optics. vol.
11, Feb. 1972, p. 249-256.
  ABS:The difference between pulsed and CW laser beam
propagation through the atmosphere is demonstrated, using a
numerical model which couples a description of the laser
beam with a description of the medium through which the
beam passes. The model is developed to find the changes
that would result from the inclusion of a correct
hydrodynamic treatment of the propagation medium. The
changes in the focal plane profile of a propagating laser
beam determined from calculations with this model are
presented.
  CLEA PAPER 2.5   72/02/00   72A19380

Non-line-of-sight electro-optic laser communications in the
middle ultraviolet
  A/JUNGE, D. M.   Naval Postgraduate School, Monterey,
Calif.
  ABS:A Monte Carlo computer simulation was developed to
model hypothesized electro-optic laser communication
systems operating in the middle ultraviolet region of the
spectrum called the solar blind. By assuming various
source, propagation, and detector characteristics as well
as certain performance parameters it is possible to predict
the effective ranges and operating characteristics of such
a system.
  AD-A050019 NPS-6177001   77/12/00   78N20501

The limitations imposed by atmospheric breakdown on the
propagation of high power laser beams
  A/LENCIONI, D. E.   Lincoln Lab., Mass. Inst. of Tech.,
Lexington.   In AGARD Opt. Propagation in the Atmosphere
12 p (SEE N76-29815 20-46)
  ABS:The results of a series of experiments on laser
induced air breakdown at 10.6 and 1.06 micrometers are
reported. Threshold intensities for breakdown were
determined for clean air, aerosols, and single particles.
The clean air threshold was found to be in good agreement
with microwave breakdown theory. The presence of aerosol
particles was found to lower the threshold by an amount
which depended mainly on particle size and laser pulse
length. Only a slight material dependence was found with
the one exception of water particles which had the least
effect on threshold. The particle induced thresholds were
found to scale as wavelength to the minus two power for 100

nsec pulse lengths. The dynamics of the particle initiated
threshold were studied. For intensities slightly above
threshold the plasma grew within the beam as an
axisymmetric volume surrounding the particle. At higher
intensities the plasma formed as a highly absorbing thin
disk which grew radially and propagated back towards the
laser.   76/05/00   76N29846

Numerical methods in high power laser propagation
  A/ULRICH, P. B.   Naval Research Lab., Washington, D. C.
In AGARD Opt. Propagation in the Atmosphere 19 p (SEE
N76-29815 20-46)
  ABS:Numerical solutions to the complex nonlinear
problems of the interaction of high energy lasers with the
atmosphere have played an important role in the
understanding and development of this important and
interesting field. Summarized are the relevant partial
differential equations that apply, the kinds of numerical
algorithms employed in their solution and representative
results of a variety of cases of interest. Comparison with
experiment is made wherever possible. Other effects which
impact the thermal blooming phenomena are also addressed.
76/05/00   76N29845

An overview of the limitations on the transmission of high
energy laser beams through the atmosphere by nonlinear
effects
  A/EDELBERG, S.   Lincoln Lab., Mass. Inst. of Tech.,
Lexington.   In AGARD Opt. Propagation in the Atmosphere
15 p (SEE N76-29815 20-46)
  ABS:The important nonlinear effects which limit high
energy laser propagation through the atmosphere are
reviewed. The two most important effects are thermal
blooming (or thermal defocussing) and air breakdown within
the beam. A third, less important effect is stimulated
raman scattering. The possibility of transmitting laser
beams through fogs, clouds or haze by boring holes through
these atmospheric media with the laser beam is also
reviewed. The laser's waveform is considered to be a train
of pulses. It is shown that the waveform design and other
important parameters such as range to the focal plane,
aperture and focal spot size, pulse intensity, etc., can be
chosen to avoid the thermal blooming of individual pulses
and air breakdown. The limit on beam propagation is then
caused by thermal blooming due to the cumulative heating by
the pulses in the train. An added set of parameters then
controls this multipulse blooming including beam slew rate,
cross wind velocity, and interpulse spacing. Parametric
tradeoffs required to satisfactorily control thermal
blooming and quantitative results for several parametric
choices are summarized.   76/05/00   76N29844

Propagation of high power laser beams through the atmosphere: An overview
A/HAYES, J. N. Naval Research Lab., Washington, D. C.
In AGARD Opt. Propagation in the Atmosphere 15 p (SEE
N76-29815 20-46)
ABS:The major categories of the thermal blooming
phenomena encountered in the propagation of high power
laser beams in the open atmosphere are developed. The basic
physical ideas behind each type of blooming phenomenon are
discussed; experimental data and theoretical formulation
are briefly presented that show the present state of
knowledge.   76/05/00   76N29843

Propagation of focused laser beams in the turbulent
atmosphere
A/RAIDT, H.   Forschungsinstitut fuer Optik, Tuebingen
(West Germany).   In AGARD   Opt. Propagation in the
Atmosphere 12 p (SEE N76-29815 20-46)
ABS:Experimental results from investigations of
instantaneous intensity distributions in focused laser
beams at 0.63 micrometer and 10.6 micrometer at distances
of approximately 1.3 km, 5 km and 8.6 km are presented and
discussed. At 0.63 micrometer the beam pattern is broken up
into several diffraction scale spots because focusing is
saturated, except for weak turbulence and short propagation
distance. At 10.6 micrometer the beam pattern is almost
uniform, as long as the beam dimensions are smaller than
the correlation length of the amplitude.   76/05/00
76N29835

Theoretical studies of the transfer of solar radiation in
the atmosphere
A/KERSCHGENS, M. J.; B/RASCHKE, E.; C/REUTER, U.
Cologne Univ. (West Germany).   (Inst. fuer Geophysik und
Meteorologie).   In AGARD   Opt. Propagation in the
Atmosphere 10 p (SEE N76-29815 20-46)
ABS:The transfer of solar radiation in one dimensional
model atmospheres has been computed for the wavelength
range from 0.2 to 3.58 micrometer with an iterative
solution of the radiative transfer equation. Absorption by
O3, H2O, CO2, O2 and aerosols has been taken into account.
The transmission in near infrared bands of CO2 and H2O is
approximated by exponential series derived from spectral
measurements. Various vertical distributions of H2O and
aerosols are considered and also two different boundaries
are used: a rough ocean surface and a bright sandy desert.
It is shown, for instance that as a result of the higher
albedo of the sand surface, the absorption increases by 5
to 7% depending on the solar height. Aerosol layers in the
lower troposphere are much more effective respective to
absorption. They may alter by almost 40% the radiative
heating.   76/05/00   76N29827

Methods for solving the equation of radiative transfer
through finite thickness layers
A/LENOBLE, J.   Universite des Sciences et Techniques de
Lille (France).   In AGARD   Opt. Propagation in the
Atmosphere 9 p (SEE N76-29815 20-46)
ABS:After recalling the general problem of radiative
transfer, the methods of solution for a plane parallel
horizontally homogeneous atmosphere are briefly reviewed
and a few numerical comparisons are shown. Then the more
difficult problems of horizontal inhomogeneities and of
sphericity are considered.   76/05/00   76N29825

Multiple scattering in planetary atmospheres
A/IRVINE, W. M.   Massachusetts Univ., Amherst.
(Dept. of Physics and Astronomy.)   In AGARD   Opt.
Propagation in the Atmosphere 11 p (SEE N76-29815 20-46)
ABS:Certain simple procedures for solving radiative
transfer problems in planetary atmospheres are reviewed:
the similarity relations relating isotropic to anisotropic
scattering, asymptotic results relating known solutions for
semi-infinite layers to desired solutions for optical
depths, and expansions relating known solutions for
conservative scattering to desired solutions for the nearly
conservative case. The complications introduced by
atmospheric inhomogeneity, surface reflection, and spectral
features are also discussed.   76/05/00   76N29824

Optical SATCOM
A/DRISCOLL, R. G.; B/DIX, E. L.   Naval Electronics
Lab. Center, San Diego, Calif.
ABS:This report covers work accomplished during the
fourth reporting period of the program. The underwater
propagation experiment has been fielded at Santa Catalina
Island, California. A complete system check of the
components which will be used for the coherent CO2 laser
propagation experiment, which is scheduled to be fielded in
Hawaii this September, has been accomplished. The
objectives of the optical SATCOM atmospheric-propagation
test plan are: Determine, qualitatively, whether optical
heterodyne communication at 10.6 micrometers (CO2 laser
wavelength) is feasible under marine weather conditions,
specifically when transmission is through clouds, and to
develop, quantitatively, data needed to validate
theoretical models of such propagation.
AD-A013196   75/06/30   76N13171

Optical SATCOM
A/LEONARD. D. R.; B/DIX. E. L. Naval Electronics Lab.
Center. San Diego. Calif.
ABS:The primary objectives of the Experiment are the
following: Determine. qualitatively. whether optical
heterodyne communications is feasible under marine weather
conditions. including transmission through clouds: and.
develop. quantitatively. data needed to validate
theoretical models of such propagation. The experiment
will be conducted in three phases: as follows: Calibration
of transceiver units: Field checkout of the units with some
support measurement at San Diego: and. Field experiment at
Hawaii. The basic technique employed will be to measure
the transceiver carrier-to-noise (C/N) ratio as a function
of the optical thickness of the cloud filling the
propagation path.
AD-A008190 75/03/31 75N25017

A model for estimating joint probabilities of cloud-free
lines-of-sight from unconditional probabilities
A/LUND. I. A.; B/GRANTHAM. D. D. Air Force Cambridge
Research Labs.. L. G. Hanscom Field. Mass.
ABS:Signals transmitted through the atmosphere in the
visible and infrared portions of the electromagnetic
spectrum can be seriously degraded by clouds between the
source and the receiver. A previously published model
yields from the probability distribution of sky cover. an
estimate of the unconditional probability of a cloud-free
line-of-sight through the atmosphere at any desired
elevation angle and geographical location. Another
published model yields an estimate of the joint probability
of a cloud-free line-of-sight from n of m observing sites.
from joint probabilities of the sky cover Categories. This
paper describes a model for estimating the joint
probabilities from the easily obtainable unconditional
probabilities only.
AD-A003160 AFCRL-TR-74-0586 74/00/00
75N21508

2c. System Performance

Atmospheric limitations of active and passive night vision systems

A/YOUNGS. E. G. D. Marconi-Elliot Avionic Systems Ltd.. Basildon (England). In AGARD Opt. Propagation in the Atmosphere 7 p (SEE N76-29815 20-46)

ABS:The ways in which the earth's atmosphere affect the image quality of night vision devices are discussed. and of particular interest here is the effect on apparent contrast. Atmospheric problems are considered that are associated with the use of supplementary illumination. Continuously emitting searchlights are briefly outlined. and techniques associated with pulsed illuminators are considered. A summary is given of a basic mathematical model for such a system. 76/05/00 76N29857

Measured visible spectrum properties of real atmospheres

A/DUNTLEY. S. Q. California Univ.. La Jolla. In AGARD Opt. Propagation in the Atmosphere 14 p (SEE N76-29815 20-46)

ABS:Measurements of the visible spectrum properties of the atmosphere which govern the apparent contrast of distant objects have been made from aircraft. spacecraft. and ground stations in various parts of the world throughout the past thirty years. Samples of these data are presented and the techniques of measurement that were used are described. Examples are given to illustrate how the data can be used to predict the limiting ranges of detection. recognition. classification. and identification of any specific object by airborne. spaceborne. and ground based observers or imaging devices. 76/05/00 76N29853

How many pictures do you have to take to get a good one?

A/FRIED. D. L. Optical Science Consultants. Yorba Linda. Calif. In AGARD Opt. Propagation in the Atmosphere 11 p (SEE N76-29815 20-46)

ABS:In short exposure imaging through turbulence. there is some probability that the image will be nearly diffraction limited because the instantaneous wave front distortion over the aperture was negligible. It is shown that the probability of obtaining a good short exposure image corresponds to a hyperspace integral in which the spatial dimensions are the independent random coefficients in an orthonormal series expansion. It is equal to the probability that a randomly chosen point in the hyperspace will lie within a hypersphere of unit radius. the points in the hyperspace being randomly chosen in accordance with the product of independent Gaussian probability distributions - one distribution for each dimension. The variances of these distributions are directly proportional to the eigenvalues of the Karhunen-Loeve equation. This hyperspace integral (involving up to several hundred dimensions) has been evaluated using Monte Carlo techniques. 76/05/00 76N29851

Computer simulation of atmospheric turbulence and compensated imaging systems

A/MCGLAMERY. B. L. California Univ.. San Diego. In AGARD Opt. Propagation in the Atmosphere 17 p (SEE N76-29815 20-46)

ABS:The earth's turbulent atmosphere severely limits the resolution of conventional ground based telescopes. Methods of reducing this limitation for ground based telescopes include post detection processing in which the blurred recorded image is processed to extract information not discernable to the human visual system. and pre-detection compensation in which the wave front deformations are dynamically corrected in the optical system before the image is recorded. Computer simulations of both of these methods are presented. The simulations demonstrate that the post detection processing method produces only moderate improvement in resolution due to signal to noise limitations while the pre-detection method gives very significant improvements. As a part of the simulations. techniques of generating instantaneous realizations of wave fronts deformed by atmospheric turbulence and their corresponding point spread functions are presented. 76/05/00 76N29850

Determination of slant visual range from lidar signatures. analysis of simulated signatures.

A/GAZZI. M.: B/VICENTINI. V.: C/PANTANI. L.: D/RADICATI. B.: E/STEFANUTTI. L.: F/WERNER. C. F/(DFVLR) Consiglio Nazionale delle Ricerche. Bologna (Italy). In AGARD Opt. Propagation in the Atmosphere 19 p (SEE N76-29815 20-46)

ABS:The measurement of the slant visual range by means of lidars involves two main problems: the extraction of the atmospheric extinction coefficient from the lidar signature and the calculation of the slant visual range from the extinction coefficient. These problems were solved for the particular situation of a landing in low visibility conditions. An equation was obtained which allows the computation of the visual range from the extinction coefficient in every hour of the day both for extended and point sources. In order to compare the different methods for the extraction of the extinction coefficient from the lidar signatures some atmospheric situations were simulated on a computer. and the lidar equation was calculated. The simulated signatures were then processed by different methods and the results were collated. A new procedure for the processing of lidar signatures was introduced. 76/05/00 76N29849

Compensated imaging
A/JUSTICE, J. W.; B/URTZ, R. P., JR. B/(RADC, Griffiss AFB, N. Y.) Defense Advanced Research Projects Agency, Arlington, Va. In AGARD Opt. Propagation in the Atmosphere 17 p (SEE N76-29815 20-46)
ABS:The presence of the atmosphere degrades the imaging performance of large telescopes. Optical phase distortion imposed by atmospheric turbulence causes a loss in resolution capability of from 10 to 30 times a system's theoretical performance. A compensated imaging approach is reported which allows the retrieval of low contrast information by active adaptation of the telescope system to atmospheric conditions. This is accomplished through the use of real time wavefront sensing coupled with fast response deformable optics. In practice, the wavefront entering the telescope is measured to determine its wavefront deformation (optical path length difference across the aperture) and a mirror is then deformed to the conjugate of the deformations, producing a near diffraction limited image on a sensor. Analysis of the wavefront correction capabilities has been completed. 76/05/00
76N29848

Optical SATCOM
A/DRISCOLL, R. G.; B/DIX, E. L. Naval Electronics Lab. Center, San Diego, Calif.
ABS:This report covers work accomplished during the fourth reporting period of the program. The underwater propagation experiment has been fielded at Santa Catalina Island, California. A complete system check of the components which will be used for the coherent CO2 laser propagation experiment, which is scheduled to be fielded in Hawaii this September, has been accomplished. The objectives of the optical SATCOM atmospheric-propagation test plan are: Determine, qualitatively, whether optical heterodyne communication at 10.6 micrometers (CO2 laser wavelength) is feasible under marine weather conditions, specifically when transmission is through clouds, and to develop, quantitatively, data needed to validate theoretical models of such propagation.
AD-A013196 75/06/30 76N13171

Optical SATCOM
A/LEONARD, D. R.; B/DIX, E. L. Naval Electronics Center, San Diego, Calif.
ABS:The primary objectives of the Experiment are the following: Determine, qualitatively, whether optical heterodyne communications is feasible under marine weather conditions, including transmission through clouds; and, develop, quantitatively, data needed to validate theoretical models of such propagation. The experiment will be conducted in three phases; as follows: Calibration of transceiver units; Field checkout of the units with some support measurement at San Diego; and, Field experiment at Hawaii. The basic technique employed will be to measure the transceiver carrier-to-noise (C/N) ratio as a function of the optical thickness of the cloud filling the propagation path.
AD-A008190 75/03/31 75N25017

REPORT DOCUMENTATION PAGE

1. Recipient's Reference	2. Originator's Reference	3. Further Reference	4. Security Classification of Document
	AGARD-LS-99	ISBN 92-835-1322-3	UNCLASSIFIED

5. Originator	Advisory Group for Aerospace Research and Development North Atlantic Treaty Organization 7 rue Ancelle, 92200 Neuilly sur Seine, France

6. Title	AEROSPACE PROPAGATION MEDIA MODELLING AND PREDICTION SCHEMES FOR MODERN COMMUNICATIONS, NAVIGATION AND SURVEILLANCE SYSTEMS

7. Presented	on 4–5 June 1979 in London, UK; 14–15 June 1979 in Boulder, USA.

8. Author(s)/Editor(s)	9. Date
Various	May 1979

10. Author's/Editor's Address	11. Pages
Various	214 pages

12. Distribution Statement	This document is distributed in accordance with AGARD policies and regulations, which are outlined on the Outside Back Covers of all AGARD publications.

13. Keywords/Descriptors	
Electromagnetic wave transmission Mathematical models Mathematical prediction Ionospheric disturbances	Atmospheric models Navigation Telecommunication Surveillance

14. Abstract

The Lecture Series will review modelling and prediction topics which have been presented at a number of meetings of the AGARD Electromagnetic Wave Propagation Panel in the last few years. Modelling and Prediction Schemes of the aerospace radio and optical propagation environment based on media characterization have become essential to meet requirements of operational accuracies in communication, navigation, and surveillance in military and civilian systems.

The lectures include the following topics:
- General modelling and prediction schemes;
- Aerospace (atmosphere, ionosphere, and the space environment) media-characterization;
- Short- and long-term prediction techniques across the RF and optical spectrum and agreement with observational data;
- Detection and communications through scattering channels;
- Adaptability of prediction techniques to radio and optical communication, navigation and surveillance systems operating in the aerospace environment; and
- Effects of geophysical disturbances on the state of the media and their predictability.

The material in this publication was assembled in support of a Lecture Series under the sponsorship of the Electromagnetic Wave Propagation Panel and the Consultant and Exchange Programme of AGARD.

AGARD Lecture Series No.99 Advisory Group for Aerospace Research and Development, NATO AEROSPACE PROPAGATION MEDIA MODELLING AND PREDICTION SCHEMES FOR MODERN COMMUNICATIONS, NAVIGATION, AND SURVEILLANCE SYSTEMS Published May 1979 214 pages The Lecture Series will review modelling and prediction topics which have been presented at a number of meetings of the AGARD Electromagnetic Wave Propagation Panel in the last few years. Modelling and Prediction Schemes of the aerospace radio and optical propagation environment based on P.T.O.	AGARD-LS-99 Electromagnetic wave transmission Mathematical models Mathematical prediction Ionospheric disturbances Atmospheric models Navigation Telecommunication Surveillance
AGARD Lecture Series No.99 Advisory Group for Aerospace Research and Development, NATO AEROSPACE PROPAGATION MEDIA MODELLING AND PREDICTION SCHEMES FOR MODERN COMMUNICATIONS, NAVIGATION, AND SURVEILLANCE SYSTEMS Published May 1979 214 pages The Lecture Series will review modelling and prediction topics which have been presented at a number of meetings of the AGARD Electromagnetic Wave Propagation Panel in the last few years. Modelling and Prediction Schemes of the aerospace radio and optical propagation environment based on P.T.O.	AGARD-LS-99 Electromagnetic wave transmission Mathematical models Mathematical prediction Ionospheric disturbances Atmospheric models Navigation Telecommunication Surveillance
AGARD Lecture Series No.99 Advisory Group for Aerospace Research and Development, NATO AEROSPACE PROPAGATION MEDIA MODELLING AND PREDICTION SCHEMES FOR MODERN COMMUNICATIONS, NAVIGATION, AND SURVEILLANCE SYSTEMS Published May 1979 214 pages The Lecture Series will review modelling and prediction topics which have been presented at a number of meetings of the AGARD Electromagnetic Wave Propagation Panel in the last few years. Modelling and Prediction Schemes of the aerospace radio and optical propagation environment based on P.T.O.	AGARD-LS-99 Electromagnetic wave transmission Mathematical models Mathematical prediction Ionospheric disturbances Atmospheric models Navigation Telecommunication Surveillance
AGARD Lecture Series No.99 Advisory Group for Aerospace Research and Development, NATO AEROSPACE PROPAGATION MEDIA MODELLING AND PREDICTION SCHEMES FOR MODERN COMMUNICATIONS, NAVIGATION, AND SURVEILLANCE SYSTEMS Published May 1979 214 pages The Lecture Series will review modelling and prediction topics which have been presented at a number of meetings of the AGARD Electromagnetic Wave Propagation Panel in the last few years. Modelling and Prediction Schemes of the aerospace radio and optical propagation environment based on P.T.O.	AGARD-LS-99 Electromagnetic wave transmission Mathematical models Mathematical prediction Ionospheric disturbances Atmospheric models Navigation Telecommunication Surveillance

media characterization have become essential to meet requirements of operational accuracies in communication, navigation and surveillance in military and civilian systems.

The lectures include the following topics:

— General modelling and prediction schemes
— Aerospace (atmosphere, ionosphere, and the space environment) media-characterization
— Short- and long-term prediction techniques across the RF and optical spectrum and agreement with observational data
— Detection and communications through scattering channels
— Adaptability of prediction techniques to radio and optical communication, navigation and surveillance systems operating in the aerospace environment
— Effects of geophysical disturbances on the state of the media and their predictability

The material in this publication was assembled in support of a Lecture Series under the sponsorship of the Electromagnetic Wave Propagation Panel and the Consultant and Exchange Programme of AGARD.

B206
4

AGARD

NATO ⊕ OTAN

7 RUE ANCELLE · 92200 NEUILLY-SUR-SEINE

FRANCE

Telephone 745.08.10 · Telex 610176

DISTRIBUTION OF UNCLASSIFIED
AGARD PUBLICATIONS

AGARD does NOT hold stocks of AGARD publications at the above address for general distribution. Initial distribution of AGARD publications is made to AGARD Member Nations through the following National Distribution Centres. Further copies are sometimes available from these Centres, but if not may be purchased in Microfiche or Photocopy form from the Purchase Agencies listed below.

NATIONAL DISTRIBUTION CENTRES

BELGIUM
Coordonnateur AGARD – VSL
Etat-Major de la Force Aérienne
Quartier Reine Elisabeth
Rue d'Evere, 1140 Bruxelles

CANADA
Defence Scientific Information Service
Department of National Defence
Ottawa, Ontario K1A OZ2

DENMARK
Danish Defence Research Board
Østerbrogades Kaserne
Copenhagen Ø

FRANCE
O.N.E.R.A. (Direction)
29 Avenue de la Division Leclerc
92 Châtillon sous Bagneux

GERMANY
Zentralstelle für Luft- und Raumfahrt-
dokumentation und -information
c/o Fachinformationszentrum Energie,
Physik, Mathematik GmbH
Kernforschungszentrum
7514 Eggenstein-Leopoldshafen 2

GREECE
Hellenic Air Force General Staff
Research and Development Directorate
Holargos, Athens, Greece

ICELAND
Director of Aviation
c/o Flugrad
Reykjavik

ITALY
Aeronautica Militare
Ufficio del Delegato Nazionale all'AGARD
3, Piazzale Adenauer
Roma/EUR

LUXEMBOURG
See Belgium

NETHERLANDS
Netherlands Delegation to AGARD
National Aerospace Laboratory, NLR
P.O. Box 126
Delft

NORWAY
Norwegian Defence Research Establishment
Main Library
P.O. Box 25
N-2007 Kjeller

PORTUGAL
Direcção do Serviço de Material
da Forca Aerea
Rua da Escola Politecnica 42
Lisboa
Attn: AGARD National Delegate

TURKEY
Department of Research and Development (ARGE)
Ministry of National Defence, Ankara

UNITED KINGDOM
Defence Research Information Centre
Station Square House
St. Mary Cray
Orpington, Kent BR5 3RE

UNITED STATES
National Aeronautics and Space Administration (NASA)
Langley Field, Virginia 23365
Attn: Report Distribution and Storage Unit

THE UNITED STATES NATIONAL DISTRIBUTION CENTRE (NASA) DOES NOT HOLD
STOCKS OF AGARD PUBLICATIONS, AND APPLICATIONS FOR COPIES SHOULD BE MADE
DIRECT TO THE NATIONAL TECHNICAL INFORMATION SERVICE (NTIS) AT THE ADDRESS BELOW.

PURCHASE AGENCIES

Microfiche or Photocopy
National Technical
Information Service (NTIS)
5285 Port Royal Road
Springfield
Virginia 22161, USA

Microfiche
Space Documentation Service
European Space Agency
10, rue Mario Nikis
75015 Paris, France

Microfiche
Technology Reports
Centre (DTI)
Station Square House
St. Mary Cray
Orpington, Kent BR5 3RF
England

Requests for microfiche or photocopies of AGARD documents should include the AGARD serial number, title, author or editor, and publication date. Requests to NTIS should include the NASA accession report number. Full bibliographical references and abstracts of AGARD publications are given in the following journals:

Scientific and Technical Aerospace Reports (STAR)
published by NASA Scientific and Technical
Information Facility
Post Office Box 8757
Baltimore/Washington International Airport
Maryland 21240, USA

Government Reports Announcements (GRA)
published by the National Technical
Information Services, Springfield
Virginia 22161, USA